Investigating the Stress and Strain fields in Porous Synthetic Bone Graft Substitute Materials with Varied Porosity Levels

By

Mouna Chetehouna

MEng (Hons) Medical Materials Science and Engineering

For the fulfilment of the degree of

Doctor of Philosophy

Supervision

Dr. Karin Hing

Professor. Antonio Munjiza

Dr. Ettore Barbieri

Queen Mary University of London

School of Engineering and Material Science

Statement of originality

I, Mouna Chetehouna, confirm that the research included within this thesis is my own work or that where it has been carried out in collaboration with, or supported by others, that this is duly acknowledged below and my contribution indicated. Previously published material is also acknowledged below.

I attest that I have exercised reasonable care to ensure that the work is original, and does not to the best of my knowledge break any UK law, infringe any third party's copyright or other Intellectual Property Right, or contain any confidential material.

I accept that the College has the right to use plagiarism detection software to check the electronic version of the thesis. I confirm that this thesis has not been previously submitted for the award of a degree by this or any other university.

The copyright of this thesis rests with the author and no quotation from it or information derived from it may be published without the prior written consent of the author.

Signature:

Date:

Acknowledgment

I would like to thank the almighty God, for seeing me through once more. A big thank you to the most important people in my life, my wonderful daughters Joory and Batoul. Thank you for baring with me, standing by me being my true friends, my children, my parents at times and my everything all the time. I dedicate this to you my babies and I pray to see all your dreams come true.

I would like to sincerely thank my first supervisor Dr. Karin Hing for this opportunity, for the support, sincerity, patience, advice and the wonderful Jam. I would like to also thank my second supervisor Professor Antonio Munjiza, for the wise advice, the fascinating methods of teaching and all the BBQs. A special thank you to my supervisor Dr. Ettore Barbieri, for shining the light during the dark times, for helping me cross the finish line by teaching, supporting and believing in me even when I stopped believing. Thank you all for enriching my life and for helping me grow both personally and intellectually.

I would like to express my sincerest gratitude to my collegues and friends Dr. Elnaz Naghibi, Dr. Richard Windslow, Dr. Halimat Raji, Dr. Fang Su, Dr. Yousef Zawahreh and Mattia Gaglione for all their advice and support. A special thank you to the soon to be Doctors and special friends Miss Feng Yang, Miss Dinara Ikramova and the wonderful Mr Yamin Abdouni, Mr Szymon Doszczeczko and Mr Jorge Pavel Victoria Tafoya. Thank you for being the best friends any one could ever ask for. Thank you for the advice, the talks, the good energy, thank you for the good times and the crazy times, and a big thank you to our Godfather Dr. Henri Huijberts for being the greatest boss ever.

A special thank you to the staff at Beal High School, for their support and understanding, and especially Ms Stylianou, Ms Chadwick, Mr Laird, Mr Sydney-Smith and Mr McKenzie. It takes a village to raise a child, and I am glad I picked your village.

This work was funded by the Engineering and Physical Science Research Council (EPSRC)

Thesis Abstract

Porous hydroxyapatite (PHA) ceramic granules have been found to be highly successful synthetic bone graft substitute (BGS) materials, encouraging rapid, good quality bone healing. Key to the success of these materials is a hierarchical multi-scale pore structure, consisting of both macro pores (Larger than 50 μm in diameter) giving the granules their characteristic foam-like pore structure, and smaller micro pores (less than 20 μm in diameter) which are found within the 'struts' or 'body' of the foam structure.

It has been widely reported that control of the level of total porosity (dominated by the macro pores) has an impact on bone healing in BGS, the rate of remodelling and the nature of bone growth. However, within porous hydroxyapatite (PHA) granules the level of strut porosity and micro porosity have also been found to be key to the rate and pattern of bone growth. This has been hypothesised to be due to the variation in the macro-structure and micro-architecture of the BGS resulting in different level of strains experienced within the niche environments of the implanted granule masses, which in turn stimulates or supresses bone growth through mechano-transduction pathways.

The aim of this study was to develop, simulate and analyse finite element models of PHA granule masses. This is to identify whether changes in the level of strut and total porosities, could alter the patterns of stresses and strains exhibited within granule masses to effect local bone formation. Models for finite element analysis (FEA) were generated from micro-CT scans of cylinders packed with granule masses of different combinations of total and strut porosities. The procedure captured the natural porous architecture in a novel approach to the analysis of PHA.

The study demonstrated that PHA granules as a material maintain their heterogeneity and density at different scales and thus lend themselves to homogenisation techniques to create representative volume entities (RVEs).

The analysis incorporated RVEs of different sizes to investigate the continuity of the material behaviour. All the models were energetically validated. They were modelled using a linear elastic model as well as a plastic non-linear one typically used in soil and powder modelling applications. The non-linear Drucker-Prager cap model, was utilised combining a mathematical approach and mechanical testing techniques, to obtain the model's parameters, in an attempt to eliminate the need for extensive mechanical tests.

FEA on the representative volumes demonstrated a wholesale change in strain levels and distribution associated with the level of porosity. Changes in strut porosities showed a direct effect on the peak strain levels within the porous structures. Where the location of both stress and strain peaks as well as fields favoured the pore waists throughout all simulations with slight variation in the precision of concentration in response to changes in strut porosity.

These observations could explain the differences observed in the structure of bone growth within BGS materials with matched total porosities but varied levels of strut porosities. Moreover, they may also explain the phenomena where by bone formation within PHA has been observed to occur simultaneously within a single pore via both endochondral and mesenchymal pathways. These results suggest that the models generated in this PhD could be used to further investigate the effect of structure and strain manipulation to control the rate and quality of bone regeneration within bone graft substitutes

Thesis Structure and Overview:

Chapter 1:

The thesis starts with introducing bone grafts and discussing bone graft substitutes and their importance to orthopaedics. The discussion continues to cover the rationale for choosing porous Hydroxyapatite as the material to investigate, and for employing a finite element approach for the analysis. The chapter also covers the background theory of bone remodelling and bone grafting. It presents the previous research findings of mechanical-signalling pathways which is the motivation for investigating the mechanical strain fields in bone graft substitutes. The chapter introduces the finite element approach, as well as representative volume entities and their relevance to the research.

Chapter 2:

This is chapter covers the experimental methods used in this research.

- Archimedes density measurements
- Scanning electron microscopy imaging to determine the porosity
- Mechanical compression testing

Chapter 3:

The chapter introduces the methods used to create 3D models from grey scale scans of porous hydroxyapatite granules using commercial software ScanIP. The meshing process as well and the investigation of density conservation within RVEs.

Chapter 4:

The chapter discusses finite element analysis methods in more detail. It demonstrates the results for the hydroxyapatite RVEs analysed using the linear elastic model obtained using

ABAQUS. The chapter discusses the results using Von Mises and axial strain colour contours, energy conservation and strain energies of the models.

Chapter 5:

The chapter introduces and discusses the second finite element analysis model used for this research, the Drucker Prager Cap plasticity model. The model is employed as a failure criteria and employs data from compression tests. The chapter discusses the results using the Von Mises colour contours and PEEQ values in conjunction with the linear elastic model results.

Chapter 6:

The chapter contains a thorough discussion of all the results and the conclusions drawn from the findings. It also discusses possible future applications and research that may stem from this research.

Table of Contents

List of Figures:

List of Tables:

Chapter 1.

Introduction and literature survey

1.1 Bone Biology and Physiology

1.1.1 Bone Tissue

Bone is an active biological tissue and is the largest constituent of the skeletal system, and its functions are varied and essential for survival. They range from providing protection for the underlying organs, blood cell production, and support of the body frame as well as acting as a reservoir for minerals. Bone plays a critical role in maintaining the homeostasis of the body by maintaining the PH levels and releasing minerals when needed. Bone is also home to progenitor cells such as the mesenchymal and hematopoietic stem cells. It also houses growth factors and cytokines. When bone loses one of its roles and functions, the results are quite negative. This can be seen clearly in cases such as osteoporosis and osteoarthritis. (Taichman, 2018).

Bone is an anisotropic composite material made of mineralised osseous tissue constituting 50% to 70% of its weight. It also contains collagen type 1 with traces of types 3 and 5, constituting the organic matrix with a percentage ranging from 20% to 40%. Collagen, is the material responsible for bone's toughness and elasticity whilst the mineral component provides it with rigidity and strength (Landis, 1995). Variation in terms of the orientation of the collagen fibres as well as the way the crystals of the mineral phase are deposited result in variations of properties of bone tissue depending on their location in the body. Water constitutes 5% to 10% of the bone tissue weight with a few lipids constituting no more than 3%. Bone is a viable tissue, and thus has its own blood vessels, and nerves. The mineral component of bone, which is also referred to as the inorganic phase, is a form of Calcium Phosphate with a similar crystallographic structure to Hydroxyapatite (HA) $Ca_{10}(PO_4)_6(OH)_2$, (Clarke, 2008).

The bone mineral also includes traces of other ions such as Magnesium, Carbonate, Sodium, Manganese as well as Fluoride (Fernández et al., 2006). Bone mineral crystals are platelet shaped, they range from 4-6 nm in thickness, 30-45 nm in width, with a length of about 100 nm. The constituents of bone tissue are subject to various factors such as age, health conditions and location in the body, these differences give rise to the variations in mechanical and structural characteristics, function and behaviour. Bone is classified according to structure into two types;

- **Cortical** (dense bone) constituting 20% of the skeleton weight
- **Cancellous** (trabecular or spongy bone) constituting 80% of the skeleton weight

Cortical bone can be thought of as a denser form of the cancellous bone. By simply considering only the difference in their porosity and packing density. Cancellous bone however, is known as spongy and trabecular hinting to the very different nature of its structure which is more porous than its counterpart. These two forms are distributed throughout the skeletal system. With trabecular bone being more abundant in the axial skeleton and cortical bone being more abundant in appendicular skeleton (Plowman, 2013).

1.1.2 Cortical Bone

Cortical or compact bone, as mentioned is quite dense due to the way the osteon assembles. The assembly is of lamellae concentric rings or sheets of densely packed osteon. The osteon is basically constructed of a central canal called the harversian canal surrounded by rings or curved lamellae of bone matrix. Between those rings there are cavities, these pockets or cavities are called lacunae which are in turn connected to one another via tubes or channels called the canaliculi. The lacunae house mature bone cells (osteocytes) as they become trapped within the lamellae after matrix formation, with their projections occupying the canaliculi.

The tight packing of the harversian system gives rise to the dense solid appearance of cortical bone. The harversian canals house the blood vessels running parallel to the axes of the structure. The vessels are connected to more blood vessels at the bone surface via perforating canals, thus insuring sufficient delivery of nutrition, hormones, drugs and other blood born substances to bone cells. This also insures sufficient waste control, as well as the opportunity to bringing progenitor cells that can differentiate into bone cells when needed for remodelling and healing purposes (Porter et al., 2009).

With only 5% of its volume dedicated to pores, cortical bone has an apparent density of 2 g/mL, with ten times more strength than cancellous bone in compression (Benzel et al., 2012), this structure serves its purpose very well as it usually surrounds bone perimeters, it is a strong structure with a Young's modulus of 17-20 GPa longitudinally and 6-13 GPa transversely as cortical bone is an anisotropic material (Mow, 1991),(Porter et al., 2009).

1.1.3 Cancellous Bone

Cancellous bone is as its name suggests spongy. It is less densely packed than its counterpart cortical bone. It has a honeycomb appearance due to the high porosity of its matrix. Instead of having canals it consists of plates which are called the trabeculae. These are surrounded by pores or struts and are arranged along stress lines which gives this type of bone its ability to withstand loads, as this arrangement provides it with the maximum strength possible. The cavities or pores contain bone marrow. The blood supply is provided via canaliculi, which are channels linking those cavities, and thus it is clear that this structure has a better blood supply than cortical bone and a larger surface area resulting in faster healing and remodelling rates. Cancellous bone behaves in a viscoelastic manner, it is isotropic and is much softer than cortical bone. Due to its viscoelasticity, its mechanical behaviour is more rate dependant than cortical bone (Clarke, 2008).

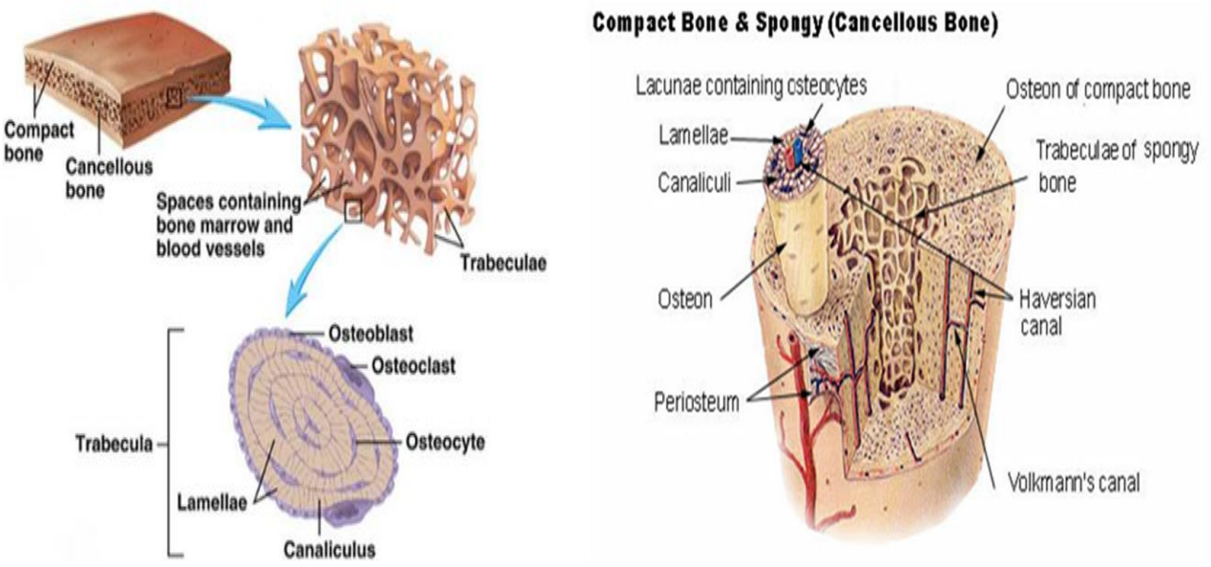

Figure 1: Schematic demonstrating the microstructure of cancellous bone and the difference in location and density between the cancellous and compact bone tissue

Cancellous bone, is not as strong with a Young's modulus ranging from 50-100 MPa subject to location, age and a number other factors (Mow, 1991). The variation in structure between the two types of bone causes variation in their function and as a result their position, as can be seen in Figure 1. (Hage et al., 2012), compact bone is almost always covering the cancellous bone structures, as both provide different mechanical roles to the skeletal structure and work together for an optimal mechanical function. The variations in structure can also be seen in terms of their application as autografts and allografts with autografts being grafts harvested from the patient and allografts being grafts harvested from donors (Clarke, 2008), (Mow, 1991).

The structure of the autografts influences the healing process and the rate of the process, this is evident during the revascularisation process, as it takes only a couple of weeks to fully complete for cancellous bone, whilst the same process takes up to two months to complete for cortical bone (Burchardt, 1983). The two categories also differ in their osteo-conductivity due to the same reason.

The quick vascularisation of the cancellous graft invites progenitor cells that differentiate into osteogenic cells, this is followed by a gradual absorbance of the necrotic graft and complete regrowth of new bone tissue replacing the graft. However, for cortical bone the process is different as its structure is not as permeable to vascularisation as is cancellous bone. For cortical bone the absorption starts at the peripheries this is than followed by a gradual invasion of vessels through the canals, however, once the entire periphery is covered with vessels the inner parts of the cortical graft will become vascularised at a faster rate. This means that during the process of bone repair or healing whilst osteoblasts (bone forming cells) initiate the bone remodelling procedure with cancellous bone grafts, it is actually osteoclasts (Bone absorbing cells) that initiate the remodelling with cortical bone.

This is evident through the mechanical changes that occur during the procedure, as they are correlated with the method of remodelling/healing process. As discussed, due to the fact that cancellous bone grafts are repaired via creating bone on their surfaces followed by absorption the process strengthens the graft initially which is the opposite of the mechanical change in cortical grafts as they weaken initially due to the osteoclasts creating space prior to laying down the newly formed bone. These are observations that were evident through studies conducted on dog and human bone (Hing, 2004), (Burchardt, 1983).

This is an important factor to keep in mind when creating or designing a bone graft substitute as it needs to not only mechanically match the type of bone it is replacing, it also needs to lend its self to the mechanisms of bone repair and remodelling that are appropriate for the site in which it will be employed. This is a strong point in favour of Hydroxyapatite based ceramics or other synthetic materials such as bio-glass bone graft substitutes, as these materials can be manufactured via a variety of methods to control their porosity, thus the synthesised graft can be application specific (Hing, 2004).

1.1.4 Bone Biology

Understanding the structure of bone is not enough to fathom its function and is insufficient to attempt to heal or repair it. To understand bone fully it should be studied from a structural, biological and physiological as well as from a chemical perspective. In the previous sections the process of bone repair, remodelling and bone cells were touched upon. In this section these processes and entities will be discussed thoroughly as understanding them is essential in designing and applying bone graft substitutes.

1.1.5 Origins of Bone Cells

Osteogenic or bone forming cells are all derived from mesenchymal progenitor cells, also called mesenchymal stem cells (MSCs) they are multipotent and can differentiate into cell lines with mono-potential capacities such as osteogenic (bone) adipocytes (fat cells), myoblasts (muscle cells), and chondrocytes (cartilage cells). The mesenchymal cells are available in the bone marrow and can also be found near bone surfaces such as the periosteum and the endosteum. The differentiation takes place as a response to biochemical and biomechanical stimuli. Biochemical factors may include organic and non-organic substances such as glucocorticoids, transforming growth factor TGF-β, Runx2 (A transcription factor) (Agamemnon et al.,1988), insulin derived growth factors IGFs, Bone morphogen proteins BMPs and Ca^{2+}(Aubin et al., 1995), (Papachroni et al*.,* 2009). Biomechanical stimuli is subjecting the cells to mechanical strain, a number of studies suggest a link between osteogenic differentiation, and up regulation of BMPs gene expressions with mechanical strain as well as sinusoidal cyclic strains (Loboa et al., 2006). Other studies have also confirmed the relationship demonstrating that small strain levels increased the RUNx expression and osteogenic gene markers, they have also demonstrated that high strains produced the opposite effect (Claes et al*.*, 2011). These facts and findings are highly relevant to this research as the strain fields imposed on PHA granules are investigated (Qi et al*.*, 2008).

The introduction of PHA granules has an influence on the differentiation of mesenchymal cells and consequently the production of bone is hypothesised to be due to the following factors (Barrère et al., 2003).

1. The PHA granules introduce an appetite layer similar to mineral tissue that is recognised by mesenchymal cells.
2. PHA granules provide a high level of free Ca^{2+} ions, inducing mesenchymal cell differentiation
3. A large rough surface area that influences the division of mesenchymal cells

1.1.6 Bone Cells

There are three types of bone cells that exist due to the differentiation of mesenchymal and hematopoietic stem cells. They are differentiated to preform specific tasks that insure the viability of bone tissue, these tasks are:

1. Production of proteins
2. Mineralisation of the collagen matrix
3. Tissue maintenance
4. Tissue resorption
5. Maintain the mineral homeostasis

The cells are classified based on their functions. The bone forming cells are called the osteoblasts. Their differentiation from MSCs requires an environment of low mechanical strain and a high Oxygen saturation. Osteoblasts are simply the osteoid forming cells. They make bone via secretion, deposition and mineralizing processes (Florencio-Silva et al., 2015). They can divide through mitosis to increase their number. Once activated osteoblasts perform many tasks in the bone tissue, these include synthesising and secreting the osteoid non-mineralised component of the bone matrix, and involvement in the calcification of osteoid.

Proliferation and differentiation of osteoblasts, are governed by certain signalling pathways that involve various factors, such as the transcription factor and core binding factor $\alpha 1$ (Cbfa1). The stromal cells derived from bone marrows have been the focus of research in the field of bone tissue regeneration, and evidence confirms strongly that combining these cells with porous ceramics can yield bone growth ectopically (Friedenstein , 1971), as well as in rodent bone defects (Anselme, 2000), (Marupanthorn et al., 2017).

Studies have confirmed that osteoblasts are quite responsive to mechanical stimulus, depending on both the type and the duration as well as rate and magnitude of the stimulus (Papachroni et al., 2009). Showing that complete lack of mechanical stimulation results in their apoptosis (Basdra et al.,1995), (Augat et al., 2005), leading to bone loss whilst modest exercise plays a major role in increasing the bone density, (Rittweger et al., 2005). These findings and others, give a pressing need to investigate the mechanical environment of bone graft substitutes and may result in a further understanding of the effect their structures may have on the local cells.

When osteoblasts are encased by osteoid they differentiate and give rise to another type of bone cells called the Osteocytes, these are the most abundant of all bone cells. Osteocytes play a major role in communication, they can be thought of as the telecommunication network of bone tissue, as they communicate with each other as well as other cells such as the osteoblasts and the surface lining cells via their cytoplasmic processes also known as dendrites (Franz-Odendaal et al ., 2006). These processes communicate via gap junctions, and through them small molecules known as signalling molecules can travel.

The processes extend all the way to the tissues vascular supply and thus can play a major role in sensing and controlling hormonal or ionic level fluctuations. Within the narrow space that separates the osteocytes from the bone matrix resides a paracellular fluid. It is believed that through its movements osteocytes can sense mechanical stimulus as they are otherwise isolated.

It is also believed that the fluid's movement is subject to the architecture as well as the composition of the matrix, thus can change with changes to the matrix's composition and the location of dwelling of the osteocytes (Schaffler et al., 2014). Osteocytes tasks include and are not restricted to, sensing and responding to skeletal environment changes through signalling to neighbouring bone cells and progenitor cells to kick-start remodelling processes (Verborgt et al., 2002).

They are active participants in the mineral homoeostasis particularly of calcium and phosphate (Fukumoto and Martin, 2009) as well as bone mass. To a degree, they are also able to manipulate the mineral levels in their surroundings through absorbing and secreting minerals through which they can directly influence the metabolic functions of the surrounding as well as the mechanical properties due to mineral changes. Their ability to change their shape can also influence the mechanical loading of the surroundings as they can directly influence the fluid flow (Gasser and Kneissel, 2017). Even during their apoptosis, which can be triggered by micro damage to the surrounding tissue, they are able to send stress signals initiating remodelling processes to replace them. Osteocytes, being the most long lived of bone cells and being so versatile in their abilities are very essential to bone health and mechano-transduction, thus, after their death an immediate response by osteoclasts takes place in order to remove them and start the remodelling processes of the damaged tissue (Verborgt et al., 2002).

Osteoclasts, the third type of bone cells, unlike osteocytes and osteoblasts are of a hematopoietic lineage. They are large and multi-nucleated, this is due to the fusion of the mono-nucleated (monocytes) precursor cells recruited by osteocytes and osteoblasts through secreting the necessary cytokines such as RANK. Osteoclast's exclusive job is the resorption of bone tissue (Ross, 2009). Osteoclasts achieve this by dissolving the bone mineral to decalcify bone tissue.

This is followed by enzyme degradation of the exposed collagen components of the matrix. In order to do this, osteoclasts have to isolate the microenvironment from the extra cellular fluid, where they attach themselves to the tissue via the mediation of specialised transmembrane proteins, thus sealing it completely before the action of degradation takes place (Ross, 2005).

Osteoclasts live to do their job, following bone resorption they go into apoptosis. This is a result of a number of triggers some of which are not fully understood. It is however believed that their detachment from the site, and the change in Calcium concentration in the extra cellular matrix are amongst the contributors of their apoptosis (Ross, 2009). Understanding these bone cells and how they function is essential to utilising the mechanisms used for natural bone remodelling process to facilitate the survival and success of the bone graft substitutes. for instance the Introduction of Hydroxyapatite has been linked to the initiation of a similar reaction to the one that kick-starts the natural bone healing processes (Holmes, 1979).

The signalling process that starts the cascade of bone healing and bone re-modelling resulting in reabsorption of the graft and the formation of new bone tissue starts from the moment any BGS is introduced. Through first interaction with the BGS's surface where proteins and protein–ion complexes such as growth factors can adhere to the surface of the graft and stimulate or supress through factor specific receptors on cell membranes and through the adsorption of cell adhesion molecules, a specific group of protein, enabling cell surface attachment by binding specialised transmembrane cell receptors such as integrins. The intracellular components of the receptors may then have interactions with the cytoskeleton, through which cell to surface adhesions enables signal transmittance to promote or supress cell responses such as proliferation or differentiation. The chemistry of the BGS can also directly stimulate the system with release of soluble ionic species that can be detected by cells' ion channels, inducing specific responses and by influencing the PH level. (Hing, 2005), (Hench, 1991).

1.1.7 Bone Healing and Remodelling

Bone cells are directly involved in bone modelling and remodelling under normal bone physiological conditions as well as after the introduction of the BGSs. (Papachroni et al., 2009). In this section the process of bone modelling and remodelling will be discussed as the ideal response that should result from the application of BGSs. Thus the knowledge of the factors that control the responses, in particular the role of mechanical stimuli, are key. To generate bone, there are only two physiological methods by which this can be achieved, these are;

1. Osteogenic bone modelling
2. Remodelling

The first one is mainly employed for generating the initial bone tissue. It is a process where the osteoblasts and osteoclasts act independently from one another, through this process the bone tissue can be formed with the aid of a cartilage template or an existing bone surface, thus no resorption via osteoclasts will be necessary, this type of modelling is known as formation modelling. Remodelling however, is quite a unique process, in which both the osteoblasts and osteoclasts work together within the same vicinity. Thus, combining bone resorption and bone formation. The osteoclasts start degrading the matrix and osteoblasts than follow this action by creating new osteoid tissue (Papachroni et al., 2009),(Gasser and Kneissel, 2017). Bone remodelling can be subdivided into two categories:

- **Non-targeted remodelling**

The non-targeted remodelling is believed to be a natural process that occurs due to the normal physiological homeostasis role of bone tissue.

- **Targeted remodelling**

The targeted remodelling starts as a response to a type of signal transmitted form the site to be remodelled.

This signal can be a stress signal caused by the apoptosis of osteocytes, a local micro-damage situation, a number of bio-chemical changes to the environment and of the most interest to this research is the changes of the mechanical stimuli (Parfitt, 2002), (Sikavitsas et al., 2001).

Targeted remodelling processes present an opportunity for manipulation in porous synthetic BGSs, potentially via a number of routes. These can include, chemical manipulation and structural manipulation such as alterations to the macro and micro structure of the graft, the latter of which will affect the graft morphology and its mechanical behaviour, the latter being the focus of this research.

1.1.8 The Processes of Bone Healing:

What stands out in the bone's capacity in repairing its self is the fact that, the healing process which is in many ways similar to other biological tissues, does not result in the formation of scar tissue. In fact, it produces new healthy and strong bone tissue. Healing in bone after injury is similar to the initial embryonic bone formation process. When bone is injured, usually as a result of a mechanical overload, its healing is carried out following a sequence of events (Mckibbin, 1978).

- Inflammation
- Callus formation
- Re-modelling
- maturation

The process can be briefly explained as a cascade of events that begin with the bleeding from the injured tissue, followed by the recruitment of leucocytes to clear the vicinity of fracture from any debris and dead tissue.

This is then followed by the formation of a hematoma (clot) which when fibro vascular tissue invades the scene which constitutes the soft callus (granulation tissue), attempting to bridge the ends of bone which in fact are suspected to have a role in the process of cell recruitment of progenitor cells and their proliferation, however unconfirmed, and providing at the very least a passive linking bridge to the viable distant tissue from which certain elements may be recruited. Soft callus is replaced with woven bone which is in turn remodelled and replaced with more organised lamellar bone (Kumar and Narayan, 2014), (Mckibbin, 1978).

This structure is initially not as strong as mature bone with a young's modulus of approximately $6.65 \pm 1.02\ \mathrm{GPa}$ (Padmanabhan et al., 2013). However, it provides the fracture fixation necessary to start the remodelling process achieving the necessary bone union for the following process. The remodelling then follows insuring the replacement of the fibrous bone structure with a much stronger organised and mature lamellar bone as the final step (Mohindra and Jain, 2017).

1.2 Bone Remodelling: A Consequence of Mechanical Signalling:

It is a fact that that bone without mechanical stimulation can atrophy and become weaker. This phenomenon is known as Disuse. Bone loss was observed in astronauts spending long periods of time in a low gravity environment. Having lost the effect of gravitational forces, their bones appeared to have lower mass due to the loss of gravitational forces and regular loading (Nagaraja and Jo, 2014).

The significance of mechanical stimulation to bone remodelling was first investigated by the pioneer of the field Julius Wolff in his 1892 publication; The Law of bone remodelling, (Brand and Claes, 1988). In it he established a law that governs the relationship between mechanical stimuli and bone remodelling. The law suggests mathematical equations governing both the macro and micro architectural changes as a direct response to mechanical demands therefore indicating the significance of loading as a factor responsible for the initiation of bone remodelling (Chen et al., 2010), (Brand and Claes, 1988), (Turner, 1998).

Various studies have indeed confirmed the strong relationship between the promotion of bone formation and exercise (Judex, Gross and Zernicke, 1997), (Vuori, 1995), (Snow-Harter et al., 2009).

The cellular response to mechanical stimulation as a process is known as mechano-transduction (Liedert et al., 2006). Information on the intrinsic mechanisms of this process remains insufficient. However, several studies have shed the light on a few observations that have clarified certain aspects of the mechanical induced cellular responses particularly in relevance to cellular reaction. Generally speaking, bone mass is proportional to the mechanical activity of the tissue (Padmanabhan et al., 2013). The density of bone was found to be directly influenced by its loading history, with the magnitude of loading having a greater effect than the frequency at which it is applied (Whalen et al., 1988).

1.2.1 The Physiological Implications of Mechanical Loading

Mechanical stimulation can influence bone regeneration in cooperation with hormones such as oestrogen and parathyroid hormones with a local regulation carried out by cytokines and specific growth factors (Mikuni-Takagaki, 1999). The mechano-transduction, by which the physical stimulus is converted to a signal transmitted to cells makes use of what is known as transduction pathways (Liedert et al., 2006). In addition to osteocytes both osteoblasts and osteoclasts are considered as mechanically sensitive cells (Frost, 1987). Mechano-transduction, has been linked to the activation of osteoblasts, changing the rates of the proliferation and matrix generation. It is believed that integrins particularly the ones of the $\beta 1$ subunits, Cadherins, and Calcium ion channels are involved in the process of converting the mechanical signals to the cellular level as active constituents of the transduction pathways (Mikuni-Takagaki, 1999). In theory all cells have the ability to sense mechanical stimulus (Weinbaum et al., 1994). In bone tissue, the sensitivity is not restricted to osteocytes and osteoblasts, osteo-progenitor cells (Chen et al., 2010) are also subject to mechanical influence. Osteocytes are considered as the primary sensor cells, while the osteoblasts are

considered to be secondary sensors, known as the effector cells, as they respond to these signals (Turner and Pavalko, 1998).

On a cellular level, cell membranes physically deform in response to applied strain. The changes to the shape of the cells, in turn give rise to changes in the fluid adjacent to them; resulting in changes in the hydrostatic pressure which in turn induces fluid shear stresses that can also be sensed by the cells. The shear stresses are a result of the flow created by the movement of the interstitial fluid (Pavalko et al., 2003),(Duncan and Turner, 1995), as this movement creates an effective electrical potential (Chakkalakal, 1989).

This electrical potential created, is essential for the activation of the voltage sensitive Calcium ion channels, their activation promotes the ions entry into the cells, their entry is a direct factor to the release of the vesicular ATP energy molecule (Damian et al., 2005). Stresses have been known to cause a change in the electromechanical environment of bone cells. Areas experiencing compression are electronegative whilst areas experiencing tension are electropositive. Although electrical charge induces bone remodelling on its own merit, stresses induced changes to the electrical environment and can thus initiate remodelling from a secondary route of its own (Alvin et al., 1956). Other ion channels such as the cation channels are also activated due to stresses particularly in osteoblasts. For example, Calcium ion channels have been shown in an in vitro study, to be the most probable route of transduction when the strain belongs to a high spectrum (Li et al., 2002). however, unlike their counterparts these channels are activated due to the stretching of the cell membranes (Pavalko et al., 2003). Gap junctions act as messengers between cells, linking the membranes of adjacent cells together through a membranous protein called connexion. These junctions are the primary messengers in the transduction pathways. There is evidence to suggest that an increase in the expression of connexion, as a direct result of mechanical strain, is due to the formation of more gap junctions to facilitate rapid transmission of signals (Higgs and Peterson, 2005). These signals are transmitted through the release of certain ions such as Na^{+}, K^{+},Ca^{+2} and Mg^{+2}, as well as similarly small signalling molecules (Doty, 1981).

When the cells experience a load, they respond by releasing signalling molecules such as Prostaglandins and Nitric Oxide. Prostaglandins are associated with gap junctions in that they induce an increase in the number of the active gap junctions available (Higgs and Peterson, 2005), (Ajubi et al., 1999).

Nitrogen oxide, which is produced during higher interstitial fluid flow rates, is believed to be a preventative of osteocyte apoptosis (Rossig et al., 2000). These are considered to be the early responses to mechanical strain. These molecular level responses are a clear demonstration of Wolff's law of bone adaptation to mechanical stresses.

1.3 Bone Grafts: An Introduction

Bone grafting is one of the most common transplant procedures taking place in surgical settings worldwide, second only to blood transfusion (Boyce et al., 1999). Bone grafts are commonly used to amend defects in bone tissue that occur due to disease, trauma or post-traumatic union processes as well as inherent defects (Prakasam et al., 2015). Bone grafting can be considered as the most reliable method that harnesses the natural bone tissue's ability to regenerate. Basic bone grafting procedures were pioneered in the 18th century (Meeder and Eggers, 1980), and have advanced ever since. The procedure of bone grafting has infiltrated different surgical and dental applications. There are a number of methods used to obtain bone grafts. The most common one and what is to date still considered to be the golden standard by surgeons; is the autograft, where bone grafts are harvested from the patient's own skeletal tissue. Autografts, are considered to be most osteo-conductive and osteo-inductive as well as osteogenic (Prakasam et al., 2015). However, there are issues associated with the necessity to harvest from patients, thus prompting researchers to find a better or at least a similar alternative that is less invasive and eliminate the issues and problems related to using autografts. These issues may include:

1- The limitation in its osteogenicity as a number of viable cells die during transplant, due to the variation in the bone biology of the patient.

2- The dual surgical sites and the infection/complication issues associated with them.
3- Increased chances of blood loss, which is a major limitation in terms of surgery.
4- Chronic pain in the donor site.

The second most common form of bone grafts, is the Allograft. It has been reported, that these grafts constitute one third of the bone grafting procedures taking place. Allografts are grafts harvested from donors of the same species as an alternative for the self-donated autografts. They have acceptable osteo-conductivity. However, due to treatments undergone after harvesting to remove any immunogenic or infections elements osteo-conductive potential is lost. Another issue that may arise despite the extensive treatments that include radiation as well as chemical treatments and freeze drying to process the grafts after harvest, is the risk of transferring disease-causing viruses and pathogens to patients (Sandhu et al.,1999). Other risks and shortfalls can also include;

1- The possibility of an immune response (transplant rejection).
2- Allografts are weaker due to the post harvesting treatments.
3- Rehydration processes prior to implantation can induce the formation of both macro and microscopic cracks decreasing thus the graft's strength.

Another bio-graft is harvested from different species, known as the Xenograft, such as grafts from porcine or bovine bone tissue. These types of grafts also undergo similar treatment processes to allografts such as the radiation and the freezing, with the addition of demineralisation or deprotonation steps. They are thus the least preferred of the previously mentioned bio grafts, this is due to limitations in their availability, mechanical properties as well as the increased risk of infections and rejections associated with using them (Laurencin, 2008).

1.3.1 Synthetic Bone Graft Substitutes:

In order to overcome the mentioned limitations, and eliminate the limitations associated with availability, and the experienced complications associated with the traditional methods of bone grafting. Alternatives to bone grafts, best known as “bone graft substitutes”, have been introduced and investigated thoroughly in the recent decades. Bone graft substitutes can be categorised as one of the following.

- Organic or Biological
- Synthetic or Inorganic (Schlickewei and Schlickewei, 2007)

Researchers have established that for a synthetic biomaterial to be considered as a bone graft substitute it needs to meet most if not all the following properties:

1- Osteoconductive; can be simply defined as the material’s ability guide bone growth upon its surface and structure.
2- Osteoinductive; Osteoinduction is the process by which organic and nonorganic factors are released from the graft stimulating the differentiation of progenitor cells into specialised bone cells (Oppenheimer at al., 2008).
3- Resorbable; degrades in the host vicinity and replaced by new bone tissue. This is due to the chemical action of the physiological environment on the material.
4- Remodellable (Hing et al., 1998).
5- No supply issues.
6- Sterilisable.
7- Mechanically suitable for the application i.e. prevents shielding. (Pryor et al., 2009).

Logically, a synthetic substitute with the same osteo-inductivity as autografts is more preferable due to its availability, the elimination of harvesting and multiple site surgeries. In addition, there is evidence indicating that grafting bone using synthetic bone graft substitutes reduces blood loss in comparison to their bio counterparts, as well as less pain associated with graft donor sites such as the case for autografts.

It has also been reported that synthetic bone graft substitutes require less operational time and consequently a reduced risk of infections (Campana et al., 2014). For the past three decades, the focus of scientists turned towards a variety of synthetic bone graft materials. The main materials investigated as synthetic bone graft substitutes are ceramics and bioactive glasses. Going back into the development of bio-ceramics as bone graft substitutes takes us to the early 1920's when scientist's realised the similar x-ray diffraction patterns between the actual bone minerals and the calcium phosphate ceramic known clinically as Hydroxyapatite (de Jong, 1926). Research has gone to show a further similarity between the two in their crystallographic structure (Posner, 1969).

Bio-glass, a specific formulation of bioactive glass developed by Larry Hench, and was shown to develop a hydroxyl-carbonate layer which is considered to be a bioactive layer that can provide bonding with the host's own bone tissue. This was believed to be due to the similarities between the carbonate layer and the bone's mineral phase both chemically as well as structurally (Pantano et al., 1974), (Ogino and Hench, 1980).

Bio-ceramics used as bone graft substitutes were later categorised as either bio-inert or bioactive. The bio-inert materials, elicit the least response by the host tissue (Best et al., 2008). Bioactive materials however, elicit a desired response within the host tissue, such as bonding and new bone tissue formation. In the 1990's a differentiating bioactivity index was introduced by Hench, who later classified bioactive materials into classes. Class A bioactive material; which allows bone tissue to grow along the interfaces between bone graft and host tissue as well as recruiting cells that differentiate into bone producing cells and consequently new bone tissue growth, thus being an osteo-integrative material also known as osteo-inductive, as well as having the basic ability to support bone growth upon the graft's surface which is known as being osteo-conductive. Class B, differs in that it can only be osteo-conductive and does not have the bioactive properties associated with class A materials (Cypher and Grossman, 1996), (Hench and West, 1996), (Wilson and Low, 1992).

1.3.2 Bio-Active Bone Graft Substitutes:

As discussed, the preferred bio-ceramics should ideally include class A bioactive property. Most importantly, they should allow sufficient penetration and integration of newly formed tissue, marrow and the necessary blood vessels. In addition to the aforementioned properties. Synthetic bone grafts should ideally demonstrate a certain level of compatibility with the host tissue mechanical properties, having a similar Young's modulus to the bone tissue in order to avoid stress shielding and/or failure of the graft if the material is too weak. Grafts also need to be tough enough to withstand initial loading, before new bone tissue reinforces the graft site and the implantation process. From the family of synthetic biomaterials, bio-ceramics and particularly those composed of Calcium, Silicon or Phosphate seem to fit the requirements both the biological and the mechanical to a good degree (Bohner, 2000), (Vikas et al.,1999).

The most popular of these bio-ceramics are:

1. Bioactive glasses and glass ceramics
2. Calcium Sulphate
3. Beta Tri-Calcium Phosphate
4. Hydroxyapatite

Bioactive glass is a product of SiO_2,CaO and P_2O_5. Bioactive glass was the first of its kind to be employed as a synthetic graft substitute by Hench, a non-porous hard material that bonds well to bone. Bioglass is known to be both osteoconductive as well as osteogenic depending on the ratios of its composition mostly dependant on the original formula introduced first by Hench in the 1970's (Hench et al, 1971), (Wilson et al.,1981), (Hench and Paschall, 1973). In the early 90's a Glass ceramic was developed by Kokubo (Kokubo, 1991), by heating a compact of powdered glass having a specific composition, which yielded an Oxyfluroapatite ($Ca_{10}(PO_4)_6\,(O,F_2\,)$.

Glass ceramics have superior mechanical properties to Bioactive glass with some of them demonstrating mechanical properties approaching the mechanical properties of natural bone tissue (Padilla et al., 2005), (Gil-Albarova et al., 2005), (Salinas and Vallet-Regí, 2007).

Glass ionomers (glass polyalkenoate cement) a cement originally developed for dental applications, when set it develops into a porous structure. It has a similar young's modulus to natural cortical bone tissue, and this overcomes the disadvantage of not being absorbed by the host or replaced by new tissue, as the similar elastic moduli reduces the risk of stress shielding (Williams and Billington, 1989), (Jonck et al., 1989). They are advantageous in that they can be loaded with desired particles for slow and controlled release, such as proteins and antibiotics, using Glass ionomers insures a more efficient release than formerly used cements such as PMMA. The glass ionomers however have to be cemented in place during surgery and has had successful results in maxillofacial and ENT applications (Wittwer et al., 1994), (Moore et al., 2001).

Alumina,Al_2O_3 can be used on its own or with other bone graft substitutes. Alumina is bioinert and does not form any bond with host tissue. Thus, they are not as popular unless porosity is introduced, allowing a level of osteo-integration (Karlsson et al., 2003). They are advantageous in terms of strength, as they are quite strong and rigid and thus suitable for applications that require resistance particularly to flexural fractures (Williams, 1990).

Calcium sulphate, has the formula $CaSO_4.\frac{1}{2}\ H_2\ O$ and is also known as plaster of Paris and used for fracture stabilisation for centuries. The interest in it as a bone graft substitute stems from its biocompatibility and its ability to support bone formation, as well as being a resorbable and osteo-conductive material (Ricci, 2003). Most importantly, calcium sulphate as a bone graft substitute is a good choice when cost and availability of other bone grafts are limited particularly in underdeveloped countries (Kumar et al., 2013). It has shown good results in filling defects with 94% bone growth in defected areas alongside 100% absorption of the calcium sulphate pallets implanted (Kelly et al., 2001).

Calcium sulphate however, is not as similar to the mineral phase of bone as for example, calcium phosphate, It is also quite weak in aqueous environments, as its dissolution rate in-vivo is quite fast and thus may not provide sufficient material stability for osteoblast adhesion (Glazer et al., 2001),) (Liljensten et al., 2003), (Hing et al., 2007).

When crystallising the structure formed can have defects, and the crystals formed after mixing with water produces randomly sized crystals that cannot be controlled, thus resulting in a variation in mechanical properties, solubility and consequently porosity. To produce uniformly sized crystals, the process of manufacturing has to be extremely controlled on a micro-scale level (Vikas et al.,1999).

1.3.3 Calcium Phosphate Ceramics

The mineral constituent of bone tissue is a ceramic calcium phosphate similar to Hydroxyapatite in its crystallographic structure yet not completely analogous to it. It is deficient in Calcium, Phosphate and the Hydroxyl group with a Calcium to Phosphorous ration of 1.37-1.87. Which is different than the ratio of the Calcium to Phosphorous in the synthetic stoichiometric hydroxyapatite which is 1.67 (Posner, 1969). It is also characterised by a having a significant level of additional trace elements due substitutions with a range of cations and anions (Hughes, 1996). The calcium phosphate family is attractive as bone graft substitute; they vary in properties as a result of the different proportions of Calcium ions to Phosphorus ions. They also readily undergo ionic substitution, this being the mechanism for the incorporation of trace elements in bone mineral (Vallet-Regí, 2010). Together, the variation of the Ca:P ratio and the incorporation of other ions are responsible for the differences in both the solubility as well as the thermal stability of various Calcium Phosphates both stoichiometric and substituted (Maeyer and Verbeeck, 1993).

1.3.4 Hydroxyapatite a Member of the Calcium Phosphate Ceramics

Hydroxyapatite is the bio-ceramic with closest crystallographic resemblance to bone tissue's own mineral content. It has the formula $Ca_{10}\,(PO_4)_6(OH)_2$. The composition of Hydroxyapatite has a percentage weight composition of Ca at 39.68%, and Phosphorus at 18.45% with a molar ratio of Calcium to Phosphorus of 1.67 (Suchanek and Yoshimura, 1998). Hydroxyapatite, is an interesting bio-ceramic for grafting applications, due to the biocompatibility with both the bone tissue of the host as well as the surrounding soft tissue (Hench, 1991).

Hydroxyapatite lends itself to the introduction of various levels of porosities and ionic substitutions, which in turn allows for a large variation in the HA grafts, lending themselves to a variety of applications as bone graft substitutes. Hydroxyapatite thus is a sophisticated and complicated structure particularly as a porous ceramic (Suchanek and Yoshimura, 1998). The major difference between stoichiometric Hydroxyapatite and the mineral phase of bone, is the lack or reduced amount of hydroxyl groups in the latter, as well as the content of carbonate (Glimcher, 2010).

Research demonstrates a strong link between the dissolution of certain ions such as Silicate and the bioactivity of this synthetic graft. The released ions are believed to have a direct influence on the cells in the vicinity as well as the recruited ones, as the ions diffuse through the blood and travel to further cells, this process is believed to be achieved via the up regulation of gene expressions of the cells thus consequently initiating their differentiation into bone producing cells (Xynos et al., 2001).

The most relevant substitution to this study is the silicon substitution, as it has been proven to enhance the graft's (Gibson et al.,1999) Silicon has been linked to the healthy metabolism of connective tissue. A study conducted on chicks demonstrated that removing Silicon from their diet resulted in lower levels of growth in comparison to Silicon fed chicks, leading to a hindrance to their skeletal tissue development (Carlisle, 1980), (Carlisle, 1972).

Another study conducted on silicon substituted hydroxyapatite coatings demonstrated an increase in the attachment, the proliferation and differentiation of osteoblasts (Thian et al., 2007). This is due to the release of Silicon ions during in-vivo applications, where they tend to bind to the Oxygen ions in the vicinity. This partnership of ions has been linked to an enhanced capability of proteins binding to graft surfaces (Schwarz and Milne, 1972). Silicate ions are usually added as a trace element substituting for the Phosphate ions, thus changing the formula from $Ca_{10}(PO_4)_6(OH)_2$ to $Ca_{10}(PO_4)_{6-x}(SiO_4)_x(OH)_{2-X}$, with X being the number of moles, as a result changing the $Ca{:}P$ ration to $Ca{:}\,P + Si$ with the value remaining at the stoichiometric 1.67 (Harden et al., 2013).

1.3.5 Mechanisms of Mechano-Transduction and Relevance to Bone Graft Substitutes

In this section the dynamics of mechanical signalling and the relationship between BGS architecture and the cellular responses and how they collectively affect the translation of these signals to influence bone tissue remodelling, will be discussed. It is however important to note, that available information on Mechano-transduction is not yet sufficient to fully explain in detail all the aspects of the process. This section will demonstrate based on the available literature the link between the architecture, in terms of the macro and micro structures of PHA bone graft substitutes and the mechanical signalling pathways discussing the possible factors that can elicit mechanically induced, desirable cellular responses and consequent bone generation.

In the discussion of bone remodelling sections 1.1.7 and 1.2.1 fluid flow was mentioned. This is the fluid within the lacunae of bone, inducing hydrostatic pressure on bone cells. The hydrostatic pressure changes due to forces applied to bone when the tissue experiences physiological loading such as, during walking or running which physically deform the bone matrix in what is known as strain. These deformations are translated into slight volume changes within these pores, as some volumes increase and some decrease creating a pressure gradient of fluid (Sikavitsas et al., 2001). The change in hydrostatic pressure drives

the interstitial fluid to flow causing in turn shear stresses acting on the osteocyte cell membranes and on their extensions through the canalicular spaces (Takai et al., 2004), (Chao et al., 2012). These pressure changes are thus important to highlight, in order to understand how loading an implanted porous BGS can lead to stimulating bone cells and consequently the bone remodelling of the BGS.

When osteocytes sense a mechanical stimulus, they release the signalling molecules such as; BMPs (bone morphogenic proteins), IGFs (Insulin like growth factors), TGF-β (transforming growth factors) and FGFs (fibroblast growth factors) as well as prostaglandins and nitric oxide. These molecules can be transferred through gap junctions or paracrine signalling pathways depending on the molecular size, to neighbouring osteoblast cells (Doty, 1981). The ability to provoke bone growth under controlled mechanical stimulation is known as Distraction osteogenesis (Qi et al., 2008).

Nitric Oxide is one of those molecules that has a direct effect on osteoblasts, with high concentrations associated with their apoptosis, and low concentrations associated with an increased activity of their proliferation and differentiation. Nitric Oxide has a short life in the blood as it binds to haemoglobin thus can only effect osteoblasts at a closer range than other hormone like circulating signalling molecules, (Mancini et al., 2000), (Hakim et al., 1996). The induced change to the membrane of osteocytes causes conformational changes to membrane proteins, such as integrin's and stretch activated channels. Some of the membrane proteins are linked to protein complexes known as mechanosomes. The mechanosomes have the ability to communicate with nuclei causing geometrical changes to specific regions of the DNA known as mechano-sensitive genes, inducing alterations to the genetic activity of cells. (Rawlinson et al.,1996), (Schmid et al., 2014). These alterations are in turn responsible for the proliferation and differentiation of osteoblasts (Pavalko et al., 2003).

Osteoblasts themselves can also sense mechanical stimulus as mentioned previously. It has been reported that osteoblasts in culture have shown sensitivity to loads of a low magnitude, provided the load is of high frequency (Ward et al., 2004). Cyclic loading was linked to the

induction of osteoblast differentiation as a direct result of osteogenic gene enhancement (Wang et al., 2012), (Wang et al., 2010).

Further in-vitro investigations have demonstrated a link between mechanical strain (stretching) of osteoblasts and an increase in growth factor expressions on these cells (Cillo et al., 2000). In terms of osteoclasts, studies have found that medium mechanical stresses have a suppressing effect upon osteoclast differentiation. The opposite is true in the absence of mechanical stimulus, with the lack of stresses linked to an increase in bone resorption. The case is different for extremely high stresses which are linked to osteoclast differentiation due to the micro-damage they create (Medsker et al., 2016). Some researchers have postulated that fluid flow may not have a direct effect on osteoclasts but that, it creates streaming electrical potentials. These in turn have been shown to effect osteoclasts and osteoblasts, with the first being attracted to the positive field and the latter to the negative one (Hillsley and Frangos, 1994). Other studies support the relationship between mechanical stimulation and osteoblast activities. Showing an enhancement of the rate of differentiation and proliferation as well as evidence of an increase in the production of collagen, phosphates, prostaglandins as well as mineralisation (Chambers et al., 1993), (Murray and Rushton, 1990).

Over expressions of a number of osteoblast genes were also observed due to mechanical stimulation. It has also been reported that mechanical stimulation causes an up-regulation of the production of growth factors such as the TGF's, IGF's and VEGF's, which are necessary for the process of bone modelling, stimulating and altering the growth of cells (Mikuni-Takagaki, 1999), in addition to their ability to induce the osteogenic differentiation of mesenchymal cells (Sumanasinghe et al., 2006).

Mature osteoblasts and osteocytes can be present or migrate to the vicinity from neighbouring bone tissue. Osteoprogenitor cells can be delivered to the site by blood due to injury, as well as through recruitment due to the actions of the attached serum proteins (Chai et al., 2011), (Kilpadi et al., 2004). There is evidence suggesting that the dendritic processes of osteocytes

carry transmembrane protein CD44, which has a receptor for Hydroxyapatite, thus allowing the integration of osteocytes along the structure of the graft (Noonan et al., 1997), (Nakamura et al., 1995).

This information provides evidence that both the mechanical properties as well as the composition and architecture can send physiochemical cues, that up-regulate the desired genetic alteration associated with osteoblast differentiation from progenitor cells. These physiochemical cues were found to accelerate the rate of differentiation , osteo-generation and integration as well as vascularisation (Mattei et al., 2015).

1.3.6 Influence of Bone Graft Substitute Porosity on Mechanics and Cellular Response

The mechanical properties of PHA granules are dependent on both the structural architecture and the porosity of the granules (Peelen and Rejda,1978), evident in the increase in UCS ,ultimate compressive stress, values from 1 -11 MPa as a response to increasing the total porosity from 50-80 %. The modulus is also affected not only by the change in porosity but also by the degree of anisotropy of the structure (Hing et al.,1999).

The architecture of PHA granules can also direct the action and behaviour of cells (Bignon et al., 2003) . Bone cells including osteoprogenitor cells (Mauney et al., 2004) can sense the mechanical properties of their environment and thus the graft that is introduced to them. Bone cells adapt by adjusting their spreading along the surface provided and through changes in their morphology. Evidence supports that cells attached to hydroxyapatite surfaces show a typical elongation, which is quantified by measuring the change in ratio of the long axis of the cell to the short axis (Nakamura et al., 2009), (Mattila and Lappalainen, 2008). These morphological changes act as a cue for the events that lead to cell-graft communication, dictating the fate of all associated cells and inevitably the outcome of grafting (Marcellini et al., 2012).

Porosity plays a major role in cell response and bone remodelling. In bone structure, cavities such as the canaliculi and lacunae are considered to be stress concentrators. Within a stress concentrator region the strain is significantly higher than the macro-strain experienced by the bone as a macro structure (Currey, 2003), (Currey, 1962).

These stress concentrations could potentially weaken a structure. However, bone tissue compensates for this through the orientation for those cavities (lacunae) and blood vessels, which tends to reduce the stress concentration effect (Currey, 1962).

PHA given its porous nature will contain stress concentrators (pores). The pores are necessary for the material's function as a bone graft substitute, but inevitably weakens it, limiting its loading capacity. However, there is a level of adaptation proportional to time duration after implantation that helps compensate for the initial weakness of the structure. A study demonstrated that after 24 weeks in vivo, PHA implants of different initial porosities of 70% and 80% and varied strut porosities (micro porosities); had similar UCSs (ultimate compressive strengths) despite of different UCS values between them initially. This indicates a level of reinforcement to the grafts as a result of bone growth. The mechanics of the BGS as a function of both levels of porosity seem to also influence the equilibrium of bone growth. (Bignon et al., 2003), (Boyde et al., 1999), (Hing, 2005) (Hing et al., 2002).

It is very important to map the strain and the strain energy responses to mechanical stimulus amongst PHA granules and the effect of the discontinuities caused by the porosity and the strut porosity of their structure. Increasing the micro porosity for instance decreases the strut modulus. When the strut modulus falls below a threshold value, this in turn caused a shift in the cellular activity equilibrium and causes them to deposit more bone to compensate for the modulus change, thus creating a greater more stable tissue apposition (O'Connor et al.,1982). Under mechanical stimulus, bone formation is responsive to the pattern of strain the stimulus creates. Bone growth seems to follow an engineering algorithm with more growth associated with areas of high strains in attempt to adapt to the new mechanical conditions. This was evident in a study conducted on rat ulnas subjected to site specific mechanical loading.

The study showed that bone growth was directed towards the areas of experiencing higher strains. This strain guided bone growth, allowed the rats' ulnas to withstand 100 time more cycles of loading than they can usually cope with (Warden et al., 2005). In a study conducted on metaphysical bone models, lower strains were found to give rise to intramembranous bone formation while higher strains induced endochondral bone formation and fibrocartilage formation (Claes et al., 2011). This research aims to create 3D finite element models of PHA bone graft substitute material at different porosity levels. The approach aims to investigate the behaviour of the material under physiological strain conditions. Findings may link the observed behaviour to possible bone growth patterns.

1.3.7 Porosity and Strain Co-Dependency

The idea behind grafting with PHA is to mimic grafting with an autograft or an allograft, where the new bone can successfully penetrate the graft and replace most of it through the process of remodelling, where the graft is removed by bone resorbing cells (osteoclasts) and phagocytic cells whilst being replaced by bone tissue made by the bone forming cells (osteoblasts) (Hing, 2005).

The interest in porous structures stemmed from the early observations of fibrous encapsulations of porous implants and tissue penetration (Hulbert et al.,1972), showing a complete occupation of their macro-pores by blood vessels, bone tissue and bone marrow fully incorporated in a manner similar to the organic bone grafts (Ling et al.,1993). Figure 2 shows a schematic first presented by Hing (Hing, 2005), demonstrating the principle of porosity in ceramic bone graft substitutes, particularly Hydroxyapatite, the level of porosity, macro and micro porosities as well as strut porosities and connectivity.

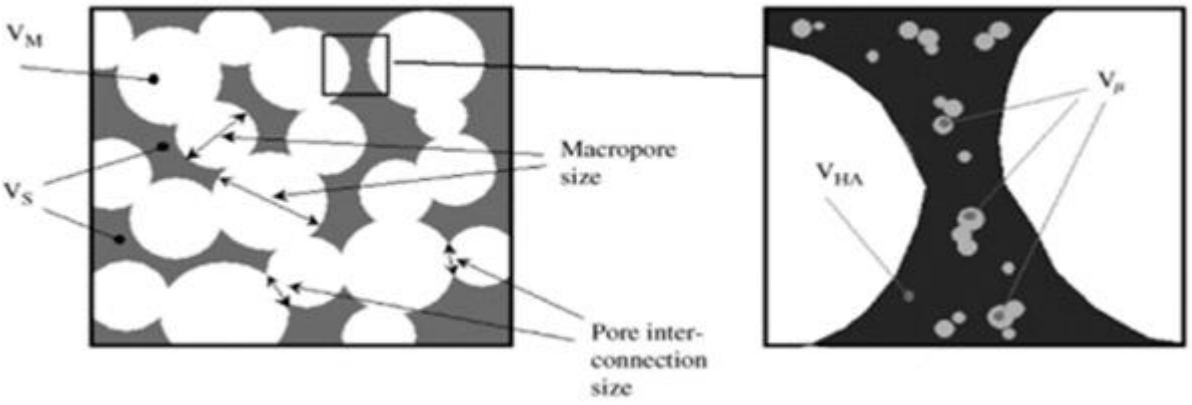

Figure 2: Schematic demonstrating volume fractions of pores and their types within the structure of hydroxyapatite. V_M And V_μ are the macro pore volume fraction and the micropore volume fraction respectively. V_s And V_H are the strut volume fraction and the hydroxyapatite volume fraction. Adding V_M and V_μ gives the total porosity of the material from which the fraction of strut porosity is given by dividing V_μ by V_s .

The interest in porosity, particularly as the prominent variable for this research is due to the effect it has on bone integration, the quality of the bone tissue modelled and the rate of bone's integration into the graft. Studies have reported a clear dependence of remodelling upon the porosity parameters of the graft (Jin et al., 2000), (Kaito et al., 2005), (Bignon et al., 2003).

Those parameters are; porosity volume, pore interconnectivity, macro and micro porosity as well as pore geometry. Pores larger than 50 µm are considered as macro. Pores of this size are linked to the ease of transportation of ions and cells (Bignon et al., 2003). Pores of 100 µm- 130 µm are viewed as a minimum for a satisfactory bone infiltration (Klawitter and Hulbert, 1971), (Orlovskii et al., 2002). Pores of less than 50 µm within the ceramic struts are considered as micro. Micro pores are believed to provide the large surface area necessary for chemical surface interactions such as ion exchange, protein adsorption and subsequently cell attachment and spreading. With faster opposition rates associated with pores larger than 20 µm (Hing et al., 2004), (Bignon et al., 2003). Pore interconnectivity or inter granular pores that act as channels are believed to influence the vascularisation of the graft, with greater penetration associated with interconnection sizes ranging between 100 – 135 µm (Komlev and Barinov, 2002), (Jin et al., 2000), (Kaito et al., 2005).

Vascularisation is an important factor to the survival of a graft. Interconnectivity along with the microarchitecture of the bone graft determine the rate and the level of vascularisation as well as complete infiltration of the graft (Oppenheimer et al., 2008). To achieve the best performance from a BGS, an optimum combination of porosity levels needs to be implemented. However, achieving this optimal combination remains to be a challenge (Woodard et al., 2007) (Kalita et al., 2003). There is a need for a compromise bringing a balance between

I. the mechanical integrity, essential for survival of the graft during implantation and throughout the first stages of the remodelling period and a
II. sufficient open porous structure and interconnectivity to allow for and sustain bone tissue integration (Hing, 2005).

Macro pores resemble the intra-trabecular spaces of bone tissue, and the micropores of sizes ≥20 μm, resemble the osteocyte lacunae. An increase in porosity is synonymous to a decrease in density associated with a decrease in the compressive strength and young's modulus of the material (Orlovskii et al.,2002) (Innocentini et al., 2010). It is true that provided the appropriate method is used, PHA can be synthesised with compressive strength values comparable to cancellous bone (Schumacher et al., 2010), (Ramay and Zhang, 2004), however, not as comparable in terms of shear and tensile strength (Charrière et al., 2003). Hence the application of such grafts are usually done with the aid of fixating devices.

The relationship between the ultimate compressive stress (σ_c) and the compression modulus (E_c) with the apparent density of hydroxyapatite (ρ) can be summed in the following relationships (Gibson, 2005), (Hing et al.,1999);

$$\sigma_c \propto c_a \rho^x \quad \text{Eq. 1}$$

$$E_c \propto c_b \rho^y \quad \text{Eq. 2}$$

With c_a and c_b are known as constants of proportionality with values of ~ 1 and ~0.5 respectively. The (x) and (y) are foam structure coefficients with a value of 1 for (x) and 2 or 3

for (y) for open and closed structures respectively (Gibson, 2005). As mentioned PHA graft substitutes are structures that include both macro and micro pores open and closed, with the micro-pores constituting what is known as strut pores. The strut pores (micro pores within the ceramic strut) increase the surface area for protein attachment (Hing et al., 2005). The change in the geometry caused by the introduction of the micro pores, could possibly be providing cells with a more favourable structure for attachment (Dalby et al., 2000), (Chong et al., 2015). In-vivo and in-vitro studies (Chan et al., 2012), (Coathup et al., 2012) demonstrated an increase in protein adsorption and osteo-conduction, as well as an increase in bone formation as a direct result of increasing the strut/micro porosity.

For the purpose of this thesis, the effects of both the macro and micro porosities on PHA structures are investigated, both on the mechanical environment of the substitute, and on the structurally induced stress and strain concentrations as well as on strain distribution. For the purpose of this thesis. The macro and micro porosities of the PHA bone graft substitute are varied. This was done in order to investigate their effect on the mechanical environment of the BGS, and on the structurally induced stress and strain concentration and distribution. By preforming a strain mapping procedure on the BGS structures using finite element analysis. The process can reveal the strain distribution within the BGS structures enabling the investigation of the mechanical environments and the possible effects on local cells when in-vivo. High local strains can lead to

- **Micro-fractures**

These are micro scale fractures typically resolved via bone healing mechanisms similar to actual fractures and associated with the formation of micro callus and woven bone

- **Micro-damage**

Which are micro scale lesions typically resolved through remodelling. Studies suggest that cells are sensitive to both micro fractures and micro damage, both caused by changes to strains, which are in turn associated with structural variation.

Strain field mapping can possibly predict bone growth patterns in a graft substitute as well as the possible cellular behaviour, through understanding the mechanical environment and the stimulation of cells through the observed mechanical strain (O'Connor et al.,1982), (Mosekilde et al., 2000).

Strain mapping of BGS has the potential to influence future modifications to the materials, that could expand their biological applications as currently the applications are limited to drug delivery, implant coating and low load bearing locations such as in spinal fusion and maxillofacial reconstruction (Prakasam et al., 2015). Simulations of these particularly interesting parameters can also minimise the need for carrying out daunting mechanical tests which can be quite tricky given that PHA grafts particularly the ones with high porosity are very brittle. The finite element analysis method is particularly useful when dealing with the granule form of the material.

1.3.8 Motivation for Investigating the Mechanical Behaviour of Porous Silicon Substituted Hydroxyapatite Ceramics

Hydroxyapatite has been investigated for orthopaedic and dental applications. It has been used in a number of forms; as porous granules, dense implants as well as coatings for implants such as hip replacements in order to improve the bonding with host tissue (Dorozhkin, 2015), (Pearson and Scammell, 2013) and create an osteo-conductive environment that enhances the implant fixation and limits thereof the reaction to foreign bodies that usually accompanies metal implants (Takashi et al., 2005). The osteo-conductive property of porous Hydroxyapatite, was reported to have exceeded the osteo-conductivity of some autografts when implanted in an onlay position i.e. on top of existing bone (Kalantarian et al., 2005).

Hydroxyapatite's porosity, particularly its micro porosity, allows for the adsorption of more osteogenic proteins via increasing the surface area of the BGS. This in turn enhances functions such as proliferation and differentiation when compared to materials of lower micro porosity volume (Hing et al., 1999), (Eggli, Muller and Schenk, 1988), (Klawitter and Hulbert, 1971), (Della et al, 1974). The macro porosity influences the processes of angiogenesis

(formation of new blood vessels) and osteogenesis (bone formation) (Sobral et al., 2011) as well as the rate of bone growth (Woodard et al., 2007). BGSs with multiscale porosity bare the closest resemblance to natural bone tissue (Innocentini et al., 2010). It has also been reported that changes in the macro porosity are more effective for manipulating the mechanical properties of bio-ceramics than changes in their micro porosity (Bignon et al., 2003). A study conducted on 3D scaffolds (Cho et al., 2010) found, that the shape of the pores had a significant effect upon Oxygen diffusion. The cone shaped pores demonstrated a superior supply of Oxygen when compared to oval shaped pores.

The level of interconnectivity of the porous BGS structure controls the degree of fluid flow within the structure and consequently the quality of bone growth (Bignon et al., 2003). They have also been linked through studies carried out in-vivo and in-vitro, to the actual depth of infiltration of the newly formed bone tissue deposition as well as the rate of at which the phenomenon takes place (Bignon et al., 2003), (Hing et al., 2002).

In order to avoid stress shielding, it is import that the rate at which the graft degrades or absorbed, matches the rate at which new bone tissue is formed, whilst maintaining the mechanical integrity of the graft particularly at the early stages as they later gain strength as a result of bone infiltration particularly when the rate of bone growth is high, a phenomenon observed even with bone grafts of low density i.e. of high porosity. It was shown that after three months post implantation the compressive strength of a porous hydroxyapatite graft increased from 2 MPa to 20 MPa (Sopyan et al., 2007), which is quite a significant increase that strengthens the case for using Hydroxyapatite grafts of high porosity e.g. > 60% of the material. Highly porous HA is linked to good in-vivo performance with a high rate of osteo-integration (Hannink and Arts, 2011), (Yoshikawa, 2005), (Sopyan et al., 2007).

Investigating the material's in-vivo mechanical responses experimentally can be difficult. Using a 3D finite element analysis approach and linking the findings to histology data from previous studies is a novel method adopted in this study to link the mechanical responses with in-vivo behaviour (Gibson and Ashby, 1988)

1.4 An Introduction to Finite Element Analysis

As computers advance along with tools and methods for simulating various structures, scales, loads and strains. Computer simulated studies, become more attractive for studying and understanding complex engineering scenarios and geometries. Finite element analysis is an engineering numerical technique that allows for the analysis of continuums through partial differential equations. This is done via the discretisation of a continua of interest into a finite number of smaller interconnected sub domains. The subdomains known as elements vary in size and geometry and are connected to each other through nodes (Whiteman, 1985), (Bathe, 2006).

Elements, contain all the material information and allow for the partial differential equations to be approximated in order to solve them using numerical model equations. The solutions, which are again an approximation of the partial differential equations are then transferred between neighbouring elements. The finite element analysis creates a meaningful solution of the approximations of the continuum. The process of discretisation is widely known as meshing and is typically carried out using appropriate software commercial or otherwise. The term finite stands for the finite number of degrees of freedom associated with each element in the mesh assembly (Whiteman, 1985), (Bathe, 2006).

There is a level of control that can be asserted over the mesh size. The geometric details of parts determine the mesh density (element size) to be used for an FEA. The choice of mesh size is also subject to the level of accuracy required, with smaller elements associated with more accurate solutions. A compromise needs to be established as denser meshes are computationally expensive. Generally, elements can be one, two or three dimensional. Within a given mesh adjacent elements are connected at nodes. Element Nodes are points identified through coordinates which define the degrees of freedom. Degrees of freedom can be displacement, rotation, temperature and electric potential depending on the type of analysis. Two and three dimensional elements having 3 and 6 degrees of freedom respectively.

Three dimensional elements are typically used for volume analysis. Along with two dimensional elements, three dimensional elements are also used for simulations that require detailed results (Bathe, 2006).

Types of elements are:

1- Elements of zero dimensions which are points, nodes are considered as 0D elements
2- Lines, which are elements of one dimension. Edges are considered as 1D elements
3- Elements of two dimensions. These include triangles and quadrilaterals. Faces are considered as two dimensional elements
4- Three dimensional elements usually employed for meshing volumes. These include tetrahedrons, hexahedrons, wedges and pyramids (Dassault Systèmes, 2014).

There are a number of factors that influence the type of elements and mesh densities for an FE analysis;

1- The level of complexity of the geometry
2- The level of detail expected from the analysis
3- The computational memory and capacity available for the analysis (Dassault Systèmes, 2014).

For the purpose of this research, it was necessary to create an FEM model able to capture the complex form of PHA granules. The complex geometry of the porous structure was captured using 3D imaging techniques. Similar approaches were conducted on bone, the investigations applied imaging techniques such as MRI, CT-Scans and ultrasound that can produce high quality images. These were used to create meshed volumes using various software and algorithms that can produce good quality meshes for analysis (Said et al., 2008), (Young et al., 2008).

Complex porous structures such as bone and porous bone graft substitutes present a number of concerns when applying a FEA technique, due to the error sources and the magnitude of

those errors, resulting from the geometry and the assumptions (simplifications) regarding boundary conditions and the application of load.

Energy conservation plots alongside convergence tests, are used to validate the modelled meshes and the assumptions made during the analysis. Three dimensional volume rendering approach though challenging, can potentially yield more realistic results than the traditional modelling approaches employing 2D simulations conducted on Hydroxyapatite. In previous studies simulating hydroxyapatite, the porosity was generated mathematically and the models tended to be in two dimensions, and did not capture the full extent of porosity, distribution of pores, strut structures or the unique connectivity and their effect on the strain distribution during loading (G.N et al., 2015), (Ozturk et al., 2010), (Palmero et al., 2009) (Sharma et al., 2018). As one of the first 3D finite element models of HA, there may be some shortfalls to this study and the models created. However, these models can be considered as a good step towards future work that can potentially change our understanding of HA as a material and its application as a bone graft substitute.

1.5 Representative Volume Entities

Despite of the availability of efficient software to preform finite element analysis on volume rendered scans of porous granules of Hydroxyapatite. Computational time and expense need to be considered for each model to be analysed. After thorough consideration it was evident that the application of representative volume entities for the purpose of this analysis is a necessity. An RVE can be defined as a sufficiently large volume of the heterogeneous material, including a sufficient amount of micro-heterogeneity thus allowing it to be considered as a statistical representative of the general properties of the material (Ullah at al., 2017). The use of representative volume entities is popular for material science applications. RVE analysis is a micromechanics approach to investigate the microstructural properties and behaviour of microscopic entities and subdomains of larger sets at the macro scale, in this case; the strut (micro) porosities. An RVE is considered as a quasi-homogeneous representative of the responses and the material behaviour of the larger scale heterogeneous

domain. Thus, linking the gross macro-mechanics to the microscopic constituents (Fritsch et al., 2007). For materials such metals, this is not necessary as their structure is completely homogeneous (Ullah et al., 2017), (Runesson et al., 2011). One of the aims of this study is to capture the natural behaviour and responses of the granular form of porous hydroxyapatite bone graft substitutes as these are the most relevant to medical applications. Heterogeneity, is a feature present throughout the scales of porous hydroxyapatite material. Smaller scales can possibly represent larger scales, as the assumption of continuum is considered to be valid. Smaller scales can be investigated if a homogenisation process is applied. Homogenisation can be thought of as a method of bridging the length scales, approximating the heterogeneous structure mechanics through the analysis of the micro elements of the representative volume.

In this case, the struts and their micro pores are analysed. Their influence on the stress and strain fields transcends the microstructures to effect the macro heterogeneous domain they constitute. The FE analysis will be based on the local strut regions where the fields concentrate. The stresses and strains will be averaged throughout the RVE structures and their energies are plotted against the global strain thus homogenising the RVE structures. Steps will be taken to validate this approach and the RVEs representativeness through their conservation of porosity and strain energies with the latter changing in accordance with the change in global size (Hollister and Kikuchi, 1992).

The rationale for applying an RVE approach for this investigation can be summed up in the following points:

1- Due to the complexity of the structure, a numerical simulation using finite element analysis can prove computationally demanding and expensive. PBGS structures require fine meshes that can conform to the contours of the model creating thus an extremely large number of degrees of freedom.

2- Modelling PBGS granules using a homogenisation approach is not common for FEA analysis of Hydroxyapatite. Adopting this approach allows for investigating the extent of representativeness of RVEs at different sizes to enable further studies on the material using similar RVEs.
3- Homogenisation and the application of representative entities allow for a better insight into the microscopic fields (micro-pores), particularly strain fields caused by stresses or strains applied to the macroscopic structure. Thus, linking the heterogeneity of the macro structure to the influence of its constituent microstructures.

Applying this method to Porous BGSs, was quite challenging. Literature was limited in terms of finite element analysis of true Porous BGS structures and the homogenisation of such structures. There is no clear information on what the building block of this architecture might be. The logical assumption would be that the building block is one granule. In this research, the granule sizes were obtained via crushing larger granules than applying a sieving technique to collect the granules ranging between 1-2 mm. The granules were packed in polymer tubes of 8 mm diameter and 16 mm height for scanning. The volume rendering techniques applied to the rendered scans do not allow for border definition between granules to be established. Treating the granule filled cylinder as a continuum. This limits the application of granule borders as boundary conditions. For obtaining RVEs, the cylinders were segmented to shorter cylinders that should include less amount of granules. The aim is to obtain an RVE with the least number of granules whilst maintaining the level of material's porosity. This is the best way to obtain statistical representatives of the material for FE analysis.

Maintaining the level of porosity is essential as the material's properties are defined by the porosity level. It is also a requirement that the RV remains to be a true representative of the material i.e. behaves similarly to the material (Hill, 1963). The segmentation to smaller constituents or volumes, is known as volume fractioning (Yu, 2016). Although having an RVE of one granule only, can be attractive, it is not quite achievable due to the lack of border definition, and does not comply with RVEs condition number two.

RVE requirements can be summed in the following

1- To behave as a mechanically statistical representative of larger volumes during the deformation processes (Trusov and Shveykin, 2017).
2- RVEs must be large enough to contain sufficient microstructural information, maintaining material properties such as the modulus, yet are significantly smaller than the global size (Drugan and Willis, 1996) (Hashin, 1983).
3- An RVE must be of a scale similar to laboratory specimens, thus allowing it to be regarded as a continuum on its own merit yet a representative of a larger scale continuum (Hashin, 1983) .
4- RVEs must obey the Hill-Mandel principle of macro-homogeneity. Which dictates that the strain energy of the RVEs should respond to the change in their global size accordingly. As the micro porosity is simulated any increase in the RVE size increases the level of micro pores contributing to the strain energy output (Hill, 1963), (Mandel, 1971), (Hill, 1972).

1.6 Research Novelty

Ceramics and particularly porous ceramics such as PHA especially in the granule form, lend themselves to be an attractive target for finite element analysis. Finite element simulations do not only serve to analyse the mechanical responses, but can be utilised further to cover the various and complex in vivo multi-axial loading conditions that grafts experience when implanted such as; muscle forces, shear forces as well as the pressure caused by aqueous flow (Hayes, 2016).

It is beyond the scope of this research to cover all the possible loading conditions. This is especially challenging when investigating PHA granules as a 3D realistic structure as obtained from scans. Which is a novel approach to adopt for the material, and has not been preceded by similar approaches prior to this study. Most of the finite element investigations in literature have been focusing on the 2D structures or on the material as part of an implant system and not as a standalone structure despite of it being used as a bone graft substitute in its granular form (Ozturk et al., 2010), (Palmero et al., 2009) (Sharma et al., 2018). This study could pave the way for future research possibilities using volume rendered realistic structures of PHA granules. This could potentially create a complete mechanical map of the material, thus influencing the way it is manufactured and used as a bone graft substitute.

1.6.1 Rational One

Simulating an as-scanned 3D structure of PHA, is a novel approach introduced in this research to field of bone graft substitutes. The simulations will be carried out on different statistically representative volume entities, and will focus on the stress and strain fields created under uniaxial compressive loading conditions. The results will be discussed in relation to documented bone growth patterns from previous publications. In an attempt to find a link between the patterns of bone deposits on the material in-vivo and the strain field distribution within the material under load.

1.6.2 Rational Two

The research will include mechanical tests carried out on PHA granules of various porosity levels from which data was used to define some of the materials' properties for FE analysis. Applied through ABAQUS software for the Drucker Prager failure model, which is traditionally used for powder compaction and soil simulations. However not yet applied to PHA granules. The rationale behind this approach is that; in several bone graft applications, PHA is used in its granular form (Hing et al., 2005). Simulation of the structures in this form allows for further research linking the Finite element results to in-vivo behaviour and patterns of bone growth. The research attempts to shed some light on the relationship between the macroscopic mechanical response and the microscopic porous structure of hydroxyapatite.

Chapter 2

2.1 Introduction:

Prior to engaging in analysis, it is essential to characterise certain relevant aspects of the material in question. Typical characterisation techniques include

1- Chemical characterisation. Typically employing X-ray diffraction and infrared spectroscopy.
2- Structural characterisation that may include one or more of the following;

a) Grain size measurements
b) Porosity measurements
c) Density measurements

3- Mechanical testing

Structural and mechanical characterisation techniques were necessary for the purpose of the study. These include:

1- Density measurements. Using the Archimedes method to obtain the total porosity
2- Micro porosity measurements. Using scanning electron microscopy
3- Mechanical testing. Applying a uniaxial compression test on PHA granules and a diametral test also known as Brazilian disc test on porous PHA discs.

The granules of the porous Silicon substituted Hydroxyapatite (PSHA) were provided by ApaTech Limited, UK. PHA and PSHA are interchangeable terms in this study used for the same material as the silicon substitution is at 0.8 wt % and irrelevant to the mechanical results. Table 1 demonstrates the nominal porosities of the materials received and used throughout the study, P-Total is the total porosity and P-Strut is the strut or micro porosity. The density measurements and SEM analysis provided data that agree with the nominal values for the batches received. Data obtained from the compression tests was used as material property

input for the Drucker Prager finite analysis model, the same applies for the Brazilian disc results where they were used to obtain parameters for the model.

Table 1: Nominal porosities of the PHA material used in the study

PHA Sample	P-Total	P-Strut	Percentage substitution of Silicon in Hydroxyapatite
SA 80-20	80 %	20 %	0.8 wt %
SA 80-30	80 %	30 %	0.8 wt %
SA 70-20	70 %	20 %	0.8 wt %
SA 60-20	60 %	20 %	0.8 wt %
SA 60-30	60 %	30 %	0.8 wt %

2.2 Characterisation Techniques:

2.2.1 Total Porosity Analysis

In order to confirm the total porosity of granules to be used for mechanical testing and scanning for FEM analysis, the density of the granules were measured using the standard Archimedes principle (Hing et al., 1999). Three specimens were analysed for each porosity combination. In this method the granules were measured dry in triplicate repeats using an electronic balance (Ohaus, Leicester, UK). The dry weight is indicated by W_{dry}. This was followed by a submergence procedure which involved placing the granule in deionised water at a temperature of 100 C^0 and boiling for one hour, this is to insure that all the pores were

(a) 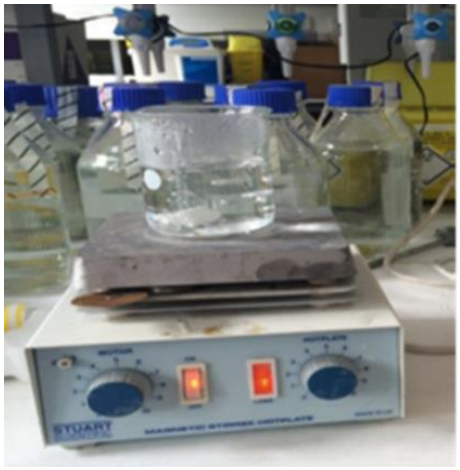 (b) 

Figure3 : Archimedes testing kit to measure the total porosity of the PHA granules

completely filled with water. The specimens were then left to cool to room temperature prior to undergoing further weighing procedures in triplicate repeats. The specimens were weighed in the submerged state, the weight is known as W_{sub}. After removing the specimen from water and allowing the excess water to drip for 3 minutes. The specimens are weighed in a saturated state also known as wet state W_{sat} . All measurements were conducted using the AP density solid kit (Ohaus, Leicester, UK). Using the density value of 3.156 gcm^{-3} for dense HA (Akao et al.,1981), and the density of water in accordance with Ohaus manual for the density of water at room temperature. The apparent and real densities of the Hydroxyapatite granules were calculated using the following equations (Hing et al., 1999)

$$D_{apparent} = \left(\frac{W_{dry}}{W_{sat} - W_{sub}}\right) \rho H_2O \quad \text{Eq. 3}$$

$$D_{real} = \left(\frac{W_{dry}}{W_{dry} - W_{sub}}\right) \rho H_2O \quad \text{Eq. 4}$$

With $D_{apparent}$ being the apparent density, and D_{real} the real density. Where the apparent density equation considers the open pores as well as the closed pores of the specimen as well as all open voids including the spaces between particles. The real density equation takes into consideration the closed pores only. Figure 4, demonstrates the difference between open and closed pores in typical porous ceramic structures.

The following equations were also used, in order to determine the closed and the total porosities of the material. Table 2 clarifies all the abbreviations used in the density calculations.

$$CS\mu = \left(1 - \frac{D_{real}}{\rho HA}\right) X\ 100 \quad \text{Eq. 5}$$

$$TP = \left(1 - \frac{D_{apparent}}{\rho HA}\right) X\ 100 \quad \text{Eq. 6}$$

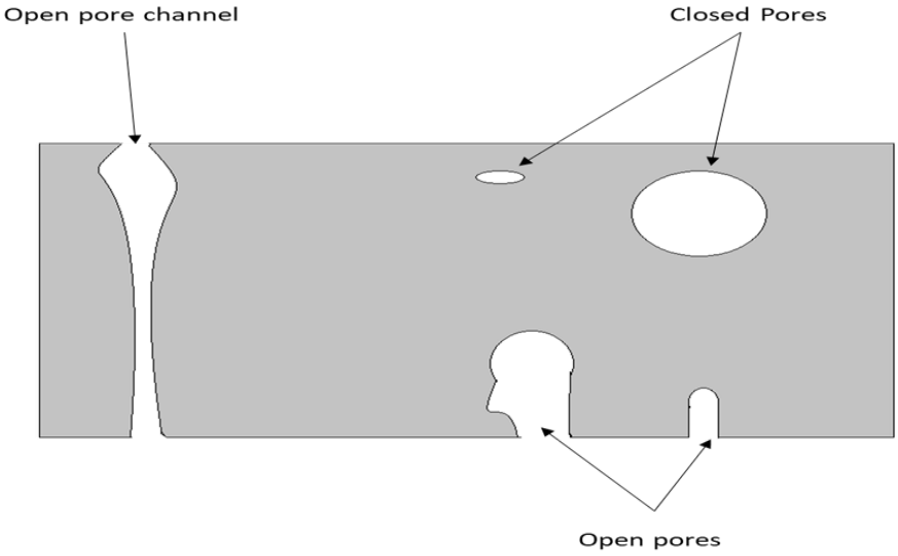

Figure 4: Schematic demonstrating the difference between open and closed pores as well as channels which constitute the structure of Hydroxyapatite bone graft substitutes.

Table 2: Abbreviations used in the density calculations

Notation	Definition
$\boldsymbol{D}$	Density
$\mathbf{D_{real}}$	Real Density
$\mathbf{D_{apparent}}$	Apparent Density
$\mathbf{W_{dry}}$	Measured Weight-Dry
$\mathbf{W_{sat}}$	Measured Weight-Saturated (Wet)
$\mathbf{W_{sub}}$	Measured Weight-Submerged
$\boldsymbol{\rho_{HA}}$	The theoretical density of Hydroxyapatite granules at 3.156g/cm^3
$\boldsymbol{\rho_{H_2O}}$	The density of deionised water
$\mathbf{CS\mu}$	Represents the closed strut porosity

2.2.2 Strut Porosity Analysis:

In order to determine the strut porosities of the specimens, scanning electron microscopy was used. The specimens required embedding and polishing procedures prior to microscopy. The granules were embedded in resin (EpoFix Resin, Struers, UK) with a hardener (EpoFix Hardner, Struers, UK), at a 1:6 ratios in a 25 mm diameter mould under vacuum using an EpoVac^{TM} vacuum embedded, and left to set for 24 hours in a fume cupboard after removal from the vacuum kit. These steps were necessary to insure that the resin penetrates the macro and the micro porosities of the specimens. After the removal of the hardened epoxy from the mould, the surface of the epoxy structure was polished in order to bring the PHA granules to the surface whilst keeping a smooth finish. In order to achieve the desired surface finish a semi manual polishing machine was used (Abramin, Struers, UK), applying water as lubricant and a range of diamond impregnated grinding pads starting with grinder sizes of 220, 600 and 1200 and polished on PoliFloc polishing pads with 3 μm diamond paste, where all grinding, polishing pads and consumables were obtained from (Abramin,Struers,UK).

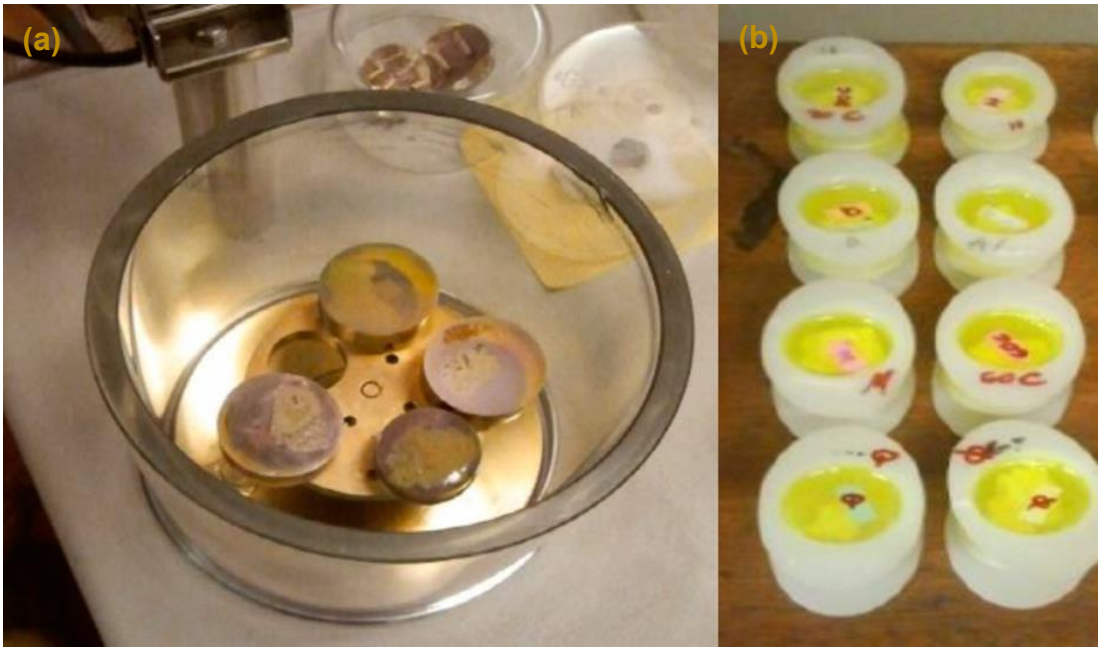

Figure 5: PHA granules embedded in epoxy resin ready for polishing. (a) gold coated embedded samples. (b) embedding in epoxy resin.

The surface was cleaned thoroughly before each change of pad. Finally, the samples are cleaned with water and methanol to prepare them for coating and microscopy. The samples were then mounted on steel studs using a carbon paste insuring connectivity to the surface coating which was chosen to be gold for the images to insure good electron conduction during the microscopy process. A small region of the sample was imaged and photomicrographs were taken at 50, 100 and 700 magnifications.

Using SEM has the advantage of producing high resolution images with high magnifications. It has a high field of view allowing a larger area of the sample to be investigated, producing images of the surfaces resembling 3D images. There are two types of electrons used by the scanning electron microscope and these are the backscattered electrons and the secondary electrons. They differ in their energy and the depth they can excite. The escape depth for secondary electrons ranges from only 5 to 50 nm, hence it is used to obtain surface data, and whilst the backscattered electrons escape depths are 100 times greater. Inelastic scattering caused by the primary beam hitting the samples generate secondary electrons. Back scattered electrons however, are generated from elastic scattering where the primary beam interacts with the nucleus (Figure 6). SEM detectors can collect secondary electrons from the thin surface of the sample whilst back scattered electrons can be collected from deeper regions of the sample due to their high energy (Moncrieff and Barker, 1978).

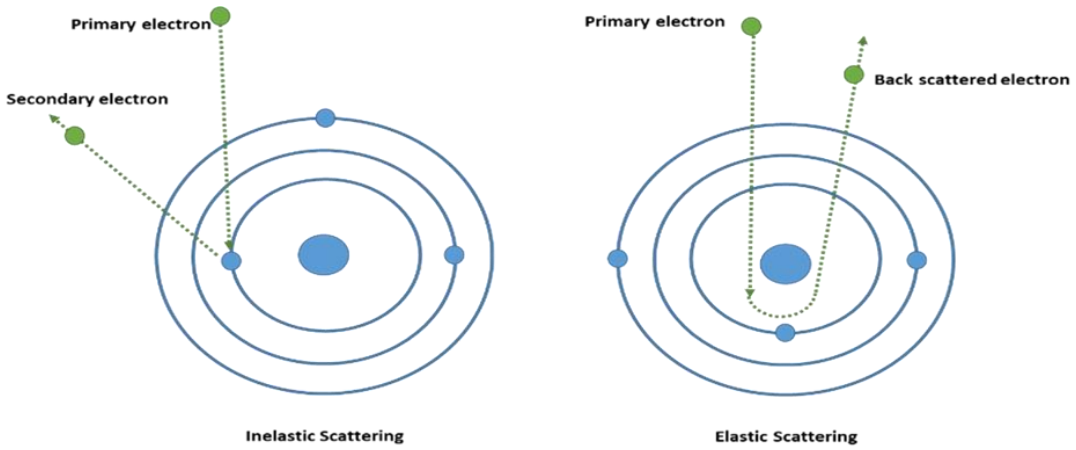

Figure 6: Schematic demonstrating the difference between backscattered and secondary electrons

As the secondary electrons during SEM are emitted from the slopes and edges of the surface layer. They result in images of good contrast between the slopes and the flat surfaces. This provides the topological data needed for this research to determine the closed and open porosities of the PHA samples used alongside the data gathered from the density investigation. Using SEM can confirm the micro-porosity within the granules' struts. To calculate the percentage occupied by micro-pores a threshold masking technique in 2D was carried out using Scan IP (Simpleware™, 2017) software. This technique allowed for the verification of the strut porosity levels in all samples. This approach is both accurate and time conserving for this type of characterisation. This is due to ability of the software to use the SEM's image own contrast to allocate a colour to the flat surfaces leaving the empty spaces or voids at zero threshold. The voids or pores can be then covered with a different mask for zero threshold in order to calculate the percentage of space occupied by the pores.

2.3 Constrained Compression Testing

The study aims to build a model that can investigate the strains within granule masses of PHA, as the granular form is clinically more relevant. The decision was made to perform constrained compression tests on granular samples to obtain data for the granular masses and evaluate their mechanical behaviour. The ultimate compressive strengths, Young's moduli and tensile strengths were also necessary for creating the finite element models. The ultimate compressive strength and Young's moduli were obtained from literature as they require different settings to the constrained granular test (Hing et al., 2005), (Campion and Hing, 2017).

A Brazilian diametral test was also conducted in this study for the purpose of obtaining values of diametral tensile strengths. However, due to the lack of variety of porosities in the form of Brazilian discs, more data was collected from literature to cover a wider range of porosities. More on the test method will be discussed in section 2.3 of this chapter.

When subjecting HA granules to mechanical tests, it is essential to keep in mind the effect of the strain rate applied to the material. Dense ceramics of total porosities lower than 40%, have a characteristic behaviour when loaded in compression. With an initial short lived elastic behaviour followed by sudden failure. Highly porous ceramics demonstrate a longer lived elastic behaviour, which is not as short lived as dense ceramics. This is due to the progression of pore walls collapsing. This phase is than followed by a sudden drop in load due to crack propagation within the struts of the material (Meille et al., 2012).

Under high strain rates, porous ceramics show an increase in brittle behaviour. This is true for many ceramics as well as some metals (Mishra and Mukherjee, 2000). Applying high strain rates during compression tests is known as shock testing, which results in a loss of strength. This could be explained by the strain not allowing the occurrence of micro-crack propagation within the material's struts as a result of a non-linear microscopic response (Zhan et al., 2007).

A strain rate of 0.5 mm/min was selected I accordance with literature review (Hing et al., 1999). A uniaxial testing approach was adopted for practicality reasons, the method has been previously adopted to investigate the mechanical behaviour of cancellous bone and PBGS (Peelen et al.,1978), (Akao et al., 1981), (Fritsch et al., 2009).

The PHA granules received from ApaTech Limited, UK, and come as irregular sized lumps for each porosity combination. The materials were crushed and sieved to collect smaller granules of diameters ranging between 1 and 2 mm. These granule sizes are easy to handle and fill into cylinders for further analysis. The testing was carried out using INSTRON equipment in combination with Blue Hill Bluehill® LE Software, with a cylindrical rig of 30 mm in diameter and 30 mm in height. The strain rate was set to 0.5 mm/min. the axial stress was calculated from the compressive load divided by the cross-section area, and the axial strain from the change in height divided by the original height of the sample. The cavity of the rig compartment was filled with 8 ml of granules giving a height of 18 mm. Figure 7 and 8 demonstrate the test set up with a schematic explaining the stresses that the granules experience due to the axial compressive stress applied. It is important to note, that only the axial stress can be measured

using this set up. Since the mechanical behaviour of PHA is density (porosity) dependent it is important to calculate the change in density that occurs during the axial compression process. This is done through measuring the initial densities of the samples through the Archimedes method. The volume of granules within the rig was also measured, this step is essential for the application of the Drucker Prager Cap model in ABAQUS as the model is density dependant.

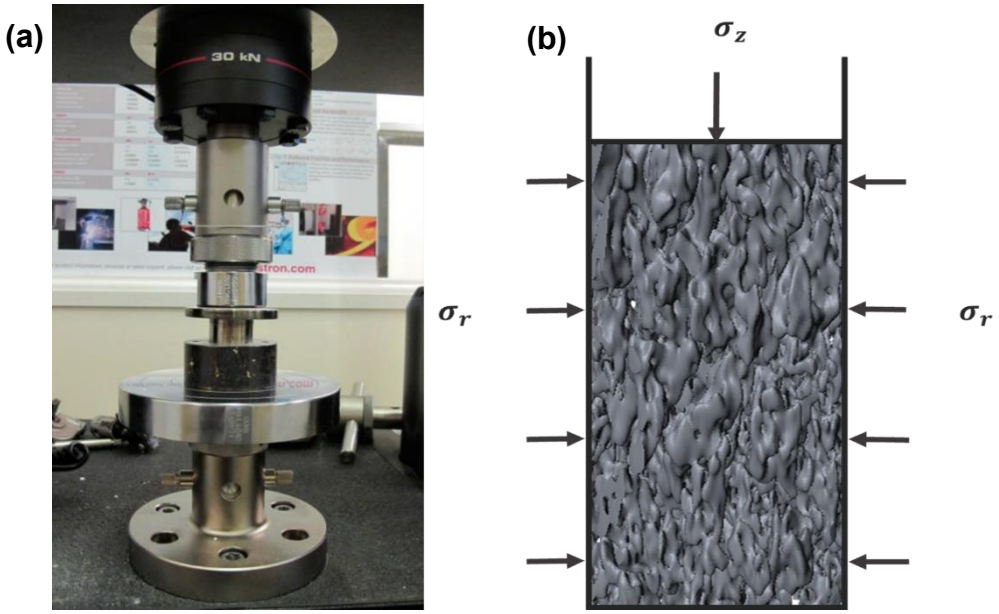

Figure 7: a) Instron machine in action, (b) a schematic demonstrating the stresses experienced by the PHA granule during uniaxial compression. The schematic demonstrates a realistic volume rendered to demonstrate the porosity of the sample and the inhomogeneity of the structure

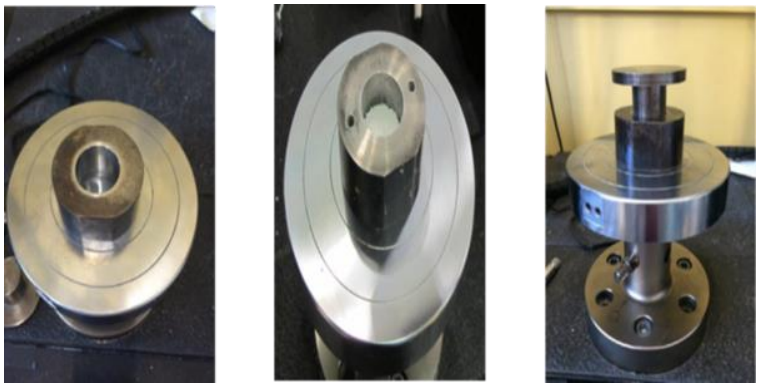

Figure 8: Cylindrical rig setting and filling with PHA granules ready for compression testing using Instron and Bluehill® Software

2.4 Brazilian Diametral Strength Test

A Brazilian test, also known as a diametral compression tests, are tests typically used on ceramic material. This is a test to failure, which can potentially provide data such as tensile strength and fracture toughness indirectly without the need for the impracticality of subjecting ceramic specimens to tensile tests that this approach has been adopted. To perform the test, a cylindrical sample of PHA is compressed between two flat surfaces along its diameter as illustrated in Figure 9. Compressing a disc in that manner causes tensile stresses to occur at the centre of the disc sample normal to the direction of load applied. A number of assumptions are accepted by scientists for these type of tests (Croquelois et al., 2017), (Li and Wong, 2013).

1- The radial pressure is assumed to be uniformly applied to the short segment of the circumferences in direct contact with the plates.
2- The friction between the cylinder sample and the plates is negligible (Li and Wong, 2013).
3- Materials tested are considered to be isotropic and homogeneous (Mellor and Hawkes, 1971).
4- Failure takes place at the centre of the disc, at the point of maximum tensile stress (Li and Wong, 2013), which can be derived using the relationship

$$\sigma = \frac{2F}{\pi D h} \quad \text{Eq. 7}$$

Where σ is the maximum is tensile stress, F is the applied force, D the diameter of the disc and h is its thickness. The discs tested in this study were Porous Hydroxyapatite discs averaging at 1mm diameter and 4 mm in height. To measure the porosity of the samples an Archimedes tests similar to the one carried out in chapter 2 on the PHA granules. The discs available were of 35%, 34% and 17% only. Ten discs in total were tested for each porosity.

Figure 9: Brazilian diametral test using the Instron machine with two flat metal plates covered by sand paper for a better grip. The picture demonstrates a typical disc failure

In order to obtain values of tensile strengths for a wider range of porosities, more values were collected from literature. Figure 9, shows the Brazilian test setting carried out using the Instron machine and Bluehill® LE Software, with two flat metal plates attached. The plates were covered by sand paper to enhance the grip on the discs. The load was applied at 1 mm/min.

2.5 Results and Discussion

2.5.1 Total Porosity and Strut Porosity Analysis

Table 3, demonstrates the results obtained from the density measurements to determine the total porosities of the batches of the material received.

Table 3: Density measurements obtained using the Archmedis method ± error

Sample	Apparent Density gcm^{-3}	Real Density gcm^{-3}	Total Porosity %
80-20	0.552 ±0.007	3.107±0.007	82.5
80-30	0.536 ±0.007	2.991±0.007	83.0
70-20	0.858 ± 0.007	3.085±0.007	72.8
60-20	1.204 ±0.007	2.984±0.007	61.8
60-30	1.167± 0.007	3.094±0.007	63.0

The results confirm the total porosity of the batches of the material received AapaTech limited, UK. The following images in Figures 10, 11 and 12 demonstrate the results of the SE microscopy applying SE electrons and employing ScanIP for analysis to determine the strut porosities.

2.5.2 Results of the Brazilian Diametral Tests

Results of the Brazilian diametral tests are listed in table. The samples demonstrated typical fracture behaviour as seen in Figure 9, with the fracture occurring at the centre where the maximum stress is located.

Table 4: Results of the diametral Brazilian tests carried out using the Instron machine with flat plates

Sample Porosity	Radial Stress in MPa $\pm$ SD
17%	11.3 ± 1.9
34%	7.5 ± 0.4
35%	8.7 ± 1.2

2.5.3 Results from SEM-Analysis of the Strut Porosities

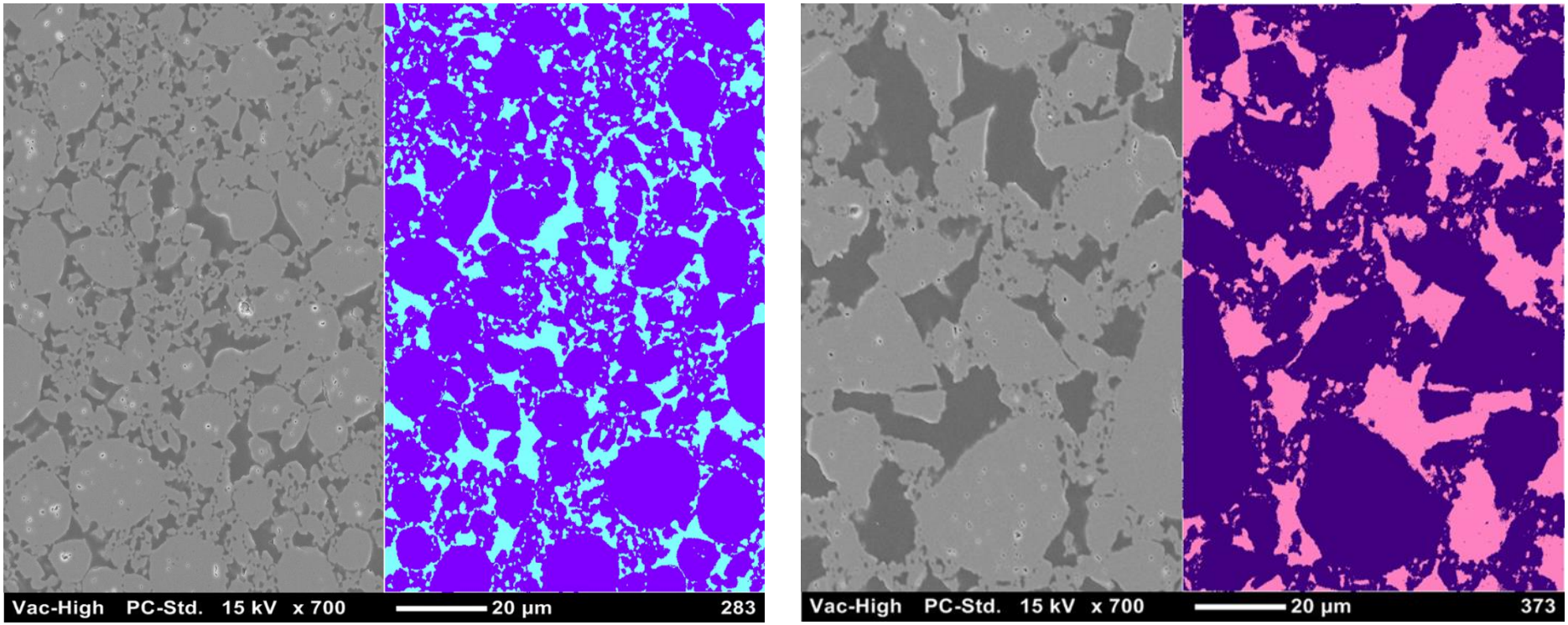

Figure 10: SEM analysis results Left 80-20 PHA granule surface under x700 magnification, using ScanIP software for pixel masks. Right 80-30 PHA granule surface under x700 magnification, using ScanIP software for pixel masks

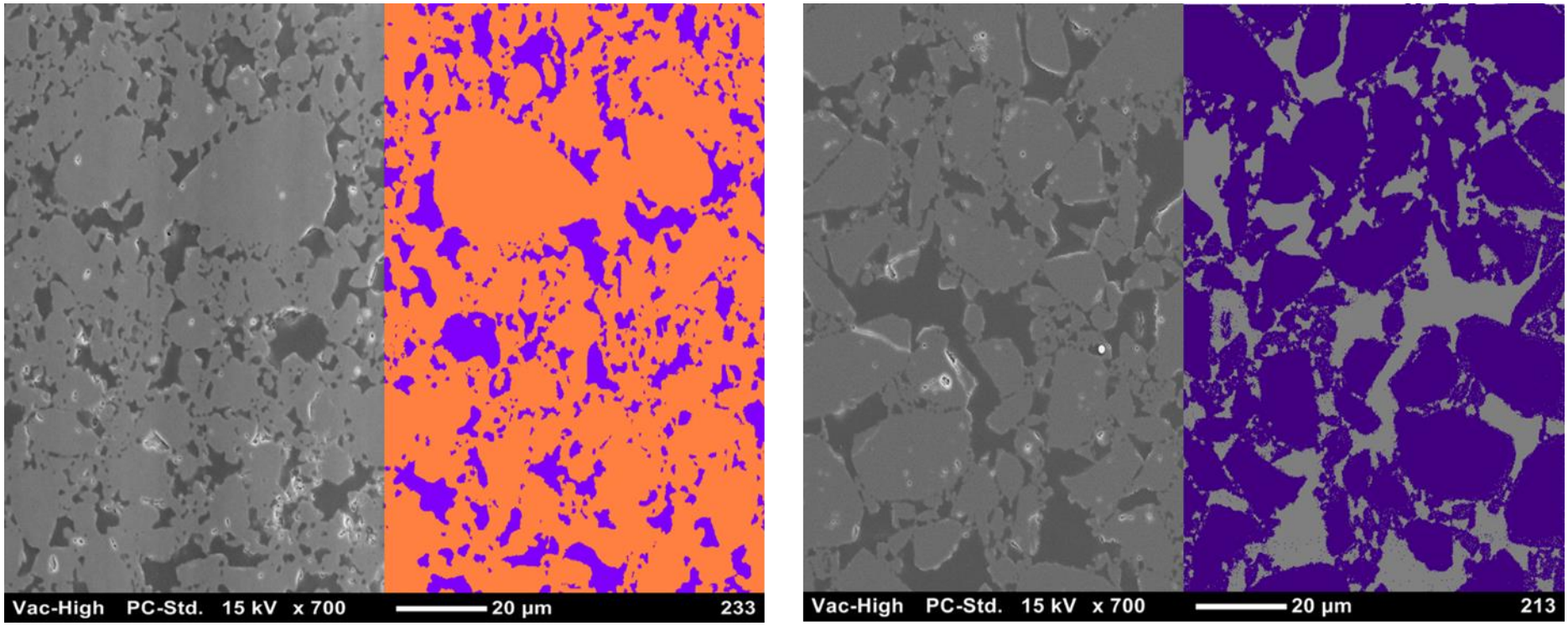

Figure 11: SEM analysis results Left 60-20 PHA granule surface under x700 magnification, using ScanIP software for pixel masks. Right 60-30 PHA granule surface under x700 magnification, using ScanIP software for pixel masks

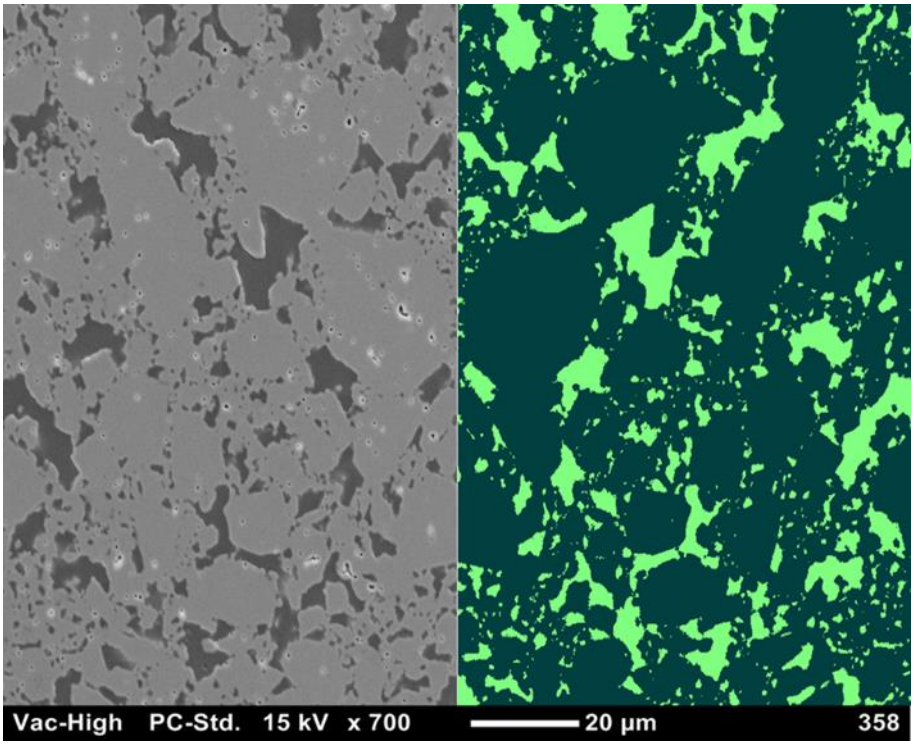

Figure 12: SEM analysis results for 70-20 PHA granule surface under x700 magnification, using ScanIP software for pixel masks

Table 5: Strut porosity results as obtained from the SEM analysis using ScanIP masking technique

Material	Strut Porosity ± SD
80-20	18.4 ± 0.3
80-30	28.2 ± 0.2
70-20	21.7 ± 0.5
60-20	20.9 ± 0.8
60-30	24.8 ± 0.7

2.5.4 Constrained Compression Test Results

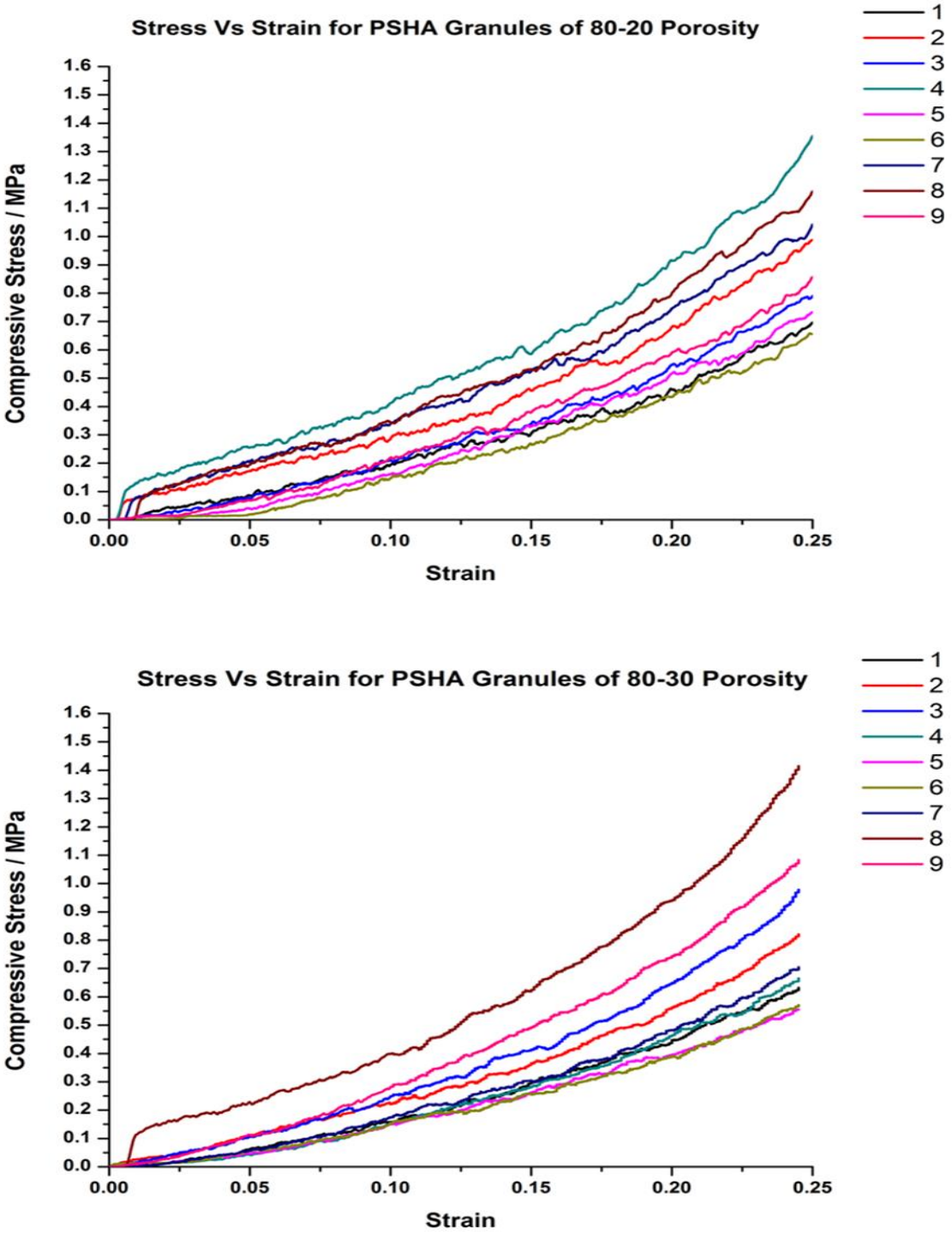

Figure 13: The graphs demonstrates the Stress Vs Strain curve constructed from raw data of the Compression test repeats for PHA granules of 80-20 and 80-30 porosity combinations respectively. Nine repeats in total for the 80-20 batch and eight for the 80-30, demonstrating similar behaviour.

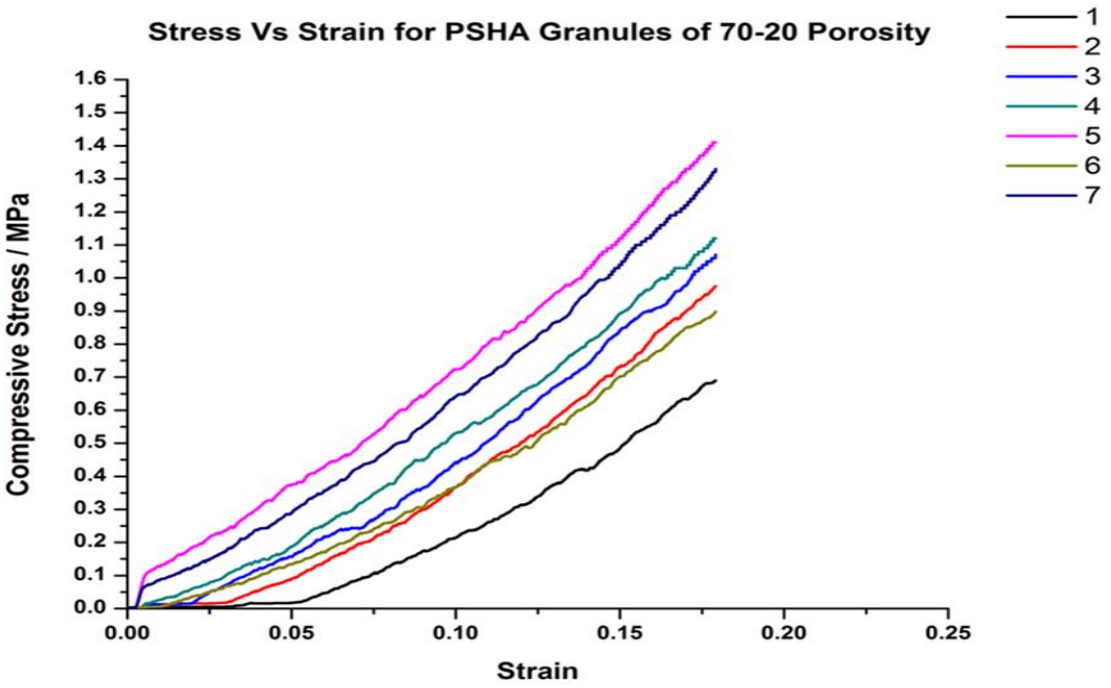

Figure 14: The graph demonstrates the Stress Vs Strain curve constructed from raw data of the Compression test repeats for PHA granules of 70-20 porosity combination. Seven repeats in total, demonstrating similar behaviour.

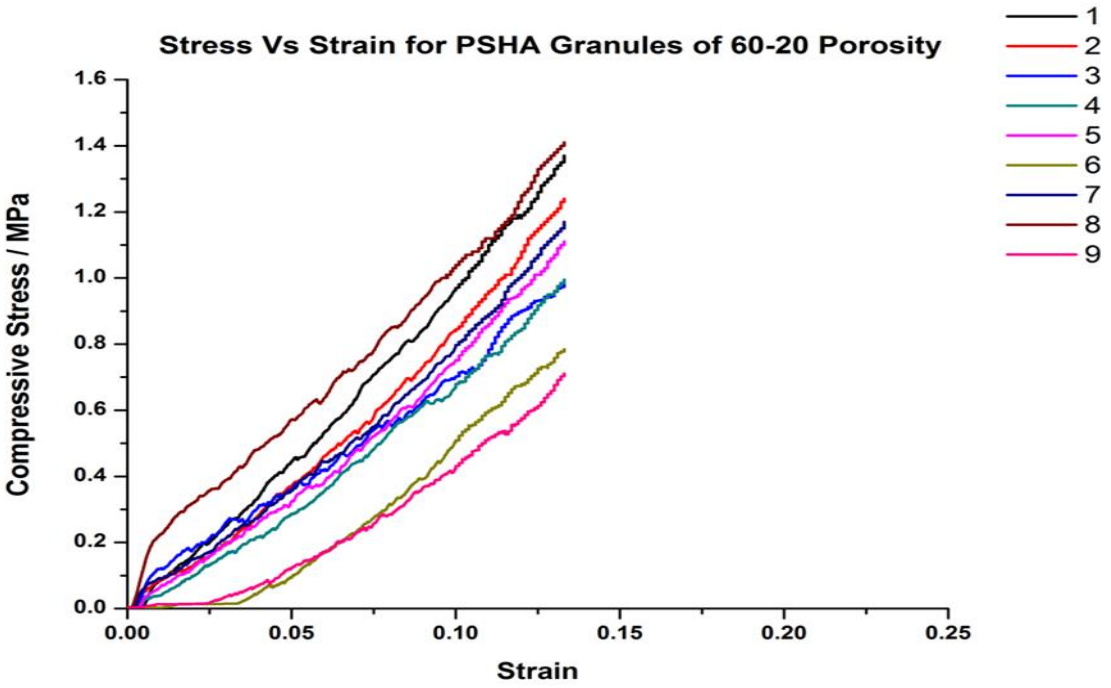

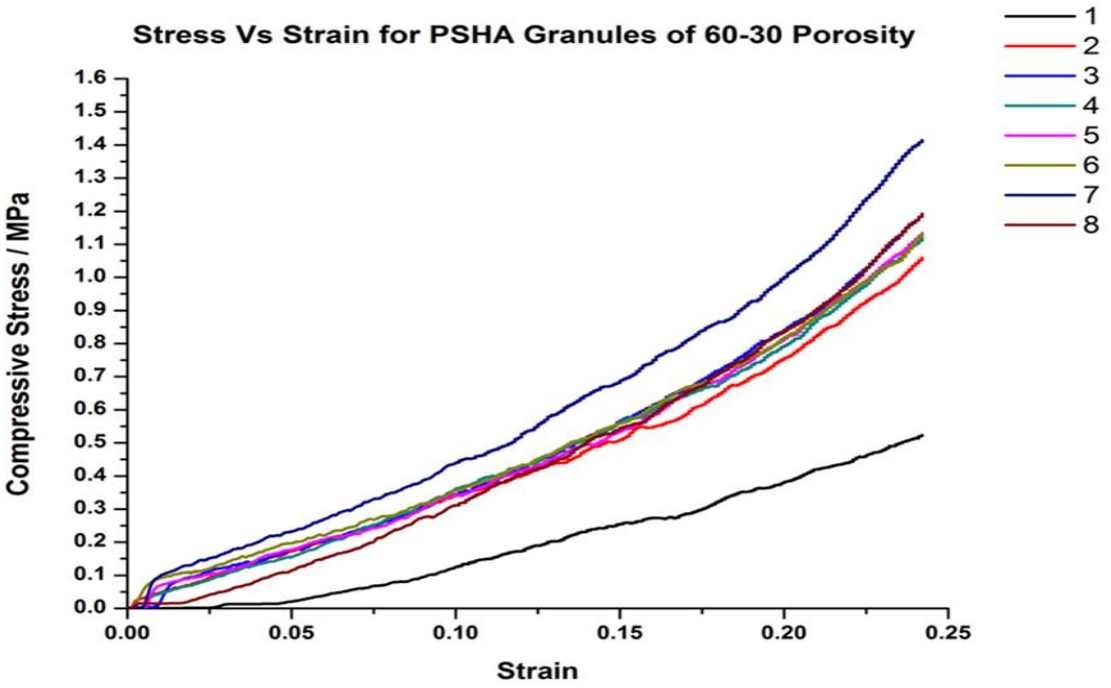

Figure 15: The graphs demonstrates the Stress Vs Strain curve constructed from raw data of the Compression test repeats for PHA granules of 60-20 and 60-30 porosity combinations respectively. Eight repeats in total for the 60-20 batch and eight for the 60-30, demonstrating similar behaviour.

2.6 Discussion:

For any given sample batch, the granules were found to behave similarly but not identically. This is possibly due to the random morphology and orientation of granules and the inhomogeneity of their porosities. All PHA granules demonstrate a typical Stress-Strain curve with an exponential increase in stress as a response to the increase in strain, as the material reacts through macro porosity than transitions slowly to reacting through micro porosity.

All samples were subjected to the same loading profile. All tests were automatically set to stop when a stress of 1.5 MPa was reached. In some cases, the tests were manually stopped when the stresses zigzag indicating damage. The tests demonstrated that the materials with largest total porosities were the easiest to strain and as the total porosity decreases straining becomes more difficult with the maximum stress allowed, either reached at a lower strains or samples damaged prior to reaching maximum allowed stress.

Segmenting these mechanical profiles using gradients as demonstrated in Figures 16-20, is an attempt to quantify the mechanical behaviour of PHA granules as a result of their porosity profile. The stress vs strain graphs can be divided into three regions;

1- The first region, where the initial stresses are experienced by the granules and the macro porosities are reacting to the load applied.
2- The transition region, where both levels of porosities (macro and micro) are involved in reaction to the load.
3- The final region, where the micro pores are experiencing a larger portion of the load applied than the first two regions.

These regions can be estimated by finding the steepest gradients for each section.

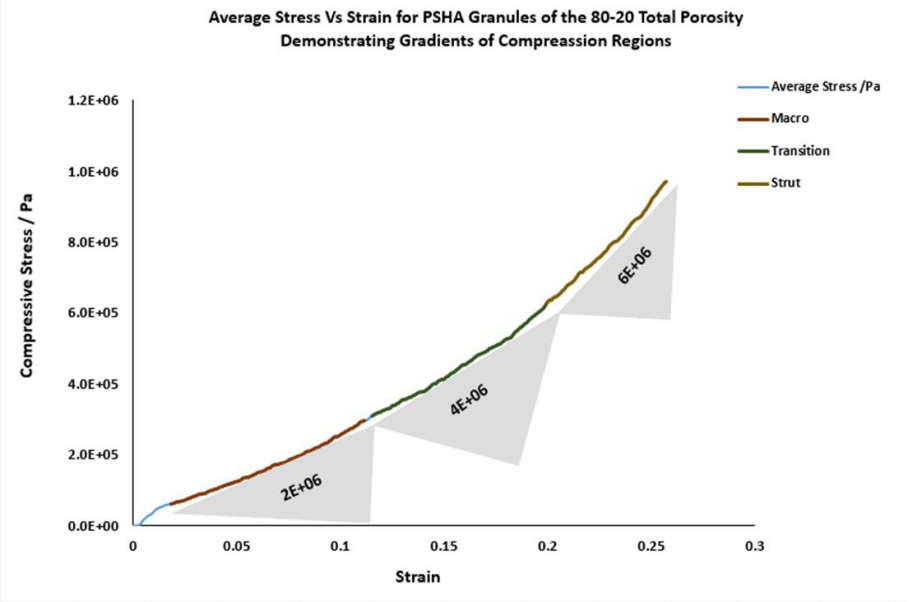

Figure 16: The averaged stress/strain graph for the 80-20 PHA granules. Grdients calculated to find the three regions dependant on the level of porosity under compression

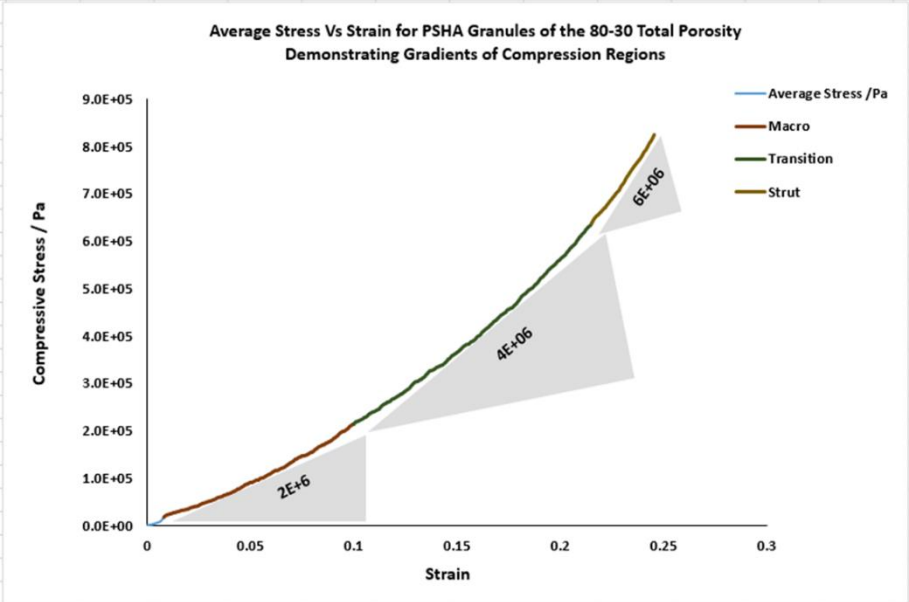

Figure 17: The averaged stress/strain graph for the 80-30 PHA granules. Grdients calculated to find the three regions dependant on the level of porosity under compression

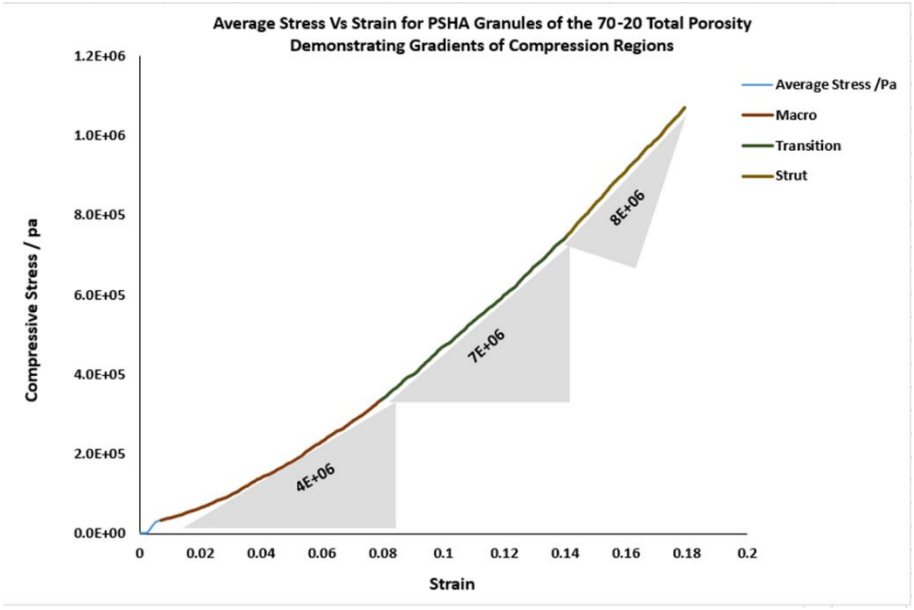

Figure 18: The averaged stress/strain graph for the 70-20 PHA granules. Grdients calculated to find the three regions dependant on the level of porosity under compression

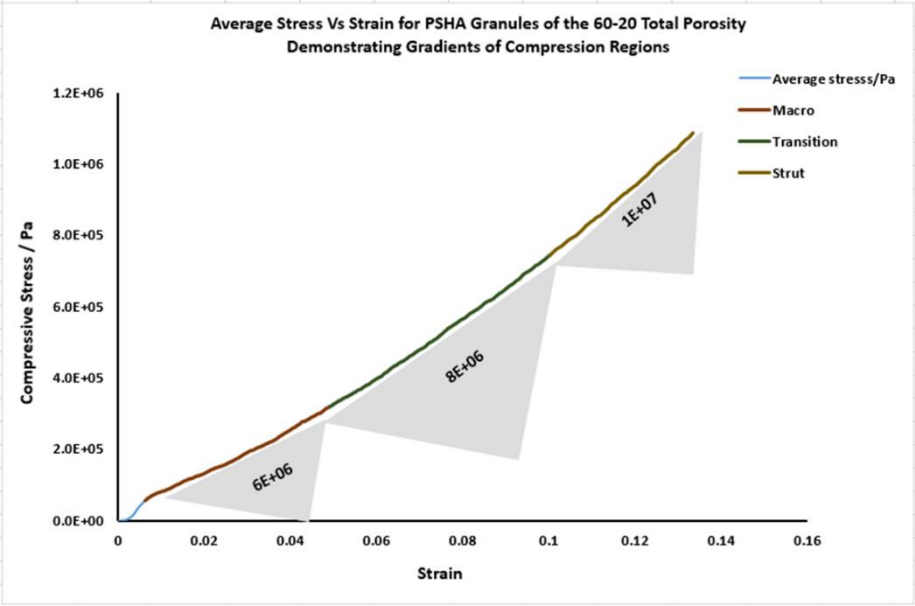

Figure 19: The averaged stress/strain graph for the 60-20 PHA granules. Grdients calculated to find the three regions dependant on the level of porosity under compression

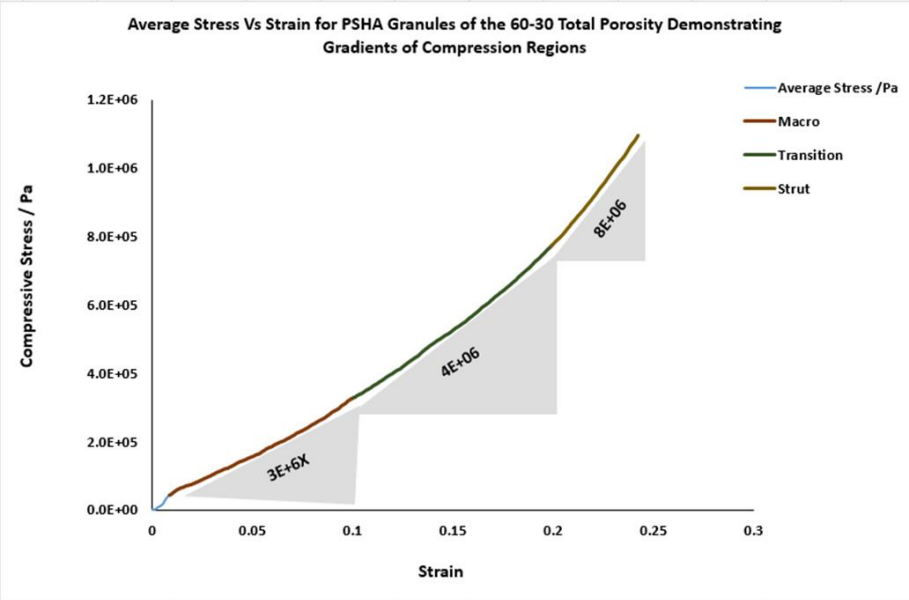

Figure 20: The averaged stress/strain graph for the 60-30 PHA granules. Grdients calculated to find the three regions dependant on the level of porosity under compression

When investigating the segmented regions of the stress strain profiles of PHA granules, it was found that;

- Regarding the first region of the stress-strain curve; PHA granules of 80% total porosities and 30% micro porosity show on average the same levels of stresses for similar strains when compared to the 20% counterparts. This is not the case for the granules from the 60% total porosity groups with the granules of 20% micro porosity demonstrating higher levels of stresses than their 30% counterparts at similar strain levels as indicated by the steeper gradient for region. The granules of the 30% micro porosity from the 80% and the 30% of 60% groups show similar stress levels in the first region at similar strains. Thus the results cannot be conclusive in regards to the behaviour of granules during the initial stages of loading. A wider range of porosity combinations need to be investigated prior to reaching a final conclusion. However, it seems that the initial response to loading in the case of the granules investigated is actually experienced by the strut (micro) porosity of the granules.
- Regarding the second region of the stress-strain curve; the gradient over this region is similar for all the granules with the 60-20 and the 70-20 showing slightly higher gradients.

These results suggest that generally granules of lower total porosity levels experience the highest stresses / strain in their transition regions, where both levels of porosities react to the load applied. However, there is no clear evidence to suggest how the micro porosity could influence this region.

- Regarding the final region; the lower total porosity combination group showed the highest gradients with 60-20 showing the steepest gradients. This suggests that micro pores are mostly effected with the denser materials. The results however cannot be decisive as there are various factors at play, such as granule movements, pore arrangement and pore sizes. The gradients of all segments are generally higher at lower total porosity levels. The gradient values suggest that the strut porosities have less of an effect on the mechanical behaviour of the samples than the total porosities. To investigate the effect of strut porosity an FE analysis is the best option. Identifying the three regions is useful when imputing the values into finite element analysis for the purpose of the failure model.

Summary

The supplied material was as described by provider. The constrained compression tests of the granules suggest that under compression, the total porosity levels had a more prominent effect on the behaviour than the strut porosity, more porosity variation is advised for future mechanical analysis. The Brazilian diametral tests have provided data that coincides with similar tests conducted on PHA of similar porosities as indicated in Figure 55, chapter 5.

Chapter 3

Generation of 3D Meshed Models of Granule Masses of PHA

3.1 Introduction:

This chapter discusses the methods applied for acquisition of raw image data of Hydroxyapatite granules. The novelty introduced in this chapter is applying a time efficient technique that can capture the intrinsic details of the material's macro porosity. The micro-CT scanning technique used for this was developed by Professor Graham Davis from the Institute of Dentistry, Barts and the London. The images were able to capture desired details for volume rendering and subsequently meshing and finite element analysis.

The chapter discusses the processing methods applied to achieve the final meshed models for finite element analysis using ABAQUS. The processes covered in this chapter are; masking, smoothing, volume rendering, creation of representative volume entities (RVEs), investigation of structural conservation and meshing.

3.2 Computerized Tomography Scanning:

CT scanners have been increasingly used in order to visualise and provide a non-destructive way for obtaining structural three dimensional information at a resolution suitable for model rendering and finite element simulation. Most typical CT scanners do not have the resolution necessary to capture the fine details of porous Hydroxyapatite. Using a μ-CT scanning approach ensures that all the finite element analysis is carried on realistic representatives of the materials' architecture and structure maintaining the complexity and inhomogeneity of their macro porosity.

3.2.1 Acquisition of Raw Images of PHA Granules

Table 6: Material specification for specimens scanned for FE analysis

Material Scanned	Total Porosity from Archimedes density analysis	Strut Porosity from SEM
80%	82.5 %	18.4 %
80%	83.0%	28.2 %
70%	72.8%	21.7 %
60%	61.8%	20.9 %
60%	63.0%	24.8 %

To gain 3D data of the macrostructure of porous hydroxyapatite for the purpose of finite element analysis. A volume of nominally 6ml of granules 1-2 mm in size, were placed in a clear silicon tube of 8 mm diameter and 16 mm length. The tubes, sealed with polymer meshes and sent to the Institute of Dentistry– Barts and The London, for CT scanning using the MuCat-2 scanner 17, with a voltage of 90 Kv, and a beam current of 0.18000 mA to obtain projections with a voxel value of 10µm.

The image data obtained from the µ-CT scanner, were extracted as stacks of images in the Bitmap file format. This was carried out using an in house software (TomView), developed by Professor Graham Davis from the Institute of Dentistry, Barts and the London. The images were imported into a commercial processing and meshing software, ScanIP (Simpleware™, 2017), where a number of steps, discussed in later sections of the chapter, were used to render the final 3D volumes and mesh them before exportation to another commercial software ABAQUS (Dassault Systèmes, 2014) as input files for FE analysis.

3.2.2 Image Processing: Applying a Mask and Creating a 3D Image View

ScanIP uses masks to create surfaces from the voxels occupied by a material, in this case the material being hydroxyapatite. As the grey scale scans include only one material, this eliminates the need to apply any grey scale mapping such as the Hounsfield Unit. The HU, is a linear attenuation coefficient typically applied in similar cases, when multiple materials are

present in the scanned images. It matches voxels to material groups such as enamel, bone, muscle or fat. As the granules scanned contained only Silicon substituted hydroxyapatite and air, this step was not necessary.

Scan IP Computational Requirements:

- CPU Processor: The speed of operations such applying filters and meshing is dependent on the processor. The recommendation from the software developers is an Intel Core i7.
- Computer memory (RAM), limits the size of data that can be processed by the software. The developers' recommendation is 16GB or more of RAM. In order to import an image file into ScanIP, the size of RAM needed is equivalent to the size of the file imported. More RAM of up to 8 times the size of the file is needed for image processing and meshing. The need for more RAM increases in correlation with the level of topological complexity of the mask, the number of masks used, as well as the size of the mask and the mesh density (Simpleware™, 2017).

The PC used for this study had 16GB RAM only. This has put constrictions on the size of data that can be processed and the level of processing that can be applied. This limitation has made it impossible to process multiple jobs simultaneously, therefore making the processing and meshing of one model very time consuming.

- Disk space; the recommended disk space is 100GB, a hard drive can be used to provide more space depending on the size of the data sets.

3.2.3 Volume Rendering:

A series of actions were performed in order to achieve the final desired volume structures for meshing using the Scan IP (Simpleware™, 2017). The structures should maintain the level of porosity from the original scans. They should not include any lone islands (small isolated regions); lone islands can hinder the meshing process and the simulation process during the FE analysis. The structures should also have smooth surfaces; rough surfaces do not produce meshes that can pass the software's quality checks.

First, the stacks of images were imported into Scan IP (Simpleware™, 2017). Before starting any image processing, a manual cropping procedure was necessary to eliminate the excess empty space in the scanned images in order to minimise the size of data. These cropping steps were preceded by a size fitting step, which was necessary to maintain the appropriate separation distance between each scanned slice in the stack depending on the dimensions of the original sample scanned and the number of slices produced. This was done by dividing the number of slices by the dimensions of the cylinder scanned, thus giving them the appropriate separation size. Figure 21, demonstrates the size fitting step, the cropping and the pixel skipping.

Due to the limited memory and computational power available, it was necessary to minimise the input data further. Therefore, another step was applied, skipping three pixels of the images along all of their three dimensions. The three pixels, were the maximum number of pixels that can be skipped before compromising on the volume detail. A volume image is basically a matrix composed of three dimensions of voxels also known as pixels. The numbers of pixels in each direction is linked to the memory used by the software for the job.

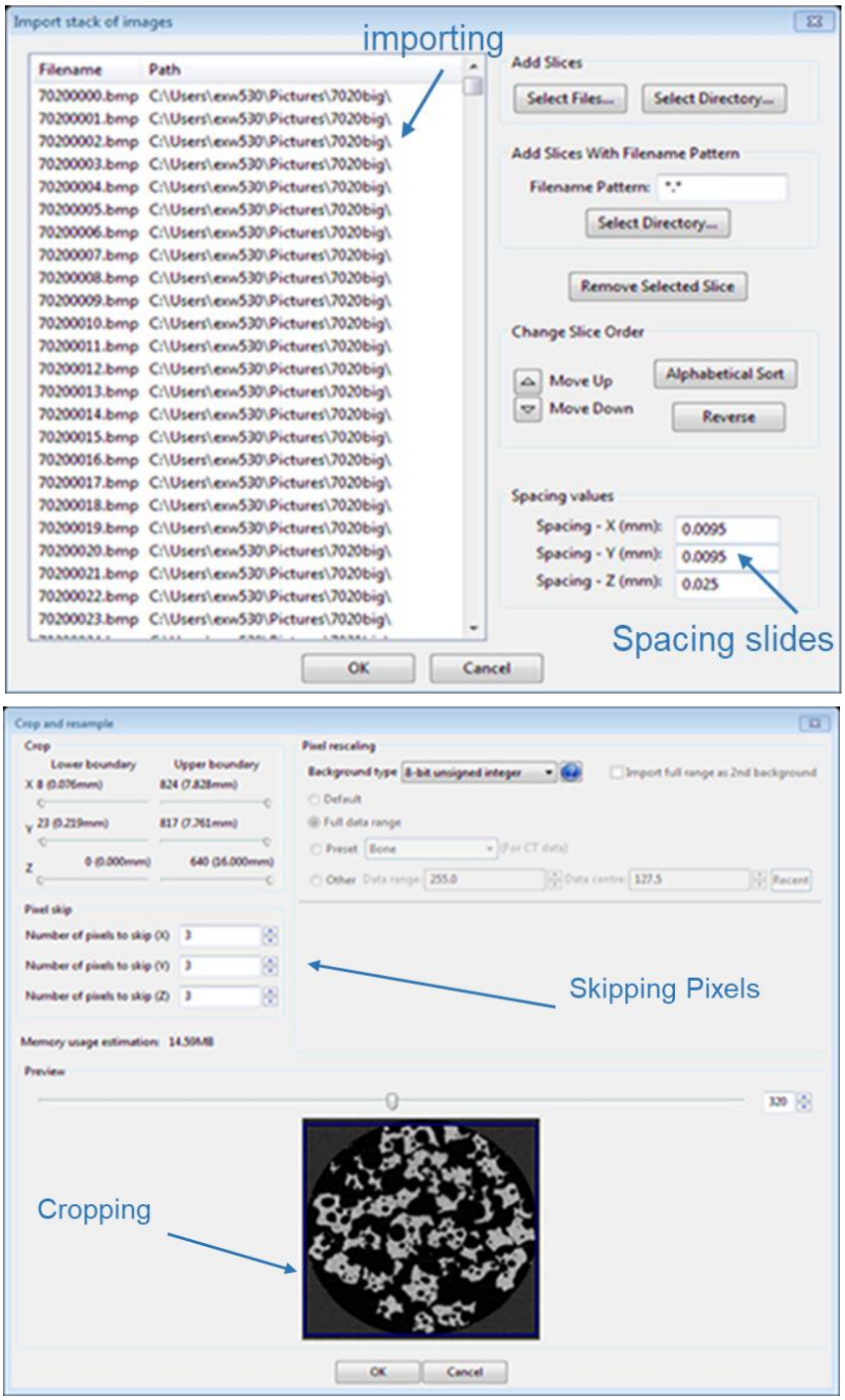

Figure 21: The images extracted from ScanIP show the process of importing the BITMAP images, sizing, pixel skipping and cropping.

Following the stacking of the grey scale images, a 3D mask was created for the voxels of interest representing PHA granules. A threshold procedure was performed using the tool “paint with threshold”, using this tool lower and upper grey scales of interest were selected. PHA granules were found from visual inspection to fall between 61-72 for the upper threshold value, whilst the empty space representing pores was set at zero as a lower boundary or threshold. The mask was then applied to the voxels of interest to render the volume of the material. Figure 22, demonstrates one slide of the stacked images and the mask result of thresh-holding which covered all the material present.

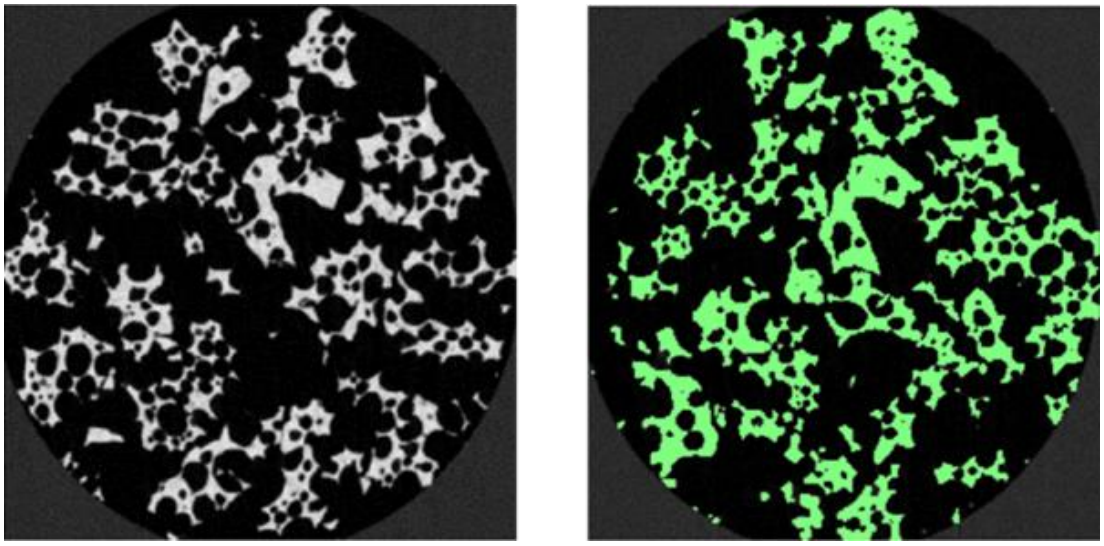

Figure 22: a slide of the 3D stacked image and the mask resulting from thresh holding procedure applied covering all the material including loan islands.

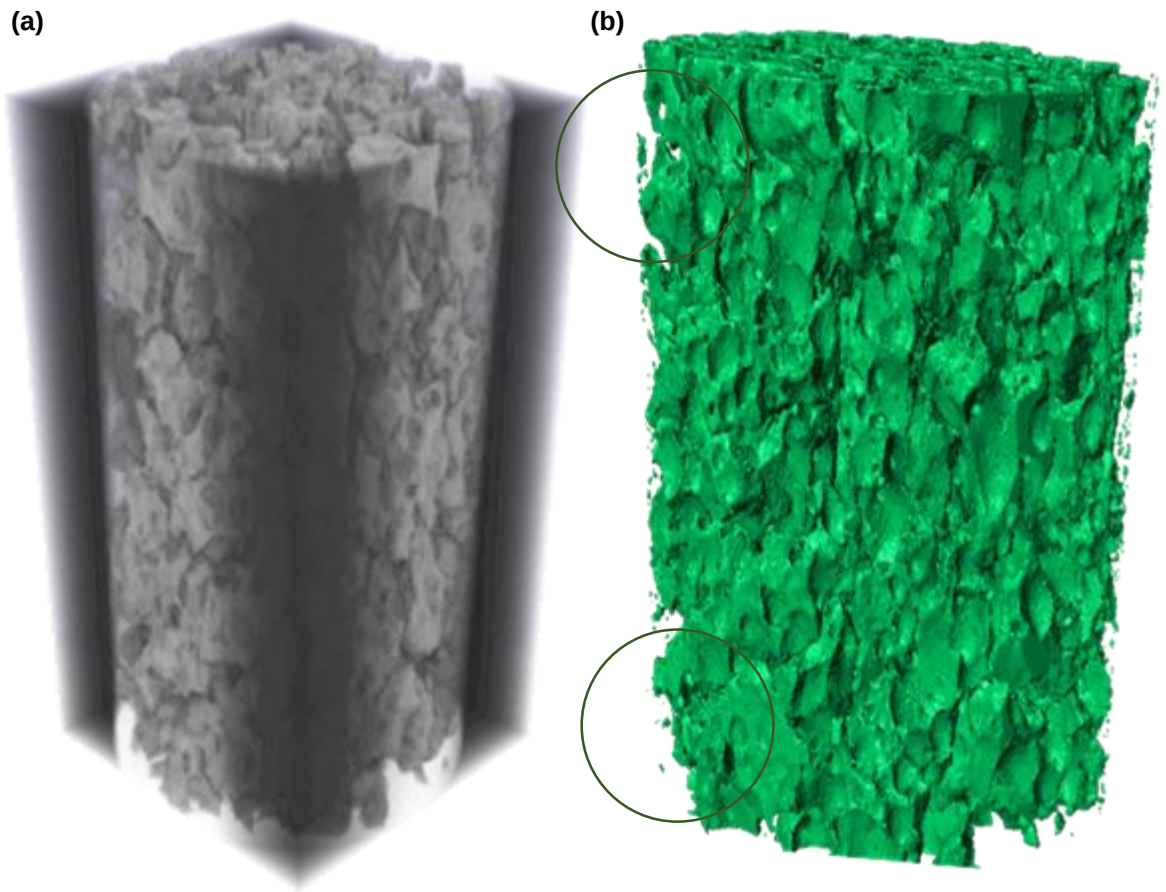

Figure 23: the 3D rendered volume of the granules from the stack of images of PHA granules, (a) volume rendered as grey scale. (b) After masking the surfaces using the threshold tools with lone islands circled.

3.2.4 Processing and Creation of 3D Models:

In Figure 23, the presence of artefacts such as lone islands, rough surfaces can be clearly seen. Meshing a mask of PHA granules from raw stacks of CT images is thus very challenging for the software. A few additional steps were performed to clean up the rendered volume to make them suitable for finite element analysis. The first step was to remove the small lone islands using a voxel value filter (Figure 24). However, this process was not 100% successful due to software limitations in detecting all the lone islands, which could be due to the complexity of the structure. Therefore, it was necessary to remove them manually, using the volume of interest tool "VOI", where careful positioning was essential to avoid deletion of core material (Figure 25).

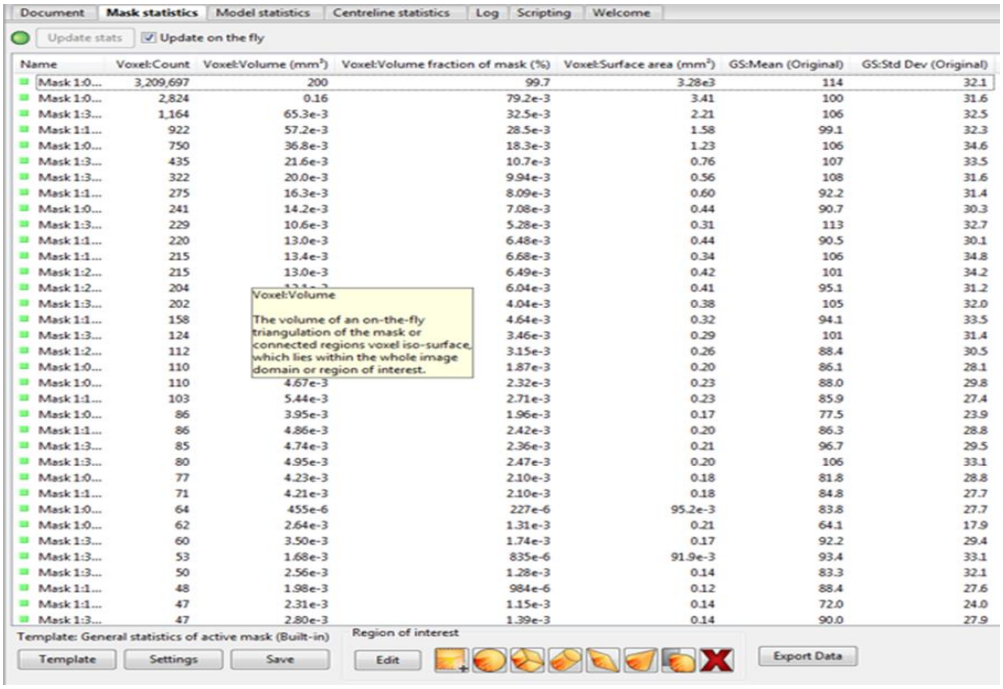

Figure 24: automated voxel filter, used to remove most of the loan islands from the rendered volume

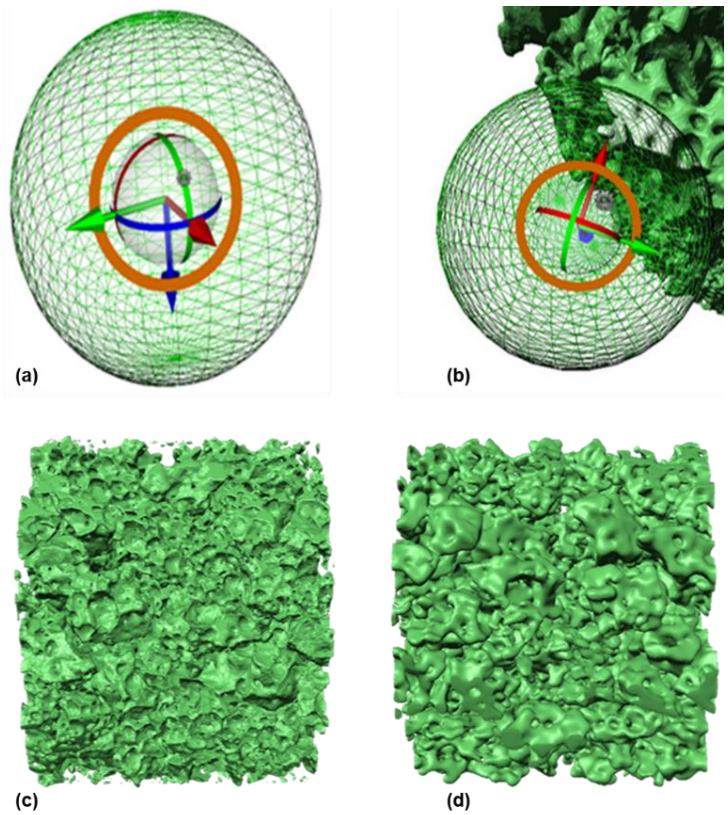

Figure 25: (a),(b) Manual removal of loan islands using the "Volume of Interest" tool within the ScanIP package. Figure (c) shows the structure raw and (d) after removing all the islands and smoothing the surfaces

The surfaces of the raw rendered volume after removing the islands remained quite rough. which complicated the meshing process (Figure 25), resulting in the software aborting the job midway, incapable of fitting elements to such difficult surfaces. After multiple job abortions it was obvious that it would be necessary to further smooth the structure in order to obtain a reasonable mesh acceptable by the finite element software. In order to achieve this, a compromise had to be made to smooth the structure for meshing without losing the essential details of the structures' original architecture and porous arrangement captured in the raw scans. The smoothing was done via applying a combination of mean and median filters. The mean filter is a noise reducing tool that works by computing the statistical mean of the neighbouring pixels from each direction. The radius measured in number of pixels, should be kept to a minimum when applying the filter, and for this application a radius value of 2-pixels was applied. The other smoothing technique applied was a median filter which is similar to the mean filter. However, the noise it reduces is related to grey level outliers, and a value of 2-pixel radius was also applied. Results are demonstrated in Figure 25. Once the masks were smooth enough.

3.3 Discretisation (Meshing) of the Volume Rendered models for FE Analysis

In order to simulate a physical structure using numerical simulation techniques employed by any commercial software such as ABAQUS (Dassault Systèmes, 2014). Discretisation is necessary to approximate the complexity of the area or domain of interest through dividing them into smaller sets or domains, also known as elements, which are not only smaller but geometrically simpler than the original larger geometry. The discretisation process is known as meshing. Techniques have come a long way to make this process as automated as possible providing high quality conforming meshes that fit the geometry of interest and captures the intrinsic details (Dassault Systèmes, 2014).

3.3.1 Self Coating

However, meshing such complex and porous structure as porous hydroxyapatite in its natural form as expected, can be very difficult. The surfaces are irregular and challenging. The surfaces are also very large due to the level of porosity, and the porous architecture is quite arbitrary. A number of procedures were used during this investigation to establish good quality meshes that are dense enough to conform to structural detail, in order to obtain accurate and efficient analysis without needing unrealistically long computational time. At first, the mesh was made on the open structure, which proved problematic for the application of boundary conditions using ABAQUS (Dassault Systèmes, 2014) as can be seen in (Figure 26). The term “Boundary conditions” is used to describe the restrictions, strains or loads applied to a model translating the mechanical environment effecting it. Boundary conditions need to be applied correctly and uniformly for an accurate output.

There is a lack of uniform surfaces necessary for BC application (Figure 26). The irregularity of the structure in turn gave rise to irregular distribution of the mesh density. This is due to the automatic mesh refinement carried out by the software, a necessary step for simulating complex structures that contain curves, pores and stress concentrators. However, this variation in the mesh density distribution within the structure does not allow for uniform BC application. To avoid inaccuracy during analysis a solution using the Scan IP software was created, by dilating the outer borders of the volume to create a thin surface on which boundary conditions can be applied without any significant effect on the output of the simulations. Figure 27, explains the process of “self-coating”. A novel method that was developed to overcome the lack of uniform closed surface.

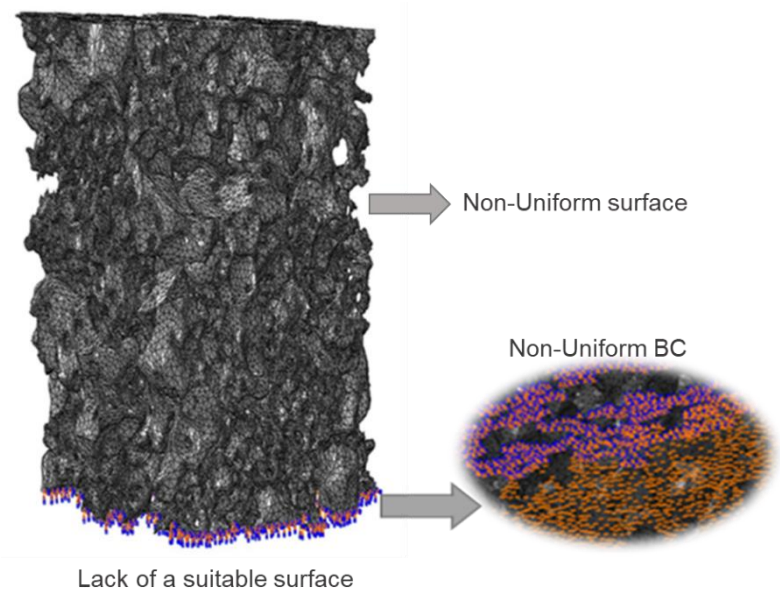

Figure 26: Demonstrates a meshed volume and the difficulty in creating boundary conditions on the open structure

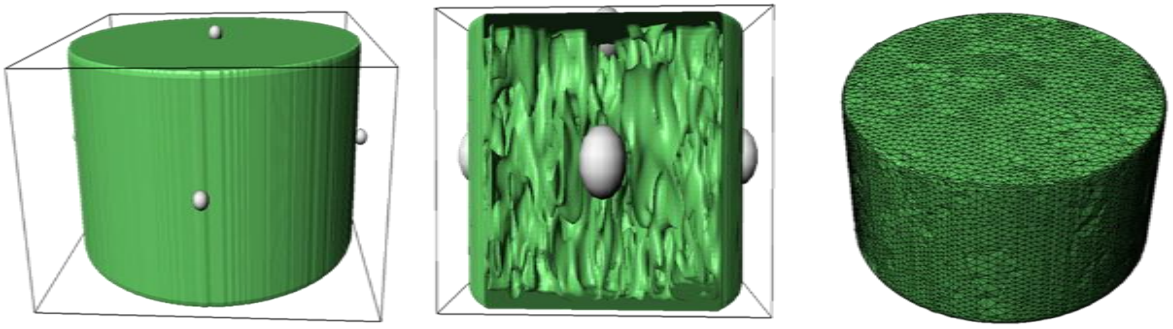

Figure 27: The process of self-coating, created by dilating the outer surfaces to form a very thin layer through which boundary conditions can be applied to the structure during the simulation process.

The volumes or models created were meshed using Scan IP (Simpleware™, 2017). The elements of choice were tetrahedral. The reason for this is that despite the advanced software, it was a challenge to create a hexagonal robust mesh for a non-uniform arbitrary structure, which is the typical choice for natural materials such as bone tissue (Blacker, 2001), as this element type produces less density and consequently less computational expenses . Hexahedral meshes through ScanIP did not pass the mesh inspection with much abortions during meshing and a high level of element distortion. Tetrahedral elements were the best

choice for the models in this research and are well suited for complex structures. More on element choice in the next section.

3.3.2 Automated Meshing for FE Analysis

The main goal was to achieve a conforming, good quality mesh, i.e. conserving the integrity of the structure originally obtained from CT scans without any debilitating distortions. Ideally a combination of good quality and low number of elements to save on computational time. This can only be achieved if hexahedral elements were to be applied, as they are the most economical. One hexahedral element has the same degrees of freedom as six tetrahedral elements thus less elements to achieve a similar accuracy.

Unfortunately, Scan IP can only produce automated meshes and does not provide many options for manual discretisation, which is essential if the structure to be meshed contains certain problematic issues with its geometry such as extensive structural fine detail, which is the case for PHA granules. Hexahedral meshes would require manual refinement as they do not conform to the contours as well as tetrahedral ones. Thus, there was again a need to compromise on the accuracy and computational speed for practical reasons (Blacker, 2001). Scan IP indeed fell short in terms of creating conforming hexagonal meshes for the structures. It remains a challenge to automate hexagonal meshes for complex structures with a large percentage of element distortion. This is a typical shortfall for hexahedral elements when used for complex geometry. Linear tetrahedral elements, which are 3D elements of linear shape functions, are typically used for complex geometries. They do however present with some disadvantages. Using these elements may cause locking, which is a phenomenon that describes the elements inability to translate the deformation kinematics.

This commonly occurs when the elements are used for bending beams or when dealing with incompressible materials. Locking in this research was avoided by increasing the density of the mesh, with the consequent long computational time due to the large number of elements. However, linear tetrahedral elements remain to be the easiest to apply for any 3D model,

irrespective of complexity as they adapt to all types of structures and topologies (Shepherd and Johnson, 2008).

Another challenge with discretising PHA granules for FE analysis, is the inability to employ a structured mesh. Which is a mesh that is spatially efficient, characterised by a regular grid. Such meshes can only be obtained for simple geometries using a hexahedral or hexahedral dominated mesh. The meshes used in this study are non-structured free meshes, which can be obtained using any type of element. The shortfalls with such meshes are the non-uniformity of the mesh grid, in addition to the more problematic computational power and storage requirements associated with them. There is however no escaping free meshing for natural structures.

Unstructured meshes are advantageous in that they provide a way to discretise those tough to mesh geometries as they are more suitable for non-uniformity. A drawback of using the ScanIP automated meshing is, the lack of an advanced method to exert control over the mesh size. The Software offers a scale of mesh coarseness, which is quite primitive. This shortfall is not very problematic, as the algorithms it applies seem to create meshes that are refined to the contours of the structure with denser meshes around curves, pores and sharp edges.

The meshes created with Scan-IP do not lend themselves to any further manipulation after exportation as they are exported in the form of orphan meshes. Orphan meshes, are volume grids with no part associated with them as is the usual case when using ABAQUS. Parts are the original volumes before meshing. Typically, all applications are conducted on parts which are then meshed in ABAQUS.

For this study creating models from orphan meshes, meant that every mesh had to be tested before accepting it as valid. There was no particular need to refine the mesh at certain areas as the level of automated refinement by ScanIP was acceptable. All meshes produced had to be diagnosed for distorted elements with a built in tool in the software “quality inspection”, which checks for deformed and problematic elements (Figure 28).

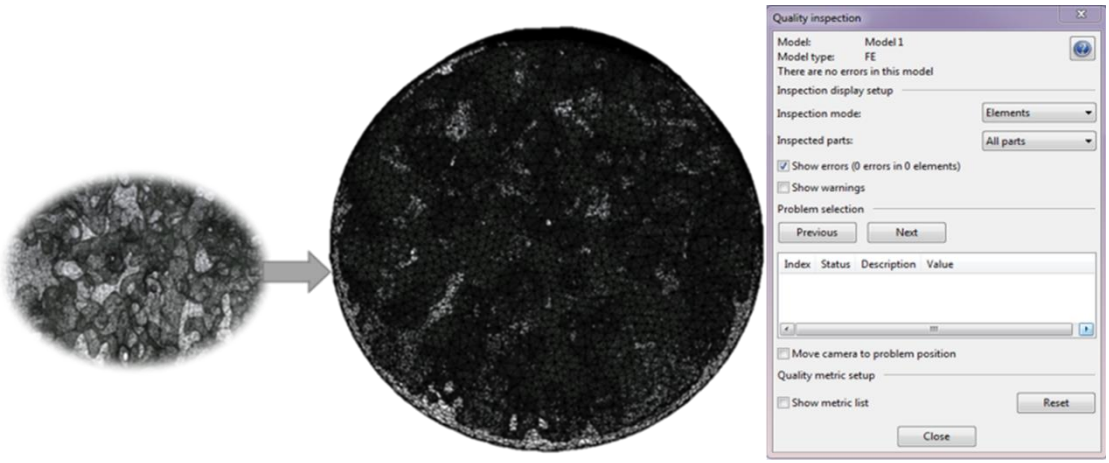

Figure 28: The process of mesh quality inspection using ScanIP before exportation as an orphan mesh for FE analysis

3.4 Representative Volume Entities

The volume rendered models were created from porous hydroxyapatite cylinders of 8mm diameter and 16 mm length. Cross sectional cuts of 4 mm, 8 mm and 12 mm long were made to the original volumes to create potential RVEs for the following reasons.

1- Meshing smaller models with a dense mesh using ScanIP is computationally more feasible given the limitations of the PC used.

2- Running FEA on the entire volume is difficult due to the complexity of the structure and the density of the meshes, which require unsupported computational time and power. It is important to note that for such a structure, only a dense mesh can conform to the structure and produce a good model for finite element analysis. The commercial software ScanIP (Simpleware™, 2017), is programmed to understand such structures and thus can only produce dense meshes for complicated topologies. Attempts to coarsen the mesh were met with abortion of jobs during the meshing processes.

3- To provide a basis for analysing PHA granules through using a representative volume entity (RVE). This approach saves on computation expense due to the model size reduction. Cuts were made with the level of porosity maintained throughout, which means any future FEA analysis can easily be carried out on RVEs given they follow the Hill-Mandel criteria discussed in chapter 1. The reason the cuts were made at different length

scales was to compare the models at different sizes, and demonstrate the stability of the RVEs in this study, and their ability to represent the materials' behaviour.

4- Cuts were made along the cross section. This approach has not been attempted before for PHA granules, thus there was no guarantee that shorter cuts can be representatives of the entire structure. Figure 29, demonstrates the cutting procedure carried out after smoothing prior to meshing in order to create RVEs for PHA granules.

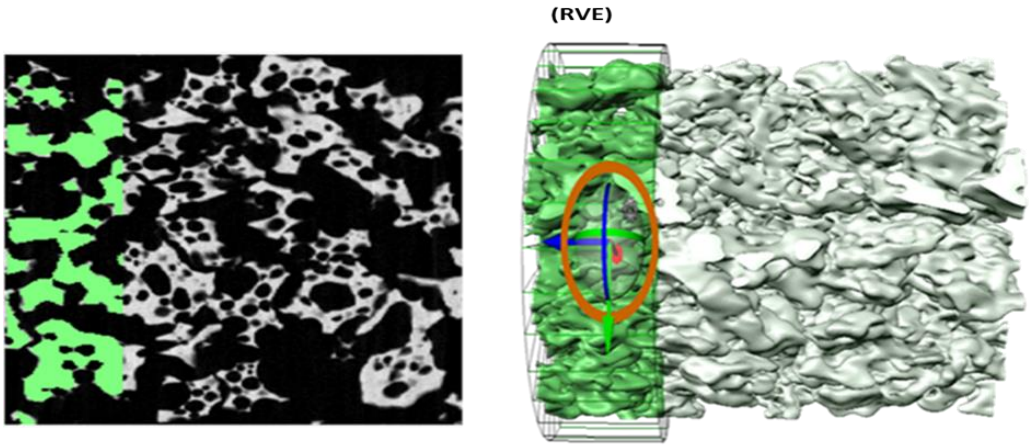

Figure 29: The cross sectional cutting procedure using ScanIP tools to create shorter RVEs from the original longer scanned tube of PHA granules. As seen, the cut goes through granules and split the surface pores converting some from closed to open pores.

The large element count need to insure accuracy has proven problematic. The 4mm sized RVE had elements of the order of hundreds of thousands, approaching a million elements for 12 mm RVEs. Table 1 in appendix contains the element numbers used for each RVE model. The volume rendered cylinders of PHA granules were cut in accordance with the requirements in section 1.5. The shortest cuts thus were 4mm in length. This cut was found to be the shortest one that maintained the material's porosity i.e. its density as well as the representative architecture.

Smaller cuts may have been possible if filters were not applied to the scanned slides to enable meshing. Three cross sectional cuts of 4mm, 8 mm and 12 mm were made for analysis. The original 16 mm long cylinder was not meshed due to computer power limitations. Figures 30 - 32, demonstrate the process of testing the RVEs, insuring that every cut has maintained the porosity level and thus the material properties of the macro structure. This was achieved via applying a second mask for the space occupied by pores using the threshold tool in ScanIP. The volume fraction they occupy can thus be calculated as the porosity percentage. The process is used to determine the conservation of porosity levels throughout the cuts. Table 7, demonstrates the results obtained from the process of applying porosity masks to the cuts.

Table 7: Results obtained from conducting volume analysis using ScanIP demonstrating the conservation of the porosity level throughout the RVE cuts created, results are in % ± 0.01 % error

PHA-Sample	VFP in 12mm RVE	VFP in 8mm RVE	VFP in 4mm RVE
80 total 20 strut	82.31 %	82.41 %	82.53 %
80 total 30 strut	83.36 %	83.36 %	83.36 %
70 total 20 strut	72.18 %	72.38 %	72.67 %
60 total 20 strut	62.23 %	62.34 %	62.54 %
60 total 30 strut	63.05 %	63.33 %	63.34 %

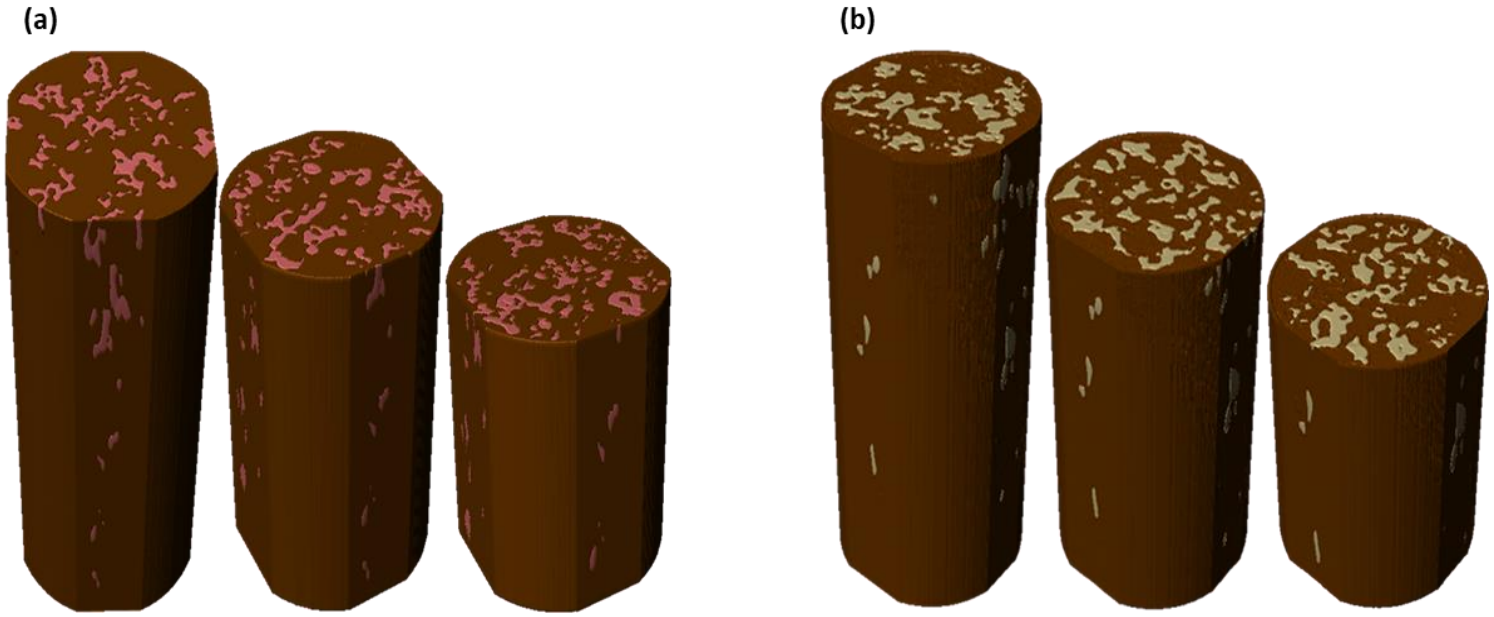

Figure 30: Volume rendered RVEs with dual masks to determain conservation of porosity after cutting to shorter cyliners. Figure (a), The RVEs created for the 8020 porous hydrsoxyapatite. The pink mask for the hydroxyapatite material and the brown mask for the empty space (porosity). Figure (b), the RVEs created for the 8030 porous hydroxyaptite, the white mask is for the material and the brown mask for empty space (porosity).

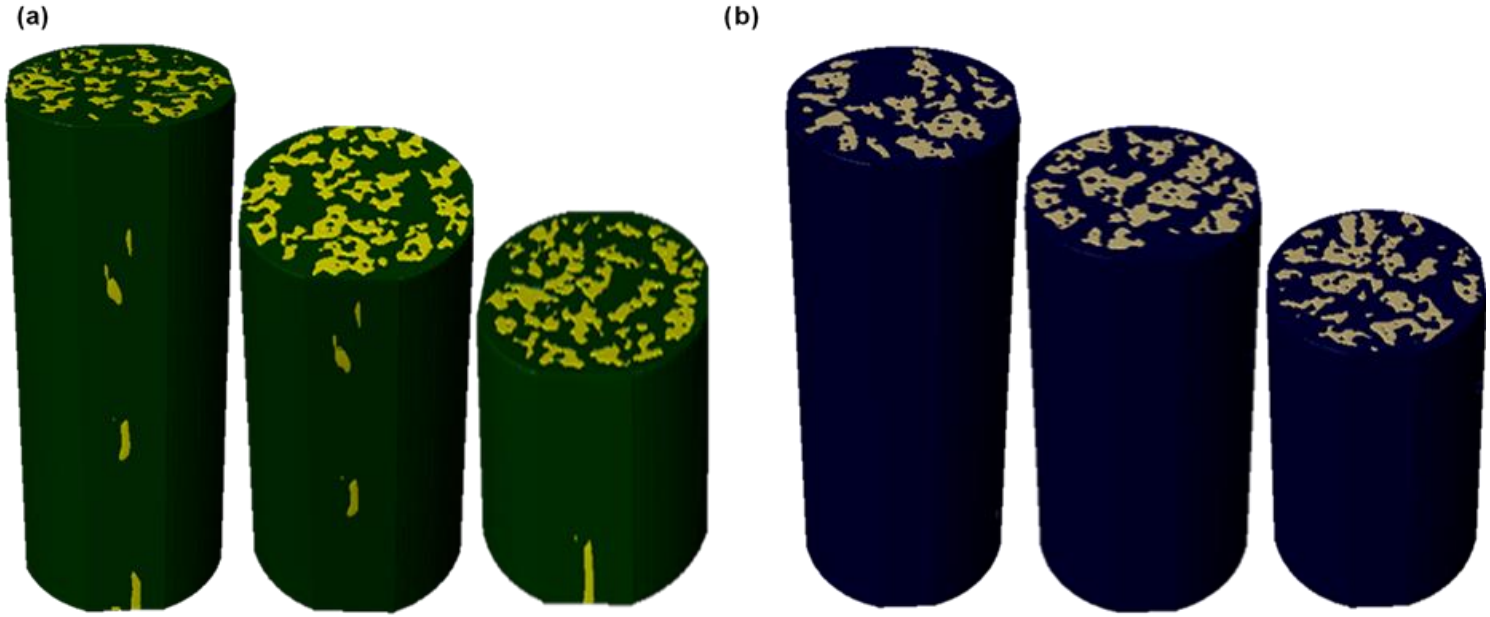

Figure 31: Volume rendered RVEs with dual masks to determine conservation of porosity after cutting to shorter cylinders. Figure (a), The RVEs created for the 60-20 porous hydrsoxyapatite. The yellow mask for the hydroxyapatite material and the green mask for the empty space (porosity). Figure (b), the RVEs created for the 60-30 porous hydroxyaptite, the white mask is for the material and the blue mask for the empty space (porosity).

Figure 32: Volume rendered RVEs with dual masks to determain conservation of porosity after cutting to shorter cyliners. The RVEs created for the 7020 porous hydrsoxyapatite. The light blue mask for the hydroxyapatite material and the dark bluen mask for the empty space (porosity)

As mentioned in section 1.4. One of the main conditions for accepting a cut of the macro structure as a true representative of the material also known as an RVE, is to maintain the material's porosity (density). It was thus essential to provide evidence that the RVEs created comply with the condition of density conservation. Evident from the previous figures and values of total porosity demonstrated in (Table 7) that the cuts created maintain their material representativeness in terms of porosity volume, and thus could be used for FEA analysis as an RVE from the perspective of material property. The second step in validating the RVEs, is to provide energetic evidence of their representativeness in accordance with the requirements in section 1.5. This will be carried out in chapter 4. This research attempts for the first time to investigate the representativeness of RVE structures of PHA granules in their natural form as scanned. This approach can be thought of as a necessary step towards widening the scope of finite element analysis of hydroxyapatite based porous graft substitutes. In summary, this chapter covered the methods necessary to create 3D models from µ-CT scans. µ-CT scans

insure the creation of realistic models for finite element analysis. In order to obtain such models, a good volume rendering and meshing software was employed. For this research the software of choice was ScanIp (Simpleware™, 2017). Through it necessary steps that render the granules fit for meshing and consequently FE analysis were employed. These steps include stacking the slices into a 3D volume, creating a mask for the volume, cleaning and filtering the volume and finally meshing it and exporting it to a finite element analysis software, ABAQUS in this case. The volumes of PHA granules were cut to create RVEs of different sizes. These were necessary to minimise the computational expenses making the analysis more feasible, and to understand the behaviour of PHA material at different scales. This chapter demonstrated conservation of density, as the RVE cuts maintain the porosity and thus structurally satisfy the first criteria of the Hill-Mandel homogeneity principle.

Summary:

The steps needed to create 3D meshed models of porous hydroxyapatite for the purpose of finite element analysis are the following:

1- High resolution scanning technique
2- Volume rendering form image data
3- Creating 3D models from volumes
4- Smoothing of topographical rough features
5- Meshing using appropriate elements

Chapter 4

Finite Element Analysis: Simulation of PHA Bone Graft Substitutes

4.1 Introduction

The purpose of this research is to use a finite element approach on three-dimensional models of true reconstructed structures of PHA BGS granules from CT scans. This is to understand the behaviour of the material and investigate the strain fields generated during physiological loading conditions as described in chapter 3. An RVE approach was conducted out of necessity due to the large element density of the scanned cylinders of PHA granules, which could not be in their entirety with the equipment available. Using the RVE approach necessitated the conduction of both structural and energetic validation techniques. Chapter 3, discussed the structural validation.

The energetic validation, described in this chapter, is concerned with the relationship between the strain energy of the models and their size. There should be a corresponding change in the strain energy of the models as the RVE sizes change. Increasing the size of an RVE should induce an increase in the registered strain energy and the opposite is true. The increase would be expected to be linear with a homogenous material (Mandel Jean, 1971), (Hill, 1972). However, in this research it is accepted that the change may be subject to some non-linear variation due to the extensive random porosity. The energy of a model should be conserved throughout the simulation procedure for it to be valid, with the energy put into the model converting totally to an energy output making the total energy of the simulation equal to zero.

4.2 Selection of Input Data for FE Analysis

4.2.1 Constitutive Models:

This research employs two constitutive model approaches. Constitutive models in finite element analysis tend to describe the responses of materials under different mechanical environments. There are three classes of constitutive models based on the relationship between stresses and strains:

1- Algebraic; $\boldsymbol{\sigma} = \boldsymbol{f}\ (\boldsymbol{\varepsilon})$

2- Differential; $d\boldsymbol{\sigma} = \boldsymbol{E}_t : d\boldsymbol{\varepsilon}$

3- Integral; $\boldsymbol{\sigma} = \frac{\delta W}{\delta \boldsymbol{\varepsilon}}$

With (σ) being stress, (ε) strain, (W) strain energy potential and (E_t) the tangential modulus (William, 2002). In this chapter, an algebraic constitutive model, linking stress and strain states to material specific parameters was used to simulate the RVEs of PHA granule masses. It treats a model as a simple linear elastic problem and can be applied to most materials. It is thus a straight forward method to establish the behaviour of the PHA models, and the representativeness of the RVEs used. This chapter will demonstrate the following:

1. Validation of the RVEs using the strain energy output. As well as the energy conservation during the simulation process to validate the FE analysis.
2. The simulation results of the FE linear elastic model applied to REVs of PHA granule masses

Thus, it is important to input the appropriate model parameters which are

- Material properties such as the elastic modulus and density
- Appropriate boundary conditions

4.2.2 Selection of Boundary Conditions and Material Parameters

4.2.2.1 Strain Levels

On application of force bone tissue and bone graft substitute materials deform. It is these deformations and the fluid flow they create that are responsible for the mechanical signalling that directs bone remodelling. In physiology, all forces experienced by bone and bone grafts are expressed as micro strains. A 1,000 $\mu\varepsilon$ applied to a dimension is equal to a 0.01% change in the original value of the dimension (Lanyon et al., 1975). Research suggests that micro-strains ranging between 1,000 to 3,000 are anabolic inducing bone remodelling (Turner et al., 1994), (Reijnders et al., 2007). Typically, habitual strains that maintain the bone's homeostasis do not exceed 400 $\mu\varepsilon$. These small strains are thus unable to induce further bone remodelling and can only maintain tissue mass (Klein-Nulend et al., 2012).

Bone remodelling through mechanical stimulus can be achieved via low strain conditions if their frequency is amplified. The opposite is true for high strain conditions (Ozcivici et al.,2010), (Price et al.,2011). Reports have demonstrated that strains of 3,400 $\mu\varepsilon$ have induced an increase in bone production by osteoblasts, whilst micro-strains larger than 5,000 $\mu\varepsilon$ can induce fractures, the severity of which is dependent on the health condition of the bone tissue. However, it was reported that higher levels of strains of up to 10,000 $\mu\varepsilon$ can induce desired bone responses, without any significant damage, given the method of mechanical strain application such as in a four-point bending tests (Robinson et al., 2006).

In fact, the same study realised that there are various strain conditions for bone cell stimulation that can vary between the two extremities of high and low strains, depending on the mechanical application method. Strains caused by pulsating fluid flow, had a stimulating effect on bone tissue at levels lower than 800 $\mu\varepsilon$. Fluid shear strains however, evoked bone stimulation at levels higher than 800 $\mu\varepsilon$.

Higher strains of 1,000 $\mu\varepsilon$ and 10,000 $\mu\varepsilon$ were reported as the lower and upper thresholds for the four point bending tests. These variations in the observed values are due to the different

mediating mechanical transduction pathways activated in accordance with the test mode and strain applied (Hughes-Fulford, 2004). The phenomenon of strain amplification can explain how low levels of applied strain can have an effect on the stimulation of bone growth in a similar way to the effect of applying high strains. Within the bone matrix, strains were found to amplify locally at the osteocyte lacuna, with evidence suggesting an amplification of up to three times the original applied value, due to the porous nature of bone tissue (Bonivtch et al., 2007). PHA granules are porous structures similar to bone tissue, and thus it is possible to encounter regions of amplified strain within the structure when subjected to physiological strains.

4.2.2.2 PHA Material Parameters

Five different total-strut porosity combinations were used each considered as a separate graft type. For each type, there were three RVEs of 4, 8 and 12 mm long with an 8 mm diameters. For each RVE, five models of different mesh densities were simulated in order to attempt a mesh convergence, despite the inevitable difficulty due to the complicated structures of the models. Tables 1 and 2 in Appendix contain the mesh densities used for each model. The multiple meshes were also needed to calculate the averages of strain energies and to ensure the accuracy of the results. A number of steps were necessary to achieve a successful simulation that closely resembles realistic settings and boundary conditions. The density values used were obtained from the Archimedes density analysis in chapter 2.

The simulation analysis was conducted on the struts of the grafts. Thus only the contribution of the strut porosities was considered when assigning the Young's moduli to the bulk. The strut porosity values were obtained from the SEM analysis in chapter 2. The strut porosity relevant moduli were obtained by combining data from literature sources (Figure 33).

An exponential fit was used to obtain a relationship from which values of the elastic moduli could be assigned to specific strut porosities as seen in Figure 33 and Table 8.

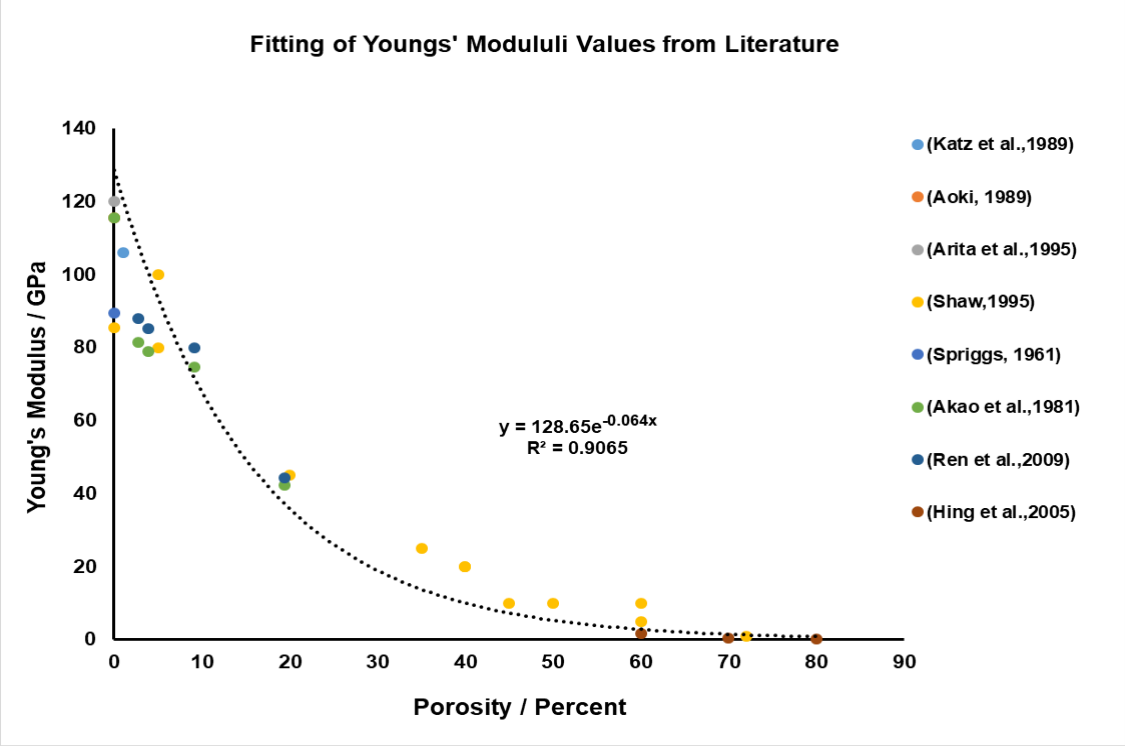

Figure 33: Young's modulus values obtained from literature for different levels of porosities for porous hydroxyapatite bone graft substitutes. An exponential fit to find a relationship from which a value for the elastic moduli can be calculated for the materials used in this research

Table 8: Young's moduli for the struts of PHA samples as determained from analysis of published data

PHA-Sample	SEM measured strut porosity	Calculated Young's Modulus in GPa
60-20	*20.9*	*34*
60-30	*24.8*	*26*
70-20	*21.7*	*32*
80-20	*18.4*	*40*
80-30	*28.2*	*21*

4.3 Technical Assembly for FE Simulation

This section details the assembly of FE models and the application of boundary conditions using ABAQUS (Dassault Systèmes, 2014). The models were exported to the ABAQUS from ScanIP as orphan meshes. This limits any further changes to the models using ABAQUS tools such as; mesh refinement and partitioning, due to the lack of parts associated with orphan meshes. Typically, the models simulated using ABAQUS are made using the same software or solid works with the latter allowing the models to be exported as a part. The expression "part" refers to the model prior to meshing. Parts are then meshed with ABAQUS tools, allowing for further changes if necessary.

Despite smoothing the external surfaces of the models using the dilation tools in Scan IP (Simpleware™, 2017), it was necessary to create an outer shell (skin), through which boundary conditions can be applied as an evenly distributed strain could not be applied as a boundary condition to an irregular mesh. The density of the elements tended to follow the contours of the materials' architectures. This lead to an uneven distribution of the strain when applying it directly to the surface elements. To overcome this issue, an analytical rigid body was created. Analytical rigid bodies are used when a smooth surface is needed for BC application. They are in direct contact with the surface elements and are not included in the simulation. Through rigid bodies the strains and the axial boundary conditions were applied via reference points associated with their governing nodes. These nodes also act as their centre of mass and are allocated an arbitrary mass value much larger than the mass of the material. This is to eliminate any noise effect during the simulation process. The rigid bodies act as the metal plates used to compress the granules during the mechanical compression tests (Figure 34). The models were created to replicate the conditions of the mechanical test discussed in chapter 2.

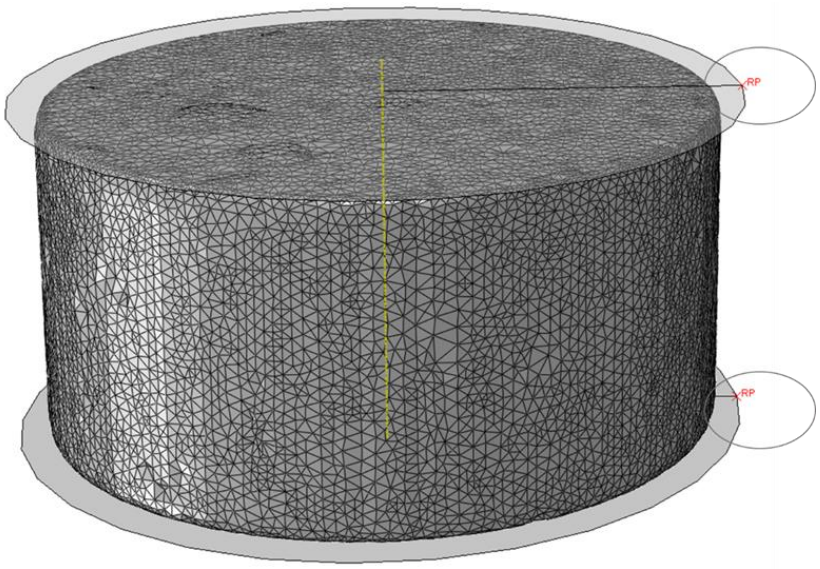

Figure 34: The figure demonstrates the two analytical rigid bodies as discs on the top and the bottom of the model acting as compression plates. The image also shows the reference points indicated as RP, BCs and arbitrary masses can be applied to the nodes of the reference point. This method ensured an even BC application.

In light of the previous discussion, the strain applied to the models should fall within physiological strain levels mentioned earlier. After various attempts to run simulations using low physiological strains. It was evident that lower strains were problematic. The lowest strain level applied that registered with the software and produced an output was the 5,000 $\mu\varepsilon$ microstrain for the 8 and the 12 mm RVEs only. Despite of the registered numerical output, there were no strain or stress distribution registered on the structures. The lack of coloured contours associated with the porous structure, does not allow for studying the stress and strain fields caused by the porosity. In order to study the fields, the strain applied was increased gradually. The strains applied were as follows 5,000$\mu\varepsilon$, 10,000 $\mu\varepsilon$, 12,000 $\mu\varepsilon$, 25,000 $\mu\varepsilon$ and 50,000 $\mu\varepsilon$.

It was evident that the thin outer layer created using ScanIP for the application of boundary conditions was causing a problem during the simulation when low strains were applied. It appeared that this skin like layer produced some sort of a shielding effect, not allowing the strain applied to be distributed through the porous structures as should be the case. Figure 35, demonstrates the shielding effect and how it diminished with increasing the strain applied from 5,000 $\mu\varepsilon$ to 50,000 $\mu\varepsilon$.

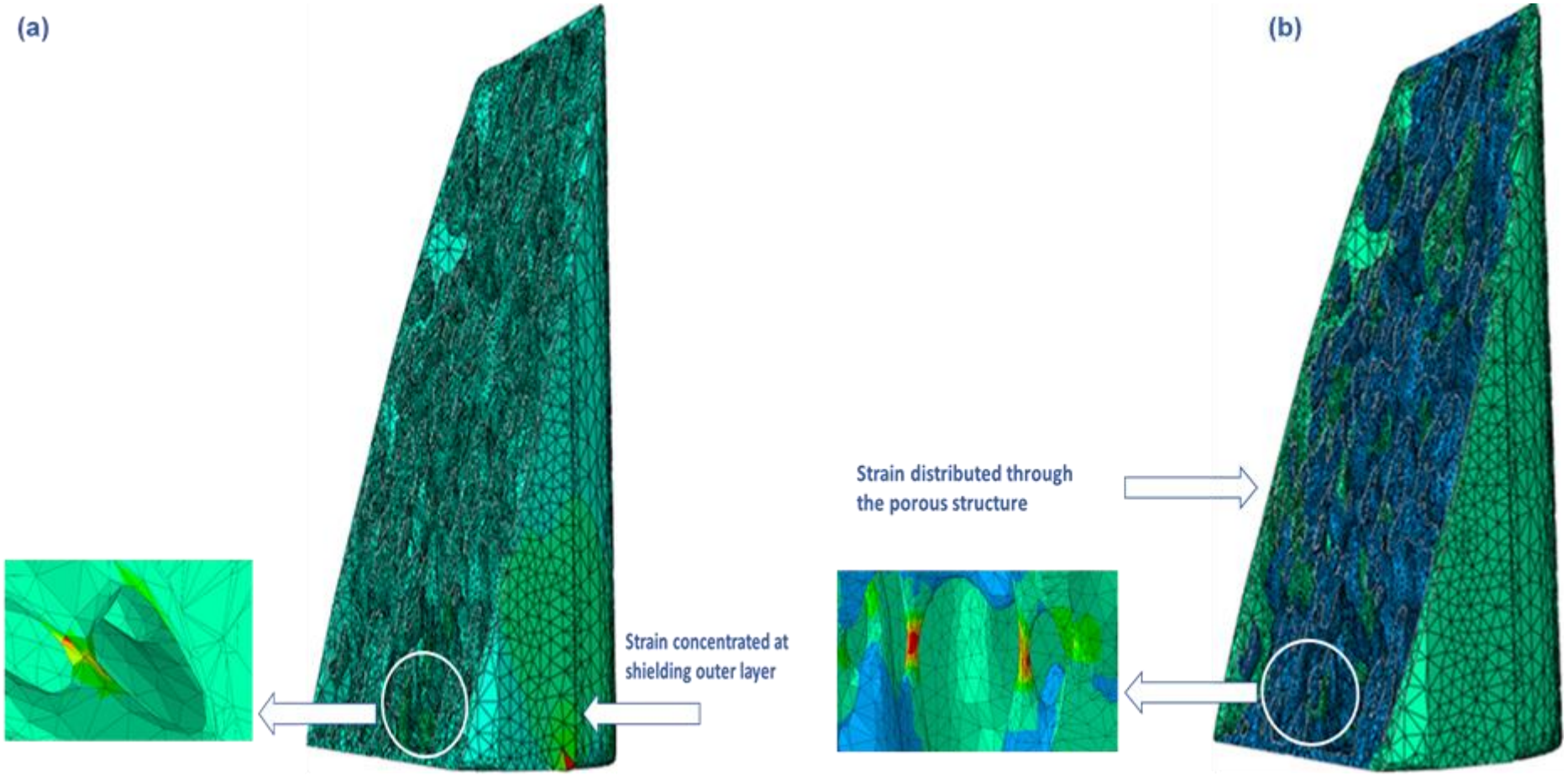

Figure 35: Figure (a) The figure demonstrates the shielding effect the thin outer layer created which did not allow the lower applied micro strains to distribute through the structure of the model. Figure (b) shows how increasing the strain eventually allowed the strain to bypass the outer layer and distribute within the model's porous architecture, which permits the investigation of stress and strain fields and the effect of porosity upon their distribution within the structure.

Therefore, to demonstrate the effect of the porosity on stress and strain distribution within the porous structure. The results demonstrated in this chapter will be from the models simulated at 50,000 $\mu\varepsilon$. This level of strain holds no physiological significance, as it is very high. However, it is the best strain level to demonstrate the distribution of stresses and strains through the body of the model. Equivalent physiological values of output stresses and strains at 5,000 $\mu\varepsilon$ were obtained through the following procedure:

- The output stresses and strains were plotted against the micro strain values applied for all the models.
- A relationship that allows the conversion of the output stresses and strains from the 50,000 $\mu\varepsilon$ models to their equivalent at the lower micro strain level of 5,000 $\mu\varepsilon$ was obtained using a linear fit. Figures 36 and 37 demonstrate the process for the 80-20 PHA models. The remaining model plots can be found in the appendix section A2.

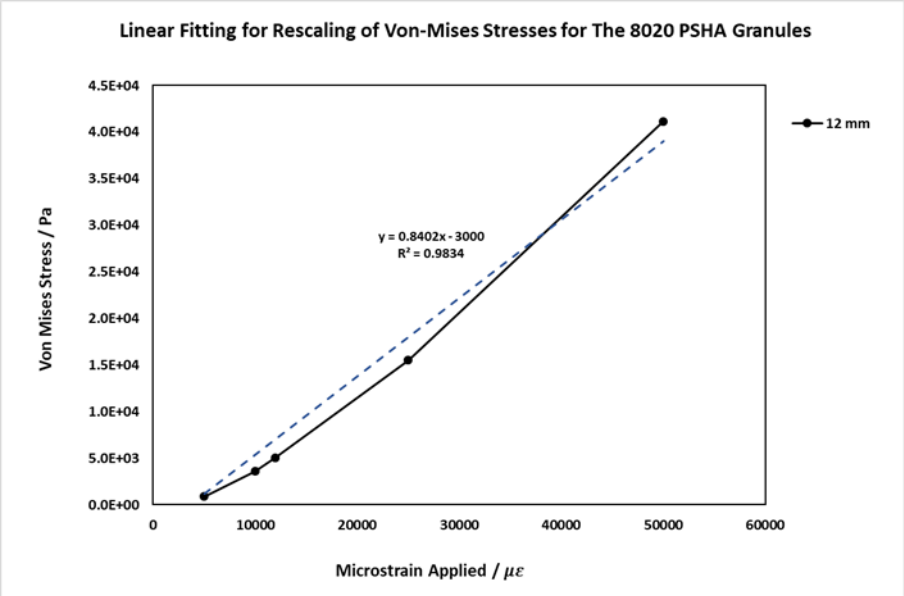

Figure 36: Plot of the averaged outputs of Von Mises stresses for the 80-20 PHA models at 12 mm as obtained from ABAQUS, against the microstrain applied. A linear fit was added to obtain a relationship used to convert the Von Mises Stress outputs for the material at 50,000 $\mu\varepsilon$ to their equivelant at 5,000 $\mu\varepsilon$.

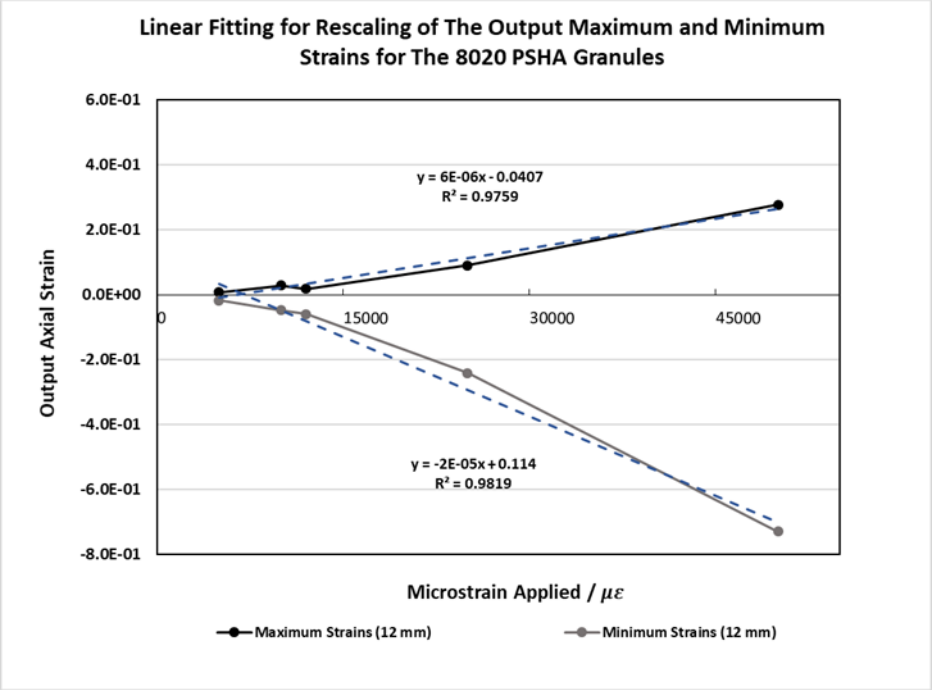

Figure 37: Plots of Maximum and Minimum axial output strains as obtained from ABAQUS plotted against the micro strain applied for the 8020 PHA models. A linear fit was added to plots to obtain a relationship for the convergence of the output strains from the models of 50,000 $\mu\varepsilon$ to their equivalent at 5,000 $\mu\varepsilon$.

4.4 Energy Validation for The Simulated RVE Models

This section includes the plots of averaged output strain energies vs output strain; these are known as energy profiles. The profiles are used to validate the RVE sizes as energetically acceptable representatives of the material in accordance with the Hill-Mandel conditions in chapter 1. These profiles provide a quantitative demonstration of the change in strain energy as a result of the change in the size of the model recorded.

The other type of energy profiles included in this section are energy conservation plots known as; simulation energy profiles. These are typically used to validate any simulation. These profiles are provided by the software to help validate the reliability of simulations. To deem a simulation valid and its results reliable, it must demonstrate that it has conserved its energy throughout its running time. The total energy of the system known as ETOTAL, must be constant at zero at all times. A valid energy profile must also demonstrate minimal energy losses. This condition is true for both static and quasi static models (Dassault Systèmes, 2014).

Ideally an energy conservation profile should have values for the artificial energy, ALLAE; which is the energy the model dissipates to control the deformation, particularly hour glassing deformation, which can be problematic if excessive as any particular energy that is registered as artificial is deemed non-recoverable by the software. A typical approach to determine the excess distortion is to compare the artificial energy with the internal energies of the models, as the relationship between the two means that if a lot of energy is needed to control the hour glassing it is lost from the strain energy.

This comparison is calculated from the ratio of the artificial energy to the strain energy, in accordance with the equation (Dassault Systèmes, 2014).

$$ALLIE = ALLAE + ALLSE$$

With $ALLIE$ being the internal energy of the model, $ALLAE$ the artificial strain energy, $ALLSE$ the strain energy (Dassault Systèmes, 2014). However, having made the mesh in a different

software and exported it as an orphan mesh, the software (ABAQUS) couldn't register the artificial energies if they existed, and thus the $ALLAE$ value equals zero in all outputs. Therefore, and in order to demonstrate the extent of the stability and validity of the models and the strain energies recorded, the approach was altered slightly to show the contribution of the strain energy to the internal energy in order to demonstrate that, despite of the unavailability of the $ALLAE$.

To further test the validity of the models; the extent of conversion of the external work done on the models $ALLWK$, and the percentage of its conversion to strain energy $ALLSE$, should also be considered. This was investigated for every model simulated. Ideally, most if not all the work done on a model should be converted to strain energy. It is understandable that a total conversion is not feasible due to various factors such as the model's complexity, the mesh quality and element deformation throughout the simulations. All the energy profiles in this section of the chapter will be for the 12 mm models simulated under 50,000$\mu\varepsilon$. The remaining validation profiles for the rest of the model sizes are included in the appendix section A-4, alongside the percentage conversion values.

Energy Profiles for the 80-20 PHA RVE Models

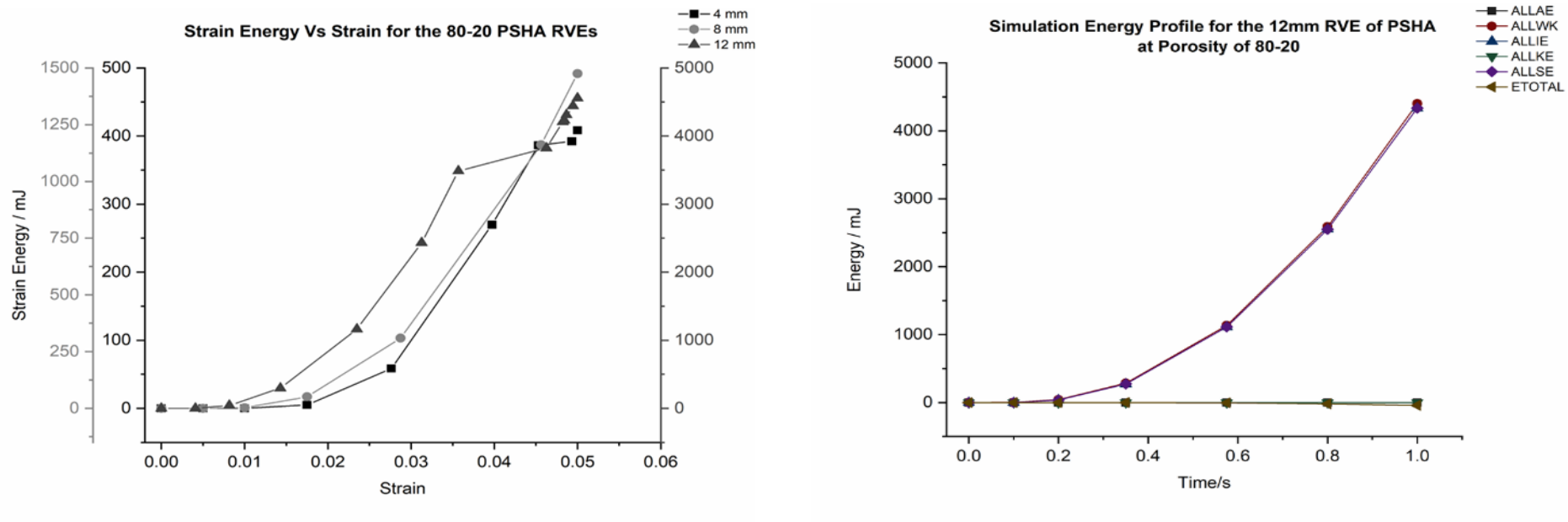

Figure 38: Left, the averaged strain energies of the simulations vs their strain for all model (RVE) sizes of the 80-20 PHA models. The profile shows a clear increase in strain energies for given strains in response to the increase in RVE model sizes for the material. The profile provides an energetic validation for all the RVEs. Right, the energy conservation profile as extracted from ABAQUS for the 12 mm RVE models only. The profile provides validation to the simulation as the total energy is zero throughout the simulation. A 100% of the ALLSE converting to ALLIE, and 96% of ALLWK converting to ALLSE. Data gathered from simulations under 50,000 $\mu\varepsilon$.

Energy Profiles for the 80-30 PHA RVE Models

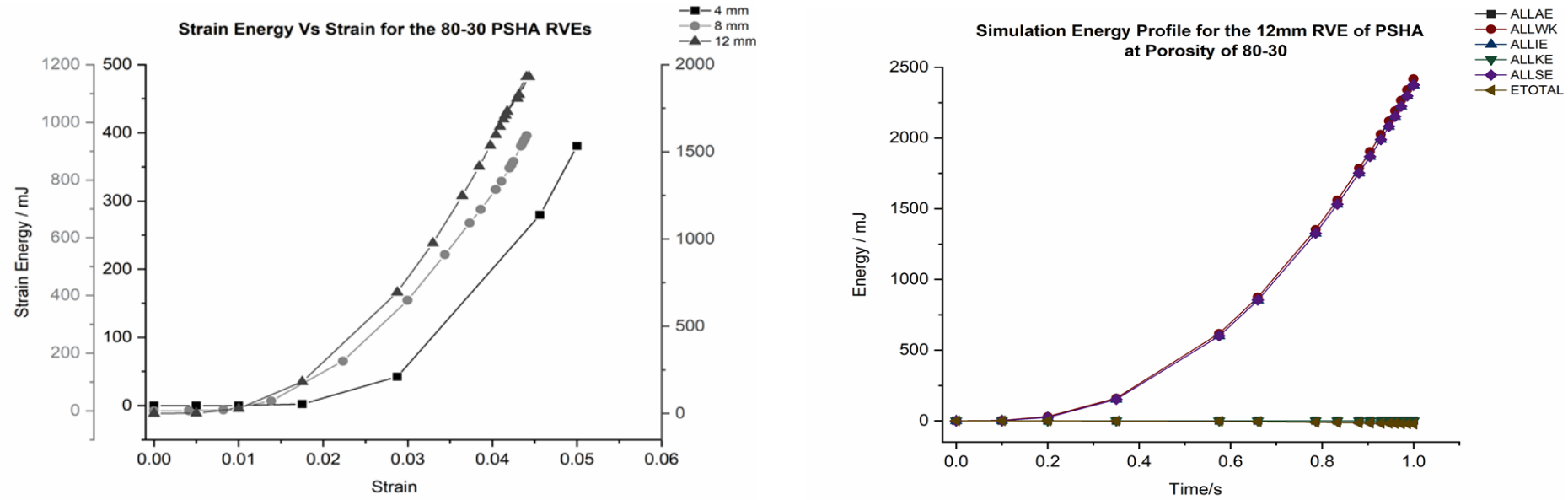

Figure 39: Left, the averaged strain energies of the simulations vs their strain for all model (RVE) sizes of the 80-30 PHA models. The profile shows a clear increase in the strain energies for given strains in response to the increase in RVE model sizes for the material. The profile provides an energetic validation for all the RVEs. Right, the energy conservation profile as extracted from ABAQUS for the 12 mm RVE models only. The profile provides validation to the simulation as the total energy is zero throughout the simulation. A 100% of the ALLSE converting to ALLIE, and 97% of ALLWK converting to ALLSE. Data gathered from simulations under 50,000 $\mu\varepsilon$.

Energy Profiles for the 70-20 PHA RVE Models

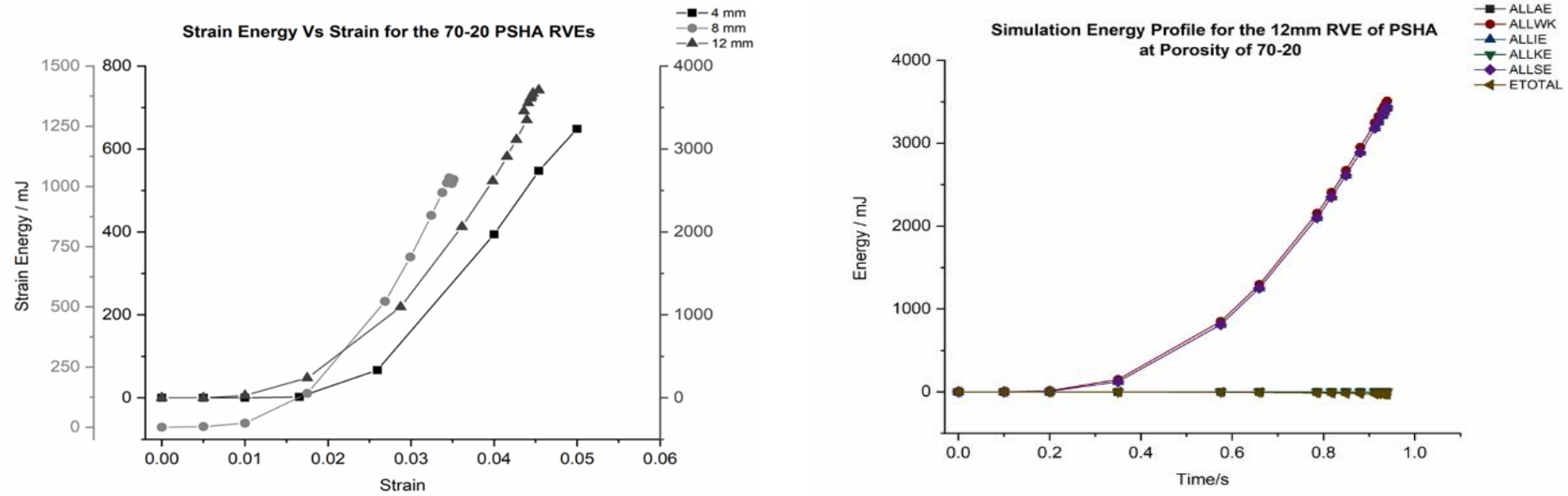

Figure 40: Left, the averaged strain energies of the simulations vs their strain for all model (RVE) sizes of the 70-20 PHA models. The profile shows a clear increase in the strain energies for given strains in response to the increase in RVE model sizes for the material. The profile provides an energetic validation for all the RVEs. Right, the energy conservation profile as extracted from ABAQUS for the 12 mm RVE models only. The profile provides validation to the simulation as the total energy is zero throughout the simulation. A 100% of the ALLSE converting to ALLIE, and 97% of ALLWK converting to ALLSE. Data gathered from simulations under 50,000 $\mu\varepsilon$.

Energy Profiles for the 60-20 PHA RVE Models

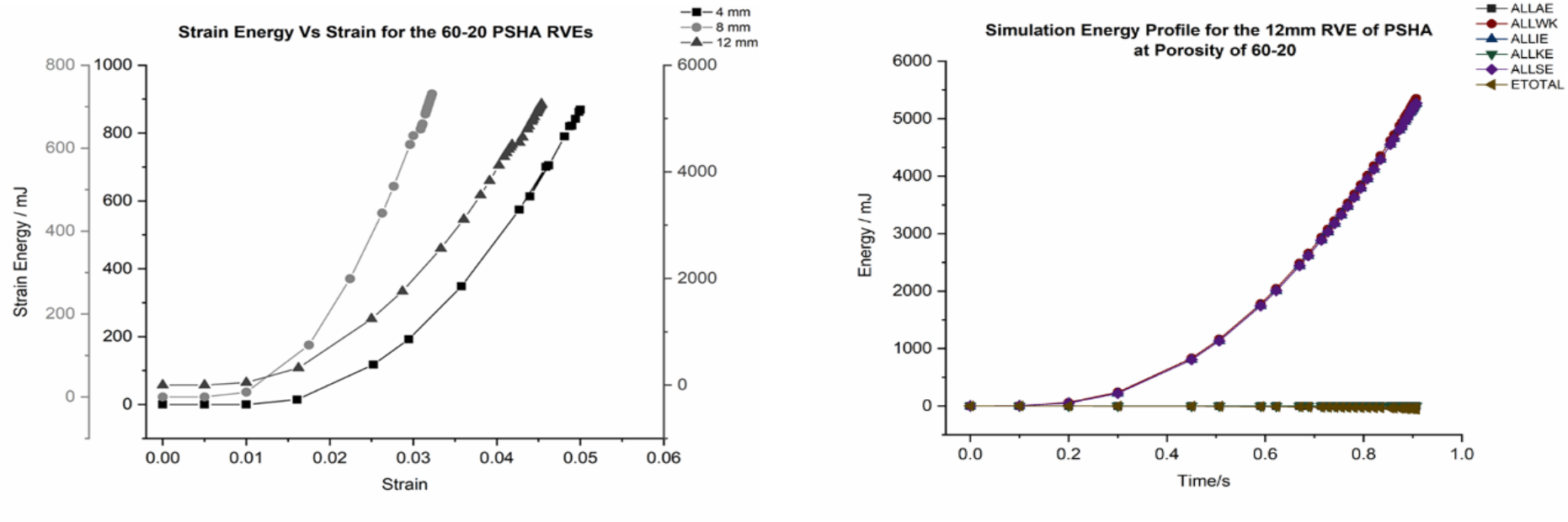

Figure 41: Left, the averaged strain energies of the simulations vs their strain for all model (RVE) sizes of the 60-20 PHA models. The profile shows a clear increase in the strain energies for given strains in response to the increase in RVE model sizes for the material. The profile provides an energetic validation for all the RVEs. Right, the energy conservation profile as extracted from ABAQUS for the 12 mm RVE models only. The profile provides validation to the simulation as the total energy is zero throughout the simulation. A 100% of the ALLSE converting to ALLIE, and 97% of ALLWK converting to ALLSE. Data gathered from simulations under 50,000 $\mu\varepsilon$.

Energy Profiles for the 60-30 PHA RVE Models

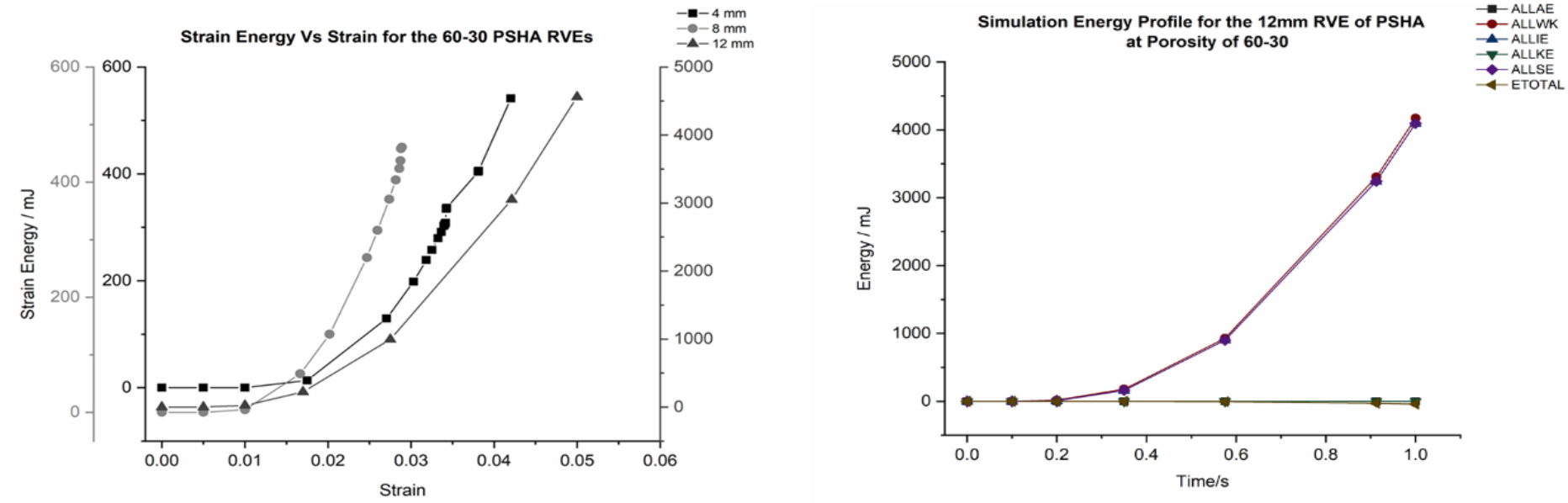

Figure 42: Left, the averaged strain energies of the simulations vs their strain for all model (RVE) sizes of the 60-30 PHA models. The profile shows a clear increase in the strain energies for given strains in response to the increase in RVE model sizes for the material apart from the 8 mm models which fell short with incomplete simulations. The profile provides an energetic validation for all the RVEs. Right, the energy conservation profile as extracted from ABAQUS for the 12 mm RVE models only. The profile provides validation to the simulation as the total energy is zero throughout the simulation. A 100% of the ALLSE converting to ALLIE, and 92% of ALLWK converting to ALLSE. Data gathered from simulations under 50,000 $\mu\varepsilon$.

The Energy plots for strain energies vs strains for all the models clear the RVEs as energetically valid representatives of the grafts. The shortfall of the 60-30 models at 8 mm is believed to be due to the simulation not going to completion rather than the size (Figure 42). The energetic validity of the 4 mm and 8 mm models is not sufficient to accept the stress and strain field outputs of their models as reliable, as they were affected by the skin shielding. The outer layer for the shorter models seemed to shield their structures and thus not allowing the for the full extent of stress and strain distribution as is the case for the larger models of 12 mm, which are more stable and thus considered as the most reliable in this study.

The energy conservation profiles in this section are for the 12 mm models only for the reasons discussed previously. The rest of the profiles are found in the appendix section A-4. All the energy profiles for the 12 mm models show simulations that run into completion reaching 1.0 on the x-axis. The total energies ETOTALs of all models remained at zero throughout the duration of the simulations, including the incomplete ones. Ideally most if not all the work done on the model should be converted to strain energy. It is understandable that a total conversion is not feasible due to various factors such as the extent of the model complexity and the mesh quality and its deformation throughout the simulations. Most of the work done $ALLWK$ was converted to strain energies ALLSE throughout the RVE models. The average percentage of work converted to strain energy is 96% for the 12 mm models, 94% for the 8 mm models and 92% for the 4 mm models. This could suggest that the increase in material volume associated with the increase in length scale provides more structural stability that reflects on the simulation of the material with a better $ALLWK$ to $ALLSE$ conversions.

The porous structure complexity of hydroxyapatite does not decrease with the increase in scale however, there is more meshed material associated with this increase which may be the reason for the healthier conversion associated with the Larger scales. More meshed material allows for less distorted elements. Within the shorter models, a large fraction of the elements faces the sudden change from material to pore, which is similar to the larger ones however, with more elements covering the solid structure than is the case for the shorter models.

The high conversions indicate that the all the models can be considered as stable. More stability could be achieved through better meshing techniques and a more sensitive software, and if possible through picking hexahedral elements rather than tetrahedral or a hybrid of both. The change in strain energy as a response to change in size indicates that energetically the RVEs are valid for simulation purposes. In order to validate the simulations. Energy output plots of the models were presented. The RVEs were all valid as models representing the material. A shortfall of the 8 mm models of the 60-30 was due to the simulations not able to complete. The 60-30 material is a dense material with a complicated porous structure. Cutting it may not have been the best option. For future studies RVE sizes should be scanned at the sizes of interest rather than cut to maintain the integrity of the granules. The energetic validity of models as RVEs for hydroxyapatite does not qualify all of them to produce reliable results. As this research shows, the shorter RVEs are more susceptible to the influence of the outer layer created to apply boundary conditions. This was not the case for the larger models of 12 mm. For future simulations larger models should be used. The thin outer layer should be avoided and a method through which boundary conditions can be applied to each node should be used in a similar manner to discrete element analysis.

4.4.1 Mesh Convergence

Mesh convergence studies are typically applied to judge the level of mesh refinement necessary. Usually a simulation will start with a coarse mesh which is then refined until the output value is unaffected by the change in mesh density. This should be consistent for at least three mesh densities, where the output starts to converge to a consistent value, which will indicate that the simulations are producing mathematically accurate solutions.

It was not possible to start with coarse meshes. It was also not feasible to insert much control on the number of elements during refinement due to the limitations of the ScanIP software which employs a leaver for mesh refinement. It was expected that the models do not demonstrate a typical convergence for the following reasons:

1. The structure is complicated, porous and contains irregular edges
2. The mesh is not structured and the shapes of certain areas in the model can give rise to element distortion during simulation
3. There were only 5 mesh densities, mesh convergence could have occurred if a wider range of mesh densities were used.

The lack of a mesh convergence however, is not a detrimental factor for this study for the following reasons:

- The mesh densities used are fine and very dense
- The models have satisfied the energy conservation validation.
- The stress outputs are similar to the mechanical test values obtained and thus the models are considered valid

Attempts at mesh convergence can be found in the appendix section A-5.

4.4.2 Validity of RVEs as FE Models

The stress and strain field results in this chapter will be from the 12 mm sized RVEs only for the following reasons

- Although the shorter RVEs were proven to be energetically valid as demonstrated in section 4.4 of the chapter through their strain energy. During simulation, they seemed to show less stress and strain concentrations with the stresses and strains being more global. The outer skin applied to enable uniform BC application, provided protection for the inner structure (Figure 43). Larger models however, have a larger material volume to skin ratio and thus the skin had less of a masking effect resulting in a more representative and realistic distribution of stresses and strains through the porous structures. This infers that the larger models are better representatives of the real scenario during loading and thus considered to be the most effective cut size for evaluation of stress and strain distributions through structures.
- The stress and strain output values seen in the following section (section 4.5) do not always maintain a linear increase with the model size increase (Figures 44 to 47). This could be due to various factors such the skin effect and samples not having a uniform structure after cuts.

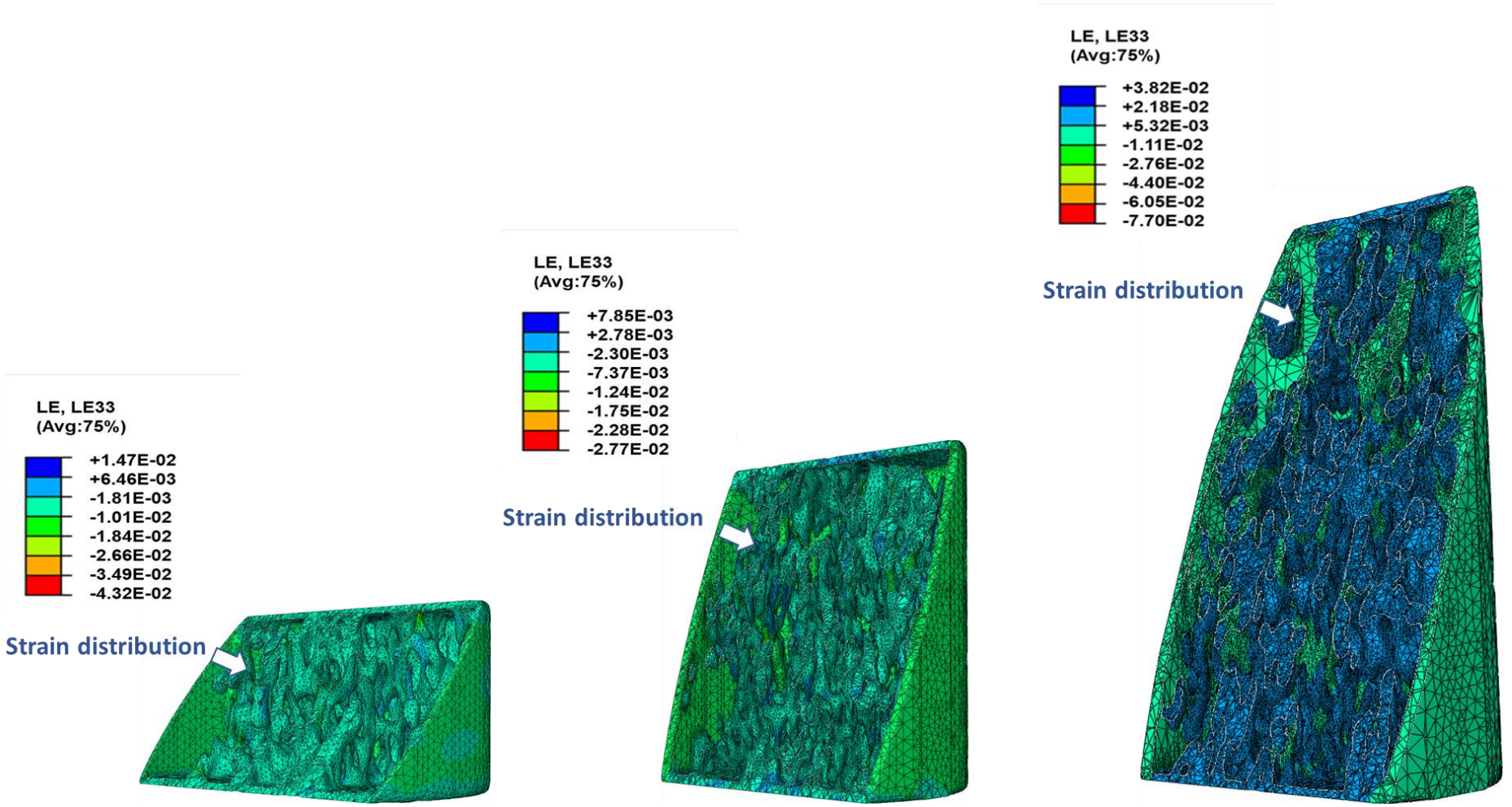

Figure 43: The images from left to right are sections from the 4 mm, 8 mm and 12 mm models respectively of the 80-20 models at 5000 $\mu\varepsilon$ micro strains (numbers after conversion from the 50,000 $\mu\varepsilon$). The images show that the 12 mm cut size is the most appropriate size to use for analysis as the strains appear to distribute within the porous structure bypassing the thin outer layer.

4.5 Application of The Linear Elastic FE Model to PHA Granule Masses

As the different sized RVE models are cuts of the same graft type, which have maintained their porosity levels. Intrinsically models of the same porosity type have the same modulus due to the assumption that the strut porosity does not vary. The stress output from the finite element analysis presented in this section show that the models at different sizes may not extrinsically act like materials of the same modulus, and thus the stress change with the increase was not always linear as seen in the following figures. This is due to the random arrangement of pores within the structure. This is to be expected with cuts as they contain different regions of the original material. Different specimens of the same material and same size models would give similar results due to the factor of porosity. There is also the fact that the controlled variable applied as a boundary condition was strain and not stress.

Stress Output

The following plots are of the averaged stress output results from the FE analysis of the 80-20 and 80-30 models strained at 10,000, 12,000, 25,000 and 50,000 $\mu\varepsilon$. The remaining plots can be found in the appendix section A-3. The plots clearly show that stress values do not always increase linearly in response to the increase in size. In Figure 45, at 50,000 $\mu\varepsilon$ for the 80-20 models, the stress dropped as the cut size increased from 4 mm to 8 mm than resumed rising as the model size increased to 12 mm. There were random unexplained drops in stresses for a number of the models of all the materials. The most stable increases happen to belong to the 80-30 material models, which could be due to the fact that they have a higher concentration of strut porosity. This can be seen in Figure 10, chapter 2 and Figure 30, chapter 3. These findings in addition to the outer skin effect on the smaller models, which was discussed earlier lead to the conclusion that all the stress and strain field results in this chapter should be of the 12 mm RVE models only.

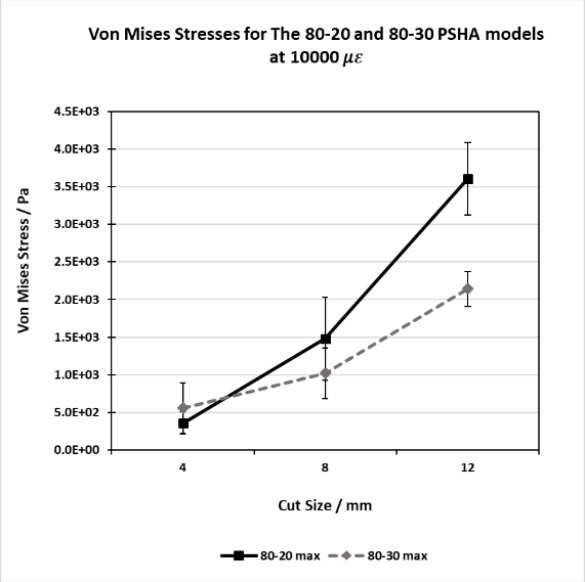

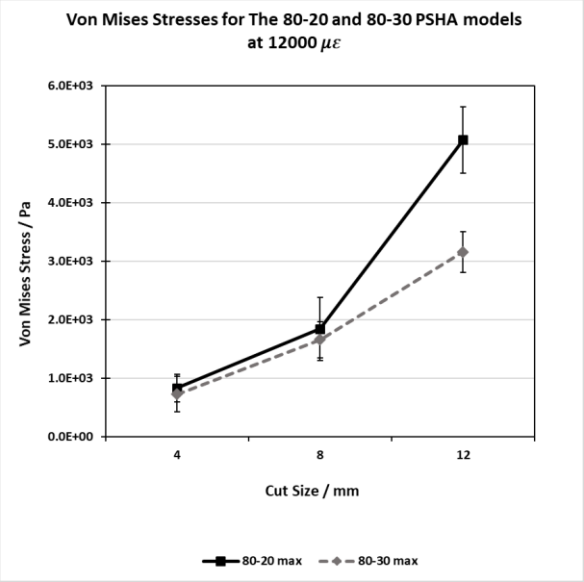

Figure 44: Von Mises avereged output from the FE analysis of the 80-20 and 80-30 PHA models at 10,000 με and 12,000 με respectively with standard error bars. The stresses seem to steadily increase when increasing the model sizes for the 80-20 models and the 80-30 models at both levels of applied strain.

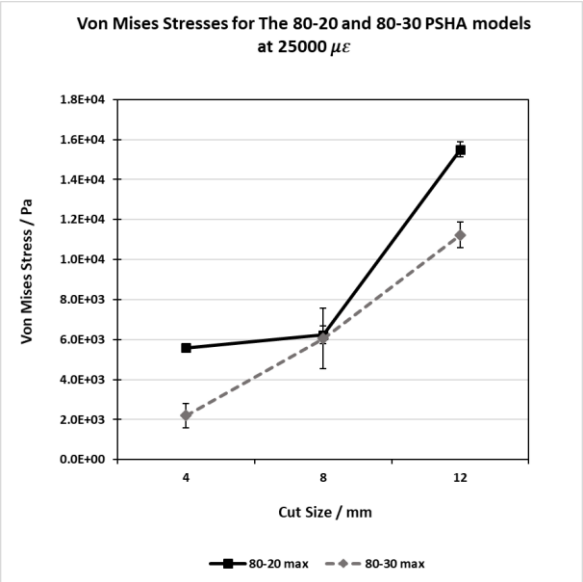

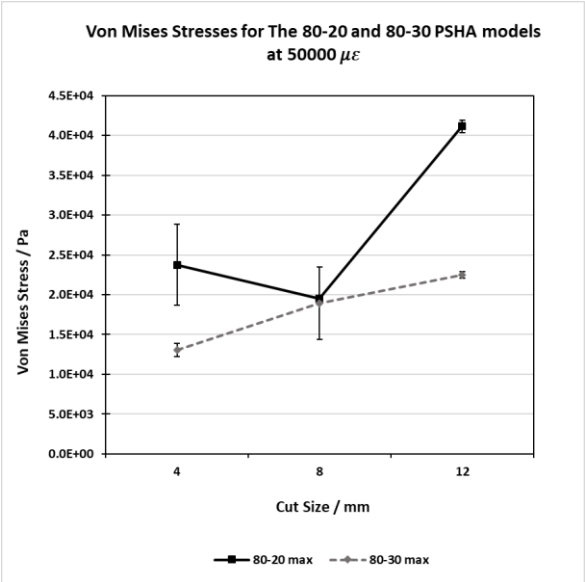

Figure 45: Von Mises avereged output from the FE analysis of the 80-20 and 80-30 PHA models at 25,000 με and 50,000 με respectively with standard error bars. The stresses seem to steadily increase when increasing the model sizes for the 80-30 models. For the 80-20 models there is an increase in output stress with increase in model size as 25,000 applied microstrains albit not as steady as models under lower microstrains. At the high applied strain of 50,000 με the stress sharply drops at the 8 mm model size and resumes increasing for the 12 mm models.

Strain Output

This section presents the axial strain outputs obtained from the FE analysis for the 80-20 and the 80-30 models. The remaining plots for the rest of the materials investigated can be found in the appendix section A-3.

The strain outputs show a more consistent trend then the stresses (Figures 46-47) with the maximum strains increasing and the minimum strains decreasing in response to the increase in model size. The maximum strains are positive and tensile. The minimum strains are negative and compressive. Both strains are output strains resulting from the micro strain applied as a boundary condition to the models. These output strains are the effectors in an in-vivo environment, initiating some of the mechano-signalling events covered in chapter one. This trend in the output strain is expected, as the boundary condition applied, in this case a controlled variable during simulation is strain. The plots are of the averaged axial strains with standard error bars as obtained from ABAQUS.

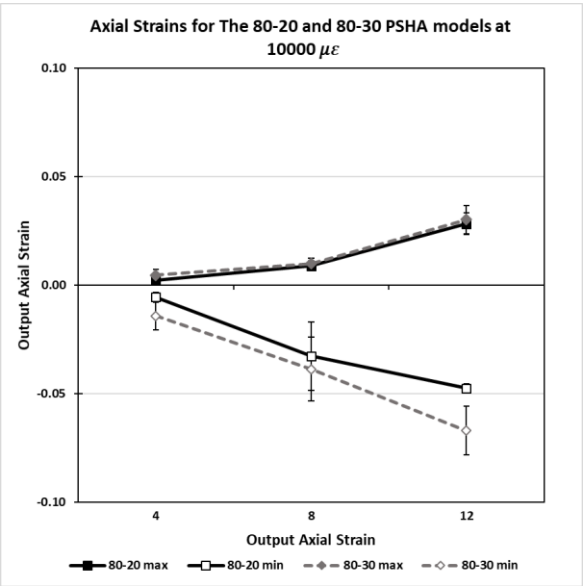

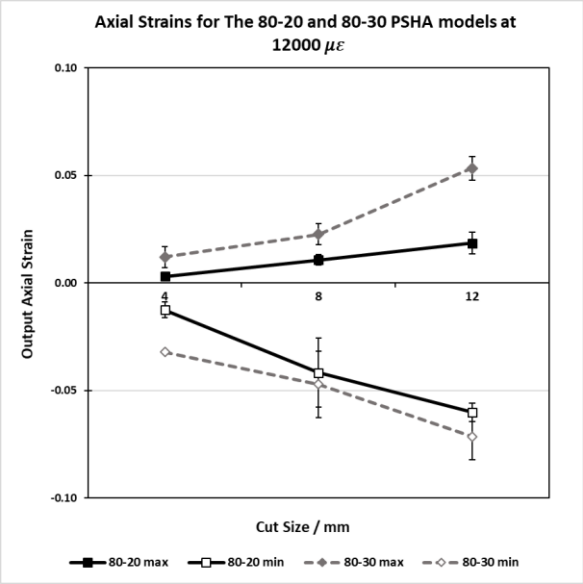

Figure 46: Axial strain avereged outputs from the FE analysis of the 80-20 and 80-30 PHA models at 10,000 με and 12,000 με respectively, with standard error bars. Both material models behave in a similar manner for both microstrain levels applied following the expected trend.

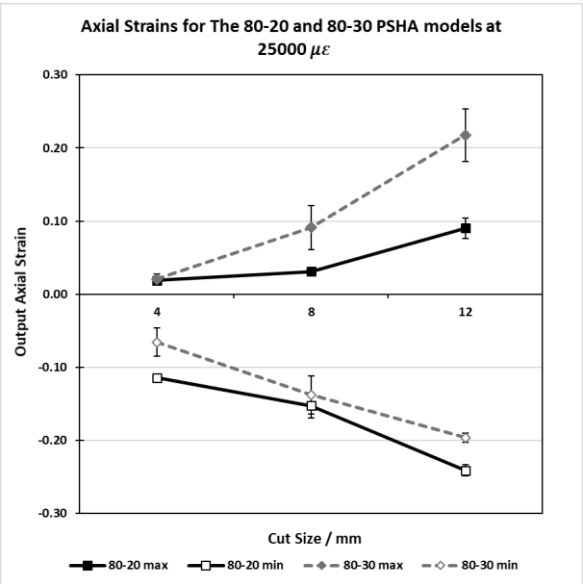

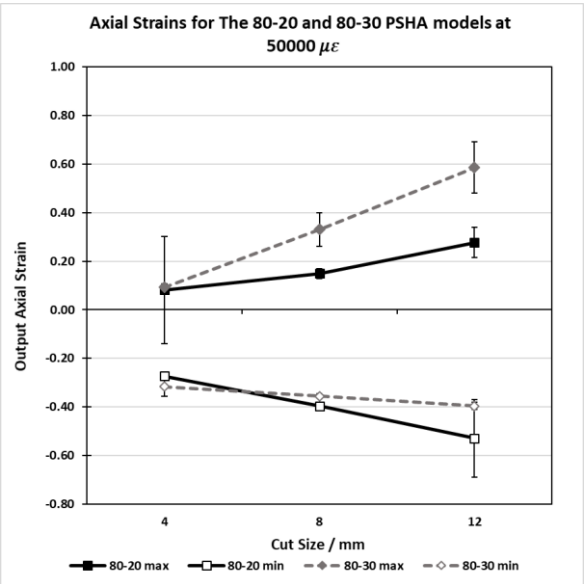

Figure 47: Axial strain avereged outputs from the FE analysis of the 80-20 and 80-30 PHA models at 25,000 με and 50,000 με , with standard error bars. The trend is followed by both materials.

4.5.1 Analysis of the Stress and Strain Fields within Simulated PHA Models of Granule Masses

The models presented in this chapter have been strained at 50,000 $\mu\varepsilon$. The output stresses are Von Mises stresses in Pascal's accompanied with a contour colour plot. As the strain applied was uniaxial, the output strains chosen were captured in the axial direction indicated in the contour plot as LE33. All the outputs have been converted to their equivalent at 5,000 $\mu\varepsilon$ using the factors obtained from linear fits as demonstrated in Figures 36 and 37 in this chapter and in section A-2 of the appendix.

The LE33 contours, help visualise the effect of the porous structure on the distribution of strain applied as output strain fields. Through them the regions experiencing compression and those experiencing tension can be identified. The results also show the regions of amplified strain. All of which are physiologically relevant, as they create the mechanical environment experienced by cells in-vivo and are responsible for kick starting mechanical signalling pathways.

Through ABAQUS, the full structure of models can be investigated easily and the regions of interest can be zoomed into and investigated from different angles. However, images of the full structure are not as clear in print and the contours appear as vague colours. The size of the models, the widespread porosity, the fine meshes, and the depth of the regions of interests within the structure all contribute to the inability to capture the true effect of the strain applied on the architecture of the models. To overcome this, and to showcase the contours the research needs to present, the stress and strain field results will be demonstrated as focused figures, zooming in at the locations of interest.

Before exploring the stress and strain fields, it is useful to consider the volume fraction of the macro and strut porosities. The strut porosity values can be found in Table 9. The total porosities of the modelled grafts are 80%, 70% and 60% with hydroxyapatite present at 20%, 30% and 40% respectively.

The grafts were modelled with the macro-porosity as an architectural feature. The strut porosity was modelled through variation in the elastic modulus of the material in the struts. The percentage of porosity in the struts, known as micro porosity was calculated using Eq. 8 provided by Dr Hing, and listed in Table 9.

$$\% \, \mu P = \% \, SP \left(\frac{\%HA}{100 - \% \, SP} \right) \quad \text{Eq. 8}$$

Table 9: Distribution of porosity within the struts and macro pores of the PHA material specimens

Material (Total Porosity)	Porosity in struts (Micro-porosity)	Porosity in macro pores
80-20	4.5	75.5
80-30	7.8	72.2
70-20	8.3	61.7
60-20	10.5	49.5
60-30	13.2	46.8

4.5.1.1 Stress and Strain Field Results for the 80-20 PHA Models

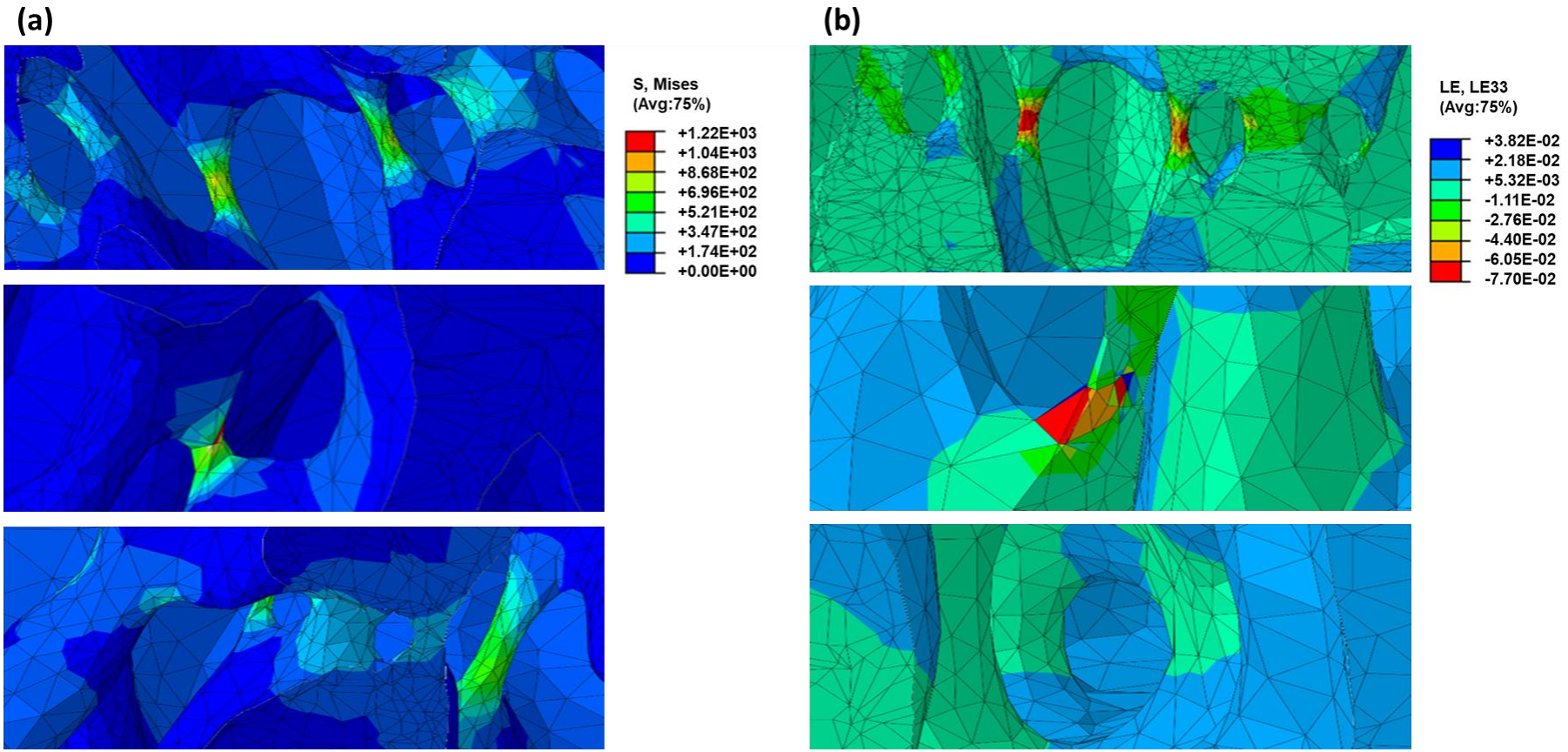

Figure 48: Figure (a) focused images of the stress fields, showing that stresses tend to concentrate at the waists (pore borders), the colour contour values are Von Mises stresses in Pascals. Figure (b) focused images of the strain fields, showing strain concentrations at the waists which tend to be compressive (-), the bulk of the struts experience tensile strain (+) as indicated by the colour contour.

4.5.1.2 Stress and Strain Field Results for the 80-30 PHA Models

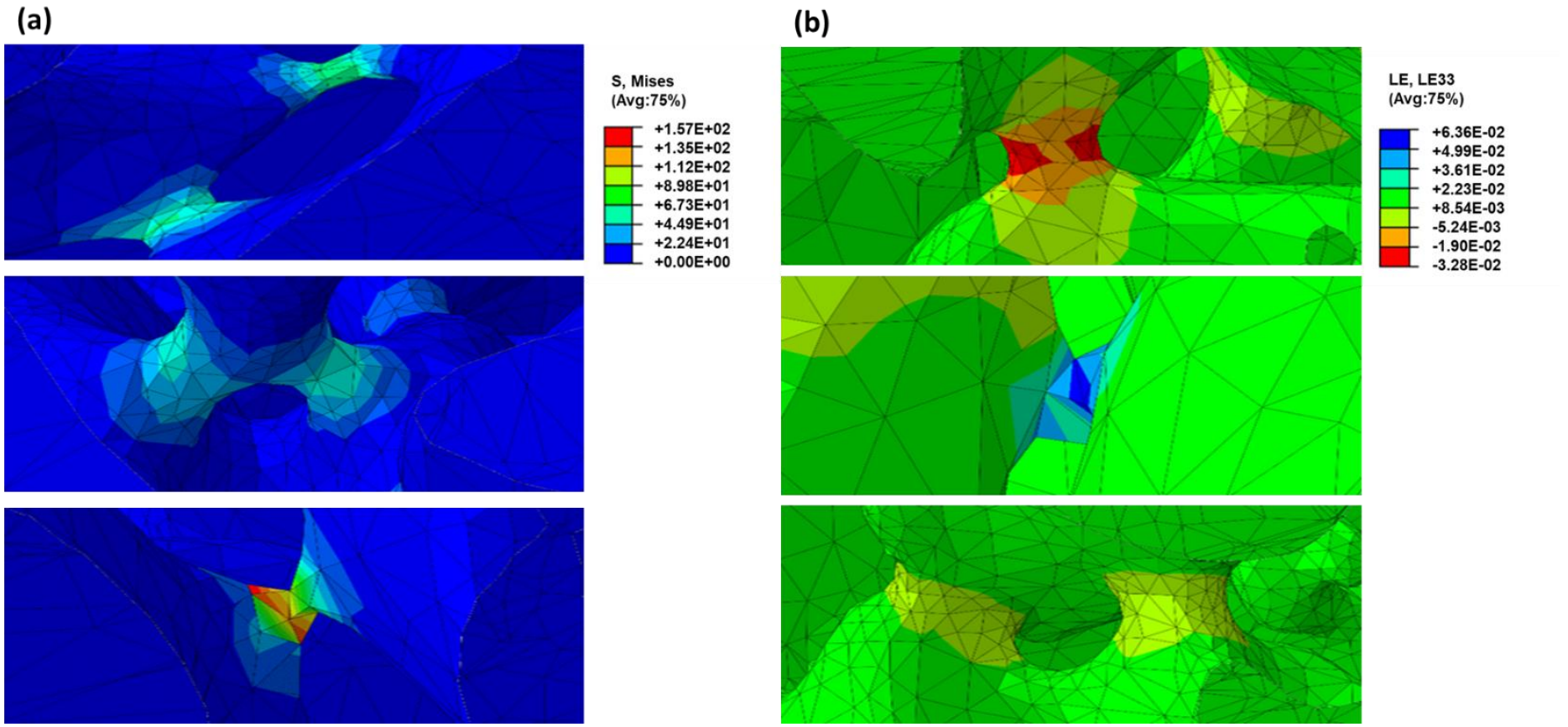

Figure 49: Figure (a) focused images of the stress fields, showing that stresses tend to concentrate at the waists (pore borders), the colour contour values are Von Mises stresses in Pascals. Figure (b) focused images of the strain fields, showing strain concentrations at the waists which tend to be compressive (-), as well as tensile (+). The bulk of the struts remain under tensile strain.

4.5.1.3 Stress and Strain Field Results for the 70-20 PHA Models

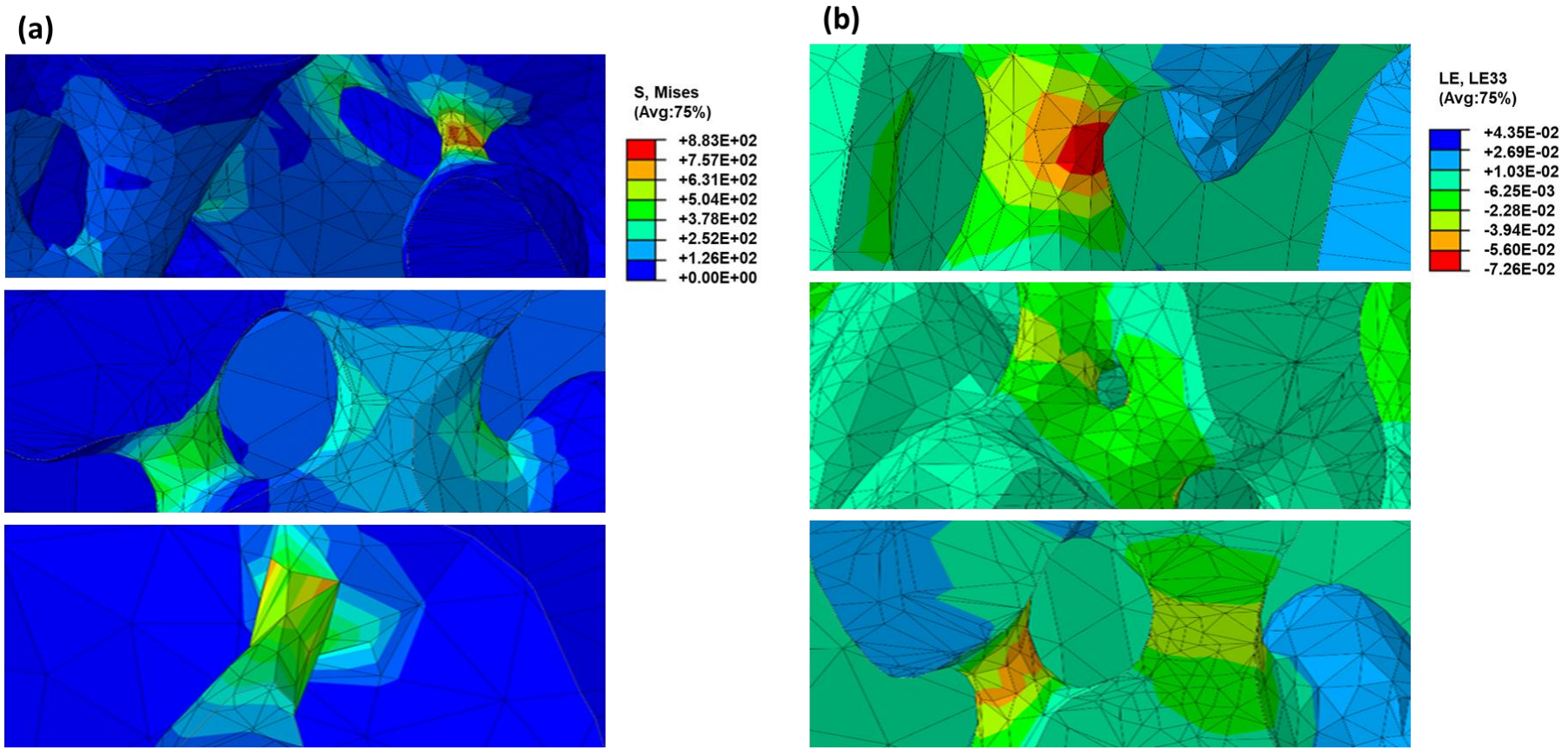

Figure 50: Figure (a) focused images of the stress fields, showing that stresses tend to concentrate at the waists (pore borders), the colour contour values are Von Mises stresses in Pascals. Figure (b) focused images of the strain fields, showing strain concentrations at the waists which tend to be compressive (-), the bulk of the struts remain under tensile strain.

4.5.1.4 Stress and Strain Field Results for the 60-20 PHA Models

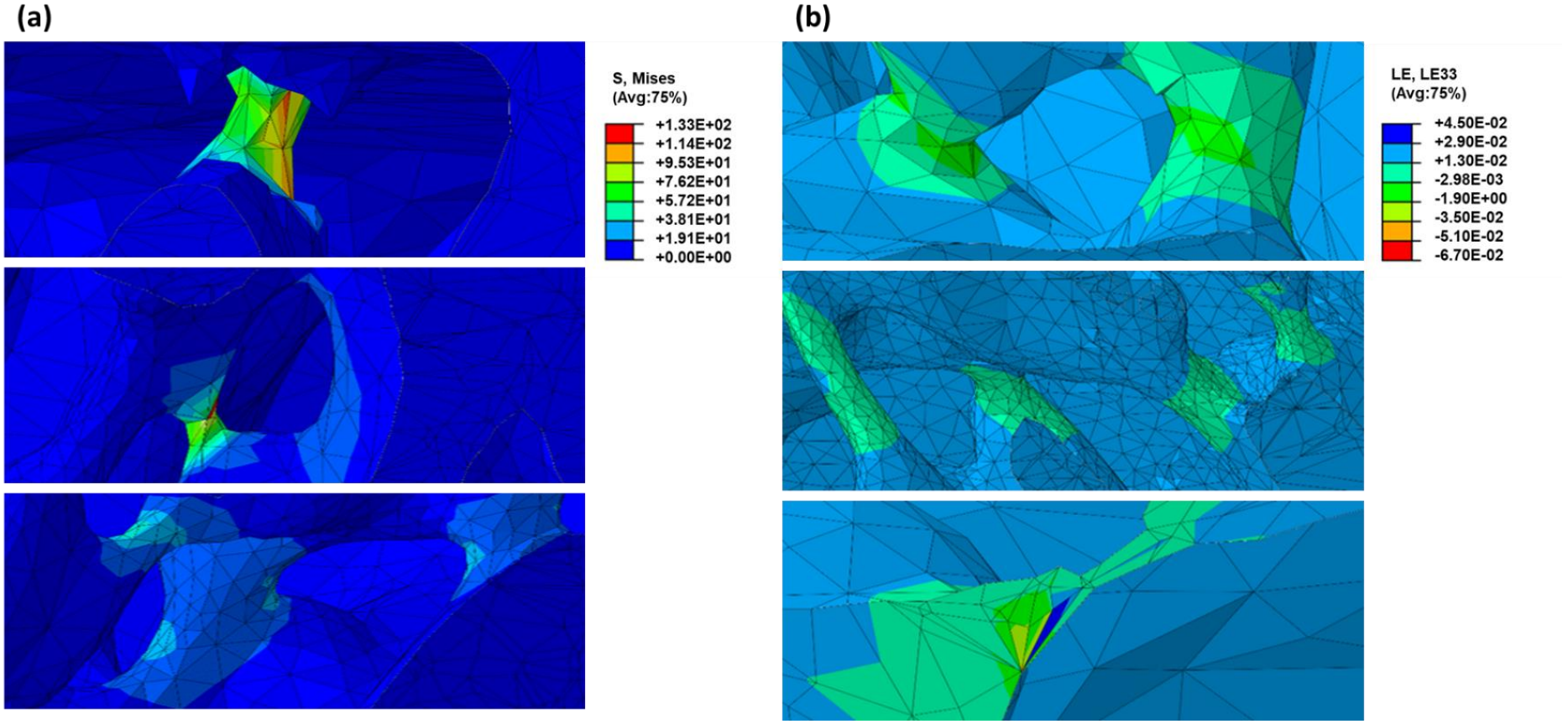

Figure 51: Figure (a) focused images of the stress fields, showing that stresses tend to concentrate at the waists (pore borders), the colour contour values are Von Mises stresses in Pascals. Figure (b) focused images of the strain fields, showing strain concentrations at the waists which tend to be compressive (-), the bulk of the struts remain under tensile strain.

4.5.1.5 Stress and Strain Field Results for the 60-30 PHA Models

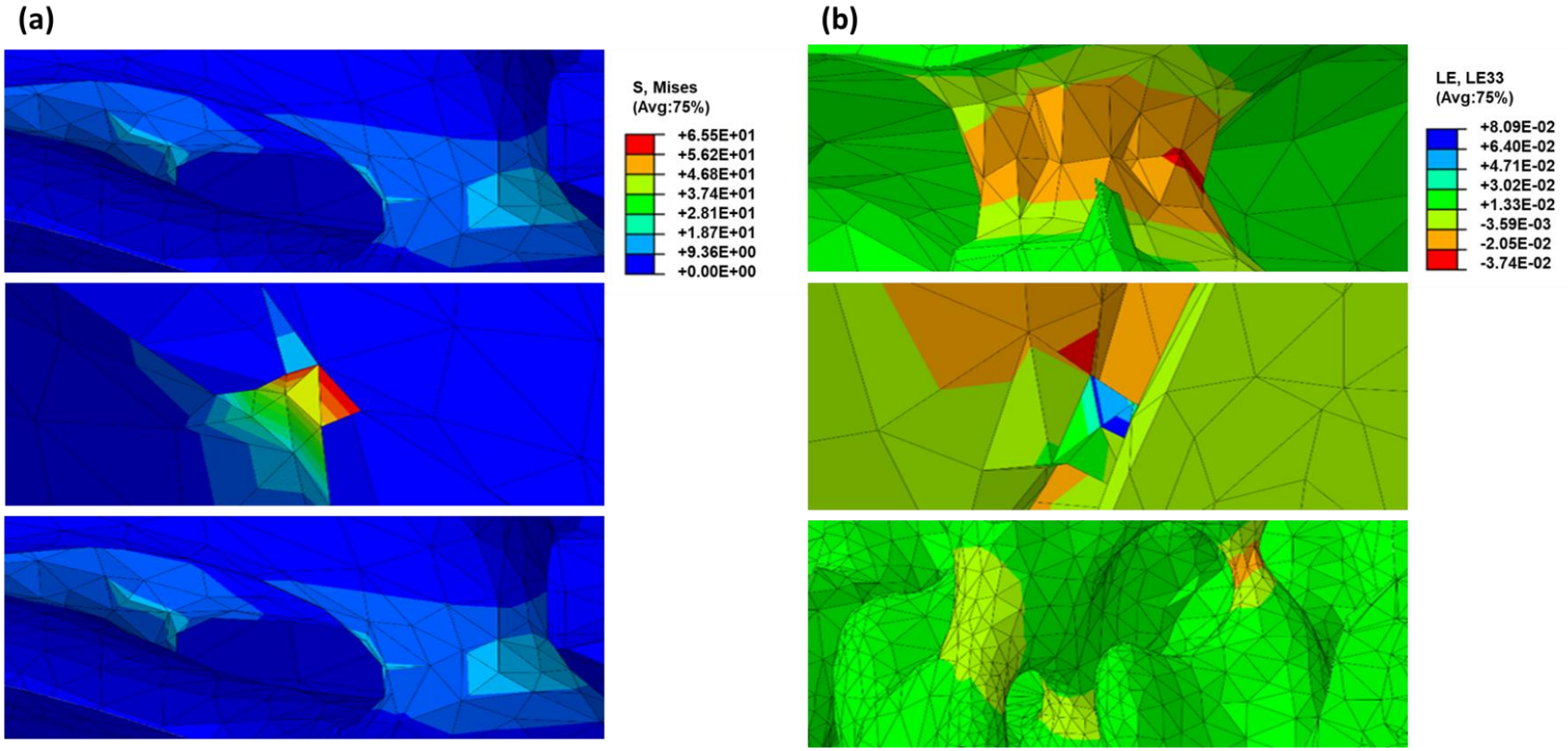

Figure 52: Figure (a) focused images of the stress fields, showing that stresses tend to concentrate at the waists (pore borders), the colour contour values are Von Mises stresses in Pascals. Figure (b) focused images of the strain fields, showing strain concentrations at the waists which tend to be compressive (-) with some pockets of (+) tensile strains, the bulk of the struts remain under tensile strain.

4.6 Evaluation of Stress and Strain Field Results

Once the stresses and strains are distributed through the structure. They tend to locate around the pore waists (pore borders). These are the borders and edges of pores. Figure 53, is a schematic demonstrating the locations of waists and nodes in PHA structures. Stresses and Strains building up at the struts (the body) of the structure reaching their highest peaks at the waists Figures 48-52 in what can be viewed as an amplification process. The bulk of the material experiences a positive strain (tensile) as a response to the compressive micro-strain applied. This changes at the pore waists to a negative (compressive) strain.

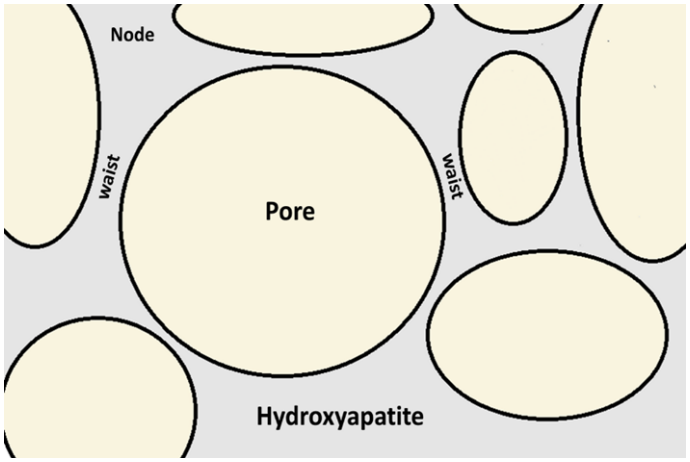

Figure 53: Porous Hydroxyapatite structure showing pores, nodes and waists

Effect of Total Porosity:

The total porosity of the models, also known as macro porosity, are architectural features of the modelled granule masses. The coloured contours and the values associated with them in Figures 48, 50 and 51 can help investigate the effect of the total porosity levels on the distribution of stresses and strains.

The results indicate the following:

1. The stress levels demonstrated a decrease in response to the decrease in the percentage of total porosities for models of similar strut porosities

2. The strain level demonstrated an increase in response to the decrease in the percentage of total porosities for models of similar strut porosities

Effect of Strut Porosity:

Changes in strut porosities demonstrated similar effects on the levels of stresses and strains as seen in Figures 48, 49 and 51, 52. However, the drops in output stresses and the increase in strain levels as a response to decreasing the percentage of strut porosities are higher than the effect seen with decreasing the total porosity (macro).

Field Distribution

The 80-30 models showed less field distribution within their structures in comparison to the 20% models of 80% total porosity. The stress and strain fields as well as their peaks concentrated at the waists only. This is not the case for the 80-20 models where the peaks can be seen at the waists, whilst the fields covered other areas of the structure in addition to the waists.

The fields of the 80-30 models occupied smaller areas of the waists than the 80-20 models. This means that the fields associated with the 80-30 models have a higher degree of focus. The contours suggest lower stress peak levels for the 80-30, yet higher strain peal levels both compressive and tensile. These observations could be due to the 80-20 models having the lowest micro-porosity volume within their struts despite of being the second highest porous material after the 80-30 (Table 9). The lack of high levels of micro porosity may also be responsible for the haphazard distribution of their fields.

The 80-30 models have thicker struts than the 80-20 models (Figure 10), (Figure 30), as well as more pores within their struts. Their thick porous struts could be providing them with the ability to channel the spread of stress and strain fields to more confined locations. This explains the inefficiency in focusing the fields within the 80-20 models, as their struts lack sufficient levels of micro porosity.

The models of 70% total porosities showed the most well distributed stress and strain fields, covering most of the pore waists in the structure. Strut porosities appeared to have more of an influence on the stress levels for the 70% models. At 20% the 70-20 models have stress peak values higher than the 80-30 models and close to the 80-20 models. This implies that the strut and micro porosities are more influential than the macro porosity.

The 60-20 modules are the least porous modules simulated in this study and the densest. The 60-20 models have the second highest level of micro porosity within their struts after the 60-30 models. Most of the structure is clear of stress and strain fields apart from a few pore waists scattered across the structure brought into a high degree of focus (Figure 51). The strain levels registered are close to the values for the 70-20 models. This could be due to their level of micro porosity which is only slightly higher than the 70-20 (Table 9). The total strut porosities of the two materials are also quite close (Table 8). This suggest that strut porosities are the major effectors in strain amplification.

The change in total porosity from 70% to 60% at 20% strut porosity, had a more pronounced effect on the stress levels than the effect of decreasing the total porosity from 80% to 70%. This suggests a link between the architecture and stress levels experienced by loaded PHA granules, particularly for materials of low total porosity levels.

The strain levels for the 60-30 are much higher than their 20% counterparts, and the highest for all the materials. The stress registered however, is lower than the 20% counterpart and indeed the lowest of all materials. The 60-30 models have the highest volume of micro porosity (Table 9) which explains the high values and degree of focus for strain peaks.

Summary:

Stress and strain fields prefer the pore waists. The results indicate that the micro pores within the struts have a channelling effect guiding the stress and strain fields to specific locations within the structures of the models. Higher values of peak strains seem to belong to models of high levels of micro porosity within their struts. They also demonstrate the most localised fields and peaks of stresses and strains within their waists, confirming that micro porosities are indeed involved in channelling the loads within PHA structures and in amplifying the strain. The level of stresses and strains appear to also be subject to the arrangement of the material and the architecture of the model which is controlled by the total porosity and the thickness of the struts. The models belonging to the 70% are very interesting in their ability to effectively distribute stresses and strains through their structures, which could be very useful to their application as bone graft substitutes.

Chapter 5

Application of the Non-Linear Drucker Prager Constitutive Model

5.1 Introduction

The Drucker-Prager Plasticity model is a widely used constitutive non-linear model, typically applied to simulate powder compaction problems. Developed by Drucker and Prager in the early 50's for soil and powder metallurgy problems (DRUCKER and PRAGER, 1952), it is applied to model the behaviour of powders and granules during compaction as the particles/granules rearrange themselves to form a tightly packed dense structure, representing the hardening and densification during compression, as well as the friction between the granules or particles. The model is particularly interested in the permanent plastic deformation that occurs during the final stages of compression with density being the variable and the elastic properties inputted as a function of density (Sinka.,et al 2009). The data from the mechanical compression tests alongside the radial strength data from tests and literature were used as material parameters for the simulation as a Cap Plasticity model in the ABAQUS's material's property section. The analysis was carried out on the materials of 20% strut porosities only, as UCS values obtained from cylindrical specimens of the same origin were only available at this strut porosity (Campion and Hing, 2017). The values are necessary for obtaining the parameters needed for the DP model. During the compression testing of the PHA granules, the pressure applied does not reach a level where the granules can be completely conciliated as is the case for powder compaction tests typically applying the Drucker Prager Criteria. Powders demonstrate hardening during compression, where the amorphous structure becomes a hard compact (usually a pill). The characteristics of the resultant compact structure are a reduction in the bulk density and an increase in strength.

From the stress vs strain profiles presented in chapter 2 for the compression tests, the granules demonstrated a level of hardening which could be due to the following;

1- The rearrangement of the granules,
2- The breaking of some struts
3- The collapse of some pores
4- The sliding of granules past each other, creating a more tightly packed structure.

The PHA models were simulated using the DP-Cap model for the following reasons:

1. Obtaining a stress vs strain profile from the simulated models for comparison with the compression test results was not a computationally feasible option due to the size of the models. The experimental data were instead inputted as a material property to investigate the real behaviour of the material under a failure criterion. As the Drucker-Prager approach uses information from the uniaxial compression tests previously conducted it can be applied for validation.
2. It was found that the stress and strain output curves of linear models and deferential models tend to overlap (Liu et al., 2018). This suggests that the Drucker-Prager model output can be used in conjunction with the linear model output to describe the behaviour of a material.

3. The Drucker Prager concept is not fully incorporated into modelling porous bio-ceramics. Literature is limited and usually apply the failure criteria to models with pre-specified geometries and volume fractions of porosity, typically modelling in two-dimensions unrealistic structures, and not on CT-scanned real three dimensional models (Fritsch, 2009a), (Liu et al., 2018).

The DP model through ABAQUS is applied to isotropic materials (Dassault Systèmes, 2014) . The model has a yield surface that is divided into three regions.

1. The shear failure surface (Fs), which represents the shear flow of the granules.
2. The transition surface, which provides a separation, and a smooth transition between the first and third region.
3. The third surface, represents the hardening occurring during compaction which is also the inelastic plastic segment, known as the cap surface Fc (DiMaggio, 1971), (Drucker and Prager, 1952).

Figure 54, adapted from (Han et al., 2008), demonstrates the three surfaces as well as the terms associated with the application of the model and the parameters necessary for its successful application using ABAQUS. However, these parameters are based on various tests that are not only extensive but technically challenging to perform on porous ceramics. These tests are uniaxial tension tests, tri-axial compression tests and shear tests in addition to the uniaxial compression tests (Shang, Sinka and Pan, 2012).

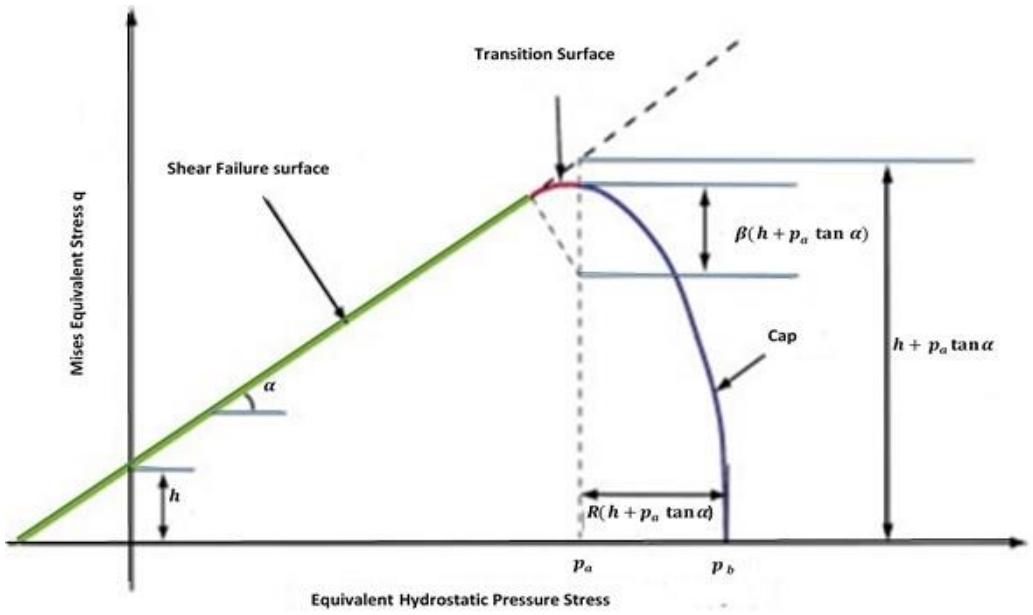

Figure 54: The Drucker-Prager Cap model. The schematic demonstrates the q vs p plane featuring all the surfaces

The parameters needed include, the friction angle which is denoted on the graph as α and the Cohesion which is h. The equation for the shear surface can be written as such,

$$Fs = q - p\,tan\ \alpha\ - h \quad \text{Eq. 9}$$

Where q is the Mises equivalent stress and is defined as,

$$q = |\sigma_z - \sigma_r| \quad \text{Eq. 10}$$

The term σ_z is the applied axial stress during the compression tests, σ_r is the radial strength. The p in the shear surface equation stands for the hydrostatic pressure stress and is obtained using the relationship

$$p = -\frac{1}{3}\,(\,\sigma_z + 2\,\sigma_r) \quad \text{Eq. 11}$$

The σ_r values were obtained from Brazilian disc diametral tests conducted in this research and from literature sources as seen in Figure 55.

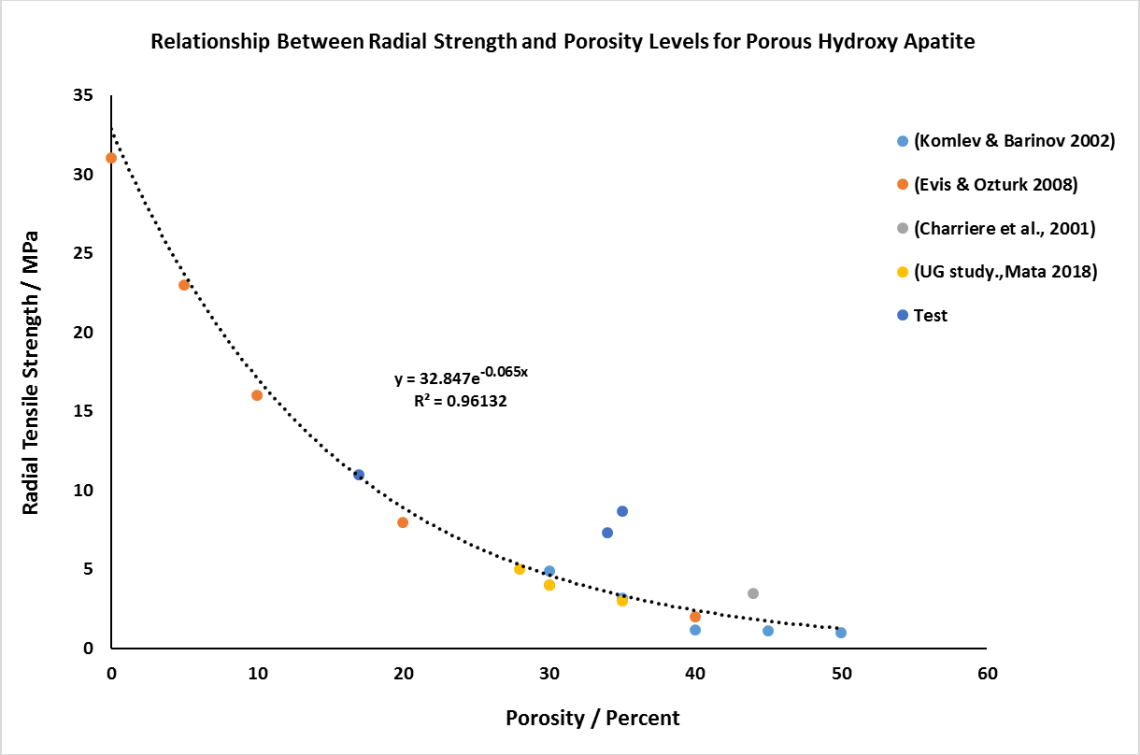

Figure 55: Radial strength values obtained from Brazilian tests from both literature sources and tests conducted for the study. The relationship between porosity and radial strength obtained through an exponential fit.

The cap surface, which is the ellipse in the figure, describes the yield surface under hydrostatic pressure. This surface requires two parameters to describe it, which are the Eccentricity, and the evolution parameter p_a, these can be obtained using triaxial tests and/or axial tests that allow radial stress measurements. The parameters needed for all the surfaces are; the eccentricity, which is the ratio of the vertical axis over the horizontal axis controlling the cap shape and is denoted by R in the following equations with a value between 1000 and 0.001,but taken as 0.001 in this study following Sinka's approach for ceramic based materials (Sinka et al., 2009), the evolution parameter, which represents hardening and/or softening that is caused by the volumetric plastic strain and is denoted as p_a, the hydrostatic compression yield strength, which describes the volumetric inelastic strain and is denoted by p_b,the friction angle denoted as α, and the transition parameter denoted as β. Which controls the smoothness of the transition surface between the F_s and the F_c surfaces.

The cap surface formula is given in Eq. 12;

$$F_c = \sqrt{(p - p)^2 + \left[\frac{R_q}{1+\beta-\frac{\beta}{\cos\alpha}}\right]^2} - R\,(h + p_a\ tan\,\alpha) = 0 \quad \text{Eq. 12}$$

And the transition surface formula in Eq. 13;

$$F_t = \sqrt{[(p - p_a)]^2 + \left[q - \left(1 - \frac{\beta}{cos\,\alpha}\right)(h + p_a\,tan\,\alpha)\right]^2} - \beta(h + p_a\ tan\,\alpha) = 0 \quad \text{Eq.13}$$

To obtain the values necessary to carry out the simulation in ABAQUS. First. The value for p_a was obtained using the following relationship

$$p_a = -\frac{[3q_A+4h\ \tan\alpha\ (1+\beta-\beta/\cos\alpha)^2]}{4\left[1+\beta-\frac{\beta}{\cos\alpha)\ \tan\beta}\right]^2} +$$

$$\frac{\sqrt{9q_A^2\ +24hq_A(1+\beta-\beta/\,cos\,\alpha)^2\ \ tan\,\alpha+8\left(3\,p_Aq_A+2q_A^2\right)[(1+\beta-\beta/\cos\alpha)\ tan\,\alpha]^2}}{4\left[1+\beta-\frac{\beta}{cos\,\alpha)\ tan\,\beta}\right]^2} \quad \text{Eq. 14}$$

This was achieved by substituting Eq.14 into Eq.15 to obtain the value for the shape parameter R ;

$$R = \sqrt{\frac{2\ (1+\beta-\beta/\ cos\,\alpha)^2}{3q_A}\ (p_A - p_a)} \quad \text{Eq. 15}$$

The values for q_A and p_A were obtained from the plot of q vs p, which was derived from σ_z and σ_r . By obtaining R , the value for p_a was obtained by substituting Eq. 15 into Eq. 16 (Sinka et al., 2009),(Han et al., 2008).

$$p_a = \frac{p_b - Rh}{(1 + R\ tan\,\alpha)} \quad \text{E.q 16}$$

The p_b value was determined using the original density of the granules before applying pressure during the compression test and working out the density from the strain value and knowledge of the die measurements i.e. volume occupied by granules, as p_b is a function of the volumetric volume strain given by the relationship;

$$p_b = f\left(\varepsilon_v^{\rho}\right) \quad \text{Eq. 17}$$

Where

$$\varepsilon_v^{\rho} = \left(\frac{\rho}{\rho_0}\right) \quad \text{Eq. 18}$$

With ρ_0 being the initial density of the granules prior to compression as given by the Archimedes tests in chapter 2, and ρ the density at the final compression state calculated from the volume the granules occupy.

5.2. Elastic Properties of the Single Crystal of PHA: in The Micro-Scale; Estimation of The Friction Angle and Cohesion Values for Porous PHA Ceramics from Uniaxial Compressive Strength Measurements

The friction angle and cohesion parameters are critical for the equations listed. These values can be obtained from uniaxial compression strength values, using the multi-scale model from Fritsch (Fritsch, 2009) to eliminate the need for extensive testing. The process was as such, Compression strength values were fitted to the multi scale model adopted from (Fritsch, 2009). This model uses the elastic properties of single crystals of hydroxyapatite bio-ceramics, particularly the shear modulus μ_c with a value of 44.9 GPa and the bulk modulus κ_c with a value of 82.6 GPa (Fritsch, 2009). The crystal compressibility χ is the ratio between those two values represented by the relationship;

$$\chi = \frac{\mu_c}{\kappa_c} = 0.54 \quad \text{Eq. 19}$$

In order to obtain the elastic properties of the polycrystalline structure in the macro-scale; the stiffness of the interface between single crystals of the bio-ceramic need to be considered as they influence the friction angle α and the cohesion h. If the assumption is made that the bulk modulus of polycrystalline Hydroxyapatite κ_{poly} is the same as the bulk modulus for the single crystal (Fritsch, 2009).

$$k_{poly} = k_c \quad \text{Eq. 20}$$

The shear modulus for the polycrystal can be obtained using the relationship (Fritsch, 2009).

$$\frac{\mu_c}{\mu_{poly}} = 1 + 3\left[\frac{5}{2}\kappa + \left(\frac{1}{8} \times \frac{\mu_c}{\mu_{poly}} + \frac{17\chi + 6}{4\chi + 57}\right)^{-1}\right]^{-1} \quad \text{Eq. 21}$$

$$\kappa = \frac{K_t\, a}{\mu_c} \quad \text{Eq. 22}$$

Where K_t stands for the stiffness of the interface, and a is the average size of single crystals. Using this relationship, the μ_{poly} , the shear modulus for the polycrystal, can be obtained, and once that is obtained it becomes possible to calculate the compressibility of the polycrystal structure χ_{poly} using the relationship (Fritsch, 2009).

$$\chi_{poly} = \frac{\mu_{poly}}{\kappa_{poly}} \quad \text{Eq. 23}$$

And the Poisson ratio for the polycrystals will be given by

$$\nu_{poly} = \frac{3-2\chi_{poly}}{6+2\chi_{poly}} \quad \text{Eq. 24}$$

Accounting for the total porosity φ to get.

$$\frac{\kappa_{poro}}{\kappa_{poly}} = 4\chi_{poly}\ \frac{1-\varphi}{4\chi_{poly}+3} \quad \text{Eq. 25}$$

$$\frac{\mu_{poro}}{\mu_{poly}} = (1-\varphi)\ \frac{1+\frac{8}{9}\chi_{poly}}{1+\frac{2}{3}\varphi+\frac{8}{9}\chi_{poly}\left(1+\frac{3}{2}\varphi\right)} \quad \text{Eq. 26}$$

5.3 Elastic properties of porous PHA including strut porosities

The general expression of the uniaxial compressive strength of PHA as a function of porosity level is adopted from (Fritsch, 2009), as it allows the establishment of a linear relationship between the cohesion and the uniaxial compression strength, as such;

$$\left[\frac{3}{4}\varphi - \left(\frac{\alpha}{\mathrm{B}_{Tt}}\right)^2\right]\Sigma^2{}_{poro,m} + \left[1 + \frac{23-50\,{\upsilon_{poly}}^2}{\left(5\nu_{poly}-7\right)^2}\ 2\varphi\right]\Sigma^2{}_{poro,d}$$

$$+ \left(\frac{\alpha}{B_{Tt}}\right)^2 h(1-\varphi)\Sigma_{poro,m} = \left(\frac{\alpha}{B_{Tt}}\right)^2 h^2\ (1-\varphi)^2 \quad \text{Eq. 27}$$

Where α is the friction angle and h, is the cohesion, $\Sigma_{poro,d}$ is the deviatoric effective stress, $\Sigma_{poro,m}$ is the mean stress, φ is the total porosity and the term B_{Tt} is a proportionality factor and can be expressed as;

$$B_{Tt} = \sqrt{-\frac{1}{3}\,\kappa^2\,\frac{\partial}{\partial\kappa}\left(\frac{\mu_c}{\mu_{poly}}\right)} \quad \text{Eq. 28}$$

Assuming f_c is the uniaxial compressive strength, of a uniaxial compression state, the stress tensor Σ is given by;

$$\Sigma = \begin{bmatrix} -f_c & 0 & 0 \\ 0 & 0 & 0 \\ 0 & 0 & 0 \end{bmatrix} \quad \text{Eq. 29}$$

Hence,

$$\Sigma_{poro,m} = -\frac{f_c}{3} \quad \text{Eq. 30}$$

And the deviatoric stress tensor Σ_d thus:

$$\Sigma_d = \Sigma - f_c\, I = \begin{bmatrix} -\frac{2}{3}f_c & 0 & 0 \\ 0 & \frac{1}{3}f_c & 0 \\ 0 & 0 & \frac{1}{3}f_c \end{bmatrix} \quad \text{Eq. 31}$$

And

$$_{poro,d} = \sqrt{\frac{1}{2}\Sigma_d : \Sigma_d} = \sqrt{\frac{1}{2}\left(\frac{4}{9}+\frac{1}{9}+\frac{1}{9}\right)f_c^2} = \frac{1}{\sqrt{3}}\,f_c \quad \text{Eq. 32}$$

Substituting Eq. 32 and Eq. 30 into Eq. 27 gives:

$$\begin{bmatrix} \frac{3}{4}\varphi - \left(\frac{\alpha}{B_{Tt}}\right)^2 \frac{f_c^2}{9} + \left[1 + \frac{23-50\,\nu_{poly}^2}{\left(5\,\nu_{poly-7}\right)^2}\,2\varphi\right]\frac{f_c^2}{3} - \\ 2\left(\frac{\alpha}{B_{Tt}}\right)^2 h(1-\varphi)\frac{f_c}{3} = \left(\frac{\alpha}{B_{Tt}}\right)^2 h^2\,(1-\varphi)^2 \end{bmatrix} \quad \text{Eq. 33}$$

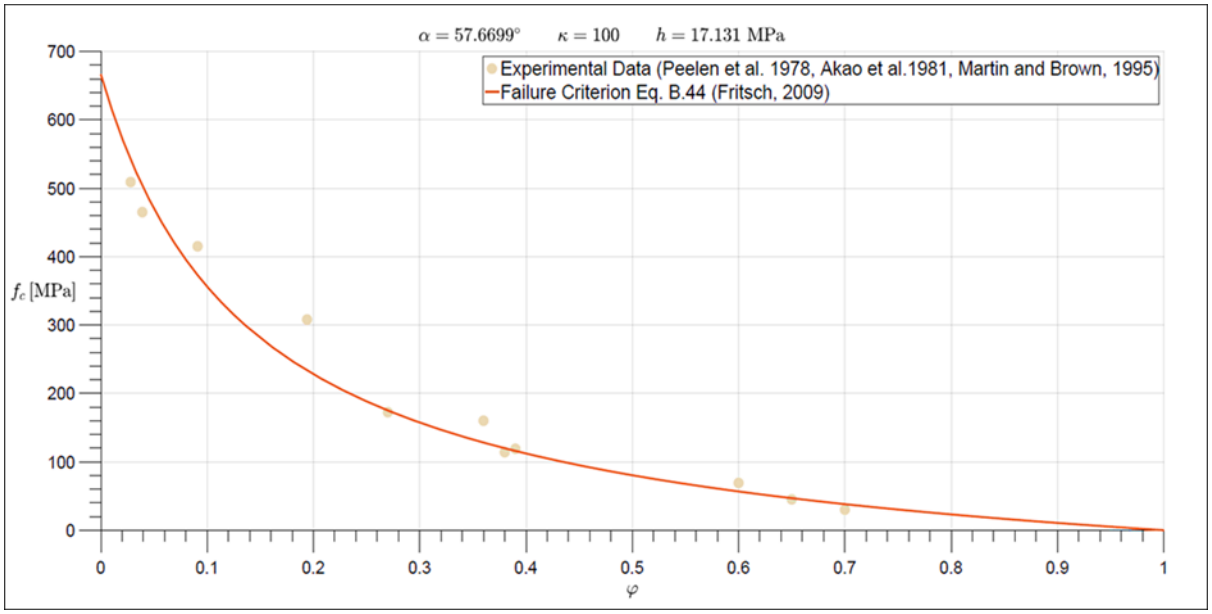

Figure 56: fitting of literature data using equation 33, adopted from Eq.B.44 by Fritsch (Fritsch, 2009)

Fitting the experimental data from literature (Peelen et al., 1978),(Martin and Brown, 1995), into Eq. 33 using a MATLAB code developed by Dr Ettore Barberie employing a non-linear least square fit (Figure 56).

From this fit, it becomes possible to extrapolate the uniaxial compressive strength of Hydroxyapatite at zero porosity f_{c_0}. The value for f_{c_0} was found to be 666.2 MPa. When solving for f_{c_0} a linear relationship between f_{c_0} and cohesion h is obtained. This relationship can be expressed as such

$$f_{c_0} = h\,\frac{\sqrt{-54\,\frac{2}{5\kappa^2}F(\kappa,\chi)\alpha^2}}{6+\frac{2}{5\kappa^2}F(\kappa,\chi)\alpha^2} - \frac{3-\frac{2}{5\kappa^2}F(\kappa,\chi)\alpha^2}{6+\frac{2}{5\kappa^2}F(\kappa,\chi)\alpha^2} = h\,G(\alpha,\kappa,\chi) \qquad \text{Eq. 34}$$

Where $F(\kappa,\chi)$ is a known function (Fritsch, 2009). Substituting equation Eq34 into Eq33 leads to Eq35, which can be fitted to the experimental data (Campion and Hing, 2017), (Figure 57).

$$\left[\frac{3}{4}\varphi - \left(\frac{\alpha}{B_{Tt}}\right)^2\right]\frac{f_c^2}{9} + \left[1 + \frac{23-50\,v_{poly}^2}{(5v_{poly}-7)^2}\,2\varphi\right]\frac{f_c^2}{3} - 2\left(\frac{\alpha}{B_{Tt}}\right)^2\frac{f_{c_0}}{G(\alpha,\kappa,\chi)}(1-\varphi)\frac{f_c}{3} = \left(\frac{\alpha}{B_{Tt}}\right)^2\left(\frac{f_{c_0}}{G(\alpha,\kappa,\chi)}\right)^2(1-\varphi)^2 \qquad \text{Eq. 35}$$

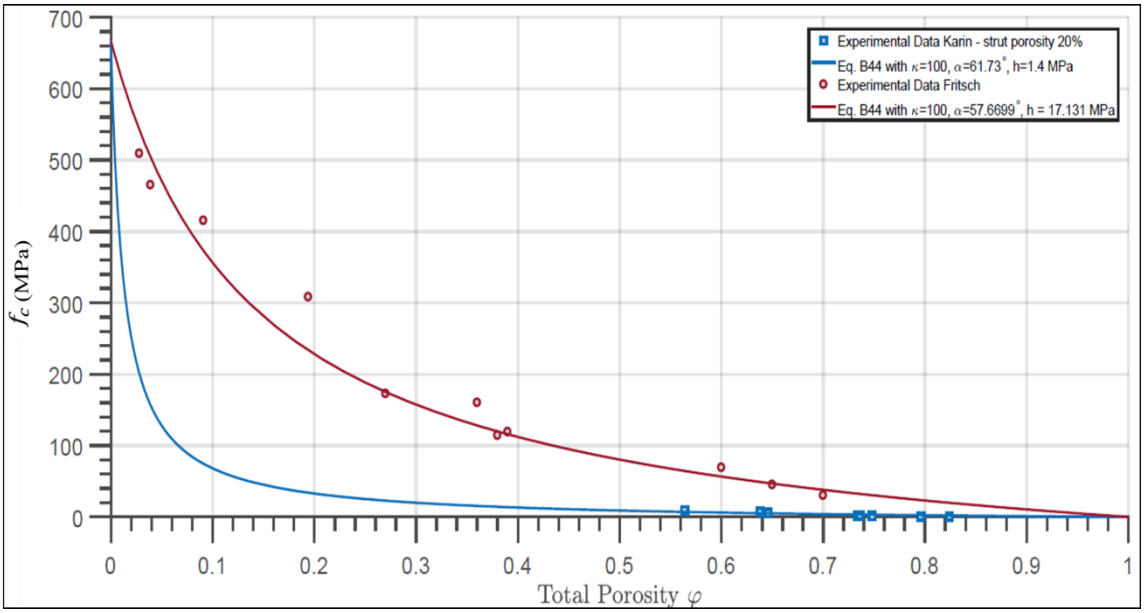

Figure 57: least square fit of experimental data using Equation 35, to obtain the necessary parameters α and h for the PHA 20% strut porosity granules for the application of the Drucker Prager Cap Model. Matlab code by Dr Ettore Barberie

5.4 Results from The FE Analysis Using The DP Criteria on Models of PHA Granular Masses:

As demonstrated in chapter 3, the porosity levels were conserved throughout the RVEs, and in chapter 4, the RVEs demonstrated that their strain energies adhere to the Hill-Mandel principle. However, for applying the DP criteria, the 12 mm RVE models were the only models simulated for the following reasons:

1. The findings from the simulation results in chapter 4 indicate that meaningful results can best be obtained from the 12 mm RVE models, due to the shielding effect of the artificial outer layer.
2. For a realistic simulation the model requires a significant amount of granules present in the RVE. The 12 mm RVEs contain the largest amount of granules of the three sizes in this study.

The Drucker Prager parameters were applied to simulate the models in ABAQUS, applying the same material properties, boundary conditions and applied strains as the linear model simulations conducted in chapter 4. The DP parameters were inputted as a subroutine in the properties section of ABAQUS, using the Plasticity Cap model and the Cap Hardening sub model options.

As the compression test data were incorporated into the calculation of the input parameters of the Drucker- Prager model. The model is expected to produce outputs that are justified by the mechanical compression results. The output data, in this chapter in conjunction with the linear model results, create a more comprehensive understanding of the material behaviour under compressive conditions (Linear model) and its failure under those conditions (DP).

The model as mentioned is a failure criteria module. This means that irrelevant of the strain applied the simulation will stop when the material fails. The output Von Misses stress values should thus be similar to the values obtained from literature for the stress at failure for the materials simulated. Incorporating the compression data from the three regions involving both the macro and micro porosities, provides the model with a complete behaviour profile. The

aim is to produce results that capture the effect of the strut porosities which are modelled through the input material properties as well as the effect of the architecture that is the due to the total porosity which includes the macro level.

The output stresses will be presented using the same methods used in chapter 4. Through Von Mises stress contour plots in Pascals, with the addition of the PEEQ values. PEEQ is the name used by the software ABAQUS for the equivalent plastic strain (Dassault Systèmes, 2014). It is a scalar parameter that measures the materials inelastic deformation. When a value above zero is registered for PEEQ it indicates that the yield strength of the material has been reached. Thus, the parameter is used here as a failure criterion for the models.

5.5 Drucker Prager Cap Model Results

5.5.1 Results for the 80-20 PHA Models at 12 mm

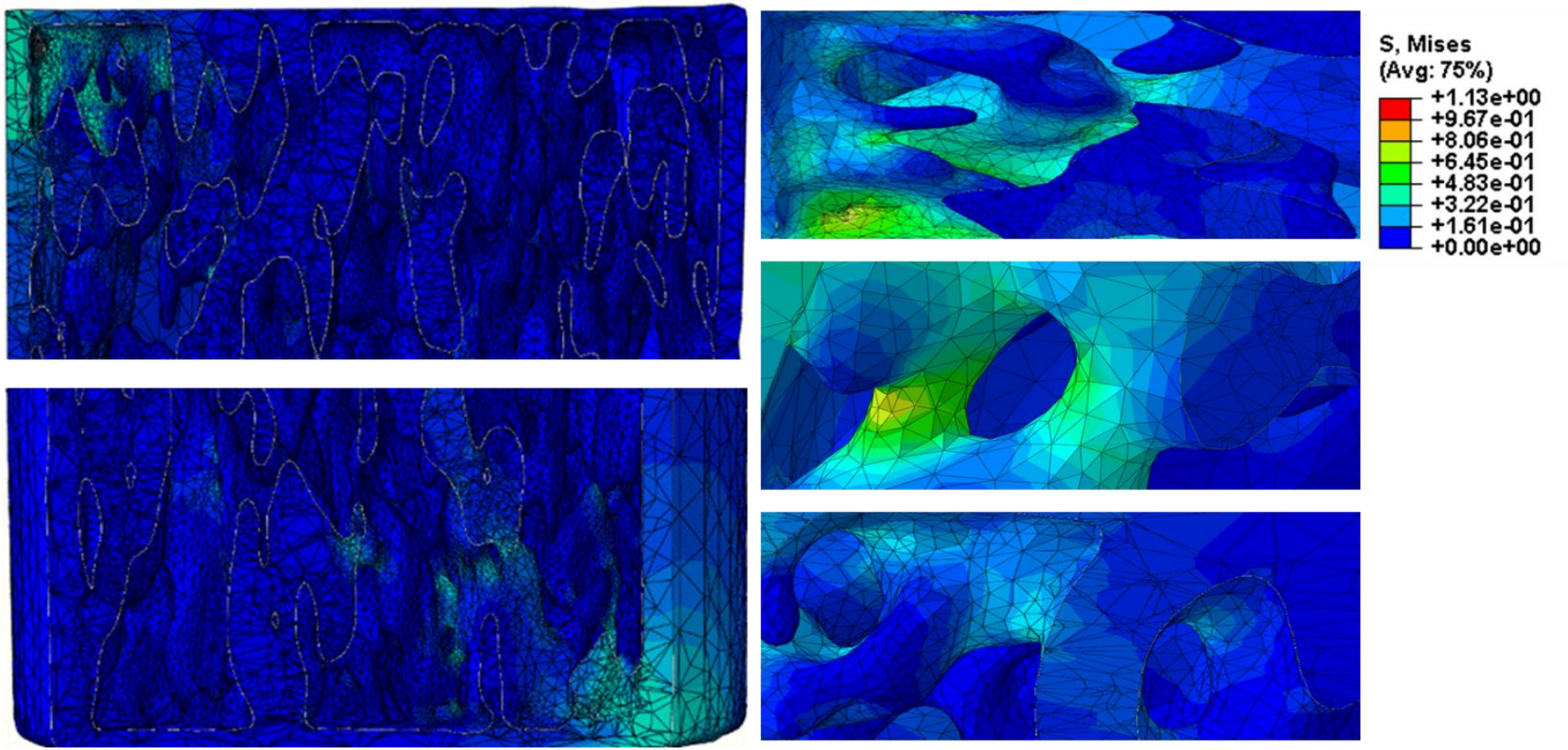

Figure 58: Simulation results showing the concentration of Von Mises stresses at the top and bottom corners of the cylindrical model, spreading towards the centre. The zoomed in images show the concentration of stresses on the waists of the pores and on the struts of the material (material body). Areas of stress concentration indicate the location of potential failure. The model was subjected to 50,000 $\mu\varepsilon$. The output stress in MPa

5.5.2 Results for the 70-20 PHA Models at 12 mm

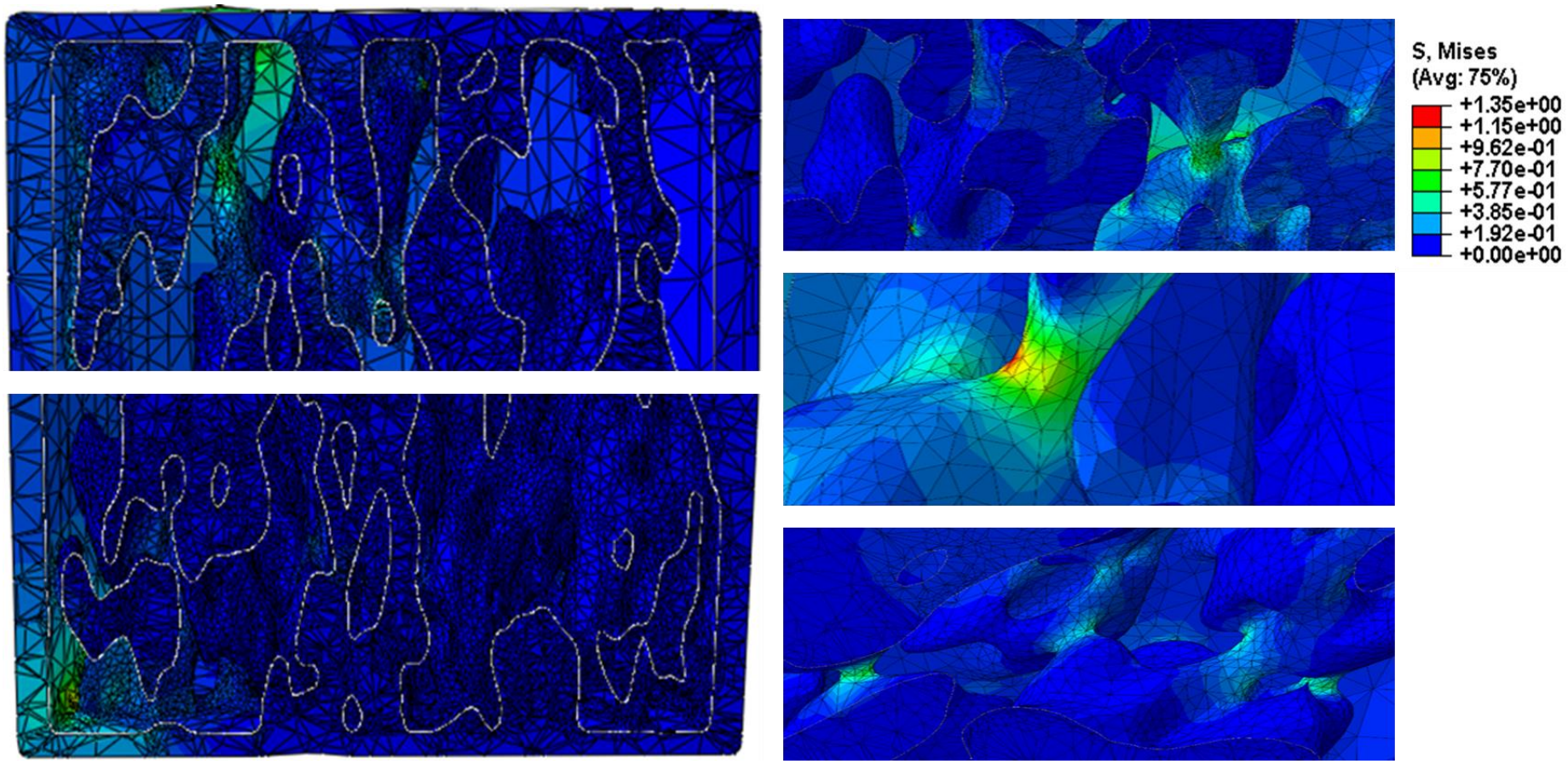

Figure 59: Simulation results showing the concentration of Von Mises stresses at the top and bottom corners of the cylindrical model, spreading towards the centre. The zoomed in images show the concentration of stresses on the waists of the pores with the struts remaining free of stress. Areas of stress concentration indicate the location of potential failure. The model was subjected to 50,000 με. The output stress in MPa

5.5.3 Results for the 60-20 PHA Models at 12 mm

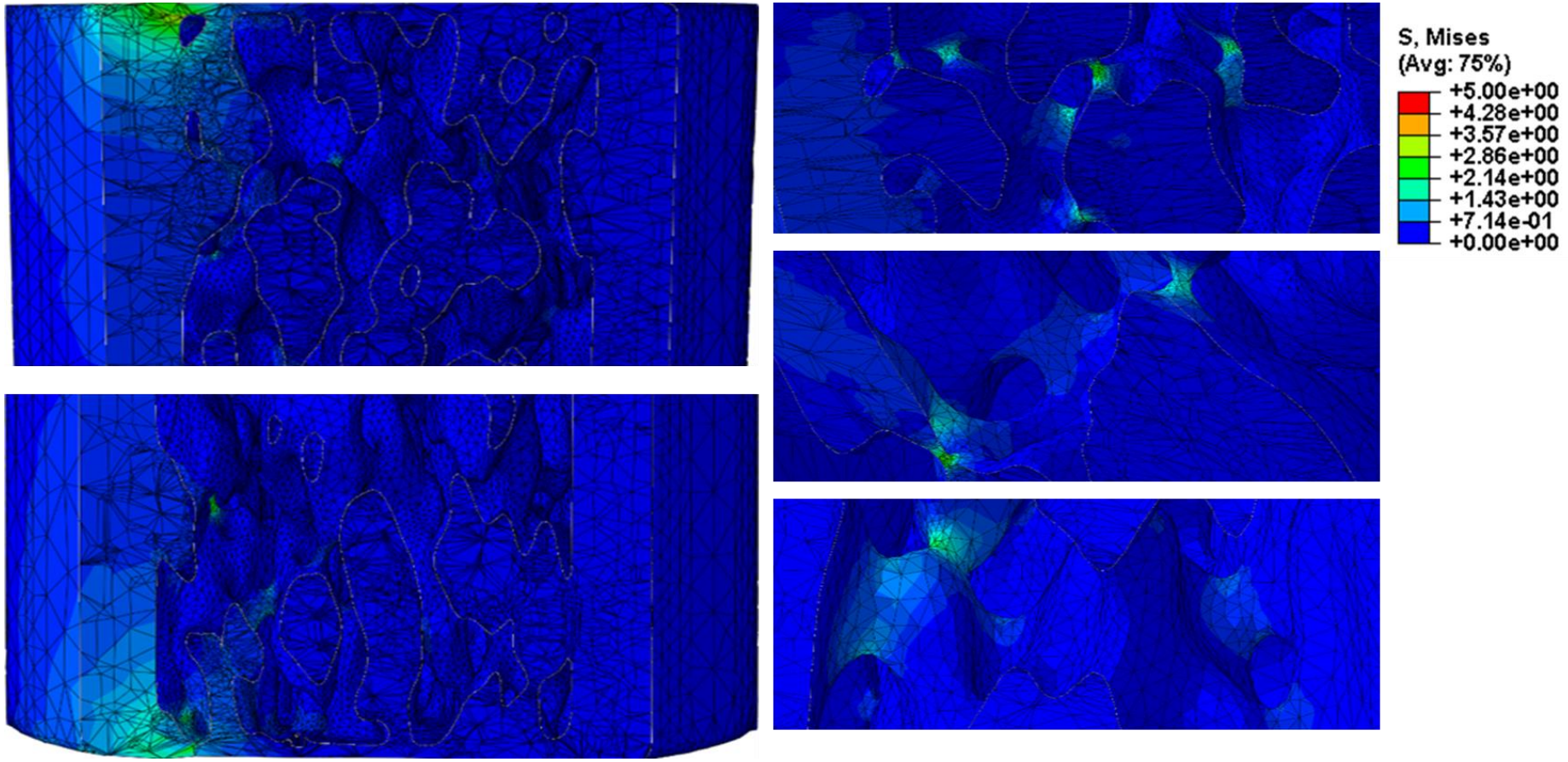

Figure 60: Simulation results showing the concentration of Von Mises stresses at the top and bottom corners of the cylindrical model, spreading towards the centre. The zoomed in images show the concentration of stresses on the waists of the pores with the struts remaining free of stress. Areas of stress concentration indicate the location of potential failure. The model was subjected to 50,000 με. The output stress in MPa

Table 10: Comparison of the output Von Mises Stress and UCS values from literature for PHA

Materials	Literature UCS stress ± STDV	Von Mises Output ± STDV
80-20	4.20e-1 ± 0.34	4.83e-1 ± 0.08
70-20	1.49e+0 ± 0.54	1.35e+0 ± 0.46
60-20	6.25e+0 ± 1.11	5.00e+0 ± 1.46

All the models experience plastic deformation (damage) as they reach the stress output levels indicated in the colour contour plots. The output stress values appear to coincide with ultimate compressive strengths reported for the same materials (Table 10),(Campion, 2017). For the 80-20 model (Figure 58), the colour contour indicates that the UCS value is achieved at the band between 6.45e-1 and 4.83e-1 (green), which constitutes the majority of the stress fields observed. This suggests that all areas experiencing the stress field are experiencing deformation. The contour of 70-20 (Figure 59) shows that the UCS value from literature for the material (Table 10), coincides with the highest band (red). The areas where the UCS is met are very confined, to small locations on the waists, which indicates that most of the struts due to the material's ability to distribute the load did not deform as much as the 80-20 model. The 80-20 model is more porous with thinner struts. Therefore, causing the spread of the stress fields to the body of material i.e. its struts. For the 60-20 models, the stress fields are minimally spread (Figure 60). They are confined to only a few pore waists within the structure. However, as the contour plot shows, the UCS value was met at the highest band (red). A very small area tucked within the structure. Indicating that most of the material does not experience much plastic deformation. It is also the strongest material of the three.

Figures 60-62 demonstrate that for all the models simulated using the DP model, the areas affected by the stress fields are located around the pores, specifically on the waists. The exception is the 80-20 models where the stress fields spread to include some struts as was the case in the linear elastic results in chapter 4. The results as seen in the figures suggest that the majority of the areas affected by the stress fields experience stresses approaching the UCS values of the material.

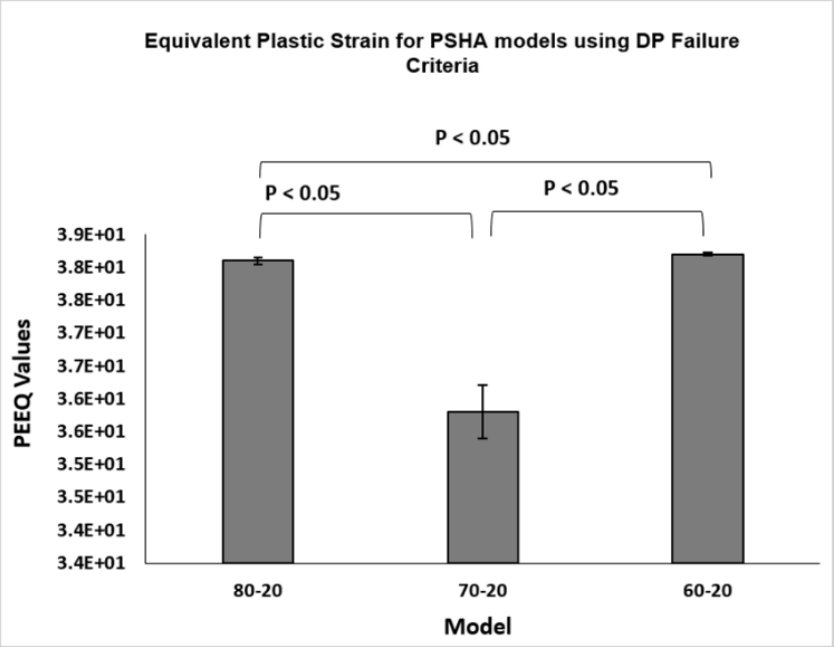

Figure 61: PEEQ values for the PHA models simulated using the DP failure Criteria. All models show values above zero indicating that the models experience failure under compressive conditions.

Figure 61, presents the averaged output equivalent plastic strains for all the models of 20% strut porosity analysed using the DP simulation model. The PEEQ values should be considered in conjunction with the Von Mises stress outputs. The PEEQ values quantify the plastic deformation experienced by the model within the regions effected by the stress fields. The 80-20 models have the thinnest struts and the highest level of porosity. The 60-20 models have the thickest struts and is the least porous material of three simulated. However, the values of PEEQ registered for 80-20 and 60-20 models are both quite high in comparison with the 70-20 models. This suggests that 70-20 models due to their ability to spread the load they experience the least plastic deformation. The 80-20 models due to their thinner structure experience higher deformation as they have less struts. Although the stresses are well distributed the thin structure forces the stress fields to spread from the pore waists to include the struts. The high PEEQ value indicates that the material experiences high deformation due to its week structure (Figure 61).

The highest PEEQ values were registered for the 60-20 models. Their thick structures mean that they have more material loaded. Their inability to spread the load as well as the other materials simulated forced the stress fields to smaller areas of the structure (waists). The high plastic deformation value suggests that the material deforms at higher stresses. This conclusion is supported by the Von Mises stress output values for the material.

Summary:

The contour plots demonstrate the following:

- All models showed stress concentration at the corners of the cylinders. The stresses spread into the structure of the model with the 80-20 showing the most widely distributed stress fields followed by the 70-20 models and finally the 60-20 models with the least level of stress field distribution.
- The stress levels are the lowest for the 80-20 models, followed by the 70-20 then the 60-20 models.
- The stress fields concentrated on the pore waists for all the models as is the case for the linear models in chapter 4. The differences are that the stress fields seem to spread from the corners of the cylinders inwards (Figures 58-60). The 80-20 models showed stress fields spreading to cover the struts, which is not the case for the rest of the models.

The results suggest that the level of total porosity dictates the strength and the ability of PHA materials to withstand compressive strains. As they control the thickness of the struts. The 80% total porosity models appeared to be the weakest of the models, expected to fail at the pore waists as well as the struts at low stresses. The 60% models appeared to be the strongest due to their thick struts, yet the least effective in spreading the load. The results suggest that they would fail at high stresses through the waists.

The 70% models were the most effective in spreading the load. Due to their unique porous structure they are able to withstand high stresses with the least deformation. Their failure is expected to be at high stresses and confined to small locations within the structure. Future research should consider exploring this behaviour further, and the possibility of bone structures behaving in such manner as a function of porosity.

Chapter 6

Discussion and Evaluation of the Models' Validity for Simulation of Stress and Strain Fields distribution in PHA granule masses

6.1 RVE Application

Simulations were constructed on representative volume entities as linear elastic models the following reasons

1- To explore the possibility of developing three-dimensional models for PHA granule masses generated from µ-CT scans in order to simulate their complex geometry.
2- To investigate the distribution of stress and strain fields within three-dimensional PHA models with various combinations of total and strut porosities.
3- To investigate the applicability of representative volume entities as a tool to facilitate the simulations of such complex structures.

It was advantageous in terms of maintaining the authentic architecture of granules to use µ-CT scans capturing the intrinsic structure. ScanIP was used to create orphan meshes for volume rendered models. Orphan free meshes of tetrahedral elements increased the complexity of the simulations, despite additional steps of smoothing and mesh validation. These elements however were the only feasible option available through the commercial software for meshing the structures. The simulated models were able to produce output data that can help understand the behaviour of the material under applied strain and map both the stress and the strain fields within the grafts.

6.1.2 Energy Conservation during Simulations for Different RVE Sizes

For a simulation to be deemed valid; the total energy of the model must be constant throughout the run at zero, or approaching zero for static and quasi static simulations, which was the case for the simulations in this study. ABAQUS provides energy profiles as outputs. The energy profiles for all models under the physiological strain of 5,000 $\mu\varepsilon$ were presented (converted from 50,000 $\mu\varepsilon$). The energy profiles provided by the software demonstrated successful energy conservation throughout the duration of all the simulations. To further test the validity of the simulations; profiles of the energy conversion of external work to strain energy , were presented and the tables of the percentage of conversion can be found in the appendix.

It appears that ABAQUS is more suited for models with more material present, particularly for a model with a very complicated porous structure. This complexity does not decrease with the increase in scale however, there is more meshed material associated with the increase, which may be the reason for the healthier conversion associated with the larger scales. More meshed material allows for less distorted elements per model. Within the shorter RVEs, a large fraction of the elements per model experience sudden changes from material to pore, which is not the case with the larger models. Another argument for using the 12 mm models to present the simulation results.

The high conversions indicate that the all the models can be considered as stable. However, better stability can be achieved through larger RVE sizes, better meshing techniques, a more equipped software, and if possible through picking elements such as hexahedral rather than tetrahedral elements or a hybrid of both.

6.1.3 Variation of Stress and Strain fields in PHA Bone Graft Substitute FE Models

Stress values did always increase linearly in response to the increase in model size. This was found to be due to the instability of the shorter models. Which in turn was related to the thin outer layer added during the volume rendering stage. The outer layer is thus considered a defect that should be avoided in future studies by applying localised boundary conditions, or compensated for its effect by using large RVEs that can overcome it.

Cutting the larger RVEs manually could have created sharp edges that influenced the inconsistencies in the stress outputs. To avoid manual cutting when creating the RVEs, μ-CT scanning can be conducted on individual granules or smaller granule masses. RVEs can be built from stacking the rendered volumes, thus avoiding any disturbance to the structure. The advantage to this approach will be the ability to have detailed borders for the granules, which would allow the application of boundary conditions on the granule boundaries consequently creating more precise finite element models that can simulate the relations of the granules to each other. Factors such as shear and crack propagation can be incorporated with this approach which can help develop a deeper understanding of the material behaviour.

6.1.4 Strain Behaviour and Distribution; Influence of Strut Porosity

Axial strains in general remained stable throughout the simulations. Peak levels of strain increased in response to decreasing the total porosity of the grafts. Higher strains were associated within models of the higher strut porosities, as can be seen with the 80-30 vs 80-20 grafts and the 60-30 vs the 60-20 grafts. The strut porosities effect on the strain energies recorded is also clear (Figures 38-42). With strain Energy recorded for 80-20 models being higher than 80-30, and the strain energy for 60-20 also higher than the 60-30 models.

The link made between the high levels of axial strains recorded for the materials of higher strut porosities could shed the light on the important role of strut porosities in the structures of PHA bone graft substitutes from a mechanical perspective. Strut pores are essential in providing

routes for the transport of signalling molecules, as well as for the nutrition necessary for their biological functions. Higher levels of micro porosity within the struts have been associated with higher levels of cell attachments in biomaterials (Bignon et al., 2003). Studies have linked high levels of strut porosities with increased osteoinductivity particularly at the early grafting stages in-vivo, whilst materials with low strut porosities demonstrate no osteoinduction irrespective of the chemical composition of the material (Chan et al., 2012),(Habibovic et al., 2005).

The results from this thesis provide the mechanical evidence for the previous findings, with PHA bone graft substitutes of higher strut porosities experiencing higher strains than their counter parts of the low strut porosity groups from the same material. These strains can be linked to the mechano-transduction pathways, higher strut porosities cause fields of higher strain levels consequently stimulating the process of osteogenesis (Coathup et al., 2011), (Chan et al., 2012).

6.1.5 Strain Amplification

There is a possible mechanical explanation for the effect of strut porosities that has been overlooked in previous studies, which could be explained by the findings of the finite element analysis results in this research. High strains were found to be associated with higher levels of strut porosities. Strut porosities appeared to act as a route to deliver the strain applied to further and deeper areas within the structure creating strain amplified regions (peaks), this amplification was higher for PHA granules with higher strut porosities. The strain amplification phenomenon was mentioned earlier in chapters 1 and 4. The results from the FE analysis on all models support the phenomenon as seen in chapters 4 and 5.

An example of an amplified strain is the $8.09\ e^{-2}$ registered for the 12 mm model at the 60-30 models (Figure 52). This output strain is equivalent to 8,000 $\mu\varepsilon$ when the strain applied to the model did not exceed 5000 $\mu\varepsilon$. In a study conducted on cortical bone, physiological strains applied at a level of 1500 $\mu\varepsilon$ were amplified near the lacunae to 7,000 $\mu\varepsilon$ and up to 15,000 $\mu\varepsilon$ at some locations (Nicolella *et al.*, 2006). These findings suggest that strain amplification is

due to architecture, which indicates that Porous hydroxyapatite BGSs resemble bone structures in their reaction to applied strain, with the porosity of the BGSs playing the role of the bone lacunae in the bone graft. Amplifications observed in the FE models were restricted to the waists. Their presence can cause micro-cracking in those areas. The micro-cracks can be used by the bone's remodelling system to start a cascade of events as mentioned in the introductory chapter, in an attempt to resolve the issue and generate bone tissue to replace the cracked (damaged) region (Fernández-Tresguerres-Hernández-Gil *et al.*, 2006), (Reilly, 2000).

Micro cracks have been considered as a reinforcement to Hydroxyapatite graft materials, as they have been shown to introduce a shielding mechanisms to the crack vicinity, these regions act to increase the fracture toughness of the bone graft material (Suchanek and Yoshimura, 1998).

These findings can have implications on the application of bone graft substitutes. As strains applied alongside other materials, in addition to physiological factors can indeed determine the reaction of the host cells to the substance. The strain- structure combination of a graft can potentially control the remodelling events that follow as well as the mass and quality of bone tissue generated as a result of those events. It is important to stress that this research suggests that values obtained using typical measurement approaches via strain gauges should not be taken as representatives of the actual local strains experienced by the porous structure.

The local strains are more relevant to cellular environments and thus could possibly be the most important in terms of bone remodelling. Various phenomena that are associated with bone graft substitutes as well as bone tissue could only be understood when the global and local strains are taken into consideration. It is also important to mention that the mode by which the strain is applied can assist in achieving the goals desired in terms of bone tissue generation. High strains can be applied only under low frequency such as the loads induced by exercise on bone tissue and grafts (Nagaraja and Jo, 2014), and as mentioned in chapter

1, lower magnitudes of strain can potentially achieve similar results in bone remodelling if applied at higher frequencies, such as the strains induced by typical muscle contractions which can be as low as 10 $\mu\varepsilon$ (Nagaraja and Jo, 2014) .

The results in this study have shown that strains amplify and concentrate depending on the variation of structure i.e. total porosity and particularly the strut porosity. This means that desired rates of bone remodelling and the quality of the bone formed through the remodelling process can be easily achieved. This can be through applying lower strains at higher frequencies given the involvement of an appropriate structure with predetermined porosity levels and through finite element analysis results as a guide. Desired local strains can be predetermined for desired results.

Prior to the application of strains in-vivo, simulation techniques can be applied to map regions of amplification, leading to a near accurate prediction of regions of bone remodelling. A simulation dictated approach can help avoid any excessive micro-cracking or graft failure during future applications of porous bone graft substitutes.

This brings the discussion to the effect of loading history on the grafts. All the FE models in this study can be considered as virgin models in terms of loading history. The strains applied during the simulations were the only strains experienced by each model conducted on static models. This is not a completely realistic scenario for bone grafts in-vivo. During these applications, there are various forms of strains such as shear and tensile as well as areas carrying residual strains not completely recovered. This is in addition to the possible micro damage caused by previous loads. These residual strains as well as micro damage can individually or collectively be responsible for several changes to the material's mechanical response in-vivo.

These effects were beyond the scope of this study, as the main aim was to model PHA granules as true three-dimensional realistic structures under compression using different constitutive finite element approaches. Thus, taking the loading history into consideration

should be a future prospect for FE analysis. This could be achieved through step simulations where the loading steps start from the point at which the previous loads end. These can be applied as initial boundary conditions (Zhao and Guo, 2014) .

6.1.6 Contribution of Total Porosity to Strain Fields within PHA Granule Masses

As demonstrated, both stresses and strains distribute similarly within PHA structures. Certain regions were more stressed and strained than other areas of the models. These areas were within close proximity to the pores (pore waists). The strain values increased from the 80% to the 70% total porosity models, then increased only slightly from 70% to 60%. Confirming that the architectural features of the models, total porosity, have an effect on the strain levels. It is important to note, that the 70% total porosity group was at a 20% strut porosity only.

The strain energies recorded for the materials do not demonstrate a very clear trend for the effect of total porosities as is the case for the strut porosities. These findings indicate that the porosities are able to control the distribution of strains within the structures of the models. The distribution of stresses as well as strains do not tend to vary in location as a result of porosity variation. They concentrate at the pore waists, which are basically the pore borders. However, stress and strain peaks show noticeable differences in response to porosity variation, particularly strut porosity.

The nodes seem to act like channels guiding the stresses and strains to the waists. The only models where the stress and strain fields were not fully contained at the waists were the 80-20 models. This seemed related to their structure having the thinnest struts and belonging to the group of the highest total porosity level. Their micro porosity levels are the lowest, another consequence of their thin struts.

The micro pores in the struts could be the channels directing stresses and strains through the structure of PHA granules. This conclusion appears plausible as the models of higher micro porosity levels have their stress and strain fields concentrated only at focused regions of the

pore waists, which was not the case for the 80-20 models with the lowest micro porosity levels of all models simulated.

Simulation figures in section 4.5.1 show that the models belonging to the high micro porosity category had the most restricted fields of stresses and strains within their waists, with the 60% total porosity models having their stress and strain fields confined to only a portion of the pore waists. The 70-20 PHA models demonstrate a behaviour that can be considered as superior to their counterparts as their structures seem to distribute the strain applied in a way that maximises its potential as a bone graft substitute and minimises the damage that may be induced by strains applied. Their micro porosity levels lay between the 80% and the 60% groups. High enough to channel the stress and strain fields to the pore waists. The difference between them and the other models is their efficiency in distributing the fields to cover most of the pore waists within the structure, spreading them more evenly. This behaviour can be explained by looking at how a fraction of the strut porosity (micro-porosity) changes with the change as the strut porosity is kept near constant.

Findings from (Hing et al., 2005) conducted on monolithic HA BGS, show that the macro pore structures within the 80-20 groups of HA are about 73% of the total volume. This value falls down to around 65% as the total porosity drops within the 70-20 structure and continues to fall to 48% as the total porosity drops with the 60-20 structure. Table 9 in chapter 4 demonstrates similar results.

These values confirm that the 70-20 porous PHA lays in the middle of other porosities in terms of their micro and macro structures. Which explains their behaviour in terms of strain distribution that is quite intermediate when compared with other groups of the same strut porosities. Thus, it is highly recommended to carry out future investigations on a wider range of grafts of different total and strut porosity combinations in order to establish a clearer understanding of the mechanical trends associated with porosity levels and their categories.

6.1.7 Strain Distribution and Possible Influence on Bone Remodelling

The FE analysis results regarding the influence of porosity levels on strain and strain distribution within the BGS structures can be linked to bone remodelling, In a study conducted on HA cylinders with different strut porosity levels implanted in rabbits (Hing et al., 2004)5, where the bone growth was monitored at different stages of the modelling processes. The study found that bone growth as well as the rate of bone growth favoured PHA structures with higher strut porosity levels. Another study by (Coathup et al., 2011), demonstrates a difference in terms of bone deposition within the structures, preferring the deep macro pores for the low level strut porosity structures and the peripheries of macro pores for the high level strut porosity implants particularly during the earlier stages of implantation.

The (Coathup et al., 2011) study postulated that their findings may possibly be linked to the effect the structure on the mechanical environment particularly as a result of micro porosity. The FE analysis carried out in this research supports the micro porosity theory. The results in chapter 4, demonstrate clearly the effect of varying the level of micro porosity on the level of strain amplification and concentration which can indeed influence the local mechano environments of the graft. The study touched upon the possibility of the micro pores acting as a regulator for nutrition delivery. In this study, another explanation is introduced, suggesting that the micro pores act as regulators for strain distribution along the structures.

The stress and strain field contours at the proximity of the pores (waists) can be linked to the histological findings from a study (Hing et al., 2004), where the results can also offer an explanation regarding the ossification patterns related to each level of strut porosity.

Studies have demonstrated that calcium phosphate based BGSs of high strut porosity levels demonstrate both endochondral (bone growth replacing collagenous tissue) and intramembranous (Direct bone growth) ossifications within a close proximity to each other (Chan et al., 2012), when the expected behaviour is to have a predominantly intramembranous ossification (Elliott et al., 1970),(Yuan et al., 2002). This is different than the pattern of

ossification found in lower strut porosity calcium phosphate-based BGSs, as they demonstrated more of the collagenous structures at the same time frames (Chan et al., 2012). Another study confirms that bone does indeed replace the soft tissue growing centripetally (Coathup et al., 2011) . These findings confirm the preference for using graft substitutes of higher levels of strut porosities. This is due to their great influence on the bioactivity of the material and the level of osteointegration in comparison with their counterparts (Hing, 2005) (Hing et al., 2004),(Chan et al., 2012).

When investigating the strain field distributions throughout the models, the strains tend to vary in a way that could have different effects on cells depending on their location within the structure of the BGS. There are two types of axial strains observed, the first one is a positive tensile strain and the second one is a negative compressive strain. What is quite noticeable in all models that the strain acting in the same direction as the micro-strains applied are mostly located in the centre of the structure. The higher most positive and negative values tend to be located at the pore waists side by side. However, the majority of the strains within the pore waists are compressive (negative). Most of the models' structures experience a positive (tensile) strain, which appears to be a reaction by the struts to the applied compressive strain.

These distributions lead to the highest value of one type strain being surrounded by the highest value of an opposing strain, with the first being the cause for the creation of the second. This could be the method through which strain amplification occurs in porous ceramics. These high values are recognised as amplifications as they tend to be much higher than the strain applied.

Physiological strains experienced by a BGS create an environment of strains opposing each other in a fashion similar to a three-point bending scenario. This scenario can only be credited to the structure's vast distribution of pores both micro and macro. The strains will concentrate at locations at close proximity to the pores amplified through the action-reaction process.

The location of amplified and concentrated strains can be predicted through finite element analysis. It is also safe to conclude that these locations which are usually at the pore

proximities are predominantly located at the waists. These areas as the results suggest are also the regions where micro-cracks can be expected to form. This conclusion is justified through the Von Mises contour results from the Drucker Prager analysis in chapter 5, which show that; the stress levels were consistent with the measured ultimate compressive strengths for the graft structures are located at the pore waists within the models. Where the stress and strain fields were found to concentrate. Future research needs to look into relating the local mechanical environments in BGSs to the bone growth in more detail. It is also beneficial to find if bone tissue experiences and distributes strain in a similar manner to Porous HA structures.

6.2 Future Work

This section will summarise the various future-work related points made throughout the thesis and introduce further directions for future work.

Recommendations for Mechanical Testing

Mechanical tests are better conducted on monolithic specimens, as opposed to granules. This allows for the accurate measurements of values such as the Young's modulus and ultimate compression strength.

For future work if possible. There should be a combination of mechanical tests carried out on monolithic as well as on granular specimens where necessary. This approach can potentially produce output relevant to clinical applications and useful for further finite element analysis.

Recommendation for Creation of RVEs

1- Micro-CT scans can be taken for individual granules from which larger structures can be constructed

2- The software used for volume rendering should allow for the exportation of parts to be meshed by the software of choice, preferably the software used for the simulation. This insures more control on the parts, the elements used and the element density

3- Software used for meshing volume renders should be able to provide a wider variety of elements for meshing purposes as well as hybrids as they can be more useful for complicated structures.

Recommendation for Future Finite Element Analysis

1- Introducing loading history into future finite element analysis of PHA
2- Introducing a larger spectrum of total-strut porosity combinations
3- Employing dynamic analysis through which investigations of study claims regarding bone sensitivity to low strain-high frequency and high strain-low frequency can be investigated
4- In the literature review the influence of shear induced by interstitial fluid within the porous bone and graft structures was discussed. Shear strain is a major factor in bone remodelling, and simulation of its effect on PHA structures as well as the method by which those structures translate and redistribute such strains is very relevant to studying the bio mechanics of BGSs. Thus shear should be explored using an FEA approach.
5- FE simulation of bone tissue alongside simulations of bone graft substitutes under similar mechanical conditions could bring to light the similarities and dissimilarities between the structures. This can consequently lead to a better match making between bone tissue, location and graft substitute.
6- It is highly recommended to link simulation results with in-vivo findings of bone formation in situ. This could help develop a deeper insight into the mechanisms of mechano-transduction, which are yet to be fully understood. As previously discussed mechano-transduction is a major factor in regulating bone growth and remodelling, every step taken towards understanding more about this important method of translating mechanical signals into biological cues, is a step towards optimising bone graft substitutes.

Bibliography

Agamemnon, E., Grigoriadis Johan., N. M. Heersche. (1988) 'Differentiation of Muscle, Fat, Cartilage, and Bone from Progenitor Cells Present in a Bone-derived Clonal Cell Population: Effect of Dexamethasone', Cell Biol, 106, pp. 2139–2151.

Ajubi, N E., E. Klein-Nulend., J. Alblas., M. J. Burger., and E. H. Nijweide. (1999) 'Signal transduction pathways involved in fluid flow-induced PGE2 production by cultured osteocytes', Am J Physiol Endocrinol Metab, 276(1), pp. E171-178.

Alvin, M. Arkin., Jacob, F. Katz. (1956) 'The Effects of Pressure on Epiphyseal Growth: The Mechanism of Plasticity of Growing Bone', The Journal of Bone & Joint Surgery, 38(5), pp. 1056–1076.

Anselme, K. (2000) 'Osteoblast adhesion on biomaterials', Biomaterials, 21(7), pp. 667–681.

Aubin, J.E., Malaval, L. (1995) 'Osteoblast and Chondroblast Differentiation', Bone, 17(2), pp. S77–S83.

Augat, P., Simon Ulrich., Liedert Astrid., Claes Lutz. (2005) 'Mechanics and mechano-biology of fracture healing in normal and osteoporotic bone', Osteoporosis International, 16, pp. 36–43.

Akao M., Aoki H. and Kato K. (1981) 'Mechanical properties of sintered hydroxyapatite for prosthetic applications', Journal of Materials Science, 16(3), pp. 809–812.

Albright J. David., Whalen A. Robert., Blacklow R. Neil. (1974) 'Hydroxyapatite formed from Coral Skeletal Carbonate by Hydrothermal Exchange', Nature, 247, pp. 220–222.

Annaz B., Hing K. A., Kayser M., Buckland T., & Di Silvio L. (2004). Porosity variation in hydroxyapatite and osteoblast morphology: A scanning electron microscopy study. Journal of Microscopy, 215(1), 100–110.

Arita I. H., Wilkinson D. S., Mondragón M. A., Castaño, V. M. (1995). Chemistry and sintering behaviour of thin hydroxyapatite ceramics with controlled porosity. Biomaterials, 16(5), 403–408.

Aoki H. (1989). In Introduction. In Bioceramics. Ed1.Oonishi H,Aoki H, Swai K. Proceedings of the 1st International Bioceramic Symposium.Pub.Ishayaku EuroAmerica,Inc,Tokyo,Japan. (Vol. 1).

Barrère Florence., Van der Valk., Chantal M. Dalmeijer., Remco A. J. Meijer., Gert Van Blitterswijk., Clemens de Groot Klaas., Layrolle Pierre. (2003) 'Osteogenecity of octacalcium phosphate coatings applied on porous metal implants.' Journal of biomedical materials research. Part A, 66(4), pp. 779–788.

Basdra E. K., Papavassiliou A. G., and Huber, L. A. (1995) 'Rab and rho GTPases are involved in specific response of periodontal ligament fibroblasts to mechanical stretching', Biochimica et Biophysica Acta (BBA) - Molecular Cell Research. Elsevier, 1268(2), pp. 209–213.

Bathe K. (2006) Finite Element Procedures Second Edition Bathe Finite Element Procedures Klaus-Jürgen Bathe. Second Edition. Prentice Hall, Pearson Education Inc, pp.148-261.

Best S., M. Porter., A. E. Thian., E. S. Huang. (2008) 'Bioceramics: Past, present and for the future', Journal of the European Ceramic Society, 28(7), pp. 1319–1327.

Benzel C. Edward. (2012) Spine Surgery 2-Vol Set E-Book. 3rd edition. Elsevier.pp.70-73

Bignon A., Chouteau J., Chevalier J., Fantozzi G., Carret, J. Laennec., Âdecine R., Paradin Guillaume. (2003) 'Effect of micro- and macroporosity of bone substitutes on their mechanical properties and cellular response', 4, pp. 1089–1097.

Bohner M. (2000) ‘Calcium orthophosphates in medicine: From ceramics to calcium phosphate cements’, Injury (31), pp.37-47.

Boyce T., Edwards J., and Scarborough N. (1999) ‘Allograft Bone: The Influence of Processing on Safety and Performance’, Orthopedic Clinics of North America, 30(4), pp. 571–581.

Boyde A., Corsi A., Quarto, R., R. Cancedda., P. Bianco. (1999) ‘Osteoconduction in large macroporous hydroxyapatite ceramic implants: Evidence for a complementary integration and disintegration mechanism’, Bone, 24(6), pp. 579–589.

Brand, R. and Claes, L. (1988) ‘Book Review’, Journal of Biomechanics, 22(2), pp. 185–187

Burchardt, H. (1983) ‘The Biology of Bone-Graft Repair’, Clinical Orthopaedics and Related Research, pp. 28–42.

Blacker, T. (2001) ‘Automated conformal hexahedral meshing constraints, challenges and opportunities’, Engineering with Computers, 17(3), pp. 201–210.

Campana, V., Milano, G., Pagano, E., .Barba, M., Cicione., C. Salonna., G. Lattanzi., W. Logroscino. (2014) ‘Bone substitutes in orthopaedic surgery: from basic science to clinical practice’, Journal of Materials Science: Materials in Medicine, 25(10), pp. 2445–2461.

Carlisle, E. M. (1972) ‘Silicon: An essential element for the chick’, Science, 178(4061), pp. 619–621.

Carlisle, E. M. (1980) ‘Biochemical and morphological changes associated with long bones abnormalities in silicon deficiency’, Journal of Nutrition, 110(5), pp. 1046–56.

Chai, Yoki. Chin, Roberts., Scott J., Schrooten, Jan., Luyten, Frank P. (2011) ‘Probing the Osteoinductive Effect of Calcium Phosphate by Using an In Vitro Biomimetic Model’, Tissue Engineering Part A, 17(7–8), pp. 1083–1097.

Chakkalakal, Dennis. A. (1989) ‘Mechanoelectric transduction in bone’, Journal of Materials Research, 4(4), pp. 1034–1046.

Chambers, T J., Evans, M., Gardner, T N., Turner-Smith, A.,Chow, J W (1993) ‘Induction of bone formation in rat tail vertebrae by mechanical loading.’, Bone and mineral, 20(2), pp. 167–78.

Chan, O., Coathup, M. J., Nesbitt, A., Ho, C. Y., Hing, K. A., Buckland, T., Campion, C., Blunn, G. W. (2012) ‘The effects of microporosity on osteoinduction of calcium phosphate bone graft substitute biomaterials’, Acta Biomaterialia, 8(7), pp. 2788–2794.

Coathup, Melanie J., Samizadeh, Sorousheh., Fang, Yvette S., Buckland, Thomas., Hing, Karin A., Blunn, Gordon W., (2011) ‘The osteoinductivity of silicate-substituted calcium phosphate’, Journal of Bone and Joint Surgery - Series A, 93(23), pp. 2219–2226.

Coathup, Melanie Jean., Blunn, Gordon William., Campion, Charlie., Ho, Chih Yuan., Hing, Karin., Angela. (2012) ‘Effect of increased strut porosity of calcium phosphate bone braft substitute biomaterials on osteoinduction’, Journal of Biomedical Materials Research - Part A, 100 A(6), pp. 1550–1555.

Charrière, E., Lemaitre, J. and Zysset, P. (2003) ‘Hydroxyapatite cement scaffolds with controlled macroporosity: fabrication protocol and mechanical properties’, Biomaterials. Elsevier, 24(5), pp. 809–817.

Charriere, E., Terrazon, S., Pittet, C., Mordasini, P., Dutoit, M., J.Lemaitre. (2001). Using Optimal Control Design Techniques. System, 22(1), 2937–2945.

Chen, Jan Hung., Liu, Chao., You, Lidan., Simmons, Craig A. (2010) 'Boning up on Wolff's Law: Mechanical regulation of the cells that make and maintain bone', Journal of Biomechanics. Elsevier, 43(1), pp. 108–118.

Cho, Dong-Woo., Kang, Hyun-Wook.,Ahn, Geunseon., Kang, Taeyun., Lee, Jin Woo., Park, Jeong Hun. (2010) 'Effect of Pore Architecture on Oxygen Diffusion in 3D Scaffolds for Tissue Engineering', Journal of Biomechanical Engineering, 132(10), p. 104506-1 -104506-5

Chong, D. S.T., Turner, L. A., Gadegaard, N., Seifalian, A. M., Dalby, M. J., Hamilton, G. (2015) 'Nanotopography and plasma treatment: Redesigning the surface for vascular graft endothelialisation', European Journal of Vascular and Endovascular Surgery. Elsevier Ltd, 49(3), pp. 335–343.

Cillo, Joseph E., Gassner, Robert., Koepsel, Richard R., Buckley, Michael J. (2000) 'Growth factor and cytokine gene expression in mechanically strained human osteoblast-like cells: Implications for distraction osteogenesis', Oral Surgery, Oral Medicine, Oral Pathology, Oral Radiology, and Endodontics, 90(2), pp. 147–154.

Claes, Lutz., Reusch, Martina., Göckelmann, Melanie., Ohnmacht, Michael., Wehner, Tim Amling., Michael, Beil., Frank T., Ignatius, Anita. (2011) 'Metaphyseal fracture healing follows similar biomechanical rules as diaphyseal healing', Journal of Orthopaedic Research, 29(3), pp. 425–432.

Clarke, B. (2008) 'Normal bone anatomy and physiology.' Clinical journal of the American Society of Nephrology : CJASN, 3 Suppl 3, pp. 131–139.

Coathup, Melanie J., Samizadeh, Sorousheh., Fang, Yvette S., Buckland, Thomas., Hing, Karin A., Blunn, Gordon W. (2011) 'The osteoinductivity of silicate-substituted calcium phosphate', Journal of Bone and Joint Surgery - Series A, 93(23), pp. 2219–2226.

Coathup, Melanie J., Hing, Karin A., Samizadeh, Sorousheh., Chan, Oliver., Fang, Yvette S., Campion, Charlie., Buckland, Thomas., Blunn, Gordon W. (2012) 'Effect of increased strut porosity of calcium phosphate bone graft substitute biomaterials on osteoinduction', Journal of Biomedical Materials Research - Part A, 100 A(6), pp. 1550–1555.

Currey, J. D. (2003) 'The many adaptations of bone', Journal of Biomechanics. Elsevier, 36(10), pp. 1487–1495.

Currey, J. D. (1962) 'Stress concentrations in bone', Quarterly journal of microscopical science, 103(1), pp. 111– 133.

Cypher, T. J. and Grossman, J. P. (1996) 'Biological principles of bone graft healing', Journal of Foot and Ankle Surgery. American College of Foot and Ankle Surgeons, 35(5), pp. 413–417.

Charlie Campion, K. A. Hing (2017) 'Porous Bone Graft Substitutes: When Less is More', in Simon Rawlinson (Ed 2) Mechanobiology: Exploitation for Medical Benefit. First Edit. John Wiley & Sons, Inc, pp. 357–358.

Croquelois, B. Girardot., J. Kopp., J. B. Tchoreloff., P. V. Mazel. (2017) 'Re-evaluation of the diametral compression test as a rupture test for pharmaceutical tablet: insertion of flat ends and defects of controlled size', Vol 23, pp. 23–44.

Dalby, M J., Di Silvio, L., Davies, G W., Bonfield, W. (2000) 'Surface topography and HA filler volume effect on primary human osteoblasts in vitro', Journal of Materials Science-Materials in Medicine, 11(12), pp. 805–810.

Dassault Systèmes (2014) 'Abaqus, Simulia'. ABAQUS Inc

Dorozhkin, S. V. (2015) 'Calcium Orthophosphate-Containing Biocomposites and Hybrid Biomaterials for Biomedical Applications', pp. 708–832.

Doty, S. B. (1981) 'Morphological evidence of gap junctions between bone cells.' Calcified tissue international, 33(5), pp. 509–512.

Drugan, W. J. and Willis, J. R. (1996) 'A micromechanics-based nonlocal constitutive equation and estimates of representative volume element size for elastic composites', Journal of the Mechanics and Physics of Solids. Pergamon, 44(4), pp. 497–524.

Duncan, R. L. and Turner, C. H. (1995) 'Mechanotransduction and the Functional Response of Bone to Mechanical Strain', Calcif Tissue Int, 57, pp. 344–358.

Drucker, D. C. and Prager, W. (1952) 'soil mechanics and plastic analysis or limit design', Quarterly of Applied Mathematics. Brown University, 10(2), pp. 157–165.

DiMaggio, F.L. (1971) 'Material Model for Granular Soils', *Journal of the Engineering Mechanics Division*, 97(3), pp. 935–950.

De Jong, W. F. (1926) 'La Substance Minérale Dans les Os', Recueil des travaux chimiques des Pays-Bas (1920), 45(6), pp. 445–448.

Eggli, P. S., Muller, W. and Schenk, R. K. (1988) 'Porous hydroxyapatite and tricalcium phosphate cylinders with two different pore size ranges implanted in the cancellous bone of rabbits. A comparative histomorphometric and histologic study of bony ingrowth and implant substitution', Journal of Clinical Orthopaedics and Related Research, (232), pp. 127–138.

Elliott, President H., T.D. Blake., T. Scales., Hill, Brockley. (1970) 'Factors Influencing Prosthetic Heterotopic Bone Formation in a', 63(November), pp. 1111–1115.

Evis, Z., and Ozturk, F. (2008). Investigation of tensile strength of hydroxyapatite with various porosities by diametral strength test. Materials Science and Technology, 24(4), 474–478.

Fernández-Tresguerres-Hernández-Gil, Isabel. Alobera-Gracia., Miguel Angel., Del-Canto-Pingarrón, Mariano., Blanco-Jerez, Luis. (2006) 'Physiological bases of bone regeneration I. Histology and physiology of bone tissue.', Medicina oral, patología oral y cirugía bucal, 11(1), pp. 47–51.

Florencio-Silva, Rinaldo., Sasso, Gisela Rodrigues Da Silva., Sasso-Cerri, Estela Simões., Manuel Jesus. Cerri, Paulo Sérgio. (2015) 'Biology of Bone Tissue: Structure, Function, and Factors That Influence Bone Cells', BioMed Research International, p. 17.

Franz-Odendaal, T. A., Hall, B. K. and Witten, P. E. (2006) 'Buried alive: How osteoblasts become osteocytes', Developmental Dynamics, 235(1), pp. 176–190.

Friedenstein A, K. A. (1971) 'Osteogenic precursor cells of bone marrow in radiation chimeras', Transplantaion, 12(2), pp. 99–108.

Fritsch, Andreas., Dormieux, Luc., Hellmich, Christian., Sanahuja, Julien. (2007) 'Micromechanics of crystal interfaces in polycrystalline solid phases of porous media: Fundamentals and application to strength of hydroxyapatite biomaterials', Journal of Materials Science, 42(21), pp. 8824–8837.

Fritsch, A., Dormieux, L., Hellmich, C., & Sanahuja, J. (2009). Mechanical behavior of hydroxyapatite biomaterials: An experimentally validated micromechanical model for elasticity and strength. Journal of Biomedical Materials Research - Part A, 88(1), 149–161.

Fritsch, A. (2009) Multiscale Explanation of Elasticity and Strength of Bone and Bone Replacement Materials Made of Hydroxyapatite, Glass-Ceramics, or Titanium: a Continuum Micromechanics Approach, Continuum. Thesis. pp.191.

Frost, H. M. (1987) 'Bone "mass" and the "mechanostat": A proposal', The Anatomical Record, 219(1), pp. 1–9.

Fukumoto, S. and Martin, T. J. (2009) 'Bone as an endocrine organ', Trends in Endocrinology & Metabolism. Elsevier Current Trends, 20(5), pp. 230–236.

Gallegos-Nieto, E., Medellín-Castillo, H. I. and de Lange, D. F. (2015) 'A complete structural performance analysis and modelling of hydroxyapatite scaffolds with variable porosity', Computer Methods in Biomechanics and Biomedical Engineering. Taylor & Francis, pp. 1225–1237.

Gasser, J. A. and Kneissel, M. (2017) 'Bone Physiology and Biology', in Bone Toxicology. Springer, pp. 27–93.

Gibson, I. R., Best, S. M. and Bonfield, W. (1999) 'Chemical characterization of silicon-substituted hydroxyapatite', J. Biomed. Mater, 44, pp. 422–428.

Genetos. Damian., Geist. Derik., Dawei Liu., Donahue., Henry, and L. Duncan. Randall.(2005) 'Fluid Shear-Induced ATP Secretion Mediates Prostaglandin Release in MC3T3-E1 Osteoblasts', JOURNAL OF BONE AND MINERAL RESEARCH, 20(1).

Gibson, L. J. (2005) 'Biomechanics of cellular solids', Journal of Biomechanics, 38(3), pp. 377–399.

Gil. Albarova., Jorge.Salinas., Antonio. J., Bueno, Lozano., Antonio L., Román, Jesus., Aldini-Nicolo Nicolo., García Barea., Agustina Giavaresi., Gianluca Fini., Giardino Milena., Roberto Vallet-Regí Maria. (2005) 'The in vivo behaviour of a sol-gel glass and a glass-ceramic during critical diaphyseal bone defects healing', Biomaterials, 26(21), pp. 4374–4382.

Glazer, Paul A., Spencer, Upshur M., Alkalay, Ron. N., Alkalay, Ron. N., Schwardt, Jeffrey. (2001) 'In vivo evaluation of calcium sulfate as a bone graft substitute for lumbar spinal fusion', The Spine Journal, 1(6), pp. 395–401.

Glimcher. C., ReyC. CombesC., DrouetM.J. (2010) 'Bone mineral: update on chemical composition and structure', Osteoporos Int, 20(June 2008), pp. 1013–1021.

Guo-Dong Zhan., Joshua D. Kuntz., Julin Wan., and A. K. M. (2007) 'Plasticity in Nano Materials', Mat.Res.Soc.Symp.Proc, 740,pp. 41-48.

Habibovic, Pamela., Yuan, Huipin., Van Der Valk, Chantal M., Meijer, Gert Van Blitterswijk., Clemens A., De Groot, Klaas. (2005) '3D microenvironment as essential element for osteoinduction by biomaterials', Biomaterials, 26(17), pp. 3565–3575.

Hage, I. S. and Hamade, R. F. (2012) 'Structural micro processing of haversian systems of a cortical bovine femur using optical stereomicroscope and matlab', ASME International Mechanical Engineering Congress and Exposition, Proceedings (IMECE), 2, pp. 595–601.

Han, L. H., Elliott, J. A., Bentham, A. C., Mills, A., Amidon, G. E., Hancock, B. C. (2008) 'A modified Drucker-Prager Cap model for die compaction simulation of pharmaceutical powders', International Journal of Solids and Structures, 45(10), pp. 3088–3106.

Hakim, T S., Sugimori, K., Camporesi, E M., Anderson, G (1996) 'Half-life of nitric oxide in aqueous solutions with and without haemoglobin', Physiological Measurement, 17, pp. 267–277.

Hannink, G. and Arts, J. J. C. (2011) 'Bioresorbability, porosity and mechanical strength of bone substitutes: What is optimal for bone regeneration', *Injury*. Elsevier Ltd, 42(SUPPL. 2), pp. S22–S25.

Harden, F. J., Gibson, I. R. and Skakle, J. M. S. (2013) 'Simplification of the synthesis method for silicon-substituted hydroxyapatite: A raman spectroscopy study', Key Engineering Materials, 529–530(1), pp. 94–99.

Hashin, Z. (1983) 'Analysis of composite materials', J. appl. Mech, 50(2), pp. 481–505.

Hayes, W. C. (2016) ‘A 20-Year Perspective on the Mechanical Properties of Trabecular Bone’, 115(November 1993), pp. 534-542.

Hench, L. L. (1991) ‘Bioceramics : From Concept to Clinic’, J.Am.Ceram.Soc, 74(7), pp. 1487–1510.

Hench, L. L. and Paschall, H. A. (1973) ‘Direct chemical bond of bioactive glass-ceramic materials to bone and muscle’, Journal of Biomedical Materials Research, 7(3), pp. 25–42.

Hench, L. L. and West. J. K. (1996) ‘Biological Applications of Bioactive Glasses’, Life Chemistry Reports, 13(3), pp. 187–241.

Hench, L. L., Splinter, R. J., Allen. W. C., Greenlee. T. K. (1971) ‘Bonding mechanisms at the interface of ceramic prosthetic materials’, Journal of Biomedical Materials Research, 5(6), pp. 117–141.

Hill, R. (1963) ‘Elastic properties of reinforced solids: Some theoretical principles’, Journal of the Mechanics and Physics of Solids, 11(5), pp. 357–372.

Hill, R. (1972) ‘On Constitutive Macro-Variables for Heterogeneous Solids at Finite Strain’, Proceedings of the Royal Society A: Mathematical, Physical and Engineering Sciences, 326(1565), pp. 131–147.

Hillsley, M. V and Frangos, J. A. (1994) ‘Bone tissue engineering: the role of interstitial fluid flow.’ Biotechnology and bioengineering, 43(7), pp. 573–81.

Hing, Karin A., Best, Serena M., Tanner, K Elizabeth., Bonfield, William., Revell, Peter A (2002) ‘Mediation of bone ingrowth in porous hydroxyapatite bone graft substitutes’, J Biomed Mater Res A. 2004 Jan 1;68(1), pp.187-200.

Hing, K. A. (2004) ‘Bone repair in the twenty-first century: biology, chemistry or engineering?’, Philosophical Transactions of the Royal Society A: Mathematical, Physical and Engineering Sciences, 362(1825), pp. 2821– 2850.

Hing, K A., Saeed, S., Annaz, B., Buckland, T., Revell, P A. (2004) ‘Microporosity Affects Bioactivity of Macroporous Hydroxyapatite Bone Graft Substitutes’, pp. 273–276.

Hing, K. A. (2005a) ‘Bioceramic bone graft substitutes: Influence of porosity and chemistry’, International Journal of Applied Ceramic Technology, 2(3), pp. 184–199.

Hing, K. A., Annaz, B., Saeed, S., Revell, PA., Buckland, T. (2005) ‘Microporosity enhances bioactivity of synthetic bone graft substitutes’, Journal of Materials Science: Materials in Medicine, 16(5), pp. 467–475.

Hing, K. A., Wilson, L. F. and Buckland, T. (2007) ‘Comparative performance of three ceramic bone graft substitutes.’ The spine journal : official journal of the North American Spine Society. Elsevier, 7(4), pp. 475–90.

Hing, K. A., Annaz, B., Saeed, S., Revell, PA., Buckland, T. (1998) ‘Histomorphological and biomechanical characterization of calcium phosphates in the osseous environment’, Proceedings of the Institution of Mechanical Engineers. Part H, Journal of engineering in medicine, 212(6), pp. 437–451.

Hing, K., Best, S. and Bonfield, W. (1999) ‘Characterization of Porous Hydroxyapatite’, Journal of materials science. Materials in medicine, 10, pp. 135–145.

Hollister, S. J., Maddox, R. D. and Taboas, J. M. (2002) ‘Optimal design and fabrication of scaffolds to mimic tissue properties and satisfy biological constraints’, 23, pp. 4095–4103.

Holmes, R. E. (1979) ‘Bone regeneration within a coralline hydroxyapatite implant’, Plastic Reconstruction Surg, 63(5), pp. 626–633.

Hughes, J. M. (1996) 'Structure and Chemistry of the Apatites and Other Calcium Orthophosphates By J. C. Elliot (The London Hospital Medical College). Elsevier: Amsterdam. Journal of the American Chemical Society, 118(12), pp. 3072–3072.

Hughes-Fulford, M. (2004) 'Signal Transduction and Mechanical Stress', Science Signaling, 2004(249), pp. re12- re12.

Hulbert, S. F., Morrison, S. J. and Klawitter, J. J. (1972) 'Tissue reaction to three ceramics of porous and non- porous structures', Journal of Biomedical Materials Research, 6(5), pp. 347–374.

Innocentini, M. D. M., Faleiros, R. K., Pisani, R., Thijs, I., Luyten, J., Mullens, S. (2010) 'Permeability of porous gelcast scaffolds for bone tissue engineering', Journal of Porous Materials, 17(5), pp. 615–627.

Gibson, L., & Ashby, M. (1998). Cellular Solids: Structure and Properties (Cambridge Solid State Science Series). Cambridge: Cambridge University Press.

Jin, Q M., Takita, H., Kohgo, T., Atsumi, K., Itoh, H., Kuboki, Y. (2000) 'Effects of geometry of Hydroxyapatite as a cell substratum in BMP-induced ectopic bone formation', Journal of biomedical materials research, 51(3), pp. 491–9.

Jonck, L. M., Grobbelaar, C. J. and Strating, H. (1989) 'Biological evaluation of glass-ionomer cement (Ketac-O) as an interface material in total joint replacement. A screening test', Clinical materials, 4, pp. 201–224.

Judex, S., Gross, T. S. and Zernicke, R. F. (1997) 'Strain gradients correlate with sites of exercise-induced boneforming surfaces in the adult skeleton', Journal of Bone and Mineral Research, 12(10), pp. 1737–1745.

Karlsson, M., Pålsgård, E., Wilshaw, P. R., Di Silvio, L. (2003) 'Initial in vitro interaction of osteoblasts with nano-porous alumina', Biomaterials, 24(18), pp. 3039–3046.

Kaito, Takashi., Myoui, Akira., Takaoka, Kunio., Saito, Naoto., Nishikawa., Masataka., Tamai, Noriyuki., Ohgushi, Hajime., Yoshikawa, Hideki. (2005) 'Potentiation of the activity of bone morphogenetic protein-2 in bone regeneration by a PLA–PEG/hydroxyapatite composite', Biomaterials. Elsevier, 26(1), pp. 73–79.

Katz, J. L., Akers, A. S., Germiller, J. A., O'Bermski, S. M., S. S. (1989). The elastic properties of apatites and TCP-calcite mixtures. Proc of First International Symposium on Bioceramics, 86–89.

Kalantarian, Behrooz., Nagy, Paul G., Wilson, Charles R., Toth, Jeffrey M., Mcintyre, Brian L. (2005) 'Experimental A 1-Year Study of Hydroxyapatite-Derived Biomaterials in an Adult Sheep Model : III . Comparison with Autogenous Bone Graft for Facial Augmentation', pp. 1044–1052.

Kalita, Samar Jyoti., Bose, Susmita., Hosick, Howard L., Bandyopadhyay, Amit. (2003) 'Development of controlled porosity polymer-ceramic composite scaffolds via fused deposition modeling', Materials Science and Engineering C. Elsevier, 23(5), pp. 611–620.

Kelly, Cynthia M., Wilkins, Ross M., Gitelis, Steven., Hartjen, Charles., Watson, J Tracy. (2001) 'The Use of a Surgical Grade Calcium Sulfate as a Bone Graft Substitute', clinical orthopaedics and related research (382), pp. 42–50.

Kilpadi, Krista L., Sawyer, Amber A., Prince, Charles W., Chang, Pi-Ling., Bellis, Susan L. (2004) 'Primary human marrow stromal cells and Saos-2 osteosarcoma cells use different mechanisms to adhere to hydroxylapatite.', J. Biomed. Mater. Res. A, 68(2), pp. 273–285.

Komlev, V. S. and Barinov, S. M. (2002) 'Porous hydroxyapatite ceramics of bi-modal pore size distribution', Journal of Materials Science: Materials in Medicine, 13(3), pp. 295–299.

Kokubo, T. (1991) ‘Bioactive glass ceramics: properties and applications’, Biomaterials, 12(2), pp. 155–163.

Kumar, G. and Narayan, B. (2014) ‘The biology of fracture healing in long bones’, Classic Papers in Orthopaedics, pp. 531–533.

Klawitter. J. J., Hulbert .S. F. (1971) ‘Application of Porous Ceramics for the Attachment of Load Bearing Internal Orthopedic Applications’, Journal of Biomedical Materials Research, 2(1), pp. 161–229.

Klein-Nulend, J., Bacabac, R. G., & Bakker, A. D. (2012). Mechanical loading and how it affects bone cells: The role of the osteocyte cytoskeleton in maintaining our skeleton. European Cells and Materials, 24, 278–291.

Laurencin, C. T. (2008) ‘Xenotransplantation in Orthopaedic Surgery’, Journal of AAOS, 16(1), pp. 4–8.

Lanyon, L. E., Hampson, W. G. J., Goodship, A. E., & Shah, J. S. (1975). Bone deformation recorded in vivo from strain gauges attached to the human tibial shaft. Acta Orthopaedica, 46(2), 256–268.

Li, Jiliang., Duncan, Randall L., Burr, David B., Turner, Charles H (2002) ‘L-Type Calcium Channels Mediate Mechanically Induced Bone Formation In Vivo’, 17(10), pp. 1795–1800.

Li, D., & Wong, L. N. Y. (2013). The brazilian disc test for rock mechanics applications: Review and new insights. Rock Mechanics and Rock Engineering, 46(2), 269–287.

Liedert, Astrid., Kaspar, Daniela., Blakytny, Robert., Claes, Lutz., Ignatius, Anita. (2006) ‘Signal transduction pathways involved in mechanotransduction in bone cells’, Biochemical and Biophysical Research Communications, 349(1), pp. 1–5.

Liljensten, Elisabeth., Adolfsson, Erik., Strid, Karl Gustav., Thomsen, Peter. (2003).Resorbable and nonresorbable hydroxyapatite granules as bone graft substitutes in rabbit cortical defects’, Clinical Implant Dentistry and Related Research, 5(2), pp. 95–102.

Ling, R. S. M., Timperley., A. J. and Linder, L. (1993) ‘Histology of cancellous impaction grafting in the femur’, The Journal of Bone and Joint Surgery, 75(5), pp. 693–696.

Liu, Chao, Z., Yan, C., Wing-Yee, Gandhi, Ronak Wang Liyun and You, L. (2012) ‘Effects of Cyclic Hydraulic Pressure on Osteocytes’, 46(5), pp. 1449–1456.

Maeyer, E. A. P. De and Verbeeck, R. M. H. (1993) ‘POSSIBLE SUBSTITUTION MECHANISMS FOR SODIUM AND CARBONATE IN CALCl U MHYDROXYAPATITE’, (1993). Cornit6 van Beheer van het Bulletin, pp. 601–609.

Martin, R. I. and Brown, P. W. (1995) ‘Mechanical properties of hydroxyapatite formed at physiological temperature’, Journal of Materials Science: Materials in Medicine, 6(3), pp. 138–143.

Mancini, L., Moradi-Bidhendi, N.,Becherini, L., Martineti, V., MacIntyre, I. (2000) ‘The Biphasic Effects of Nitric Oxide in Primary Rat Osteoblasts Are cGMP Dependent’, Biochemical and Biophysical Research Communications. Academic Press, 274(2), pp. 477–481.

Mandel Jean (1971) ‘Plasticit´e Classique et Viscoplasticit´e’, in course held at the Department of Mechanics of Solids. Springer-Verlag, pp. 100–120.

Marcellini, S., Henriquez, J. P. and Bertin, A. (2012) ‘Control of osteogenesis by the canonical Wnt and BMP pathways in vivo: Cooperation and antagonism between the canonical Wnt and BMP pathways as cells differentiate from osteochondroprogenitors to osteoblasts and osteocytes’, BioEssays, 34(11), pp. 953–962.

Marupanthorn,Kulisara.,Tantrawatpan,Chairat.,Kheolamai,Pakpoom.,Tantikanlayaporn, Duangrat., Manochantr, Sirikul. (2017) 'Bone morphogenetic protein-2 enhances the osteogenic differentiation capacity of mesenchymal stromal cells derived from human bone marrow and umbilical cord', International Journal of Molecular Medicine, 39(3), pp. 654–662.

Mattei, Giorgio., Ferretti, Concetta., Tirella, Annalisa., Ahluwalia, Arti., Mattioli-Belmonte, Monica. (2015) 'Decoupling the role of stiffness from other hydroxyapatite signalling cues in periosteal derived stem cell differentiation', Scientific Reports. Nature Publishing Group, 5(October 2014), pp. 1–14.

Mattila, Pieta K. and Lappalainen, Pekka. (2008) 'Filopodia: molecular architecture and cellular functions', Nature Reviews Molecular Cell Biology. Nature Publishing Group, 9, p. 446.

Mauney, J. R.,Sjostorm, S., Blumberg, J., Horan, R., O'Leary, J. P., Vunjak-Novakovic, G., Volloch, V.,Kaplan, D. L. (2004) 'Mechanical Stimulation Promotes Osteogenic Differentiation of Human Bone Marrow Stromal Cells on 3-D Partially Demineralized Bone Scaffolds in Vitro', Calcified Tissue International, 74(5), pp. 458–468.

Mckibbin, B. (1978) 'The biology of fracture healing in long bone', The Journal of Bone and Joint Surgery, 60-(B) 2, pp. 62–150.

Medsker, Brock., Forno, Erick., Simhan, Hyagriv., Juan, C. (2016) 'Physical and mechanical regulation of macrophage phenotype and function', Cell Mol Life Sci, 70(12), pp. 773–779.

Meeder, P. and Eggers, C.H. (1994), 'The history of autogenous bone grafting', Injury ,Volume 25, Supplement 1, Pages SA2–SA4.

Mikuni-Takagaki, Y. (1999) 'Mechanical responses and signal transduction pathways in stretched osteocytes', Journal of Bone and Mineral Metabolism, 17(1), pp. 57–60.

Moore, W. R., Graves, S. E. and Bain, G. I. (2001) 'Synthetic bone graft substitutes', ANZ Journal of Surgery, 71(6), pp. 354–361.

Mosekilde, L., Ebbesen, E. N., Tornvig, L., Thomsen, J. S. (2000) 'Trabecular bone structure and strength - remodelling and repair', *J Musculoskelet Neuronal Interact*, 1(1), pp. 25–30.

Mukul, Mohindra and Jitesh, Kumar Jain. (2017). Fundamentals of Orthopedics. 2nd Ed, New Delhi, India: Jaypee Brothers,Medical Publishers Pvt Ltd, pp. 9-21.

Mow, Van., Wilson, C. Hayes. (1991) Basic Orthopaedic Biomechanics. Philadelphia, United States: Raven Press. (1st Ed), pp. 93-142.

Murray, D. W. and Rushton, N. (1990) 'The effect of strain on bone cell prostaglandin E2 release: A new experimental method', Calcified Tissue International, 47(1), pp. 35–39.

Meille, S., Lombardi, M., Chevalier, J., & Montanaro, L. (2012). Mechanical properties of porous ceramics in compression: On the transition between elastic, brittle, and cellular behavior. Journal of the European Ceramic Society, 32(15), 3959–3967.

Mellor, M., Hawkes, I. (1971). Engineering geology -elsevier publishing company, Amsterdam -printed in the Netherlands measurement of tensile strength by diametral compression of discs and annuli, 5, 173–225.

Mishra, R. S., Mukherjee, A. K. (2000). An analysis of the role of grain size on superplasticity of gamma-titanium aluminides. Journal of Materials Science, 35, 147–151.

Moncrieff, D. A., & Barker, P. R. (1978). Secondary electron emission in the scanning electron microscope. Scanning, 1(3), 195–197.

Nagaraja, M. and Jo, H. (2014) 'The Role of Mechanical Stimulation in Recovery of Bone Loss—High versus Low Magnitude and Frequency of Force', Life, 4(2), pp. 117–130.

Nakamura, Hiroaki., Kenmotsu, Shin-ichi., Sakai, Hideo., Ozawa, Hidehiro. (1995) 'Localization of CD44, the hyaluronate receptor, on the plasma membrane of osteocytes and osteoclasts in rat tibiae', Cell and tissue research, 280, pp. 225–233.

Nakamura, Miho., Nagai, Akiko., Tanaka, Yumi., Sekijima, Yasutaka., Yamashita, Kimihiro. (2009) 'Polarized hydroxyapatite promotes spread and motility of osteoblastic cells', pp. 2–3.

Noonan, K. J., Stevens, J. W., Tammi, R. (1997) 'Spatial Distribution of Cd44 and Hyaluronan in the Proximal Tibia of the Growing Rat', Journal of Pediatric Orthopaedics, 17(2), p. 273.

Nicolella, Daniel P., Moravits, Donald E., Gale, Adrian M., Bonewald, Lynda F., Lankford, James (2006) 'Osteocyte lacunae tissue strain in cortical bone', Journal of Biomechanics, 39(9), pp. 1735–1743.

O'Connor, J. A., Lanyon, L. E. and MacFie, H. (1982) 'The influence of strain rate on adaptive bone remodelling', Journal of Biomechanics, 15(10), pp. 767–781.

Ogino, M. and Hench, L. L. (1980) 'Formation of Calcium Phosphate Filmes on Silicate Glasses', Journal of NonCrystalline Solids, 38–39(i), pp. 673–678.

Oppenheimer, A. J., Tong, L. and Buchman, S. R. (2008) 'Craniofacial Bone Grafting : Wolff's Law Revisited', Craniomaxillofacial trauma & reconstruction, 1(1), pp. 49–61.

Orlovskii, V. P., Komlev, V. S. and Barinov, S. M. (2002) 'Hydroxyapatite and hydroxyapatite-based ceramics', Inorganic Materials, 38(10), pp. 973–984.

Ozturk, F., Evis, Z. and Toros, S. (2010) 'Finite element simulation of diametral strength test of hydroxyapatite', AIP Conference Proceedings, 1315, pp. 259–264

Ozcivici, E., Luu, Y. K., Rubin, C. T., & Judex, S. (2010). Low-Level vibrations retain bone marrow's osteogenic potential and augment recovery of trabecular bone during reambulation. PLoS ONE, 5(6).

Padilla, S.,Román, J., Carenas, A., Vallet-Regí, M. (2005) 'The influence of the phosphorus content on the bioactivity of sol-gel glass ceramics', Biomaterials, 26(5), pp. 475–483.

Padmanabhan, T., Swarup, S. and Paul, S. (2013) 'Comparison of strain generated in bone by "platform-switched" and "non-platform-switched" implants with straight and angulated abutments under vertical and angulated load: A finite element analysis study', Indian Journal of Dental Research, 24(1), p. 8.

Palmero, P., Lombardi, M., Montanaro, L., Tirillò, J., Bartuli, C., Valente, T., Marcassoli, P.,

Cabrini, M., (2009) 'Development and mechanical characterization of hydroxyapatite micro/macro-porous scaffolds by an innovative gel-casting process', *11th International Conference and Exhibition of the European Ceramic Society 2009*, 1, pp. 448–455.

Pantano, C. G., Clark, A. E. and Hench, L. L. (1974) 'Multilayer Corrosion Films on Bioglass Surfaces', Journal of the American Ceramic Society, 57(9), pp. 412–413.

Papachroni, Katerina K.,Karatzas, Demetrios N.,Papavassiliou, Kostas A., Basdra, Efthimia K., Papavassiliou, Athanasios G. (2009) 'Mechanotransduction in osteoblast regulation and bone disease', (April).15(5), pp. 208-215.

Parfitt, A. M. (2002) 'Targeted and nontargeted bone remodeling: Relationship to basic multicellular unit origination and progression', Bone, 30(1), pp. 5–7.

Pavalko, Fred M., Norvell, Suzanne M., Burr, David B., Turner, Charles H., Duncan, Randall L., Bidwell, Joseph P. (2003) 'A model for mechanotransduction in bone cells: The load-bearing mechanosomes', Journal of Cellular Biochemistry, 88(1), pp. 104–112.

Pearson, R. G. and Scammell, B. E. (2013) 'Bone graft substitutes currently available in orthopaedic practice the evidence for their use', 95(5), pp. 583–597.

Peelen, J. G. J., Rejda, B. V. and de Groot, K. (1978) 'Preparation and properties of sintered hydroxylapatite', Ceramurgia International. Elsevier, 4(2), pp. 71–74.

Porter, J. R., Ruckh, T. T. and Popat, K. C. (2009) 'Bone tissue engineering: A review in bone biomimetics and drug delivery strategies', Biotechnology Progress, 25(6), pp. 1539–1560.

Posner, A. S. (1969) 'Crystal chemistry of bone mineral', Physiological reviews, 49(4), pp. 760–792.

Prakasam, Mythili., Locs, Janis., Salma-Ancane, Kristine., Loca, Dagnija., Largeteau, Alain., Berzina-Cimdina, Liga. (2015) 'Fabrication, Properties and Applications of Dense Hydroxyapatite: A Review', Journal of Functional Biomaterials, 6(4), pp. 1099–1140.

Pryor, Landon S., Gage, Earl., Langevin, Claude-jean., Herrera, Fernando., Breithaupt, Andrew D., Gordon, Chad R.,Afifi, Ahmed M., Zins, James E., Meltzer, Hal., Gosman, Amanda., Cohen, Steve R., Holmes, Ralph (2009) 'Review of Bone Substitutes', 44195(212), pp. 151–160.

Price, Christopher., Zhou, Xiaozhou., Li, Wen., Wang, Liyun (2011) 'Real-time measurement of solute transport within the lacunar-canalicular system of mechanically loaded bone: Direct evidence for load-induced fluid flow', Journal of Bone and Mineral Research, 26(2), pp. 277–285.

Plowman, Sharon., Smith. D. (2013) Exercise Physiology for Health Fitness and Performance. 4th edn. Baltimore: Wolters Kluwer, pp 489-490.

Qi, M.,Hu, J.,Zou, S., Chen, H., Zhou, H., Han, L. (2008) 'Mechanical strain induces osteogenic differentiation : Cbfa1 and Ets-1 expression in stretched rat mesenchymal stem cells', pp. 453–458.

Ramay, H. R. and Zhang, M. (2004) 'Biphasic calcium phosphate nanocomposite porous scaffolds for loadbearing bone tissue engineering', Biomaterials. Elsevier, 25(21), pp. 5171–5180.

Rawlinson, S. C. F., Pitsillides, A. A. and Lanyon, L. E. (1996) 'Involvement of different ion channels in osteoblasts' and osteocytes' early responses to mechanical strain', Bone, 19(6), pp. 609–614.

Ricci, William M., J. Borrelli., D. Prickett. (2003) 'Treatment of Nonunions and Osseous Defects With Bone Graft and Calcium Sulfate', (411), pp. 245–254.

Rittweger, Jörn., Frost, Harold M., Schiessl, Hans., Ohshima, Hiroshi., Alkner, Björn, Tesch Per., Felsenberg, Dieter. (2005) 'Muscle atrophy and bone loss after 90 days' bed rest and the effects of flywheel resistive exercise and pamidronate: Results from the LTBR study', Bone. Elsevier, 36(6), pp. 1019–1029.

Ross, F. P. (2009) 'Osteoclast Biology and Bone Resorption', Primer on the Metabolic Bone Diseases and Disorders of Mineral Metabolism: Seventh Edition, pp. 16–22.

Ross FP, T. S. (2005) 'alphavbeta3 and macrophage colony-stimulating factor: partners in osteoclast biology', Immunol Rev, 208, pp. 88–105.

Rossig, L., Haendeler, J., Hermann, C., Malchow, P., Urbich, C., Zeiher, A. M., Dimmeler, S. (2000) 'Nitric oxide downregulates MKP-3 mRNA levels: Involvement in endothelial cell protection from apoptosis', Journal of Biological Chemistry, 275(33), pp. 25502–25507.

Runesson, Kenneth., Steinmann, Paul., E. Magnus., Menzel, Andreas., Larsson, Fredrik. (2011) 'Homogenized Material Properties', Constitutive Modelling of Engineering Materials – Theory and Computation. Vol. I. General Concepts and Inelasticity, 1, pp. 339–364.

Ren, F., Case, E. D., Morrison, A., Tafesse, M., & Baumann, M. J. (2009). Resonant ultrasound spectroscopy measurement of Young's modulus, shear modulus and Poisson's ratio as a function of porosity for alumina and hydroxyapatite. Philosophical Magazine, 89(14), 1163–1182.

Rath Bonivtch, A., Bonewald, L. F., & Nicolella, D. P. (2007). Tissue strain amplification at the osteocyte lacuna: A microstructural finite element analysis. Journal of Biomechanics, 40(10), 2199–2206.

Reijnders, Christianne M A., Bravenboer, Nathalie., Tromp, Annechien M., Blankenstein, Marinus., A. Lips, Paul. (2007) 'Effect of mechanical loading on insulin-like growth factor-I gene expression in rat tibia', The Journal of endocrinology, 192(1), pp. 131–140.

Robinson, John A., Chatterjee-Kishore, Moitreyee., Yaworsky, Paul J., Cullen, Diane M., Zhao, Weiguang., Li, Christine., Kharode, Yogendra., Sauter, Linda., Babij, Philip Brown., Eugene. L., Hill, Andrew A., Akhter, Mohammed P., Johnson, Mark., Lecker, Robert R., Komm, Barry S., Bex, Frederick J. (2006) 'Wnt/β-catenin signaling is a normal physiological response to mechanical loading in bone', Journal of Biological Chemistry, 281(42), pp. 31720–31728.

Reilly, G. C. (2000) 'Observations of microdamage around osteocyte lacunae in bone', *Journal of Biomechanics*, 33(9), pp. 1131–1134.

Said.R., Chang. J., Young, P., Tabor. G., Coward, S. "Image-Based Meshing of Patient-Specific Data: Converting Medical Scans Into Highly Accurate Computational Models," 2008 2nd International Conference on Bioinformatics and Biomedical Engineering, Shanghai, 2008, pp. 1672-1676.

Salinas, Antonio J., Vallet-Regí, María. (2007) 'Evolution of ceramics with medical applications', Zeitschrift fur Anorganische und Allgemeine Chemie, 633(11–12), pp. 1762–1773.

Sandhu, H. S., Grewal, H. S. and Parvataneni, H. (1999) 'bone grafting for spinal fusion', Orthopedic Clinics of North America, 30(4), pp. 685–698.

Schaffler, Mitchell B., Cheung, Wing Yee., Majeska, Robert., Kennedy, Oran (2014) 'Osteocytes: Master orchestrators of bone', Calcified Tissue International, 94(1), pp. 5–24.

Schlickewei, W. and Schlickewei, C. (2007) 'The Use of Bone Substitutes in the Treatment of Bone Defects – the Clinical View and History', pp. 10–23.

Schmid, Hamrock and Jacobson. (2014) 'Stresses and Deformations in Cylinders', Fundamentals of Machine Elements. (3rd Ed). CPC Press. pp 134-141.

Schumacher, M., Deisinger, U., Ziegler, G., Detsch, R. (2010) 'Indirect rapid prototyping of biphasic calcium phosphate scaffolds as bone substitutes: Influence of phase composition, macroporosity and pore geometry on mechanical properties', Journal of Materials Science: Materials in Medicine, 21(12), pp. 3119–3127.

Schwarz, K. and Milne, D. B. (1972) 'Growth-promoting effects of silicon in rats', Nature, 239(5371), pp. 333–334.

Sharma, Rajeev., Pandey, Aditi., Awasthi, Shikha., Nisar, Ambreen., Nair, Jitin., Midha, Swati., Upadhyaya, Anish., Kanhed, Satish., Balani, Kantesh., Ghosh, Sourabh., Patel, Anup Kumar., Goel, Sneha. (2018) 'Microporous Hydroxyapatite Ceramic Composites as Tissue ngineering Scaffolds: An Experimental and Computational Study', Advanced Engineering Materials, 20(7), p. 1701062.

Sikavitsas, V. I., Temenoff, J. S. and Mikos, A. G. (2001) 'Biomaterials and bone mechanotransduction', Biomaterials, 22(19), pp. 2581–2593.

Snow-Harter, Christine., Bouxsein, Mary L., Lewis, Barbara T., Carter, Dennis R., Marcus, Robert (2009) 'Effects of resistance and endurance exercise on bone mineral status of young women: A randomized exercise intervention trial', Journal of Bone and Mineral Research, 7(7), pp. 761–769.

Sobral, Jorge M., Caridade, Sofia G.,Sousa, Rui A.,Mano, João F.,Reis, Rui L. (2011) 'Three-dimensional plotted scaffolds with controlled pore size gradients: Effect of caffold geometry on mechanical performance and cell seeding efficiency', Acta biomaterialia. Acta Materialia Inc., 7(3), pp. 1009–1018.

Sopyan, I.,Mel, M.,Ramesh, S.,Khalid, K. A. (2007) 'Porous hydroxyapatite for artificial bone applications', Science and Technology of Advanced Materials, 8(1–2), pp. 116–123.

Suchanek, W. and Yoshimura, M. (1998) 'Processing and properties of hydroxyapatite-based biomaterials for use as hard tissue replacement implants', Journal of Materials Research, 13(1), pp. 94–117.

Sumanasinghe, R. D., Bernacki, S. H. and Loboa, E. G. (2006) 'Osteogenic Differentiation of Human Mesenchymal Stem Cells in Collagen Matrices: Effect of Uniaxial Cyclic Tensile Strain on Bone Morphogenetic Protein (BMP-2) mRNA Expression', Tissue Engineering, 12(12), pp. 3459–3465.

SimplewareTM (2017) 'SimplewareTM ScanIP'. Mountain View, USA: Synopsys, Inc. Available at: https://www.synopsys.com/simpleware.html.

Shaw John. (1995). Fabrication and characterisation of pourous hydroxyapatite. Queen Mary University of London. PhD Thesis.

Spriggs, R. M. (1961). Expression for Effect of Porosity on Elastic Modulus of Polycrystalline Refractory Materials, Particularly Aluminum Oxide. Science of Sintering, 18(1), 68–70.

Sinka, I. C., Cocks, A. C. F. and Pan, J. (2009) 'Constitutive Model Development for Powder Compaction and Implementation into Abaqus' 2009 SIMULIA Customer Conference, pp. 1–11.

Shang, C., Sinka, I. C., Pan, J. (2012) 'Constitutive Model Calibration for Powder Compaction Using Instrumented Die Testing', Experimental Mechanics, 52(7), pp. 903–916.

Study, Undergraduate Project. (2017). Multiscale Modelling and Mechanical Characterization of Porous Hierarchical Hydroxyapatite. Supervisor: Alvaro Mata, Queen Mary.

Taichman, R. S. (2018) 'Review article Blood and bone: two tissues whose fates are intertwined to create the hematopoietic stem-cell niche', 105(7), pp. 2631–2640.

Takai, Erica., Mauck, Robert L., Hung, Clark T.,Guo, X. Edward (2004) 'Osteocyte viability and regulation of osteoblast function in a 3D trabecular bone explant under dynamic hydrostatic pressure', Journal of Bone and Mineral Research, 19(9), pp. 1403–1410.

Takashi, Asazuma., Kazunori, Masuoka., Takao, Motosuneya., Takashi, Tsuji., Hiroki, Yasuoka., and K. F. (2005) 'Posterior Lumbar Interbody Fusion Using Dense Hydroxyapatite Blocks and Autogenous Iliac Bone', Journal of Spinal Disorders & Techniques, 18(February), pp. 41–47.

Tay Vikas, B. K. B., Patel, V. and Bradford, D. S. (1999) 'Calcium sulfate- and calcium phosphate-based bone substitutes mimicry of the mineral phase of bone', Orthopedic Clinics of North America, 30(4), pp. 615–623.

Thian, E. S., Huang, J., Best, S. M., Barber, Z. H., Bonfield, W. (2007) 'Silicon-substituted hydroxyapatite: The next generation of bioactive coatings', Materials Science and Engineering C, 27(2), pp. 251–256.

Trusov, P. V and Shveykin, A. I. (2017) 'On Motion Decomposition and Constitutive Relations in Geometrically Nonlinear Elastoviscoplasticity of Crystallites', 20(4), pp. 377–378.

Turner, C. H., Turner, Charles H., Forwood, M. R., Rho, J. Y., Yoshikawa, T. (1994) 'Mechanical loading thresholds for lamellar and woven bone formation', Journal of Bone and Mineral Research, 9(1), pp. 87–97.

Turner, C. H. and Pavalko, F. M. (1998) 'Mechanotransduction and functional response of the skeleton to physical stress: The mechanisms and mechanics of bone adaptation', Journal of Orthopaedic Science. Elsevier, 3(6), pp. 346–355.

Turner, C. H. (1998) 'Three rules for bone adaptation to mechanical stimuli', Bone, 23(5), pp. 399–407.

Ullah, Z., Kaczmarczyk, L. and Pearce, C. J. (2017) 'Three-dimensional nonlinear micro/meso-mechanical response of the fibre-reinforced polymer composites', Composite Structures, 161, pp. 204–214.

Vallet-Regí, M. (2010) 'Evolution of bioceramics within the field of biomaterials', Comptes Rendus Chimie, pp. 174– 185.

Verborgt, Olivier., Tatton, Nadine A., Majeska, Robert J., Schaffler, Mitchell B. (2002) 'Spatial distribution of Bax and Bcl-2 in osteocytes after bone fatigue: Complementary roles in bone remodeling regulation?', Journal of Bone and Mineral Research, 17(5), pp. 907–914.

Vuori, I. (1995) 'Exercise and physical health: Musculoskeletal health and functional capabilities', Research Quarterly for Exercise and Sport, 66(4), pp. 276–285.

Wang, Liang., Zhang, Xizheng., Guo, Yong., Chen, Xuezhong., Li, Ruixin., Liu, Lu., Shi. Caihong., Guo, Chun., Zhang, Yan. (2010) 'Cellular Physiology and Biochemistr y Biochemistry Involvement of BMPs / Smad Signaling Pathway in Mechanical Response in Osteoblasts', Cell Physiol Biochem, 300161(106), pp. 1093–1102.

Wang, Liang., Li, Jian Yu., Zhang, Xi Zheng., Liu, Lu., Wan, Zong Ming., Li, Rui Xin., Guo, Yong. (2012) 'Involvement of p38MAPK/NF-κB signaling pathways in osteoblasts differentiation in response to mechanical stretch', Annals of Biomedical Engineering, 40(9), pp. 1884–1894.

Ward. K., Alsop. C., Caulton. J., Rubin C., Adams. J., Mughal. Z. (2004) 'Low magnitude mechanical loading is osteogenic in children with disabling conditions', Journal of Bone and Mineral Research, 19(3), pp. 360–369.

Warden. S., Hurst. J., Sanders. M., Turner. C., Burr. D., Li. J. (2005) 'Bone adaptation to a mechanical loading program significantly increases skeletal fatigue resistance', Journal of Bone and Mineral Research, 20(5), pp. 809– 816.

Weinbaum, S., Cowin, S. C. and Zeng, Y. (1994) 'A model for the excitation of osteocytes by mechanical loadinginduced bone fluid shear stresses', Journal of Biomechanics, 27(3), pp. 339–360.

Whalen, R. T., Carter, D. R. and Steele, C. R. (1988) 'Influence of physical activity on the regulation of bone density', Journal of Biomechanics, 21(10), pp. 825–837.

Whiteman. J.R. (1985) 'The mathematics of finite elements and applications'. 1st Ed. Uxbridge, England: Elsevier Inc, pp. 43-52.

Williams, J. A. and Billington, R. W. (1989) 'Increase in compressive strength of glass ionomer restorative materials with respect to time: a guide to their suitability for use in posterior primary dentition', Journal of Oral Rehabilitation, 16(5), pp. 475–479.

William, K.J. (2002). Constitutive models for engineering materials. Encyclopedia of Physical Science and Technology, University of Colarado, pp. CMM2–CMM56.

Williams, David F. (1990) Concise Encyclopedia of Medical and Dental Materials. 1st edn. Pragamon 1990, pp. 28-34

Wilson, J. and Low, S. B. (1992) 'Bioactive ceramics for periodontal treatment: comparative studies in the Patus monkey', Journal of applied biomaterials : an official journal of the Society for Biomaterials, 3(2), pp. 123–129.

Wittwer, C., Devlin, A., Hatton, P., Brook. I., Downes. S. (1994) 'The release of serum proteins and dye from glass ionomer (polyalkenoate) and acrylic cements: a pilot study', Journal of Materials Science: Materials in Medicine, 5(9–10), pp. 711–714.

Woodard, J., Hilldore, A., Lan, S., Park, C., Morgan, A., Ann. J., Eurell. C., Clark. S., Wheeler. M., Jamison. R., Wagoner. A. (2007) 'The mechanical properties and osteoconductivity of hydroxyapatite bone scaffolds with multiscale porosity', 28, pp. 45–54.

Wu, C., Li, Y., Haga, J., Wang, N., Lian, I., Su, F., Usami, S., Chien, S. (2006) 'Roles of MAP kinases in the regulation of bone matrix gene expressions in human osteoblasts by oscillatory fluid flow', Journal of Cellular Biochemistry, 98(3), pp. 632–641.

Xynos, I., Edgar, A. Buttery., Hench, L., Polak, J. (2001) 'Gene-Expression Profiling of Human Osteoblasts Following Treatment With the Ionic Products of Bioglass® 45S5 Dissolution', Journal of Biomedical Materials Research, 55, pp. 151–157.

Yashavantha, Kumar C., Nalini, K., Menon. J., Patro, D., Banerji, B. (2013) 'Calcium sulfate as bone graft substitute in the treatment of osseous bone defects, a prospective study', Journal of Clinical and Diagnostic Research, 7(12), pp. 2926–2928.

Yoshikawa, H. (2005) 'Bone tissue engineering with porous hydroxyapatite ceramics', pp. 131–136.

Young, P., Beresford-West, T., Coward, S., Notarberardino, B., Walker, B., Abdul-Aziz, A. (2008) 'An efficient approach to converting three-dimensional image data into highly accurate

computational models', Philosophical Transactions of the Royal Society A: Mathematical, Physical and Engineering Sciences, 366(1878), pp. 3155– 3173.

Yu, W. (2016) 'An Introduction to Micromechanics', Applied Mechanics and Materials, 828, pp. 3–24

Yuan, H., Van, Den., Doel, M., Li, S., Van Blitterswijk, C., De Groot, K., De Bruijn, J. (2002) 'A comparison of the osteoinductive potential of two calcium phosphate ceramics implanted intramuscularly in goats', Journal of Materials Science: Materials in Medicine, 13(12), pp. 1271–1275.

Zhao, J. and Guo, N. (2014) 'Bridging the micro and macro for granular media: A computational multi-scale paradigm', Geomechanics from Micro to Macro, pp. 747–752.

Appendix

A-1 Mesh densities used for simulations

Table 11: Mesh densities for the 4 and 8 mm models

Material	RVE size in mm	number of elements	Material	RVE size in mm	number of elements
80-20	4mm	400237	80-20	8mm	902586
80-20	4mm	400385	80-20	8mm	906251
80-20	4mm	400585	80-20	8mm	906763
80-20	4mm	402004	80-20	8mm	924297
80-20	4mm	424067	80-20	8mm	941684
80-30	4mm	440255	80-30	8mm	808264
80-30	4mm	446547	80-30	8mm	824656
80-30	4mm	450160	80-30	8mm	833429
80-30	4mm	452785	80-30	8mm	835439
80-30	4mm	463820	80-30	8mm	844073
70-20	4mm	506362	70-20	8mm	870765
70-20	4mm	513314	70-20	8mm	903601
70-20	4mm	513420	70-20	8mm	911064
70-20	4mm	519640	70-20	8mm	925091
70-20	4mm	519895	70-20	8mm	932209
60-20	4mm	529182	60-20	8mm	846342
60-20	4mm	533912	60-20	8mm	848579
60-20	4mm	545185	60-20	8mm	848650
60-20	4mm	559695	60-20	8mm	942822
60-20	4mm	559800	60-20	8mm	941901
60-30	4mm	445386	60-30	8mm	834177
60-30	4mm	445848	60-30	8mm	857353
60-30	4mm	450963	60-30	8mm	876382
60-30	4mm	453694	60-30	8mm	880572
60-30	4mm	464957	60-30	8mm	880684

Table 12: Mesh densities for the 12 mm models

Material	RVE size in mm	Number of elements
80-20	12mm	1394125
80-20	12mm	1397184
80-20	12mm	1397912
80-20	12mm	1404573
80-20	12mm	1406446
80-30	12mm	1276469
80-30	12mm	1282509
80-30	12mm	1282733
80-30	12mm	1288593
80-30	12mm	1289850
70-20	12mm	1180748
70-20	12mm	1181194
70-20	12mm	1186747
70-20	12mm	1187673
70-20	12mm	1192922
60-20	12mm	985286
60-20	12mm	986974
60-20	12mm	1375157
60-20	12mm	1482122
60-20	12mm	1963534
60-30	12mm	1022761
60-30	12mm	1026181
60-30	12mm	1030947
60-30	12mm	1034643
60-30	12mm	1428097

A-2 Rescaling Stress and Strain outputs with linear fitting

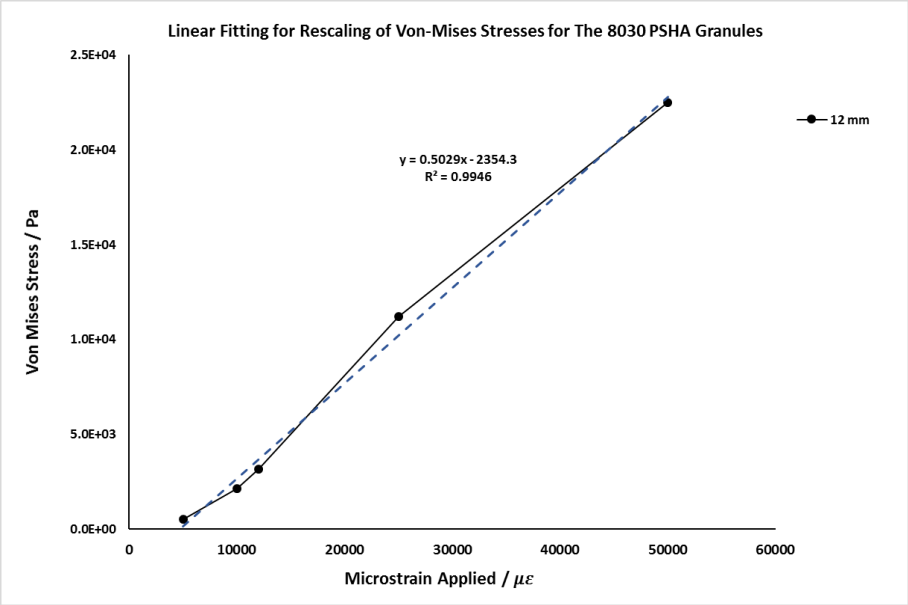

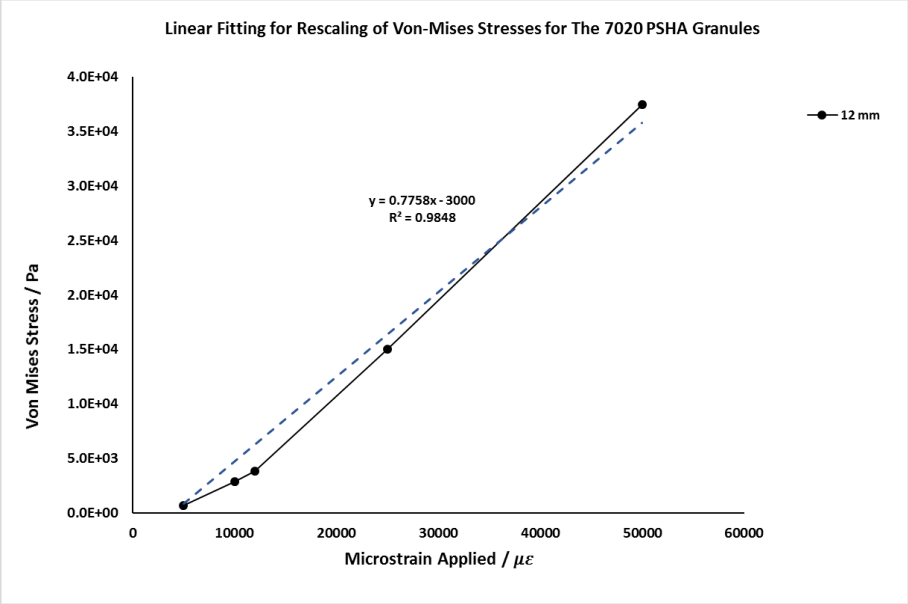

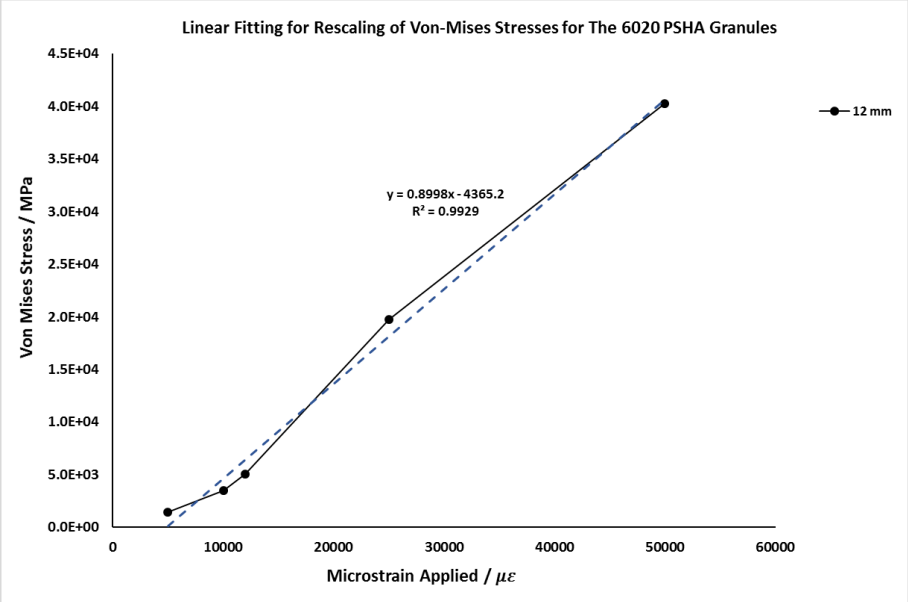
Linear Fitting for Rescaling of Von-Mises Stresses for The 6020 PSHA Granules
Von Mises Stress / MPa
Microstrain Applied / με
y = 0.8998x - 4365.2
R² = 0.9929
12 mm
4.5E+04
4.0E+04
3.5E+04
3.0E+04
2.5E+04
2.0E+04
1.5E+04
1.0E+04
5.0E+03
0.0E+00
0
10000
20000
30000
40000
50000
60000

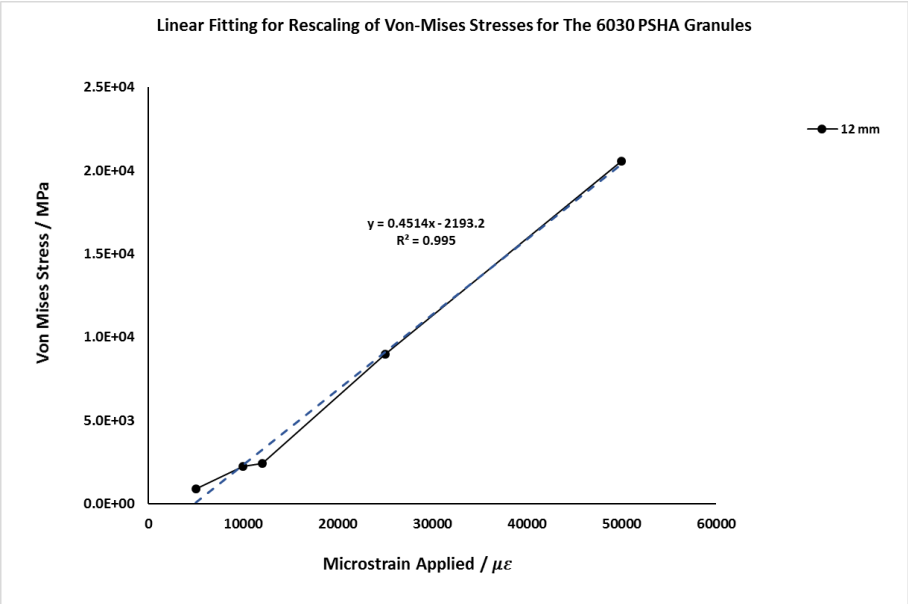
Linear Fitting for Rescaling of Von-Mises Stresses for The 6030 PSHA Granules
Von Mises Stress / MPa
Microstrain Applied / με
y = 0.4514x - 2193.2
R² = 0.995
12 mm
2.5E+04
2.0E+04
1.5E+04
1.0E+04
5.0E+03
0.0E+00
0
10000
20000
30000
40000
50000
60000

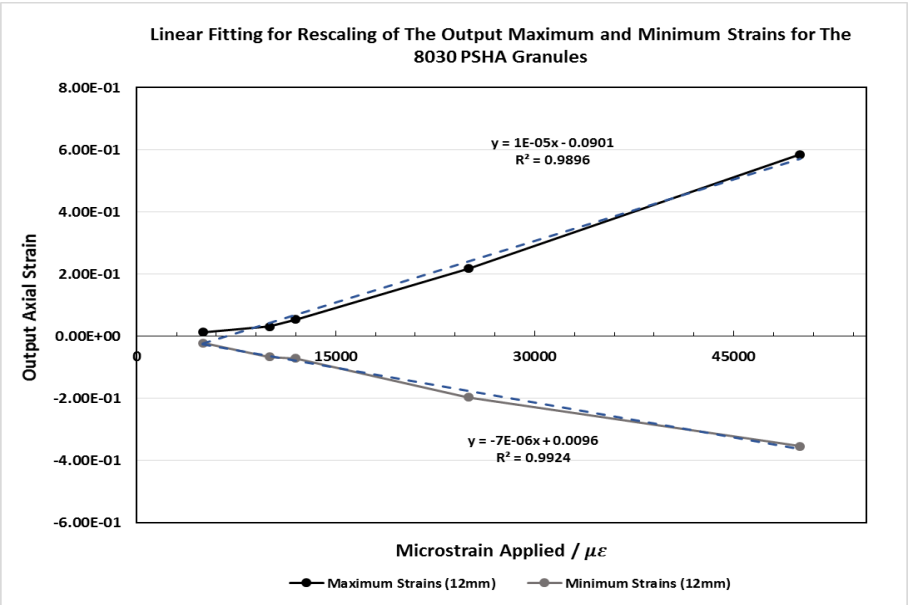
Linear Fitting for Rescaling of The Output Maximum and Minimum Strains for The 8030 PSHA Granules
Output Axial Strain
Microstrain Applied / με
y = 1E-05x - 0.0901
R² = 0.9896
y = -7E-06x + 0.0096
R² = 0.9924
Maximum Strains (12mm)
Minimum Strains (12mm)
8.00E-01
6.00E-01
4.00E-01
2.00E-01
0.00E+00
-2.00E-01
-4.00E-01
-6.00E-01
0
15000
30000
45000

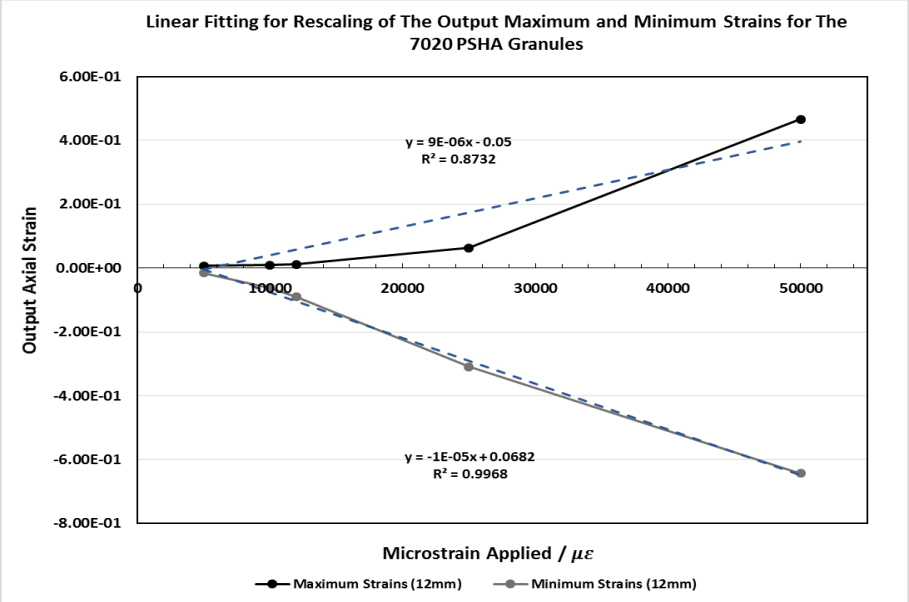
Linear Fitting for Rescaling of The Output Maximum and Minimum Strains for The 7020 PSHA Granules
6.00E-01
4.00E-01
2.00E-01
0.00E+00
-2.00E-01
-4.00E-01
-6.00E-01
-8.00E-01
0
10000
20000
30000
40000
50000
Output Axial Strain
y = 9E-06x - 0.05
R² = 0.8732
y = -1E-05x + 0.0682
R² = 0.9968
Microstrain Applied / με
Maximum Strains (12mm)
Minimum Strains (12mm)

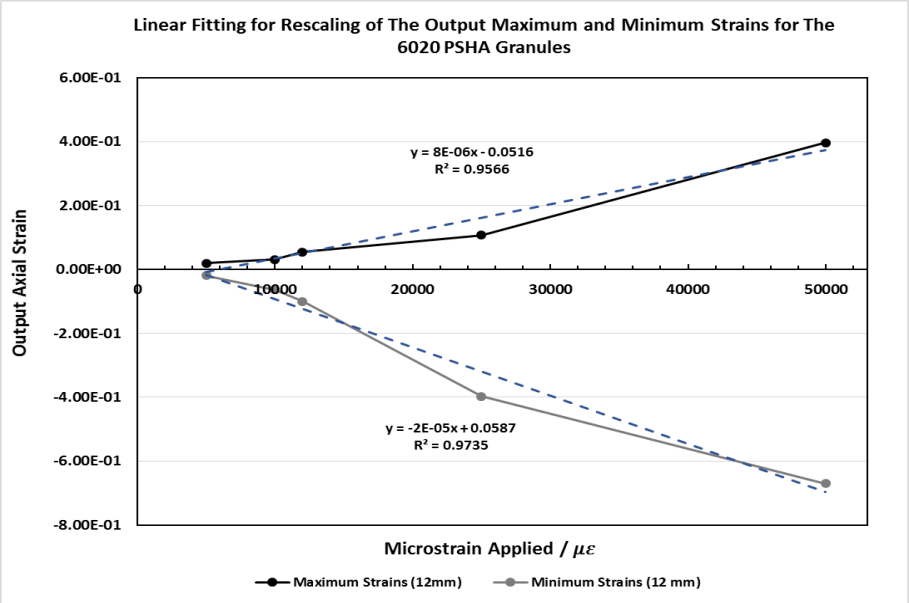
Linear Fitting for Rescaling of The Output Maximum and Minimum Strains for The 6020 PSHA Granules
6.00E-01
4.00E-01
2.00E-01
0.00E+00
-2.00E-01
-4.00E-01
-6.00E-01
-8.00E-01
0
10000
20000
30000
40000
50000
Output Axial Strain
y = 8E-06x - 0.0516
R² = 0.9566
y = -2E-05x + 0.0587
R² = 0.9735
Microstrain Applied / με
Maximum Strains (12mm)
Minimum Strains (12 mm)

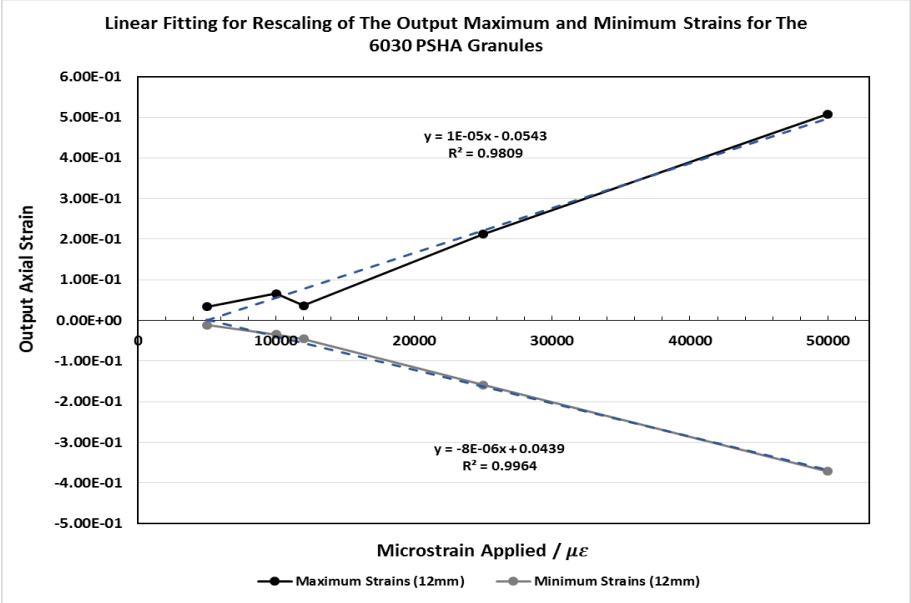
Linear Fitting for Rescaling of The Output Maximum and Minimum Strains for The 6030 PSHA Granules
6.00E-01
5.00E-01
4.00E-01
3.00E-01
2.00E-01
1.00E-01
0.00E+00
-1.00E-01
-2.00E-01
-3.00E-01
-4.00E-01
-5.00E-01
0
10000
20000
30000
40000
50000
Output Axial Strain
y = 1E-05x - 0.0543
R² = 0.9809
y = -8E-06x + 0.0439
R² = 0.9964
Microstrain Applied / με
Maximum Strains (12mm)
Minimum Strains (12mm)

A-3 Stress and strain

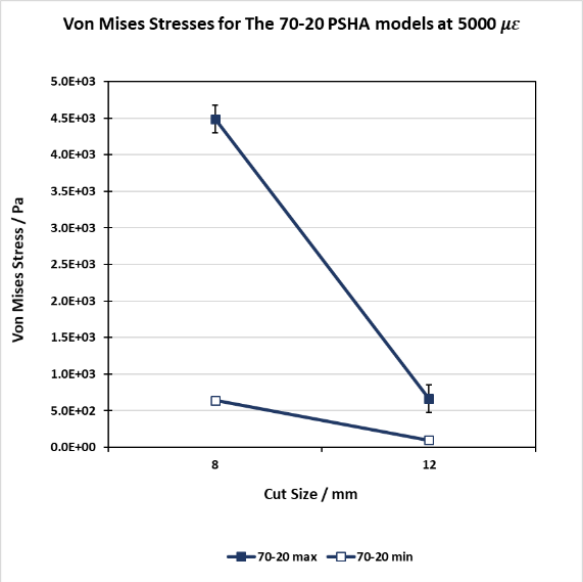

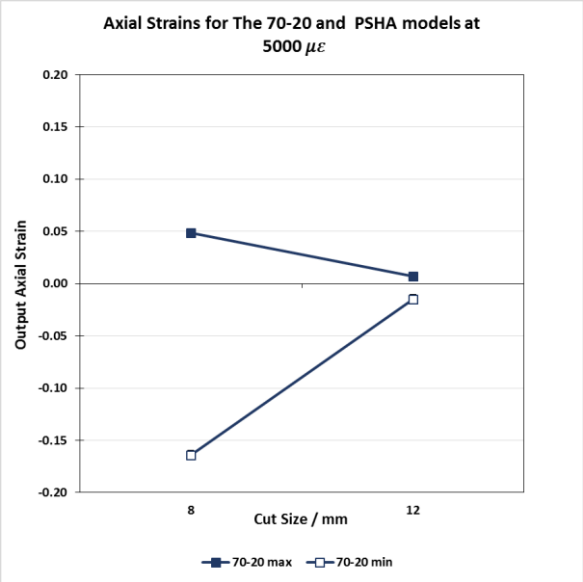

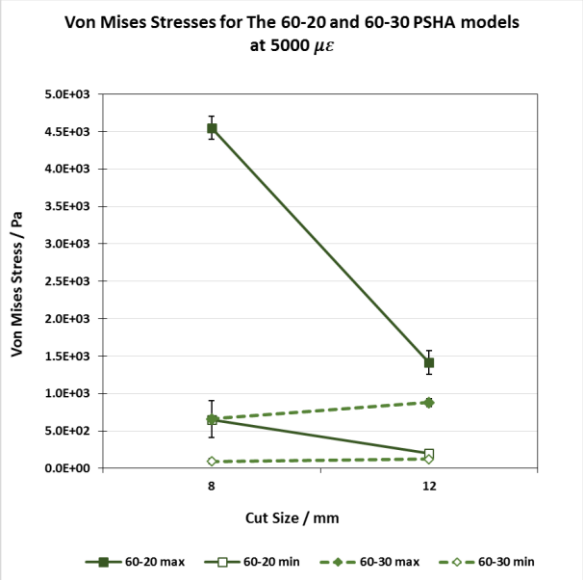

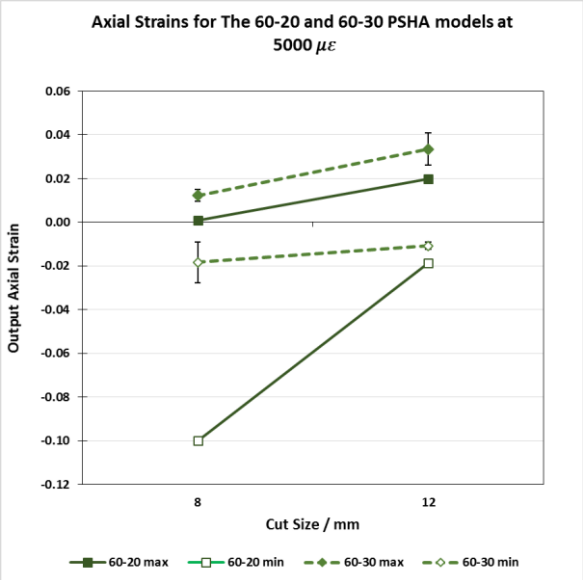

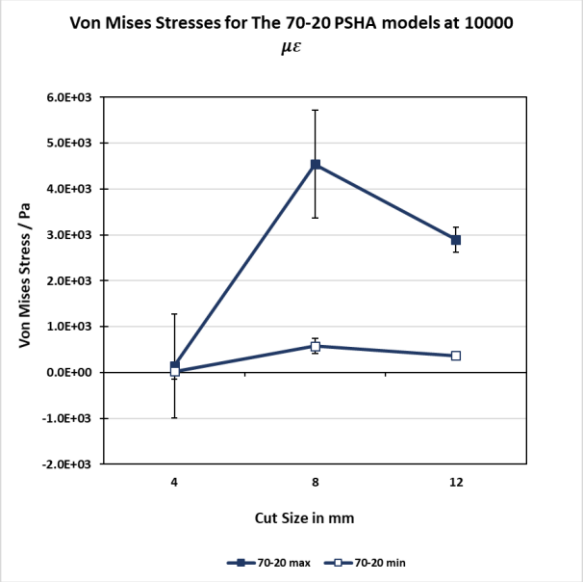
Von Mises Stresses for The 70-20 PSHA models at 10000 με
Von Mises Stress / Pa
6.0E+03
5.0E+03
4.0E+03
3.0E+03
2.0E+03
1.0E+03
0.0E+00
-1.0E+03
-2.0E+03
4
8
12
Cut Size in mm
70-20 max
70-20 min

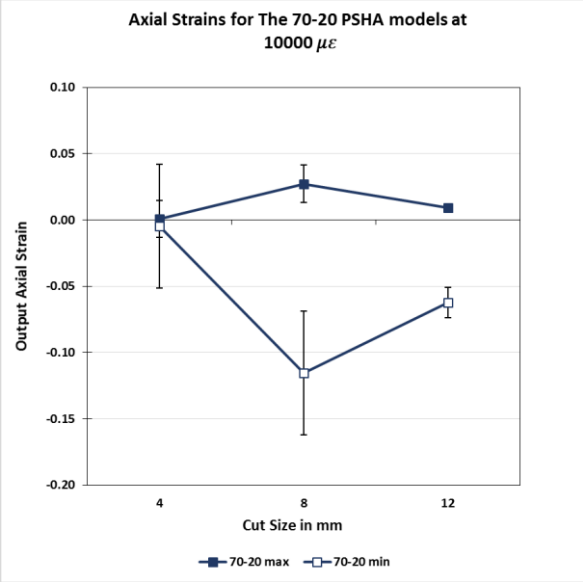
Axial Strains for The 70-20 PSHA models at 10000 με
Output Axial Strain
0.10
0.05
0.00
-0.05
-0.10
-0.15
-0.20
4
8
12
Cut Size in mm
70-20 max
70-20 min

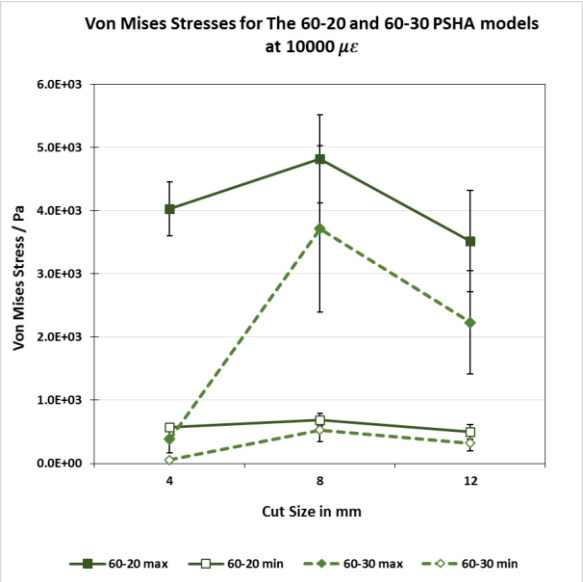
Von Mises Stresses for The 60-20 and 60-30 PSHA models at 10000 με
Von Mises Stress / Pa
6.0E+03
5.0E+03
4.0E+03
3.0E+03
2.0E+03
1.0E+03
0.0E+00
4
8
12
Cut Size in mm
60-20 max
60-20 min
60-30 max
60-30 min

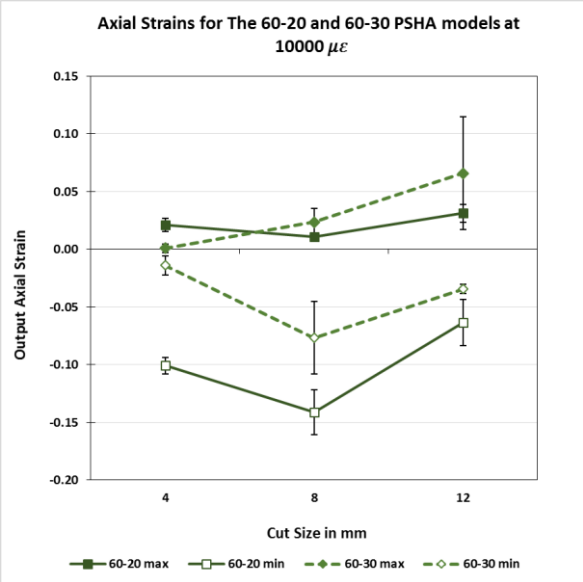
Axial Strains for The 60-20 and 60-30 PSHA models at 10000 με
Output Axial Strain
0.15
0.10
0.05
0.00
-0.05
-0.10
-0.15
-0.20
4
8
12
Cut Size in mm
60-20 max
60-20 min
60-30 max
60-30 min

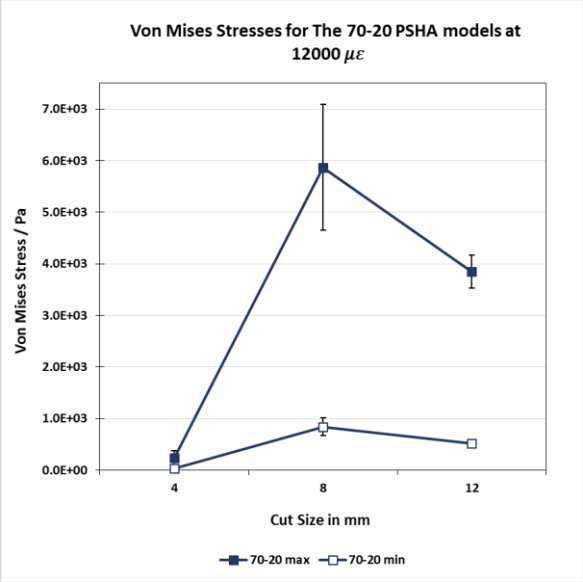
Von Mises Stresses for The 70-20 PSHA models at 12000 με
Von Mises Stress / Pa
7.0E+03
6.0E+03
5.0E+03
4.0E+03
3.0E+03
2.0E+03
1.0E+03
0.0E+00
4
8
12
Cut Size in mm
70-20 max
70-20 min

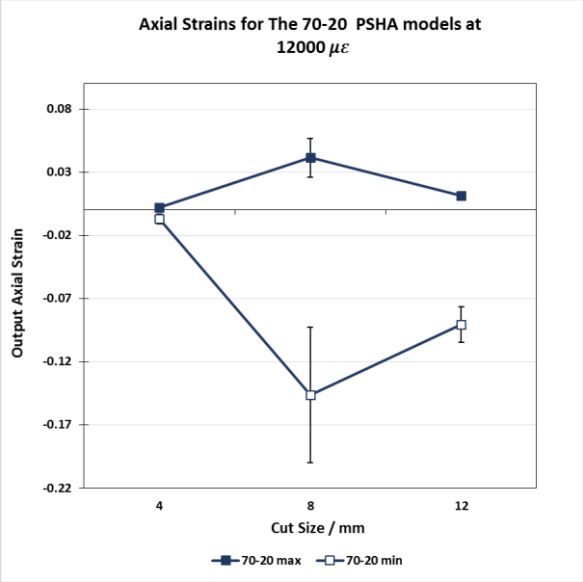
Axial Strains for The 70-20 PSHA models at 12000 με
Output Axial Strain
0.08
0.03
-0.02
-0.07
-0.12
-0.17
-0.22
4
8
12
Cut Size / mm
70-20 max
70-20 min

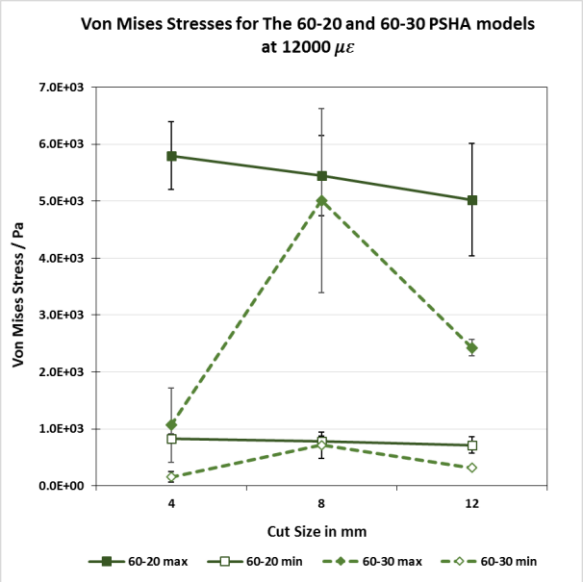
Von Mises Stresses for The 60-20 and 60-30 PSHA models at 12000 με
Von Mises Stress / Pa
7.0E+03
6.0E+03
5.0E+03
4.0E+03
3.0E+03
2.0E+03
1.0E+03
0.0E+00
4
8
12
Cut Size in mm
60-20 max
60-20 min
60-30 max
60-30 min

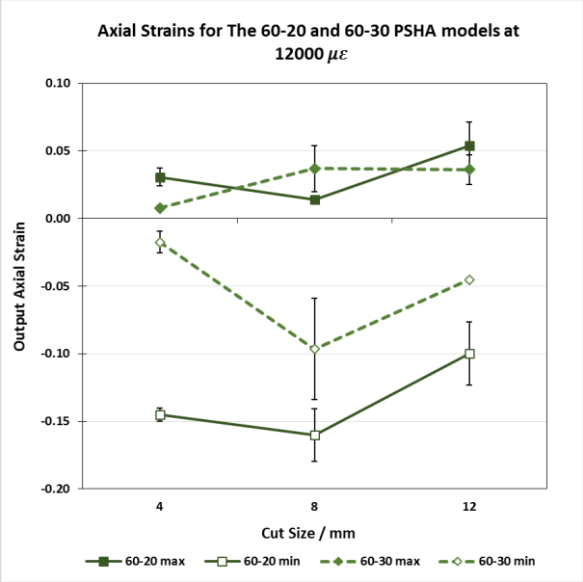
Axial Strains for The 60-20 and 60-30 PSHA models at 12000 με
Output Axial Strain
0.10
0.05
0.00
-0.05
-0.10
-0.15
-0.20
4
8
12
Cut Size / mm
60-20 max
60-20 min
60-30 max
60-30 min

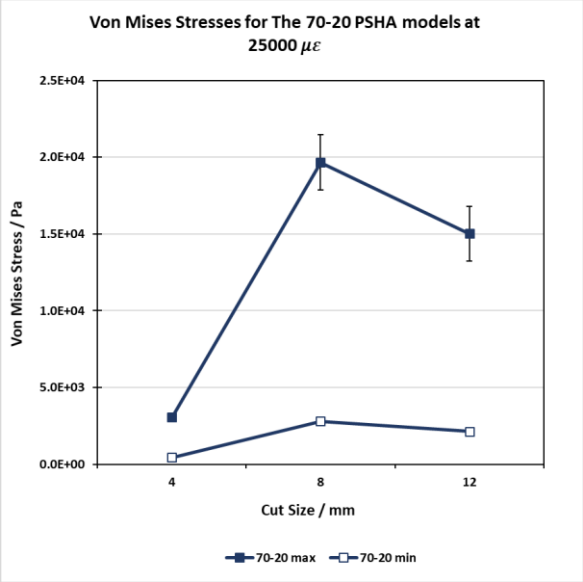
Von Mises Stresses for The 70-20 PSHA models at 25000 με
Von Mises Stress / Pa
2.5E+04
2.0E+04
1.5E+04
1.0E+04
5.0E+03
0.0E+00
4
8
12
Cut Size / mm
70-20 max
70-20 min

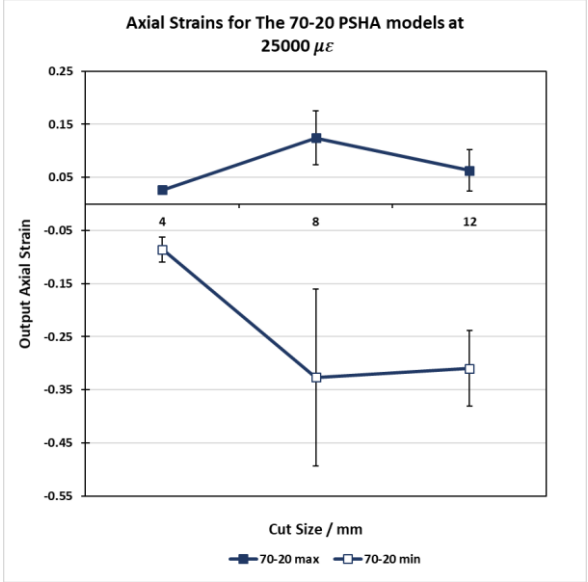
Axial Strains for The 70-20 PSHA models at 25000 με
Output Axial Strain
0.25
0.15
0.05
-0.05
-0.15
-0.25
-0.35
-0.45
-0.55
4
8
12
Cut Size / mm
70-20 max
70-20 min

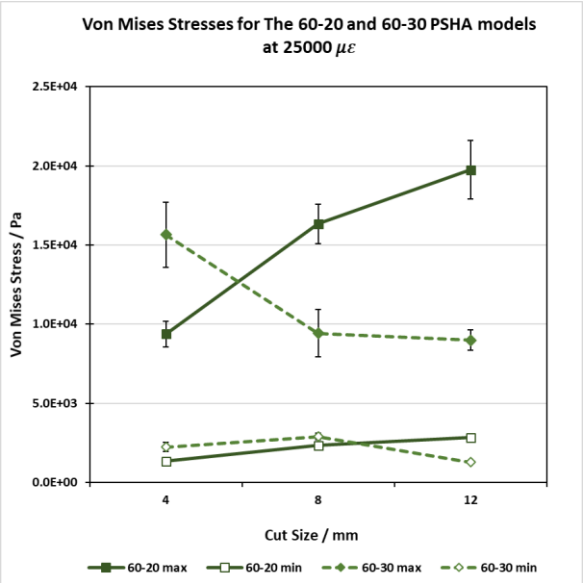
Von Mises Stresses for The 60-20 and 60-30 PSHA models at 25000 με
Von Mises Stress / Pa
2.5E+04
2.0E+04
1.5E+04
1.0E+04
5.0E+03
0.0E+00
4
8
12
Cut Size / mm
60-20 max
60-20 min
60-30 max
60-30 min

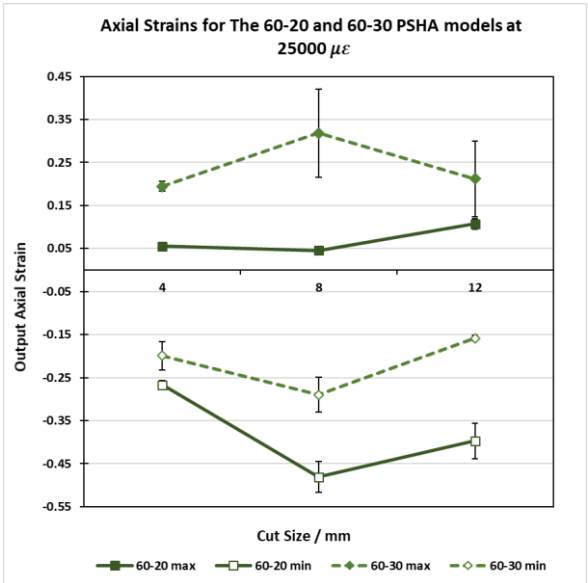
Axial Strains for The 60-20 and 60-30 PSHA models at 25000 με
Output Axial Strain
0.45
0.35
0.25
0.15
0.05
-0.05
-0.15
-0.25
-0.35
-0.45
-0.55
4
8
12
Cut Size / mm
60-20 max
60-20 min
60-30 max
60-30 min

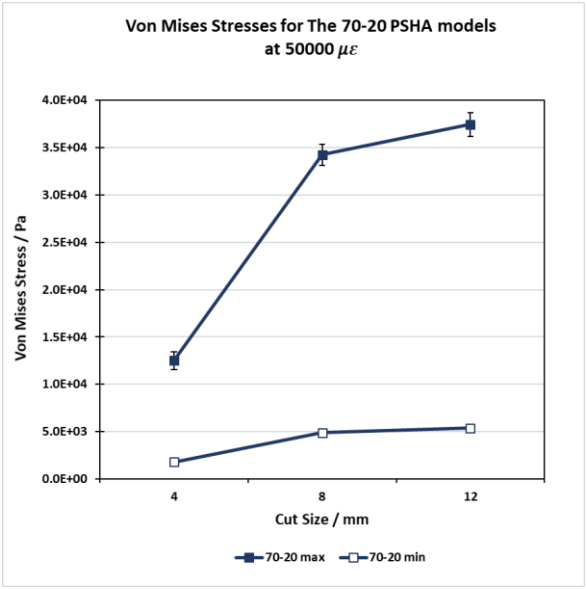
Von Mises Stresses for The 70-20 PSHA models at 50000 με
Von Mises Stress / Pa
4.0E+04
3.5E+04
3.0E+04
2.5E+04
2.0E+04
1.5E+04
1.0E+04
5.0E+03
0.0E+00
4
8
12
Cut Size / mm
70-20 max
70-20 min

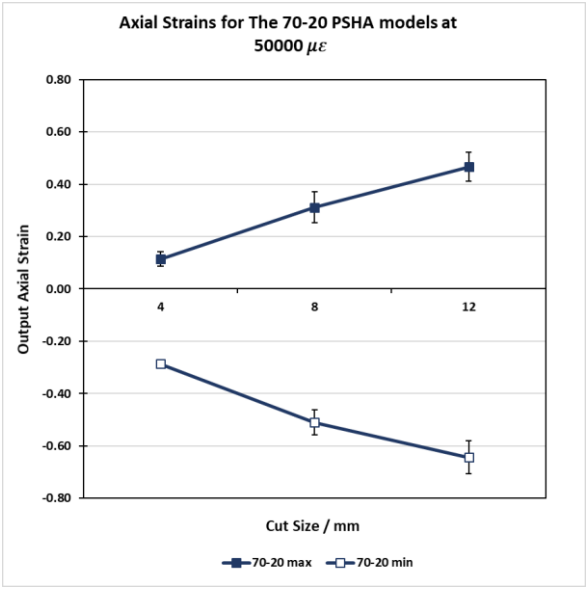
Axial Strains for The 70-20 PSHA models at 50000 με
Output Axial Strain
0.80
0.60
0.40
0.20
0.00
-0.20
-0.40
-0.60
-0.80
4
8
12
Cut Size / mm
70-20 max
70-20 min

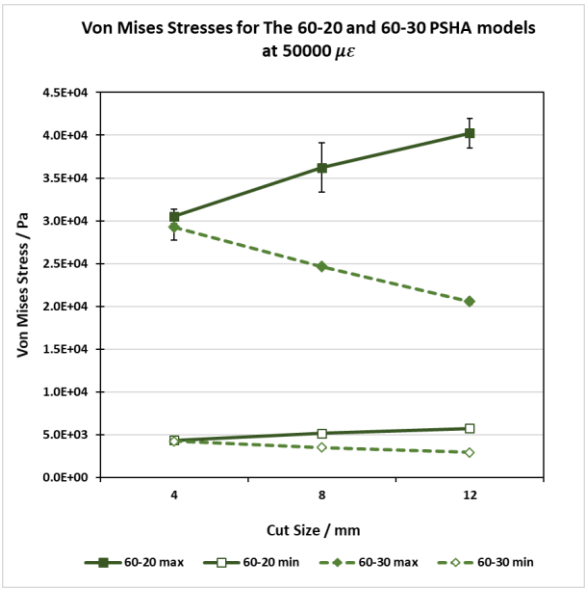
Von Mises Stresses for The 60-20 and 60-30 PSHA models at 50000 με
Von Mises Stress / Pa
4.5E+04
4.0E+04
3.5E+04
3.0E+04
2.5E+04
2.0E+04
1.5E+04
1.0E+04
5.0E+03
0.0E+00
4
8
12
Cut Size / mm
60-20 max
60-20 min
60-30 max
60-30 min

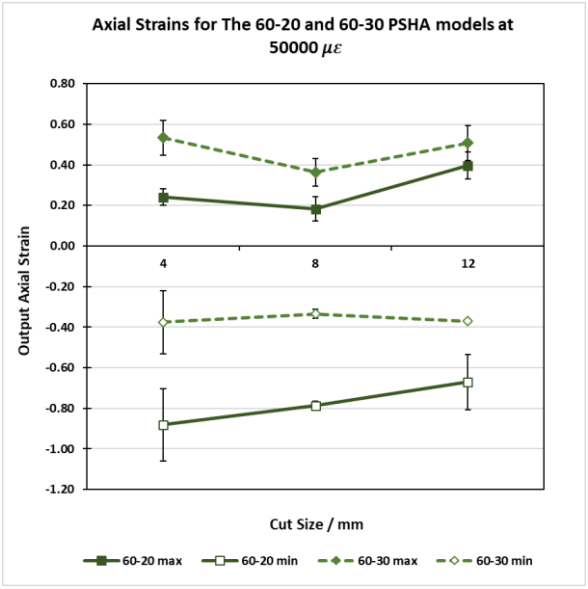
Axial Strains for The 60-20 and 60-30 PSHA models at 50000 με
Output Axial Strain
0.80
0.60
0.40
0.20
0.00
-0.20
-0.40
-0.60
-0.80
-1.00
-1.20
4
8
12
Cut Size / mm
60-20 max
60-20 min
60-30 max
60-30 min

A-4 Energy Conservation Profiles for the 4mm and 8mm models

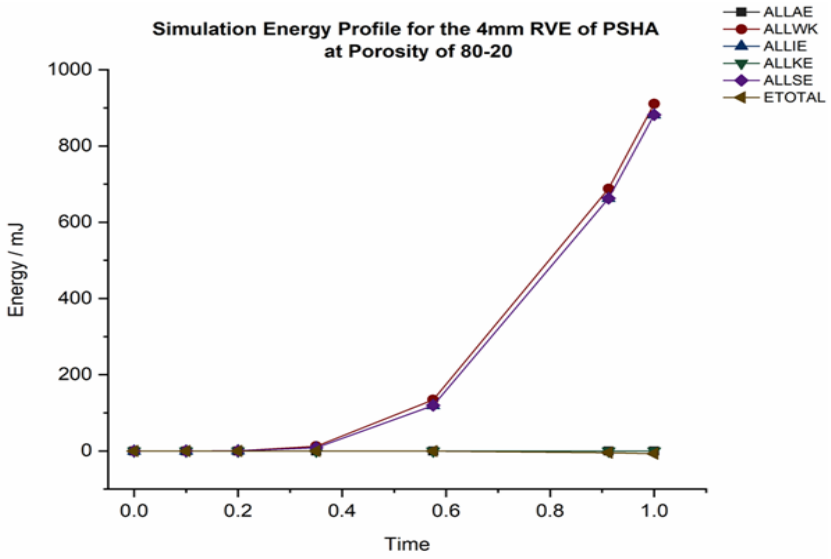

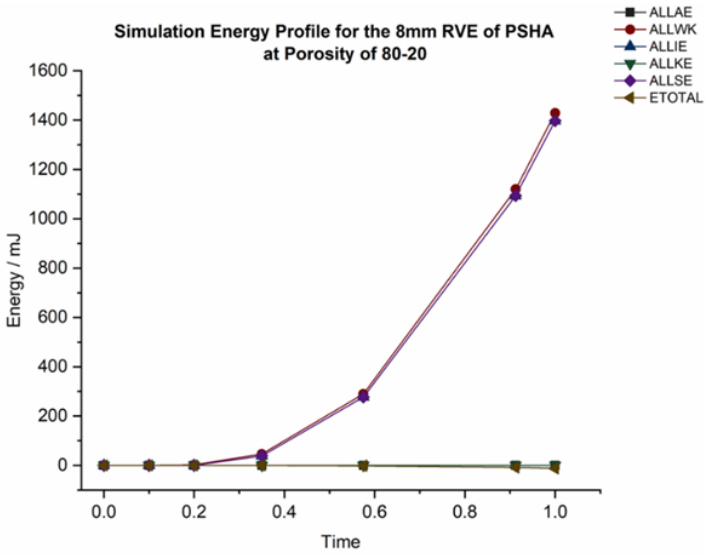

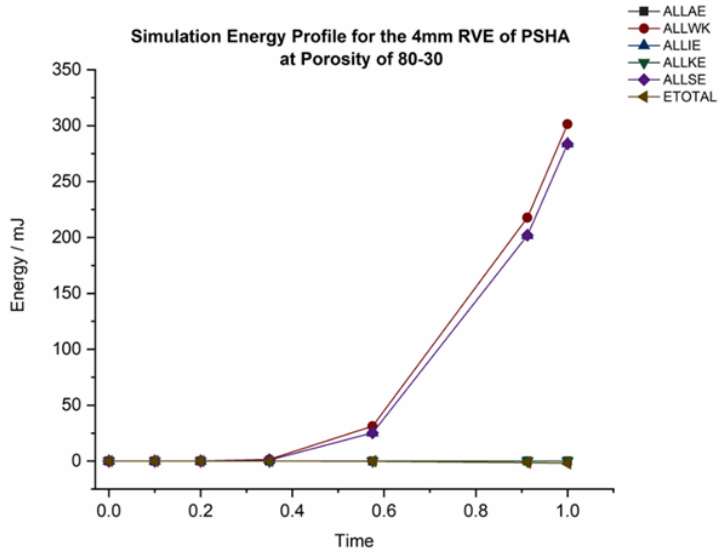
Simulation Energy Profile for the 4mm RVE of PSHA
at Porosity of 80-30
ALLAE
ALLWK
ALLIE
ALLKE
ALLSE
ETOTAL
Energy / mJ
Time
0
50
100
150
200
250
300
350
0.0
0.2
0.4
0.6
0.8
1.0

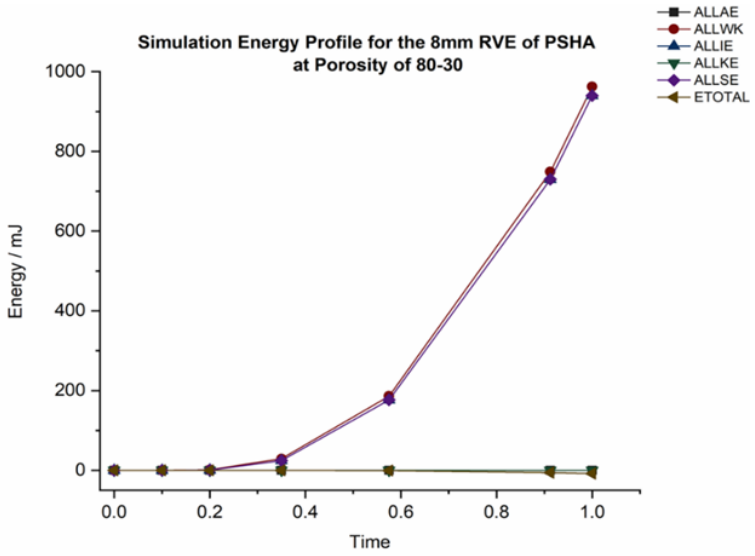
Simulation Energy Profile for the 8mm RVE of PSHA
at Porosity of 80-30
ALLAE
ALLWK
ALLIE
ALLKE
ALLSE
ETOTAL
Energy / mJ
Time
0
200
400
600
800
1000
0.0
0.2
0.4
0.6
0.8
1.0

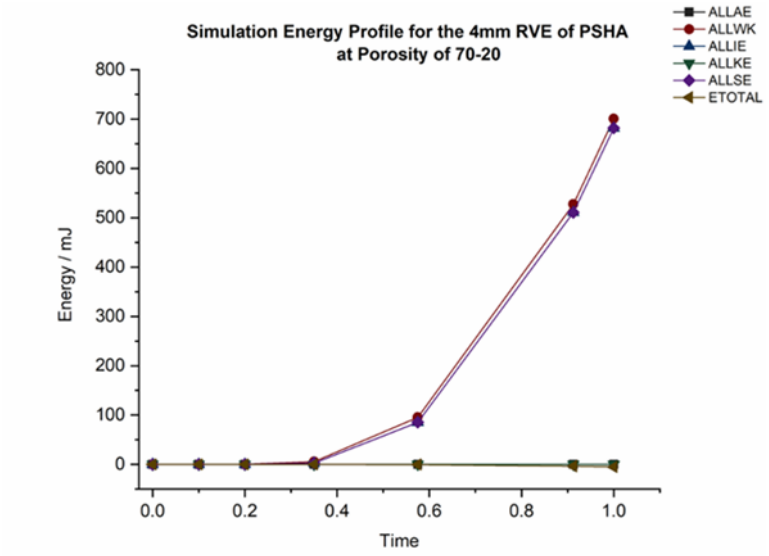
Simulation Energy Profile for the 4mm RVE of PSHA
at Porosity of 70-20
ALLAE
ALLWK
ALLIE
ALLKE
ALLSE
ETOTAL
Energy / mJ
Time
0
100
200
300
400
500
600
700
800
0.0
0.2
0.4
0.6
0.8
1.0

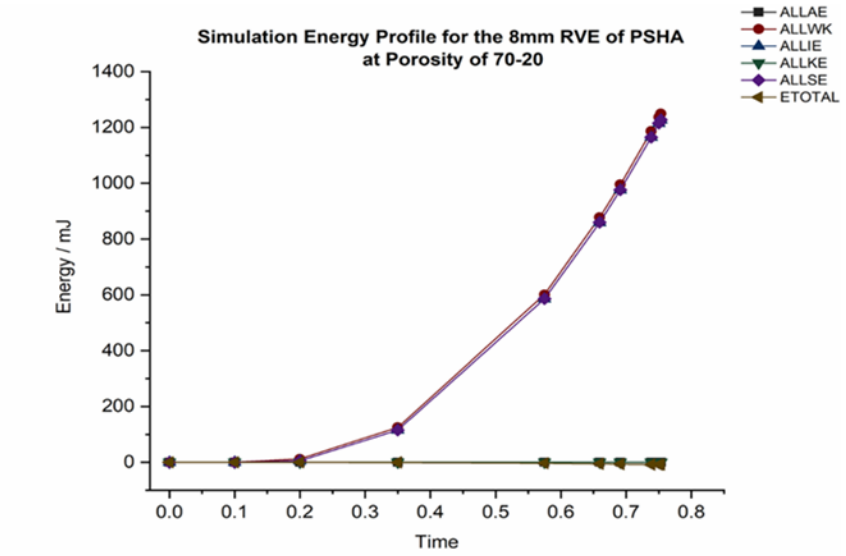
Simulation Energy Profile for the 8mm RVE of PSHA
at Porosity of 70-20
ALLAE
ALLWK
ALLIE
ALLKE
ALLSE
ETOTAL
Energy / mJ
Time
0
200
400
600
800
1000
1200
1400
0.0
0.1
0.2
0.3
0.4
0.5
0.6
0.7
0.8

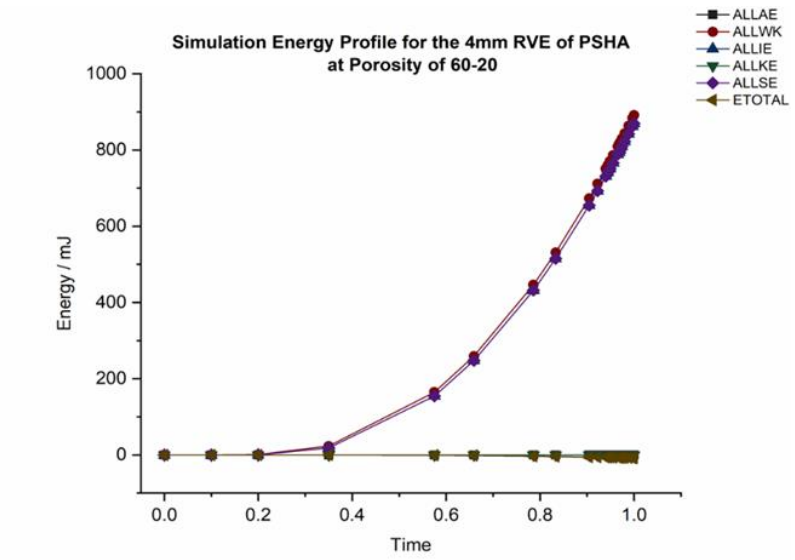
Simulation Energy Profile for the 4mm RVE of PSHA
at Porosity of 60-20
ALLAE
ALLWK
ALLIE
ALLKE
ALLSE
ETOTAL
Energy / mJ
Time
0
200
400
600
800
1000
0.0
0.2
0.4
0.6
0.8
1.0

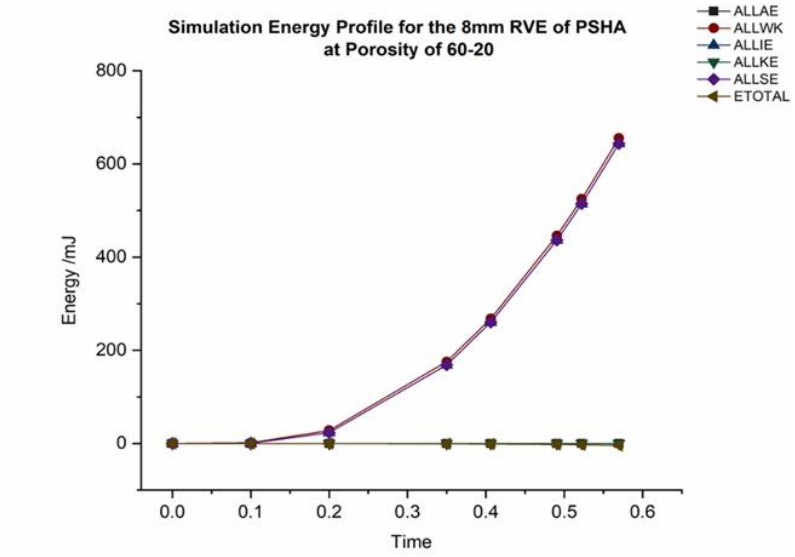
Simulation Energy Profile for the 8mm RVE of PSHA
at Porosity of 60-20
ALLAE
ALLWK
ALLIE
ALLKE
ALLSE
ETOTAL
Energy /mJ
Time
0
200
400
600
800
0.0
0.1
0.2
0.3
0.4
0.5
0.6

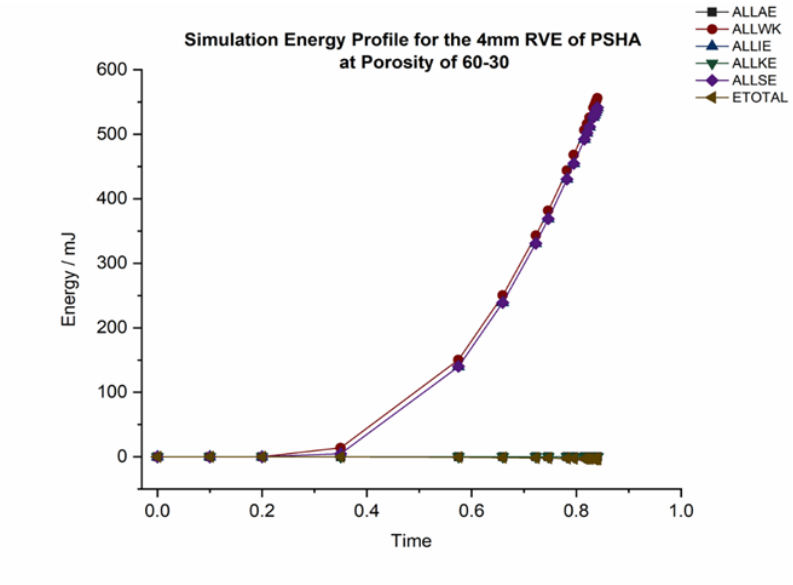
Simulation Energy Profile for the 4mm RVE of PSHA at Porosity of 60-30
ALLAE
ALLWK
ALLIE
ALLKE
ALLSE
ETOTAL
Energy / mJ
Time
0
100
200
300
400
500
600
0.0
0.2
0.4
0.6
0.8
1.0

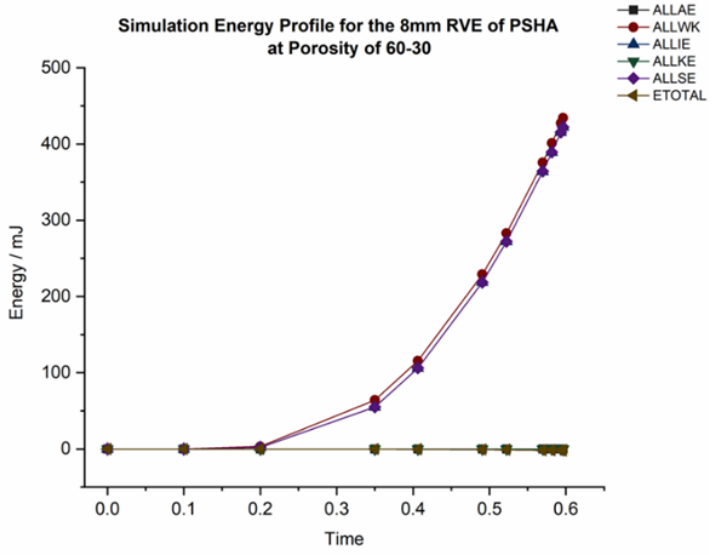
Simulation Energy Profile for the 8mm RVE of PSHA at Porosity of 60-30
ALLAE
ALLWK
ALLIE
ALLKE
ALLSE
ETOTAL
Energy / mJ
Time
0
100
200
300
400
500
0.0
0.1
0.2
0.3
0.4
0.5
0.6

Energy conversion values

Material	RVE	Strain applied / $\mu\varepsilon$	Model	ALLSE contribution to ALLIE %
8020	4	50000	All	100
8020	8	50000	All	100
8020	12	50000	All	100
8030	4	50000	All	100
8030	8	50000	All	100
8030	12	50000	All	100
7020	4	50000	All	100
7020	8	50000	All	100
7020	12	50000	All	100
6020	4	50000	All	100
6020	8	50000	All	100
6020	12	50000	All	100
6030	4	50000	All	100
6030	8	50000	All	100
6030	12	50000	All	100

Material	RVE	Strain applied	Model	ALLWK contribution to ALLSE %
82% - Hydroxyapatite	4mm	50000	All Models	88
82% - Hydroxyapatite	8mm	50000	All Models	93
82% - Hydroxyapatite	12mm	50000	All Models	96
83% - Hydroxyapatite	4mm	50000	All Models	87
83% - Hydroxyapatite	8mm	50000	All Models	93
83% - Hydroxyapatite	12mm	50000	All Models	97
72% - Hydroxyapatite	4mm	50000	All Models	93
72% - Hydroxyapatite	8mm	50000	All Models	96
72% - Hydroxyapatite	12mm	50000	All Models	97
62% - Hydroxyapatite	4mm	50000	All Models	94
62% - Hydroxyapatite	8mm	50000	All Models	96
62% - Hydroxyapatite	12mm	50000	All Models	97
63% - Hydroxyapatite	4mm	50000	All Models	96
63% - Hydroxyapatite	8mm	50000	All Models	94
63% - Hydroxyapatite	12mm	50000	All Models	92

Section A-5 Mesh convergence